Aerosol and Surface Properties Remote Sensing using AATSR

Haiyan Huang

Submitted for the degree of Doctor of Philosophy in Physics

Trinity term 2013

Atmospheric, Oceanic and Planetary Physics

Department of Physics

University of Oxford

Abstract

This thesis describes a new algorithm based on the optimal estimation approach for the retrieval of atmospheric aerosol and surface properties from the Advanced Along-Track Scanning Radiometer (AATSR). This algorithm is a further development on the Oxford-RAL Retrieval of Aerosol and Cloud (ORAC). The new algorithm is set up to use both visible and infrared channels of AATSR to retrieve aerosol optical depth (AOD), effective radius, white sky albedo at four wavelengths (550, 670, 870, and 1600 nm), surface temperature and aerosol layer height.

This thesis can be divided into three main parts : 1) the development of the new ORAC algorithm, 2) comparisons of the retrieved AOD with the aerosol products from visible-channel ORAC retrieval: GlobAEROSOL, and with the measurements from AErosol RObotic NETwork (AERONET), and 3) validations of the retrieved sea surface temperature (SST) with the measurements from ship-based radiometers (Infrared Sea surface temperature Autonomous Radiometer, ISAR) and the measurements from drifting buoys.

In this thesis aerosols are assigned to four classes, marine clean at two different relative humidities, spherical dust and non-spherical dust. The estimated retrieval error is 0.012 in AOD and 0.083 K in SST. Comparing with the GlobAEROSOL products, the new algorithm (denoted by ORAC) retrieves lower AOD (0.071 ± 0.012) (median ± RMS) and higher sea surface albedo globally (0.067 ± 0.006). The lower AOD, which also occurs in regional scales, is a promising result as previous studies showed GlobAEROSOL overestimated AOD especially over open ocean. The comparison with ground-based measurements (AERONET) shows a good agreement between ORAC AOD and AERONET AOD over ocean, the correlation is 0.820 at 550 nm and 0.807 at 870 nm, and the differences in AOD between the two datasets are 0.067 ± 0.214 for 550 nm and 0.064 ± 0.167 for 870 nm. In contrast weaker corrections,

0.312 at 550 nm and 0.275 at 870 nm, are found over land, and the median difference between the two datasets are nearly 0.2 for both 550 μm and 870 μm.

For three collocation criteria, the ORAC retrieved SST shows very high correlations with ISAR measurements (better than 0.980). Comparing with ISAR, ORAC SST has positive biases (0.150 to 0.117 K) and relative significant root mean squares (RMS) (0.481 to 0.430 K). Comparing with the drifting buoy measurements, the bias in retrieved SST is -0.067 ± 0.366 K for all the matches and -0.003 ± 0.298 K for the matches under high wind speed conditions (≥ 6 ms^{-1}). The error analysis indicates the uncertainties in temperature profile, water vapour profile, surface emissivity and forward model may affect the accuracy of retrieved SST.

These validation results suggest that the new ORAC algorithm is a successful approach to aerosol and surface retrieval over ocean, which is able to add to the current knowledge by improving current estimates of aerosol and surface properties. Most validation results presented in this thesis are under conditions of low AOD, it can been seen that the retrieved SST is not severely biased. Further validation is required to estimate the performance of ORAC at different levels of aerosol loading.

Contents

List of Figures

List of Tables

Chapter 1

Atmospheric aerosols and sea surface temperature

1.1 Atmospheric aerosols

1.1.1 Definition of atmospheric aerosols

Atmospheric aerosols are minute liquid or solid particles suspended in the atmosphere, with typical diameters ranging over four orders of magnitude from a few nanometers to tens of micrometers. Aerosols are usually assigned into one of the following three size categories: nucleation mode (diameter ≤ 0.1 μm), accumulation mode (0.1 μm $<$ diameter ≤ 2.5 μm) and coarse mode (diameter > 2.5 μm). The nucleation mode and accumulation mode together constitute fine mode particles. In general, the fine mode particles dominate with respect to number of particles but contribute little to particle mass, coarse mode aerosols are small in number compared to the fine mode but contain the large portion of mass. Aerosols can be formed by processes occurring on land or water and then ejected directly into the atmosphere as particles (primary aerosols), or formed in the atmosphere from precursor gases (secondary aerosols). Primary aerosols come from both natural and anthropogenic sources, such as ocean wave breaking, biomass burning, volcanic eruption, and fossil fuel burning. Secondary aerosols are created in the atmosphere from precursor gases such as sulphur dioxide (SO_2), nitrogen oxides (NO_x), volatile organic compounds (VOC_s). Precursor gases originate from dimethyl sulphide (DMS) oxidation, biomass burning, vegetation emission, industry and vehicle release. The bulk of aerosols is present in the lower troposphere, where aerosol concentrations are typically 1 to 2 orders of magnitude higher than in the upper troposphere (Huang et al., 2009; Liu et al., 2009). Depending on aerosol properties and meteorological conditions, the lifetimes of aerosols span from a few minutes to weeks. Two types of mechanism are responsible for removing aerosols from the atmosphere: dry deposition and wet deposition. Dry deposition removes particles through gravitational settling or collision with gas molecules, gravitational settling is more efficient for large particles, and collision is more efficient for small particles. Wet deposition involves precipitation, aerosols can be incorporated into cloud droplets, and transported to the ground by precipitation (rain out), or hit by falling raindrops and deposited with raindrops (sweep out). Sweep out is more important for larger particles and rain out is efficient for all particles. The geographically localized sources and sinks, as well as relatively short lifetimes, give aerosols extreme spatial and temporal inhomogeneities, indicating local-scale influences. Aerosols regularly travel over long distances with large-scale circulations, demonstrating the global scope of influences (Kulmala et al., 2000; Andreae and Crutzen, 1997; Hildemann et al., 1991). Figure 1.1 illustrates the processes involved in the production, growth, and removal of aerosols in the atmosphere.

1.1.2 Aerosol effects

Atmospheric aerosols affect the entire planet through their roles in the atmospheric chemistry, influences on air quality and human health, as well as effects on climate. In order to quantify the effects on climate the concept of radiative forcing is defined, it shows the changes in the radiative budget of the Earth due to changes in specific atmospheric components. For example, according to IPCC (2007), the increase in

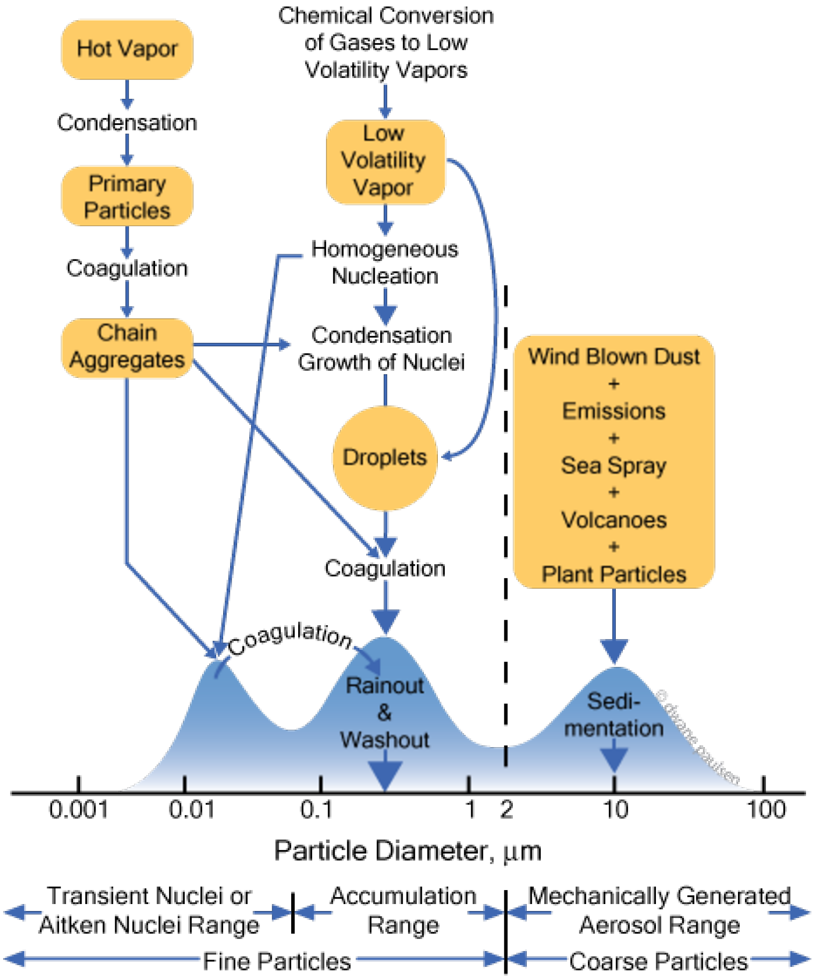

Figure 1.1: Idealised schematic of the distribution of particle surface area of atmospheric aerosol, including sources and sinks for the modes. (Seinfeld and Pandis, 1998; Whitby and Cantrell, 1976).

greenhouse gases over the industrial period exerts a net warming influence (positive forcing) on the Earth's climate, and the associated warming radiative forcing is estimated to be 2.3 ± 0.2 Wm^{-2}. Unlike greenhouse gases, which are long-lived and fairly uniformly distributed over the Earth, aerosols are heterogeneously dispersed due to their short lifetimes and strong tropospheric interactions. As a consequence, aerosol radiative forcing is much more complex and associated with a large uncertainty. The uncertainty in aerosol radiative forcing is one of the great contributors to the uncertainty in climate change.

Atmospheric aerosols can influence the radiative budget of the Earth directly and indirectly. Direct radiative forcing is the influence of aerosols on the planet albedo by scattering and absorbing short and long wave radiation, thereby altering the radiative balance of the Earth-atmosphere system. Direct radiative forcing relates to their abilities of scattering and absorbing solar and infrared radiation. Many studies have been carried out to access aerosol direct radiative forcing, either using ground-based measurements (Garca et al., 2012; Alam et al., 2011; Yu et al., 2006), or satellite measurements (Thomas et al., 2013; Benas et al., 2011; Kaufman et al., 2005; Bellouin et al., 2005), or model calculations (O'Donnell et al., 2011; Schulz et al., 2006). Significant differences exist between different measurements/models, the magnitude and sign are highly variable. On a global average, scattering predominates and the sum of direct radiative forcing is almost negative. According to IPCC (2007), the direct radiative forcing of anthropogenic aerosols is between -0.9 and -0.1 Wm^{-2} with best estimate of -0.5 Wm^{-2}. Based on fifteen global aerosol models, Myhre et al. (2012) report the direct radiative forcing due to anthropogenic aerosols has a range from -0.58 to -0.02 Wm^{-2} with a mean of -0.30 Wm^{-2}. Based on satellite measurements, Yu et al. (2006) estimate the direct radiative forcing is -5.5 ± 0.2 Wm^{-2} for global ocean, while over land it is -4.9 ± 0.7 Wm^{-2}. Based on satellite and in situ measurements Thomas et al. (2013) evaluate the global mean of direct radiative forcing to be -6.7 ± 3.9 Wm^{-2}. For regional scales, the direct radiative forcing can be up to ten times greater than the global mean, especially over the areas close to the sources

(Alam et al., 2011; Benas et al., 2011; Kim et al., 2011).

Aerosol indirect radiative forcing includes their impacts on cloud albedo (first indirect effect) and cloud lifetime (second indirect effect). Aerosols can act as cloud condensation nuclei (CCN) or ice nuclei (IN) on which water vapour condenses when relative humidity increases. The microphysical and radiative properties of a cloud are closely linked to the nature of CCN or IN from which it forms. As most of aerosols are large enough to be CCN, the number of CCN is roughly proportional to the number of aerosols (Rosenfeld et al., 2011, 2008). For a given cloud, an increase in the population of aerosols leads to an increase in the number of CCN and a reduction in cloud drop size; reduced cloud drop sizes enhance the cloud albedo and ultimately increase the amount of solar radiation reflected back to space and cool the atmosphere and the Earth's surface (Andreae et al., 2004; Charlson and Heintzenberg, 1995; Twomey, 1977). On the other hand, reduced cloud drop sizes can suppress precipitation and prolong cloud lifetime and further reduce solar radiation reaching the Earth's surface.

The effects of indirect radiative forcing on climate system are much poorer understood and quantified than the direct forcing. The indirect radiative forcing is significant but the magnitude and sign of it are not fully understood, as exemplified, e.g., by the results of Wilcox (2010); Sandu et al. (2008); Xue et al. (2008); Wood (2007); Feingold et al. (2007). According to IPCC (2007) this effect is between -1.8 and -0.3 Wm^{-2} with best estimate of -0.7 Wm^{-2} on a global scale.

Aerosols also have a semi-direct forcing which is associated with the ability of absorbing radiation. Absorbing aerosols, such as black carbon or silica dust, are capable of changing temperature profile by absorbing solar or infrared radiation. The absorbing aerosols concentrated in the low troposphere can change the low level convergence and cloud formation. It is believed that absorbing aerosols suspended near clouds can contribute to cloud evaporation, hence lead to a loss in cloud cover (Bollasina et al., 2008; Menon et al., 2002; Chung et al., 2002).

Aerosol radiative forcing has important implications to large/regional scale atmospheric circulations. Several studies (Wang, 2013; Pandithurai et al., 2008; Wild et al., 2005; Giorgi and Bi, 2002; Meywerk and Ramanathan, 1999) show that the reflecting or absorbing aerosols can lead to a cool surface temperature by blocking radiation reaching the surface, with a consequent temperature gradient between the area underneath the aerosol layer and surrounding regions, as well as a reduced evaporation rate. The cooling effect is strongest in the northern Hemisphere owing to heavy anthropogenic aerosol loading and frequent occurrence of dust storms, and the temperature gradient can cause a shift of Intertropical Convergence Zone (ITCZ) as well as the associated rainfall belt.

In addition to the radiative forcing on climate, aerosols are of importance to the ecosystem. The radiation incident upon the Earth's surface from the Sun that has not been altered by the atmosphere is defined as direct radiation. The radiation scattered by the atmosphere and incident upon the surface with different angles is defined as diffuse radiation. Several studies show that an increased aerosol loading leads to an increase in diffuse radiation (Qian et al., 2007; Kvalevag, 2007; Picchiazzi and Gautier, 2003). It is believed that diffuse radiation is more important for photosynthetic efficiencies because it comes from evenly distributed directions around plants, instead of from a single direction as direct radiation. Crop scientists have long recognized that the photosynthetic efficiency for diffuse radiation is higher than that for direct radiation (Kanniah et al., 2012; Gu et al., 2002; Spitters et al., 1986). An increase in aerosol loading potentially leads to an increase in ecosystem productivity.

Remote sensing has been widely applied for monitoring the Earth's surface parameters, such as surface albedo, surface temperature, and classification of surface features. For such applications radiation received by satellite sensors is altered by the atmosphere, and is not the same as that leaving the Earth's surface. In order to correct the atmospheric effects, the optical characteristics of the atmosphere must be known. The atmospheric gas scattering can be well-calculated by Rayleigh theory because of the small size of molecules. Gas absorption is usually minimized by choosing spectral bands free of strong absorption. However, aerosol scattering and absorption are difficult to characterize due to the high inhomogeneities in time and space. The correction of aerosol effects relies on a number of aerosol optical characteristics.

1.1.3 Aerosol optical properties

Aerosols can scatter and/or absorb incident radiation at different wavelengths. The scattering and absorption of a particle is determined by its size and chemical composition as well as the wavelength of incident radiation. The angular distribution of the scattered radiation of an aerosol particle can be assigned into two theoretical frameworks according to its size parameter x:

$$x = \frac{2\pi r}{\lambda}, \tag{1.1}$$

where r is the characteristic radius of the particle and λ is the wavelength of the incident radiation. The first category is Rayleigh scattering corresponding to the regime of $x \ll 1$, it usually refers to molecules or small spherical particles. The intensity of scattered radiation of Rayleigh scattering has a strong dependence on the incident wavelength. The second category is Mie scattering which can be applied to particles of arbitrary sizes, and can be used to describe the scattering of most of the aerosol particles. Mie theory is a complete analytical solution of Maxwell's equations for spherical particles. Rayleigh scattering is an extreme example of Mie scattering, in practice Rayleigh scattering is preferred if applicable because of its simple mathematical form.

The other term governing the scattering and absorption of an aerosol particle is the refractive index $\tilde{n}(\lambda)$ which is strongly dependent on its chemical composition and incident wavelength:

$$\tilde{n}(\lambda) = m(\lambda) + i\tilde{k}(\lambda), \tag{1.2}$$

where the real part $m(\lambda)$ represents scattering and the complex part $\tilde{k}(\lambda)$ is responsible for absorption.

Atmospheric aerosols are from a variety of sources and processes, and of a wide range of concentrations, sizes, shapes and chemical compositions. When a parallel radiation beam of wavelength λ passes through a thin layer of atmosphere, the incident radiation is attenuated by scattering and absorption of gases and aerosol particles, and only part of the incident radiation is transmitted in the forward direction (Figure 1.2). Following the Beer-Lambert-Bouguer Law, the intensity of transmitted radiation L can be calculated as:

$$L = L_0 e^{-k^{ext}(\lambda) l}, \tag{1.3}$$

where L_0 is the intensity of incident radiation; $k^{ext}(\lambda)$, referred to as the extinction coefficient, is a measure of the fraction of radiation lost from the incident radiation per unit thickness in a medium and usually has a unit of m^{-1} or km^{-1}, l is the distance of the radiation travels through the medium.

Both gases and aerosols are responsible for the extinction of the incident radiation:

$$k^{ext}(\lambda) = k_a^{ext}(\lambda) + k_g^{ext}(\lambda), \tag{1.4}$$

where $k_a^{ext}(\lambda)$ and $k_g^{ext}(\lambda)$ are the aerosol extinction coefficient and the gas extinction coefficient respectively. As extinction is the total effect of scattering and absorption, the extinction coefficient can be written as :

$$\begin{aligned} k_a^{ext}(\lambda) &= k_a^{sca}(\lambda) + k_a^{abs}(\lambda), \\ k_g^{ext}(\lambda) &= k_g^{sca}(\lambda) + k_g^{abs}(\lambda), \end{aligned} \tag{1.5}$$

where $k_a^{sca}(\lambda)$ is the aerosol scattering coefficient, $k_a^{abs}(\lambda)$ is the aerosol absorption coefficient, $k_g^{sca}(\lambda)$ and $k_g^{abs}(\lambda)$ are the gas scattering coefficient and the gas absorption coefficient respectively.

For a collection of particles, the $k_a^{ext}(\lambda)$ is given by:

$$k_a^{ext}(\lambda) = \int\limits_0^\infty \sigma_a^{exp}(\lambda, r) n(r)\, dr, \tag{1.6}$$

where $\sigma_a^{exp}(\lambda, r)$ is the extinction cross section of particles with radii between r and $r + dr$ for wavelength λ:

$$\sigma_a^{exp}(\lambda, r) = \sigma_a^{sca}(\lambda, r) + \sigma_a^{abs}(\lambda, r), \tag{1.7}$$

where $\sigma_a^{sca}(\lambda, r)$ and $\sigma_a^{abs}(\lambda, r)$ are aerosol scattering cross section and absorption cross section, $n(r)$ represents the number of particles with radii between r and $r + dr$, i. e. size distribution.

When particles are considered to be spherically shaped, the scattering efficiency $Q_a^{sca}(\lambda, r)$, absorption efficiency $Q_a^{abs}(\lambda, r)$ and extinction efficiency $Q_a^{ext}(\lambda, r)$ at wavelength λ can be calculated as:

$$\begin{aligned} Q_a^{sca}(\lambda, r) &= \frac{\sigma_a^{sca}(\lambda, r)}{\pi r^2}, \\ Q_a^{abs}(\lambda, r) &= \frac{\sigma_a^{abs}(\lambda, r)}{\pi r^2}, \\ Q_a^{ext}(\lambda, r) &= \frac{\sigma_a^{ext}(\lambda, r)}{\pi r^2}. \end{aligned} \tag{1.8}$$

The lognormal distribution is the most suitable representation for the size distribution of atmospheric aerosols:

$$n(r) = \frac{N_0}{\sqrt{2\pi}} \frac{1}{\sigma} \frac{1}{r} \exp\left[-\frac{(\ln r - \ln r_m)^2}{2\sigma^2} \right], \tag{1.9}$$

where r_m is model radius, σ is spread of the distribution, and N_0 is total particle number density.

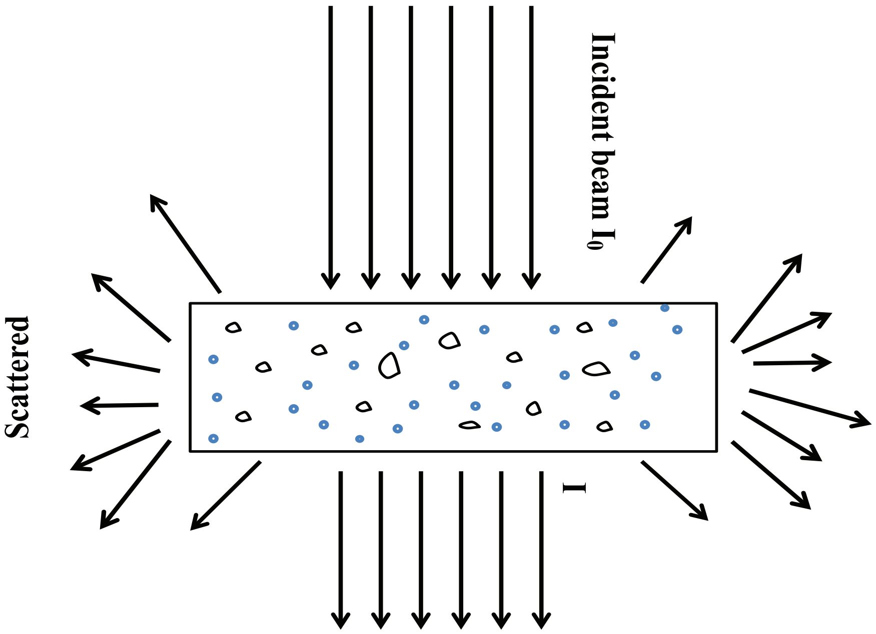

Figure 1.2: A parallel radiation beam passing through a thin atmospheric layer consisting of different aerosol particles.

For a population of spherical aerosols with a size distribution $n(r)$, the volume scattering/absorption/extinction coefficients $\beta_a^{sca}/\beta_a^{abs}/\beta_a^{ext}$ can be written as:

$$\beta_a^{sca}(\lambda) = \int_0^\infty \pi r^2 Q_a^{sca}(\lambda, r) n(r)\, dr,$$
$$\beta_a^{abs}(\lambda) = \int_0^\infty \pi r^2 Q_a^{abs}(\lambda, r) n(r)\, dr,$$
$$\beta_a^{ext}(\lambda) = \int_0^\infty \pi r^2 Q_a^{ext}(\lambda, r) n(r)\, dr. \tag{1.10}$$

Aerosol optical depth, AOD, $\tau(\lambda)$ is a measure of the amount of incident radiation scattered or/and absorbed by aerosols and is defined as the column integral of spectral aerosol extinction coefficients over the depth of the layer dz:

$$\tau(\lambda) = \int_{z}^{z+dz} \beta_a^{ext}(\lambda, z)\, dz. \tag{1.11}$$

In atmospheric science AOD often corresponds to the integrated aerosol extinction coefficients over a vertical path from the Earth's surface to outer space. It is a dimensionless quantity and the values of AOD vary widely, depending on the vertical profile of the aerosol extinction, which in turn is a complex function of aerosol physical and chemical properties.

Ångström exponent α is used to describe the spectral dependence of AOD between two wavelengths:

$$\alpha = -\frac{\log \frac{\tau(\lambda)}{\tau(\lambda_0)}}{\log \frac{\lambda}{\lambda_0}}, \tag{1.12}$$

where $\tau(\lambda)$ is the optical depth at wavelength λ, $\tau(\lambda_0)$ is the optical depth at the reference wavelength λ_0. Ångström exponent is inversely proportional to the size of particles, i. e. , high Ångström values are associated with smaller aerosol particles, and vice versa.

The relative contribution of scattering to extinction is expressed as the ratio between scattering coefficient and extinction coefficient, and is known as single scattering albedo $\omega(\lambda)$:

$$\omega(\lambda) = \frac{\beta_a^{sca}(\lambda)}{\beta_a^{ext}(\lambda)} = \frac{\beta_a^{sca}(\lambda)}{\beta_a^{abs}(\lambda) + \beta_a^{sca}(\lambda)}. \tag{1.13}$$

The value range of $\omega(\lambda)$ is $0 \leq \omega(\lambda) \leq 1$, more absorbing and smaller particles have lower $\omega(\lambda)$, for a pure absorber, $\omega(\lambda) = 0$ while for a pure scatterer $\omega(\lambda) = 1$. The $\omega(\lambda)$ can be calculated with Mie theory. For most of the atmospheric aerosols, $\omega(\lambda)$ is greater than 0.8 at 550 nm (Heintzenberg et al., 1997), Figure 1.3 shows the common range of $\omega(\lambda)$ for key aerosol types, summarised from Bergstrom et al. (2007); Schnaiter et al. (2006); Dubovik et al. (2002); Hess and Schult (1998). Particles with a $\omega(\lambda)$ greater than 0.85 are generally considered to cool the planet, and those with less than 0.85 tend to warm the planet (Hansen et al., 1981). The direct radiative forcing of aerosols is very sensitive to $\omega(\lambda)$, a change of 0.1 in $\omega(\lambda)$ can change the sign of direct radiative forcing (Hansen et al., 1997).

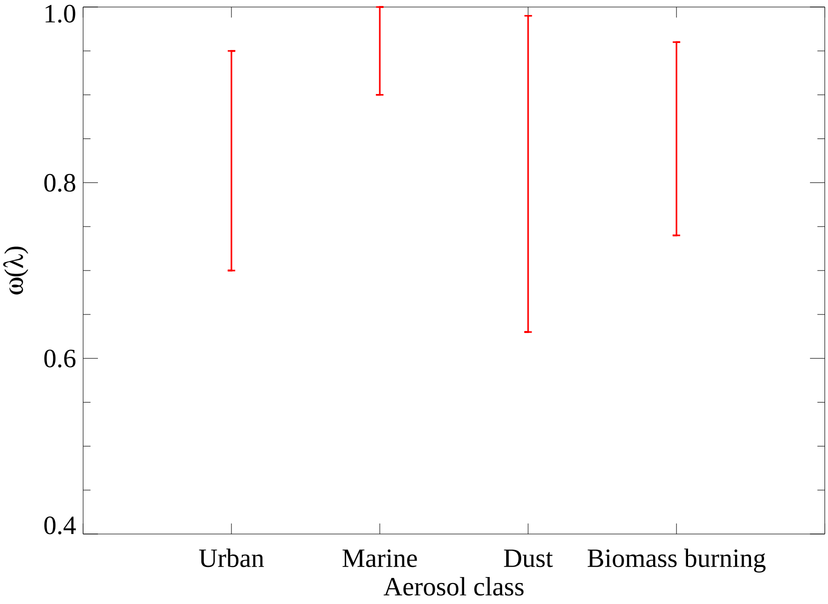

Figure 1.3: Value range of single scattering albedo $\omega(\lambda)$ at 500 nm or 550 nm of key aerosol types, summarised from Bergstrom et al. (2007); Schnaiter et al. (2006); Dubovik et al. (2002); Hess and Schult (1998).

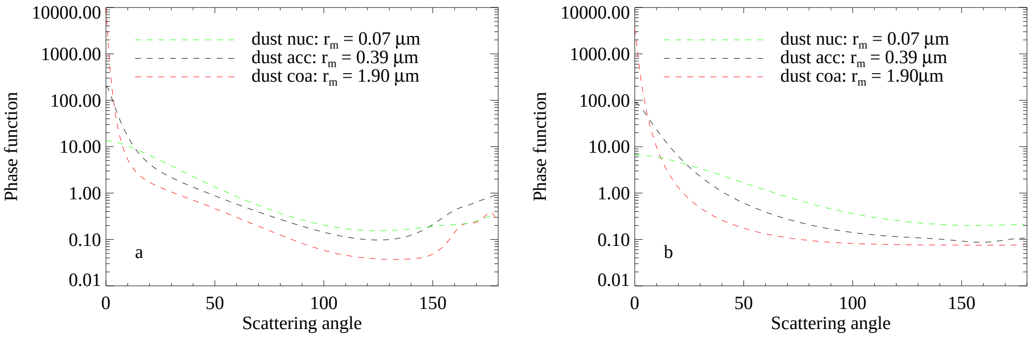

Figure 1.4: Phase functions calculated for lognormal aerosol size distributions; the aerosol properties are given in Table 1.1; dust nuc: dust nucleation mode, dust acc: dust accumulation mode, dust coa: dust coarse mode; r_m is aerosol mode radius of lognormal distribution; a) $\lambda = 550$ nm, and b) $\lambda = 11$ μm.

parameter	dust (nucleation)	dust (accumulation)	dust (coarse)
volume density N_0 (cm^{-3})	269.5	30.5	0.142
width of distribution σ	1.95	2.00	2.15
mode radius r_m (μm)	0.07	0.39	1.90
refractive index $\tilde{n}$, 550 nm	$1.53 - 0.0055i$	$1.53 - 0.0055i$	$1.53 - 0.0055i$
refractive index $\tilde{n}$, 11 μm	$1.83 - 0.2000i$	$1.83 - 0.2000i$	$1.83 - 0.2000i$

Table 1.1: Microphysical properties of dust aerosols (Hess and Schult, 1998) used in the calculation of phase function in Figure 1.4.

The intensity of radiation scattered by a particle is strongly dependent on the angle between the incident radiation and the scattered radiation θ, particle size and the wavelength of incident radiation. Phase function $\tilde{P}(\lambda, r, \theta)$ describes the angular distribution of the scattered intensity by a particle:

$$\tilde{P}(\lambda, r, \theta) = \frac{L(\lambda, r, \theta)}{\int_0^\pi L(\lambda, r, \theta) \sin\theta \, d\theta}, \tag{1.14}$$

where $L(\lambda, r, \theta)$ is the intensity scattered in the direction of θ, r is the radius of the particle. The phase function of a collection of particles with a size distribution of $n(r)$ can be given as:

$$P(\lambda, \theta) = \frac{1}{\beta_a^{ext}} \int_0^\infty \pi r^2 Q_a^{sca}(\lambda, r) \tilde{P}(\lambda, r, \theta) n(r) \, dr. \tag{1.15}$$

As illustrated in Figure 1.4, the phase function of a collection of particles is influenced by the incident wavelength and particle size. When particle sizes are small as compared to the incident wavelength, the phase function tends to be systematic in forward and backward directions, with increasing particle sizes, the radiation is more scattered in the forward direction. For large particles, the radiation is concentrated in the angle between 0° to 20°.

Asymmetry parameter (anisotropy factor) for a single aerosol particle, $\tilde{g}(\lambda, r)$, represents the degree of asymmetry of the phase function. Its expression is derived

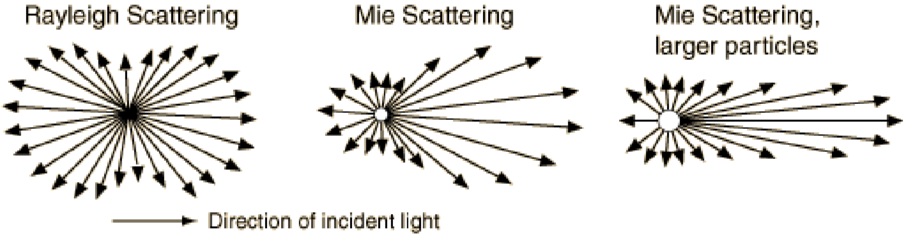

Figure 1.5: Schematic description of light scattering by particles with different size parameters. The size parameter is increasing from left to right; taken from http://hyperphysics.phy-astr.gsu.edu/hbase/atmos/blusky.html.

from the cosine weighted average of the phase function over the scattering plane:

$$\tilde{g}(\lambda, r) = \frac{1}{2}\int_{0}^{\pi} \tilde{P}(\lambda, r, \theta)\cos\theta\sin\theta\, d\theta. \tag{1.16}$$

The range of $\tilde{g}(\lambda, r)$ is from -1 for entirely backscattering particles to 1 for entirely forward scattering particles, if $g = 0$ then the radiation is scattered equally in backward and forward directions. As shown in Figure 1.5, $\tilde{g}(\lambda, r)$ is strongly dependent on particle size and incident radiation wavelength. The phase function of small particles is systematical both in forward and backward directions, while large particles favor forward directions. In reality the value of $\tilde{g}(\lambda, r)$ is from 0.6 to 0.8 (Andrews et al., 2006; Haywood and Shine, 1995). For a collection of aerosols with a size distribution $n(r)$, the asymmetry parameter $g(\lambda)$ is:

$$g(\lambda) = \frac{1}{\beta_a^{sca}(\lambda)}\int_{0}^{\infty} \pi r^2 Q_a^{sca}(\lambda, r)\tilde{g}(\lambda, r)n(r)\, dr. \tag{1.17}$$

Figure 1.6 represents the values of g for key aerosol types summarised from Bergstrom et al. (2007); Schnaiter et al. (2006); Dubovik et al. (2002); Hess and Schult (1998).

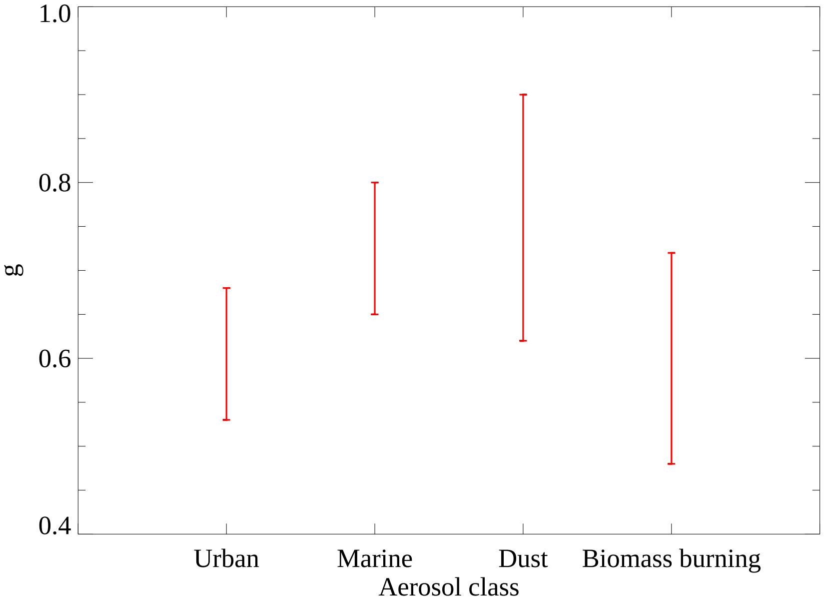

Figure 1.6: Same as Figure 1.3, but for asymmetry parameter g.

According to Hansen and Pollack (1970), the extinction coefficient, single scattering albedo, phase function and asymmetry parameter of a population of aerosols with size distribution $n(r)$ are mainly dependent on the mean particle radius for extinction, which is defined as effective radius r_e:

$$r_e = \frac{\int\limits_0^\infty \sigma_a^{ext}(r) r n(r)\, dr}{\int\limits_0^\infty \sigma_a^{ext}(r) n(r)\, dr}, \tag{1.18}$$

where σ_a^{ext} can be expressed as:

$$\sigma_a^{ext}(r) = \pi r^2 Q_a^{ext}(r), \tag{1.19}$$

assuming the extinction efficentcy $Q_a^{ext}(r)$ of a material is constant, cancel it from Equation 1.18:

$$r_e = \frac{\int\limits_0^\infty r^3 n(r)\, dr}{\int\limits_0^\infty r^2 n(r)\, dr}. \tag{1.20}$$

1.1.4 Aerosol classes

Unlike greenhouse gases which are generally long-lived and well-mixed across the globe, atmospheric aerosols are distributed unevenly, and the properties of atmospheric aerosols vary rapidly and are highly correlated to the sources. At any place in the atmosphere, atmospheric aerosols exist as mixtures of several components emitted from different origins. An aerosol class is a mixture of various components that may have different sizes, shapes, chemical compositions. A number of common classes used in remote sensing are described below.

1.1.4.1 Urban

Atmospheric aerosol particles in the populated cities and their downwind regions are dominated by urban aerosols resulting from fossil fuel combustion, including industrial activity, traffic emission and domestic heating. Urban aerosols are short-lived (days), relatively small in size (diameter $\leq 2.5\ \mu$m) and consist mostly of fine mode particles that can be harmful to human health. In spite of their short lifetimes, urban aerosols can travel long distances from sources to downwind regions, demonstrating local to global scale influences. Northeast America, eastern Asia, and Europe are of high loadings of urban aerosols.

The principal components of urban aerosols are sulphate, nitrate, organic carbon (OC) and black carbon (BC). According to IPCC (2007), sulphate aerosols are produced via sulphur dioxide (SO_2) in the atmosphere, and fossil fuel combustion is the main source of SO_2 (about 72%). Several studies show that sulphate aerosols impact the climate by reflecting the incoming solar radiation back to space, and the direct radiative forcing is estimated to be from -0.9 to -0.3 Wm^{-2}. OC consists of many complex chemical compounds that are released either as primary particles or organic gases. Like sulphate aerosols, OC particles are also important scatterers and the estimated direct radiative forcing due to OC from fossil fuels spans from -0.24 to -0.02 Wm^{-2} (IPCC, 2007; Kanakidou et al., 2005; Cooke et al., 1999; Penner et al., 1998). BC is a product from incomplete combustion, according to Ramanathan and Carmichael (2008), about 40% of BC is produced by fossil fuels. Recent researches show that BC particles have the ability to absorb solar radiation, and lead to enhanced low level convergence and precipitation (Cappa et al., 2012; Jacobson, 2004; Wang, 2004; Jacobson, 2002; Koch, 2001).

1.1.4.2 Biomass burning

Biomass burning aerosols are produced from forest or grassland fires, including human-induced burning for land clearing and agriculture, as well as naturally occurring burning caused by lightnings. The highest proportion of biomass burning occurs in tropical regions where fires are associated with agricultural activities and forest destruction. Dense smoke plumes are found annually downwind of southern America (August-October), central America (April and May), southern Africa (July-September) and central Africa (January-March) (Kaufman et al., 2002). Biomass burning is an important source of trace gases and atmospheric particles (Reid et al., 2005; Simoneit, 2002; Palacios-Orueta et al., 2004; Andreae and Merlet, 2001). Plumes from biomass burning are dominated by fine mode particles with a median diameter of $0.1 - 0.15$ μm, the composition of particles depends on fuel type and stage of burning process (Janhll et al., 2010; Jacobson, 2001b).

The two major components of biomass burning aerosols are BC and OC, although the ratio of BC to OC is generally small, the warming effect exerted by BC may cancel the cooling effect caused by OC by a few tenths of Wm^{-2}. In spite of the warming effect of BC, the net radiative forcing of biomass burning aerosols is negative over the majority of the globe. The estimates of BC and OC emissions vary in a wide range due to insufficient observations and complexities of the associated physical and radiative processes: consequently the calculated radiative forcing varies widely depending on the mixing assumptions and size distributions (Haywood and Boucher, 2000; Myhre et al., 2003; Iacobellis et al., 1999; Penner et al., 1998, 1992).

1.1.4.3 Wind-blown dust

Wind-blown dust aerosols are soil particles lofted from the Earth's surface into the atmosphere by wind erosion. The process taking soil particles from the surface into the atmosphere depends on wind intensity, soil wetness, soil texture and land cover. Wind-blown dust sources include deserts, dry lake beds, semi arid fringes and dry regions where vegetation has been disturbed by human activities. The major source regions are distributed over northern Africa, the Arabian peninsula, central and southern Asia, as well as Australia. The estimated total source strength is from 1000 to 3000 Tg/yr and some studies suggest that 20% to 50% of the total dust burden originates from anthropogenic activities (Seinfeld and Pandis, 1998; I. N and Toon, 1996; Tegen et al., 1996). Wind-blown dust aerosols are relatively large in size (radius $\geq$ 0.6 μm) and generally fall out of the atmosphere after a short flight. However, they can be taken to high altitudes by intense dust storms and travel long distance from source regions. The long distance transport plays an important role in climate as well as in the ecosystem by adding nutrients to soils and to the oceans (Ginoux et al., 2001; Prospero, 1998).

Wind-blown dusts can be entrained by numerous atmospheric phenomena, redistribute energy by scattering and absorbing both solar and terrestrial radiation (El-Metwally et al., 2011; Zhang et al., 2010). Although the radiative forcing has been recognized for decades, the precise values are difficult to determine owing to uncertainties in chemical composition, size distribution, inhomogeneities in time and space as well as the spherical assumption. According to IPCC (2007), the global mean short wave radiative forcing is negative (-0.46 – -0.06 Wm^{-2}) due predominately to scattering, and global mean long wave forcing is positive (0.05 – 0.34 Wm^{-2}). Wang et al. (2013) estimate the global means of short wave (long wave) radiative forcing due to spherical dust particles and non-spherical dust particles are -0.55 (0.052) Wm^{-2} and -0.48 (0.049) Wm^{-2} respectively. Local or regional mean of radiative direct forcing due to dust may be extremely high (at magnitude of 10 Wm^{-2} for short wave and 1 Wm^{-2} for long wave) (Valenzuela et al., 2012; El-Metwally et al., 2011; Kohler et al., 2011).

1.1.4.4 Marine

Aerosols in the marine environment comprise two distinct types: 1) primary sea salt aerosols which are produced by the bursting of bubbles and mechanical disruption of wave crests by the wind, thus the production of sea salt aerosols is strongly dependent on wind speed (Monahan et al., 1986; Blanchard, 1983); 2) secondary aerosols in the form of non-sea-salt (nss) sulphate and organic species, produced by gas to particle conversion processes. The source strength of marine aerosols is estimated to be within a range of 1000 to 10000 Tg/yr (Gong et al., 1998; Tegen et al., 1997; Erickson and Duce, 1988). Approximately 72 % of the Earth's surface is covered by ocean, marine aerosols constitute an important part to the global aerosol loading and contribute about 44 % to the global AOD (O'Dowd and Leeuw, 2007). An important characteristic of marine aerosols is substantially low optical depth, especially over open ocean.

The size of marine aerosols spans over four orders of magnitude (about 0.01 to 10 μm in diameter), correspondingly the lifetimes also span a wide range. Marine aerosols play a important role in affecting the atmospheric radiative balance, scattering solar radiation, absorbing terrestrial radiation and emitting long wave radiation. Estimates of direct radiative forcing of marine aerosols vary widely (Dobbie et al., 2003; Takemura et al., 2002; Grini et al., 2002; Jacobson, 2001a). According to IPCC 2001, the global mean radiative forcing due to marine aerosols falls in a range of -1.51 to -5.03 Wm^{-2}. Unlike wind-blown dust aerosols, sea salt particles are very efficient CCN. By acting as CCN, they indirectly modulate the atmospheric radiative balance through their effective contributions to cloud formation and precipitation (Lehahn et al., 2011; Yoon and Brimblecombe, 2002). Various regional-based studies suggest that the indirect radiative forcing resulting from sea salt aerosols (-7 to -2 Wm^{-2}) may exceed their direct radiative forcing (Vinoj and Satheesh, 2004).

Besides the classes described above, there are some other classes used by different algorithms, such as marine pollution which is influenced by outflows from continents, volcanic ash which comes from volcanic eruptions, and continent clean which takes place at remote continental areas free of anthropogenic activities.

1.1.5 Aerosol satellite remote sensing

Atmospheric aerosol radiative forcing is one of the greatest uncertainties in climate predication. The uncertainty stems from the complex effects of aerosols in the atmosphere, and a lack of knowledge of aerosol properties and distributions. A better understanding of aerosol properties and distributions can improve the current understanding of aerosol radiative forcing. Because of short lifetimes, aerosols are highly variable both in time and space: satellite remote sensing has the advantage of providing extensive coverage in the shortest time interval, thereby allowing for better tracking of the regional and global properties. Retrieving certain aerosol properties from satellite remote sensing began in the mid-1970s, and a number of satellite sensors have been used, most notably AVHRR, TOMS, SeaWiFS, MODIS, and ATSR series (ATSRs). Table 1.2 summarises the major satellite sensors used for aerosol survey. Many satellites were originally designed for other purposes, for example, AVHRR was primarily used for monitoring weather systems and sea surface temperature (SST), TOMS was used for ozone detection, while the ATSRs were designed for global SST observation.

The spectral radiation detected by a satellite sensor is composed of solar radiation reflected by the Earth's surface and scattered by the atmosphere, as well as thermal emissions of surface and the atmosphere. The radiation reflected or emitted by the surface also interacts with the atmosphere. Retrieving aerosol properties from satellite remote sensing is a very challenging task, because the aerosol contribution to the observed signals at the satellite level must be separated from the contributions of the underlying surface and other atmospheric compositions, and in general

Table 1.2: Summary of major satellite sensors used for aerosol observation, modified from Chin et al. (2009) and King et al. (1999).

platform/instrument	year coverage	spatial coverage	main aerosol parameters
NIMBUS, EP, ADEOSI/TOMS	1979-2001	global land and ocean	optical depth, absorbing index, single-scattering albedo
AURA/OMI	2005-present	global land and ocean	optical depth, absorbing aerosol index, single-scattering albedo, absorbing optical depth
PARASOL/POLDER-1, -2	1997-present	global land and ocean	Ångström exponent, optical depth, fine-mode fraction, non-spherical fraction
ICESAT/ GLAS	2003-2009	global land and ocean	extinction/backscatter
CALIPSO/CALIOP	2006-present	global land and ocean	extinction/backscatter, depolarization ratio
NOAA/AVHRR	1981-present	global ocean	Ångström exponent, optical depth
TERRA, AQUA/MODIS	2000-present	global land and ocean	optical depth, fine-mode fraction, Ångström exponent, effective radius and asymmetry factor (only for ocean)
SEASTAR/SEAWiFS	1997-2010	global ocean	Ångström exponent, optical depth
MSG/SEVIRI	2002-present	global land and ocean	Ångström exponent, optical depth
TERRA/MISR	2000-present	global land and ocean	Ångström exponent, optical depth, small, medium, large fractions, non-spherical fraction
ERS-2/ATSR-2	1995-2011	global land and ocean	Ångström exponent, optical depth, effective radius
ENVISAT/ AATSR	2002-2012	global land and ocean	Ångström exponent, optical depth, effective radius
ENVISAT/MERIS	2002-2012	global land and ocean	Ångström exponent, optical depth
Sentinel 3/SLSTR	2014-	global land and ocean	Ångström exponent, optical depth

the contribution of aerosol is relatively small compared to the surface contribution, especially over bright surfaces. Ideally, an algorithm of aerosol retrieval from satellite measurements must be sensitive enough to the presences or changes of aerosols and free of interference from other factors. Most of aerosol remote sensing retrievals rely primarily on visible/near-infrared spectral domains and have been proven to be a success in supplying high quality datasets for comprehensive aerosol research. However, infrared spectra have been used to a more limited extent.

Using infrared spectra in aerosol retrieval is advantageous, particularly over bright surfaces, i. e. over desert or snow (Gangale et al., 2010; DeSouza-Machado et al., 2006; Merchant et al., 2006; Ellrod and Connell, 2003; Yu et al., 2002; Ackerman, 1997). Over bright surfaces it is difficult for visible spectra to distinguish aerosol contribution from the overwhelming surface signals. In contrast, the lofted aerosols may have a thermal contrast which can be detected by infrared spectra. Because of the longer wavelength, radiation in the infrared domain is sensitive to large particles, such as coarse mode wind-blown dust or sea salt. Moreover, infrared remote sensing provides a way to retrieve other parameters, for example, aerosol layer height and surface temperature; with infrared spectra it is also possible to do aerosol retrieval during the nighttime.

1.2 Sea surface temperature

SST is an important parameter in the climate system, and is closely related to the Earth's energy balance, atmospheric and oceanic circulation patterns and anomalies (Kanamitsu and Hwang, 2006; Mantua and Hare, 2002; Klein et al., 1999; Rodwell et al., 1999; Mann et al., 1998; Kaplan et al., 1998). Approximately 72 % of the globe is covered by ocean and because of the large heat capacity of water, ocean is an important thermal storage for the climate. The interactions between ocean and the atmosphere, including the exchanges of long wave radiation, momentum, heat associated with evaporation and condensation, take place via the uppermost layer of ocean. SST is one of the most important properties governing these interactions. SST is also a variable widely used for describing ocean circulation and dynamics. The abnormality in SST of the tropical central and western Pacific ocean has been linked to the Southern Oscillation Index and the El Niño phenomenon. SST has an important role in climate model and numerical weather prediction (NWP) as a boundary condition. A good knowledge of SST is therefore germane to the understanding of ocean physical processes, weather forecasting and climate change.

1.2.1 SST definition

The term SST is quite ambiguous, and can define many temperatures in the upper ocean depending on the depth below ocean surface. The vertical temperature variability of the upper ocean is complex. Following the standardised system used by the Group for High Resolution Sea Surface Temperature (GHRSST) (https://www.ghrsst.org/) (Figure 1.7), five types of SST are defined (Donlon et al., 2002; Emeryand et al., 2001; Barton, 2001) (Table 1.3).

temperature	depth represented	instrumentation
interface SST	infinitely thin	no instrument
skin SST	$\sim 10\ \mu$m	infrared radiometer
sub skin SST	~ 1 mm	microwave radiometer
subsurface SST (or bulk SST)	~ 1 m	buoy, ship, etc.
foundation SST	~ 10 m	buoy, ship, etc.

Table 1.3: The five SST definitions used by the Group for High Resolution Sea Surface Temperature (GHRSST), modified from Bogdanoff (2010).

Interface SST, SST_{int}, is defined as the temperature at the precise air-sea interface, it is a theoretical concept and cannot be measured with current technology.

Skin SST, SST_{skin}, represents the temperature of water across a very thin layer of $\sim 10\ \mu$m below ocean surface. It can be measured by an infrared radiometer operating in $10 - 12\ \mu$m spectrum. It is generally several tenths of a Kelvin cooler than the temperature measured just below the skin layer, resulting from evaporative and radiative processes which dominate this layer, the cooling is referred to as skin effect.

Sub skin temperature, SST$_{subskin}$, represents the temperature of water below skin layer, with a depth of about 1 mm from ocean surface. It can be well-measured by low frequency ($6 - 12$ GHz) microwave radiometers (Gentemann et al., 2004; Wentz et al., 2000).

Subsurface temperature, or bulk SST, SST$_{bulk}$, is any temperature of the water beneath the sub skin layer. Bulk temperature depends on depth and is influenced by the absorption of solar radiation. During the daytime, the absorption of solar radiation tends to raise the temperature of the upper few metres if wind is too weak to mix the heat deeper; a stratification develops and the temperature would be a few Kelvins warmer than that measured at deeper depths, sometimes it may compensate for the skin effect. The buoy sensors are typically located at a depth of $0.5 - 1$ m thus measurements obtained by buoy-based sensors are bulk temperatures.

Foundation SST, SST$_{fnd}$, is defined as the temperature of the water column at a height of $\sim$10 m where is free of diurnal variation.

Due to the high emissivity of water in infrared spectra, the infrared satellite sensors cannot penetrate to the depth of bulk temperature: the temperatures measured by infrared sensors are skin temperature. Because of the strong temperature gradient of the upper ocean, skin temperature, which measures the temperature at ~ 10 μm, cannot be directly compared to bulk temperature which represents temperature of ~ 1 m depth. Measurements of skin temperature need to be converted to equivalent bulk SST for applications in climate research and oceanography. The differences between skin SST and bulk SST are caused by skin effect and diurnal thermocline effect. Skin effect is caused by the combination of net long wave radiative flux, latent and sensible heat loss from the ocean to the atmosphere. This produces a cool layer of a few micrometres depth at the ocean surface. This thin layer is almost always present, although it may be compensated for by solar heating. Absorption of solar radiation

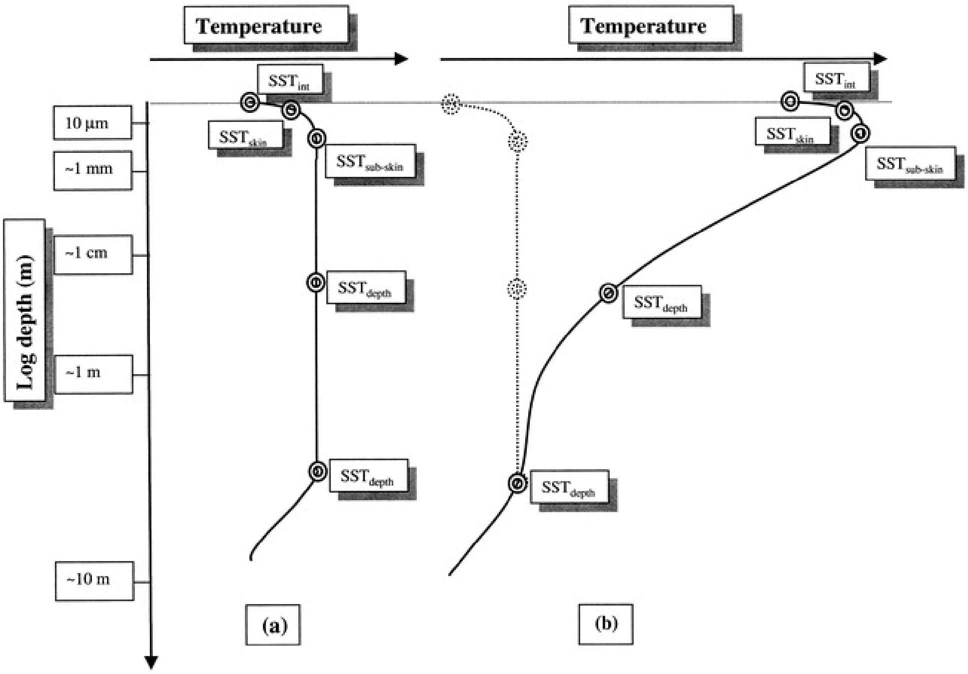

Figure 1.7: Idealized temperature profiles of the near-surface layer (∼10 m depth) of the ocean during (a) nighttime and daytime during strong wind conditions and (b) daytime low-wind speed conditions and high isolation resulting in thermal stratification of the surface layers, taken from Donlon et al. (2002).

can warm the upper ocean; if temperature saturation caused by the warming is strong enough to suppress shear-induced mixing, a warm layer with a depth of a few metres will be formed. The temperature of this layer can be a few Kelvins warmer than than deeper layers. The warming is caused by absorption of solar radiation thus follows a diurnal cycle. Formation and strength of the warm layer are strongly influenced by wind speed and incoming solar radiation. Many models have been proposed to simulate the skin effect and thermocline effect based on net radiative flux, wind stress and turbulent state (Sykes et al., 2011; Gentemann et al., 2003; Donlon et al., 2002; Murray et al., 2000).

1.2.2 SST satellite remote sensing

Monitoring of SST from satellite infrared sensors has been operating over decades. Most retrievals of SST from satellite measured brightness temperatures (BTs) at the top of atmosphere (TOA) are carried out using the split-window methodology, which expresses the retrieved SST as a linear function of BTs multiplied by retrieval coefficients (McClain et al., 1985):

$$SST = a_0 + \sum_{1}^{n} a_i BT_i, \tag{1.21}$$

where n is the total number of infrared channels, BT_i is the brightness temperature (BT) obtained from channel i, a_0 and a_i are retrieval coefficients. The retrieval coefficients can be derived empirically by regressing the BTs against in situ SST measurements, or theoretically by using a radiative transfer model and a set of atmospheric profiles. Bias in SST may arise from errors in retrieval coefficients, instrument errors, undetected cloud and aerosols (Merchant et al., 2008). In recent years optimal estimation (OE) has been applied for retrieving SST from satellite imaginary (Merchant et al., 2013, 2009).

1.2.3 Aerosol effects on satellite remote sensing of SST

Satellite remote sensing has been extensively used for retrieval of surface parameters, however the signals measured by satellite are contaminated by the atmosphere. The atmospheric effects include scattering and absorption by gases and aerosols. Although the retrieval of SST is usually made in an atmospheric window where gas absorption is at a minimum, the influence of atmosphere is not negligible. Aerosols can scatter and absorb solar radiation, as well as absorb and emit long wave radiation. The effects of aerosols on the TOA radiation depend on aerosol size, loading as well as chemical composition. In general aerosols are small enough to act as Rayleigh scatterers in the infrared spectral region and have a relatively small impact. For particles with a size larger than 1/10 of the incident wavelength Mie scattering predominates. Most of the SST retrievals based on Equation 1.21 take aerosol effects into account in the process of generating retrieval coefficients a_i. As those corrections are limited to a mean aerosol level, the retrievals can be biased when aerosol loading is elevated above certain values, such as volcanic ash or dust plumes.

It has been demonstrated that a sufficiently violent volcanic eruption can inject substantial amounts of aerosols into the stratosphere; aerosols in the stratosphere may remain for a few months to years, and can cause a measurable change in climate. It has been shown that the presence of stratospheric aerosols released from the eruption of Mount Pinatubo biased the early versions SST datasets. Merchant et al. (1999), Donlon and Robinson (1998b) attribute the negative deficits in ATSR SST to the presence of a significant loading of stratospheric aerosols during the eruption of the Mount Pinatubo in June 1991. Walton et al. (1998) indicate that after this eruption the global mean bias of AVHRR SST measurements is about -0.5 K and higher in tropical latitudes (up to -2.0 K). Reynolds (1993) also reports that the volcanic ash emitted from the Mount Pinatubo eruption biased SST retrieved from AVHRR by more than 1 K. After adjusting the pre-launch coefficients, the ATSR (AATSR) dual-view retrieval allows SST to be retrieved highly robust (~ 0.1 K) (Iacovazzi, 2009; Merchant et al., 1999; Merchant and Saunders, 1998; Donlon and Robinson, 1998a, e.g.).

The contamination from tropospheric aerosols, such as wind-blown dust, is more regular than volcanic aerosols, affecting satellite derived SST accuracy in ocean areas located downwind of source regions. Ruescas et al. (2011) investigate the Medspiration Match-up Database and show that over the Mediterranean Sea there is a obvious correspondence between high bias in satellite derived SST and high aerosol concentration. Using sixteen years' SST from reprocessed AVHRR Pathfinder data, Nalli and Reynolds (2006) demonstrate a detectable relationship between SST bias and aerosol loading. Vazquez-Cuervo and Armstrong (2004) compare SST observations from ATSR-2 and AVHRR, and show that bias in SST is closely correlated to aerosol index (AI) from TOMS. Noyes et al. (2006) validate AATSR SST with ship-based radiometers over the Caribbean Sea; the results show that Saharan dust causes a warm bias in dual-view SST and a cold bias in nadir-view SST. Diaz et al. (2001) explore the association between TOMS AI and systematic bias in AVHRR SST, and the results show that the presence of dust aerosols increases the systematic error SST significantly (as much as 1.74 K). Using LOWTRAN simulations, Rao (1992) and Coll and Caselles (1994) indicate the SST depression due to marine aerosols is linearly correlated to AOD. However, Franois (1999) and Brown et al. (1997) point out that for SST retrieval no marine aerosol correction is needed and LOWTRAN tends to overestimate marine aerosol effects.

Several techniques have been developed to correct aerosol effects in SST retrieval. These techniques can be grouped into two major categories: the first category, which is denoted by 1 in Table 1.4, is to estimate the offset (ΔSST) between the uncorrected SST and the reference SST (i.e. in situ SST), and then correct the retrieved SST by adding the ΔSST. The second category (denoted by 2 in Table 1.4) corrects the aerosol effects by tuning coefficients a_i in Equation 1.21 for different aerosol conditions. Table 1.4 is a summary of previous research about aerosol correction in SST retrievals.

reference	SST instrument	aerosol instrument	aerosol type	technology	day/night
Griggs (1985)	AVHRR	AVHRR	volcanic	1	day
Walton (1985)	AVHRR	AVHRR	volcanic	2	night
May et al. (1992)	AVHRR	AVHRR	dust	1&2	day
Reynolds (1993)	AVHRR	AVHRR	volcanic	2	night
Brown et al. (1997)	ATSR	–	trop&stra	2	day&night
Merchant et al. (1999)	ATSR	–	volcanic	2	day&night
Nalli and Stowe (2002)	AVHRR	AVHRR	dust&volcanic	1	day
Merchant et al. (2006)	SEVIRI	–	dust	2	night

Table 1.4: Previous research about aerosol corrections in SST retrieval.

1.3 Aim of this work

In general, the importance of aerosols has two aspects: the radiative forcing on climate and the influence in satellite remote sensing of surface properties.

The main objective of this thesis is to develop a new algorithm based on the optimal estimation scheme (OE) for retrievals of aerosol and surface properties from the Advanced Along-Track Scanning Radiometer (AATSR) which is on-board the European Space Agency (ESA) satellite ENVISAT. AATSR makes use of a conical scan to give a dual-view of the Earth's surface, on-board calibration targets and mechanical coolers to maintain the thermal environment necessary for optimal operation of the infrared detectors. With such features, AATSR offers unique opportunities to explore aerosol information, and the dual-view system makes it possible to do a good atmospheric correction and extract accurate SST. The OE scheme can retrieve aerosol and surface properties simultaneously, thus it is capable of making a dynamic aerosol correction to surface properties.

The new algorithm is developed from the Oxford-RAL Aerosol and Cloud (ORAC), which is designed for aerosol and cloud retrievals from satellite measurements. The primary development of the new algorithm from the previous version is the inclusion of infrared channels which enable the retrieval of SST. The results generated by the new algorithm will be tested with data from both space-based and ground-based measurements, and a theoretical error budget of the retrieved SST will be established in order to understand the error sources.

1.4 Outline of this thesis

The next Chapter of this thesis (Chapter 2) describes the main characteristics of the AATSR instrument and the principles of the new algorithm. It starts with a description of the instrument, and followed by an explanation of the retrieval theory of the new algorithm.

Chapter 4 and Chapter 5 will be dedicated to the validation of the new algorithm. In Chapter 4 the retrieved AOD and Ångström exponent will be evaluated by comparing with the aerosol products from satellite measurements (GlobAEROSOL) and from ground-based measurements (AERONET). Chapter 5 deals with the accuracy of the retrieved SST. For that purpose, the retrieved SST will be validated with the measurements from ship-based radiometers and with the measurements from drifting buoys. Chapter 3 will provide an error analysis of the retrieved SST. In this chapter an evaluation of the contributions from retrieval terms to the retrieved SST bias will be presented. Chapter 6 discusses the relationship between AOD and wind speed over ocean based on GlobAEROSOL dataset. Chapter 7 ends the thesis with a synopsis of the findings and suggestions for future improvements of the algorithm.

Chapter 2

AATSR Instrument and the modified ORAC retrieval algorithm

2.1 Overview of AATSR instrument

AATSR is the third in the Along-Track Scanning Radiometers series (ATSRs) onboard the European Space Agency's Environment satellite (Envisat) platform, which is in a polar orbit approximately 800 km above the Earth's surface. The overpass time is selected to be $\sim$ 10:00 a.m. local solar time to optimise the illumination conditions for the optical sensors. The ATSRs were designed with the primary objective of providing global SST at the high levels of precision (0.3 K) required for climate research. The AATSR has two novel features: an exceptionally stable on-board calibration system and a dual-view system. Two black body reference targets for infrared calibration are viewed on each scan and the designed calibration uncertainties are no more than 0.1 K. The dual-view system acquires two near-simultaneous observations of the same area of the Earth's surface at an angle of approximately 55° from the zenith (forward view) first and then about ninety seconds later at an angle close to vertical (nadir view) as the satellite moves forward; the viewing geometry of the AATSR is shown in Figure 2.1. This feature allows for an improved atmospheric correction. The AATSR field of view (FOV) comprises two curved swaths, which are about 512 km wide with 555 pixels across the nadir swath (with a spatial resolution of 1 km at the centre) and 371 pixels across the forward swath, as shown in Figure 2.2.

The AATSR measures radiance at nadir and along track at seven channels centred at 0.55, 0.67, 0.87, 1.6, 3.7, 11.0 and 12.0 μm. The channel locations, band widths, averaged instrumental noises as well as primary applications are given in Table 2.1. In this thesis, for convenience the first four channels (0.55, 0.67, 0.87 and 1.6 μm) are referred to as visible channels and the remaining three (3.7, 11.0 and 12.0 μm) are referred to as infrared channels.

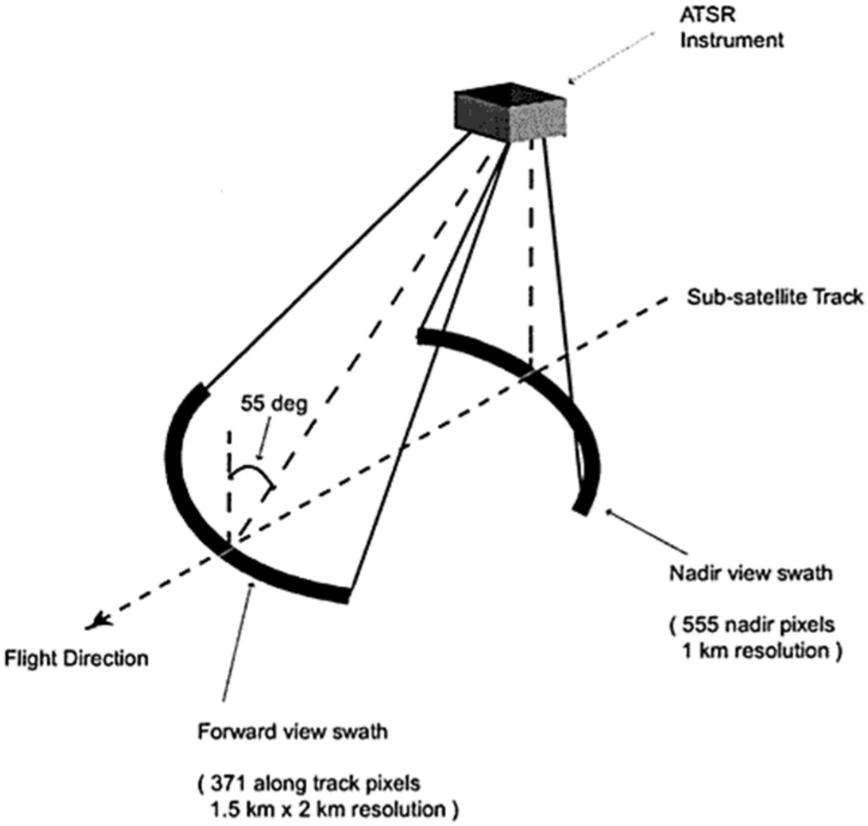

Figure 2.1: AATSR viewing geometry, taken from ESA (2007).

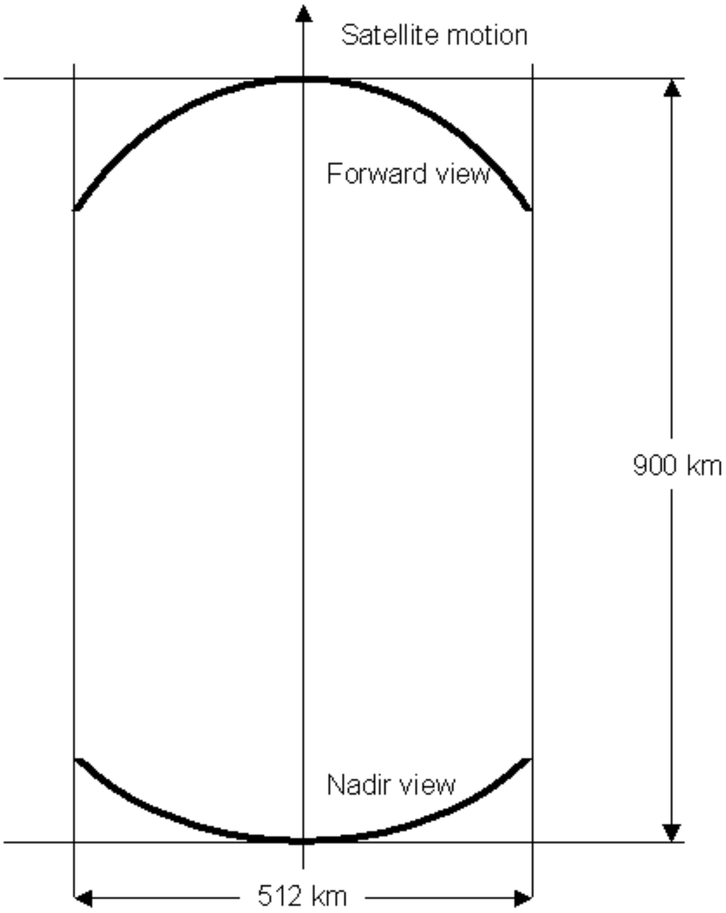

Figure 2.2: AATSR swath, taken from ESA (2007).

2.2 The retrieval scheme

2.2.1 Inverse problem

The total radiance above the atmosphere L^{TOA} is composed of the solar radiance reflected by the atmosphere-Earth system, thermal emission from the atmosphere and from the Earth's surface:

$$L^{TOA} \propto (L_s^R, L_a^R, L_s^E, L_a^E), \tag{2.1}$$

- L^{TOA}: total radiance at the TOA,

channel	central wavelength	band width	averaged noise	primary application
0.55 μm	0.555 μm	0.02 μm	2.40 %	chlorophyll
0.66 μm	0.659 μm	0.02 μm	3.20 %	vegetation index
0.87 μm	0.865 μm	0.02 μm	2.00 %	vegetation index
1.6 μm	1.61 μm	0.30 μm	3.30 %	cloud clearing
3.7 μm	3.70 μm	0.30 μm	0.05 K	SST
11 μm	10.85 μm	1.00 μm	0.03 K	SST
12 μm	12.00 μm	1.00 μm	0.03 K	SST

Table 2.1: AATSR channel locations, bandwidths, averaged instrumental noises and applications (Sayer, 2008; Smith, 2008; Llewellyn-Jones et al., 2001), for visible channels the noise is given as percentage of measured TOA reflectance and given in a unit of Kelvin in infrared channels.

- L_s^R: solar radiance reflected by the Earth's surface and modified by the atmosphere,
- L_a^R: solar radiance reflected/rescattered by the atmosphere,
- L_s^E: thermal radiance emitted by the Earth's surface and modified by the atmosphere,
- L_a^E: thermal radiance emitted by the atmosphere.

Each term in Equation 2.1 carries specific signatures of particular quantities interacting with radiance along the atmospheric path from the Earth's surface to the TOA. At a given wavelength λ and viewing geometries θ_o, θ_v, L^{TOA} varies with surface and atmospheric properties:

$$L^{TOA}(\lambda, \theta_o, \theta_v) = f(\tau_a, \tau_g, R_s, B_s, \epsilon_s, B_a, \ldots), \tag{2.2}$$

where θ_o and θ_v are solar zenith angle (illumination angle) and satellite zenith angle (viewing angle), τ_a and τ_g are aerosol optical depth and gas optical depth, R_s is surface reflection, B_s is surface blackbody radiance, B_a is atmospheric blackbody radiance, ϵ_s is surface emissivity, f is defined as forward function which describes the physical relationships between L^{TOA} and quantities of interest τ_a, τ_g, R_s, B_s ϵ_s, B_a, ...

The first step of building a retrieval algorithm is to decide the forward function f, however, in reality the true f is unknown therefore it is approximated by forward model F. More generally, considering a system has multiple measurements $\mathbf{y}$ (measurement vector) and can be described by a number of quantities $\mathbf{x}$ (state vector), Equation 2.2 can be rewritten as:

$$\mathbf{y} = \mathbf{f}(\mathbf{x}), \tag{2.3}$$

then approximate $\mathbf{f}$ with $\mathbf{F}$:

$$\mathbf{y} = \mathbf{F}(\mathbf{x}). \tag{2.4}$$

The purpose of a retrieval algorithm is to invert Equation 2.4 to obtain the state of the system:

$$\mathbf{x} = \mathbf{F}^{-\mathbf{1}}(\mathbf{y}). \tag{2.5}$$

Equation 2.5 is defined as the inverse problem, and has been widely applied in remote sensing.

The second step of building an algorithm is to solve Equation 2.5 efficiently to produce acceptable retrieval solutions. Commonly, measurements are with errors $\boldsymbol{\xi}$, and the actual relationship between measurements and state becomes:

$$\mathbf{y} = \mathbf{F}(\mathbf{x}, \mathbf{b}) + \boldsymbol{\xi}, \tag{2.6}$$

where $\mathbf{b}$ denotes parameters that influence measurements but are not included in the state vector (auxiliary data), Equation 2.5 becomes:

$$\mathbf{x} = \mathbf{F}^{-\mathbf{1}}(\mathbf{y}, \mathbf{b}, \boldsymbol{\xi}). \tag{2.7}$$

2.2.2 Optimal estimation scheme

Solving Equation 2.7 can be regarded as mapping a point in measurement space ($\mathbf{y}$) to a point in state space ($\mathbf{x}$). Measurements come with uncertainties resulting from precision of the instruments, the measurement uncertainties are only known statistically and can be described by probability distribution functions (pdf). Generally, remote sensing problems are ill-posed, a point in $\mathbf{y}$ could be from various regions in $\mathbf{x}$ described by some pdf, rather than from a single point. Therefore the retrieval ends up with a set of mathematically acceptable solutions (Rodgers, 2000). Thus additional information (*a priori*) of the state vector ($\mathbf{x_a}$) is required to constrain the solutions to fall within physically reasonable limits. A general strategy of seeking the solution most consistent with both measurements and *a priori* information is the optimal estimation (OE) approach. OE identifies the most appropriate solution by finding the maximum of conditional pdf, $A(\mathbf{x}|\mathbf{y}, \mathbf{x}_a, \mathbf{b})$, of the state $\mathbf{x}$ with respect to the measurements $\mathbf{y}$, *a priori* state $\mathbf{x}_a$ and all other parameters influence measurements but are not retrieved, $\mathbf{b}$. Assuming the errors in $\mathbf{y}$, $\mathbf{x_a}$ and $\mathbf{b}$ have Gaussian distributions with zero mean and variance given by $\mathbf{S_y}$, $\mathbf{S_x}$ and $\mathbf{S_b}$ respectively, and applying Bayes theorem, the general form of the solution can be written as:

$$\begin{aligned} -2\ln A(\mathbf{x}|\mathbf{y}, \mathbf{x_a}, \mathbf{b}) \ \propto \ & (\mathbf{y} - \mathbf{F}(\mathbf{x}))^T \mathbf{S_y^{-1}} (\mathbf{y} - \mathbf{F}(\mathbf{x})) \\ & + (\mathbf{x} - \mathbf{x_a})^T \mathbf{S_x^{-1}} (\mathbf{x} - \mathbf{x_a}) \\ & + (\mathbf{b_t} - \mathbf{b})^T \mathbf{S_b^{-1}} (\mathbf{b_t} - \mathbf{b}), \end{aligned} \tag{2.8}$$

where $\mathbf{F}(\mathbf{x})$ is the forward modelled measurements, $\mathbf{b_t}$ is the true value of $\mathbf{b}$. Maximising $A(\mathbf{x}|\mathbf{y}, \mathbf{x_a}, \mathbf{b})$ is equivalent to minimizing:

$$\begin{aligned} \mathbf{J}(\mathbf{x}) \ = \ & (\mathbf{y} - \mathbf{F}(\mathbf{x}))^T \mathbf{S_y^{-1}} (\mathbf{y} - \mathbf{F}(\mathbf{x})) \\ & + (\mathbf{x} - \mathbf{x_a})^T \mathbf{S_x^{-1}} (\mathbf{x} - \mathbf{x_a}) \\ & + (\mathbf{b_t} - \mathbf{b})^T \mathbf{S_b^{-1}} (\mathbf{b_t} - \mathbf{b}), \end{aligned} \tag{2.9}$$

where $\mathbf{J}(\mathbf{x})$ is known as the retrieval cost. The minimization of $\mathbf{J}(\mathbf{x})$ is done with respect to state vector $\mathbf{x}$ thus it is independent of $\mathbf{b}$, so Equation 2.9 is reduced to:

$$\begin{aligned}\mathbf{J}(\mathbf{x}) &= (\mathbf{y}-\mathbf{F}(\mathbf{x}))^T\mathbf{S_y^{-1}}(\mathbf{y}-\mathbf{F}(\mathbf{x})) \\ &\quad +(\mathbf{x}-\mathbf{x_a})^T\mathbf{S_x^{-1}}(\mathbf{x}-\mathbf{x_a}).\end{aligned} \tag{2.10}$$

The first and second derivatives of $\mathbf{J}$ with respect to $\mathbf{x}$ are given by:

$$\begin{aligned}\mathbf{J}' &= \frac{\partial \mathbf{J}}{\partial \mathbf{x}} = \mathbf{K_x^T S_y^{-1}}(\mathbf{y}-\mathbf{F}(\mathbf{x})) + \mathbf{S_x^{-1}}(\mathbf{x}-\mathbf{x_a}), \\ \mathbf{J}'' &= \frac{\partial^2 \mathbf{J}}{\partial \mathbf{x}^2} = \mathbf{K_x^T S_y^{-1} K_x} + \mathbf{S_x^{-1}},\end{aligned} \tag{2.11}$$

where matrix $\mathbf{K_x}$ is the weighting function, describing the partial derivatives of the forward model with respect to $\mathbf{x}$:

$$\mathbf{K_x} = \frac{\partial \mathbf{F}(\mathbf{x})}{\partial \mathbf{x}}, \tag{2.12}$$

which shows the sensitivity of measurements to state variables. Assuming that the $\mathbf{K_x}$ is independent of $\mathbf{x}$, the solution for Equation 2.9 can be expressed as:

$$\hat{\mathbf{x}} = (\mathbf{S_x^{-1}} + \mathbf{K_x^T S_y^{-1} K_x})^{-1}(\mathbf{S_x^{-1} x_a} + \mathbf{K_x}^T\mathbf{S_y^{-1}}\mathbf{F}(\mathbf{x})). \tag{2.13}$$

2.3 ORAC

The purpose of this thesis is to create a retrieval algorithm for aerosol and surface properties. The starting point is the Oxford-RAL Retrieval of Aerosol and Cloud (ORAC) algorithm, which is an OE scheme for aerosol and cloud retrievals from satellite measurements, heritages from Enhanced Cloud Processor (ECP) (Watts et al., 1998) and has many versions implemented with different channels and surface treatments emphasising the retrieval of cloud or aerosol. The algorithm developed and used here is based on the version described by Thomas et al. (2011) and Sayer (2008). The main development from the previous ORAC aerosol retrieval scheme is that the former version only uses visible channels for aerosol retrieval, this version uses both visible and infrared channels. The inclusion of infrared channels enables the retrievals of aerosol layer height and surface temperature. The measurement vector **y** is composed of 12 elements: the observations of 0.55, 0.67, 0.87, 1.60, 11 and 12 μm at nadir and forward views. The 3.7 μm channel is not currently implemented due to the strong component of solar radiation in the daytime. The full state vector **x** is

$$\mathbf{x} = \left(\tau_{0.55}, r_e, R_{SLW(0.55)}, R_{SLW(0.67)}, R_{SLW(0.87)}, R_{SLW(1.6)}, T_s, P_a\right),$$

where $\tau_{0.55}$ is the AOD at 0.55 μm, r_e is the effective radius (μm), $R_{SLW(0.55)}$, $R_{SLW(0.67)}$, $R_{SLW(0.87)}$ and $R_{SLW(1.6)}$ are the surface white sky albedo at four visible channels, T_s is the surface temperature (K) and P_a is the aerosol layer height (hPa).

Because of the different radiative transfer processes of visible and infrared spectra, in ORAC two different forward models, one for visible channels and the other for infrared channels, are employed to simulate the relationships between measurements (**y**) and state variables (**x**).

2.3.1 Forward model for visible channels

The working principle of the visible forward model used in the new version of ORAC is the same as the previous version (some modifications have been done to fit in the infrared channels). The visible forward model has been described in detail by Thomas et al. (2011) and Sayer (2008), it is briefly presented in this section for completeness.

Satellite measurements at visible spectra consist of solar radiance scattered by the atmosphere, reflected by the Earth's surface, and modified by the atmosphere through the path from the Earth's surface to the TOA. The forward model is a three-layer radiative transfer model which is schematically shown in Figure 2.3. Assuming the Earth's surface reflection follows a bidirectional reflectance distribution function (BRDF) and considering a series of multiple reflections and transmissions between the Earth's surface and the aerosol layer, the radiative process of visible spectra is summarized by Equation 2.14.

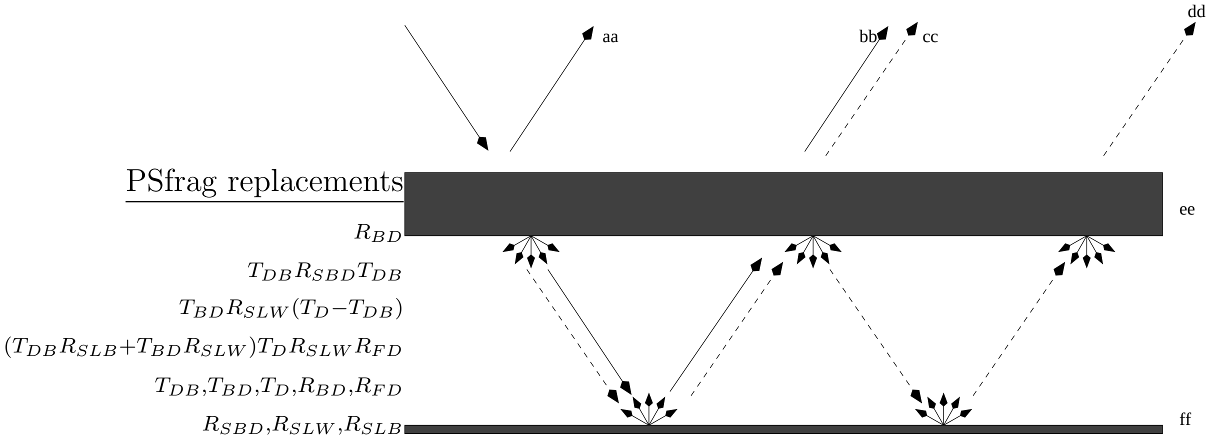

Figure 2.3: Aerosol layer−surface interactions using the simplified BRDF model, given by Gareth Thomas.

$$\begin{aligned}
R^{TOA}(\theta_o,\theta_v,\phi) = R_{BD}(\theta_o,\theta_v,\phi) &+ T^{\downarrow}_{DB}(\theta_o)R_{SBD}(\theta_o,\theta_v,\phi)T^{\uparrow}_{DB}(\theta_v) \\
&+ T^{\downarrow}_{DB}(\theta_o)R_{SLB}(\theta_o)T^{\uparrow}_{BD}(\theta_v) \\
&+ T^{\downarrow}_{BD}(\theta_o)R_{SLW}T^{\uparrow}_{D}(\theta_v) \\
&+ T^{\downarrow}_{DB}(\theta_o)R_{SLB}(\theta_o)R_{FD}R_{SLW}T^{\uparrow}_{D}(\theta_v) \\
&+ T^{\downarrow}_{BD}(\theta_o)R_{SLW}R_{FD}R_{SLW}T^{\uparrow}_{D}(\theta_v) \\
&+ T^{\downarrow}_{DB}(\theta_o)R_{SLB}(\theta_o)R_{FD}R_{SLW}R_{FD}R_{SLW}T^{\uparrow}_{D}(\theta_v) \\
&+ T^{\downarrow}_{BD}(\theta_o)R_{SLW}R_{FD}R_{SLW}R_{FD}R_{SLW}T^{\uparrow}_{D}(\theta_v) \\
&+ \dots \qquad (2.14)
\end{aligned}$$

- R^{TOA}: reflectance at the TOA for a given wavelength,

- θ_o: solar zenith angle (illumination angle),
- θ_v: satellite zenith angle (viewing angle),
- ϕ: relative azimuth angle,
- R_{BD}: bidirectional reflectance of the aerosol layer,
- R_{FD}: diffuse reflectance of the aerosol layer,
- T_{BD}: diffuse transmission of the aerosol layer,
- T_{DB}: direct transmission of the aerosol layer,
- T_D: total transmission, $T_D = T_{BD} + T_{DB}$.
- R_{SBD}: surface bidirectional reflectance, describes the reflectance of direct illumination into a viewing angle, depends on both solar and satellite zenith angles.
- R_{SLB}: black sky albedo, also referred to as directional hemispherical reflectance, describes the diffuse reflectance of a direct illumination without diffuse component, is an integral of bidirectional reflectance over all viewing directions, and is a function of illumination angle.
- R_{SLW}: white sky albedo (bi-hemispherical reflectance) is the reflectance of a surface under diffuse or indirect light, it is isotropic and independent of the geometries.

Two approximations are made to simplify the BRDF (Thomas et al., 2009; Sayer, 2008):

- Directionality in the diffusely-scattered radiance from the direct illumination ($T^{\downarrow}_{DB} R_{SLB}$) is lost as it is transmitted through the atmosphere. That is to say that for pure diffuse radiance from any direction the surface acts as Lambertian surface.

- When taken as a pair the surface and the atmosphere act as Lambertian reflectors, so any directionality left in the reflected illumination ($T^{\downarrow}_{DB}R_{SBD}$) is lost in that proportion which is reflected back towards the ground. Hence after the first pair of surface-atmosphere reflections, the R_{SLW} and T_D may be used for subsequent reflections.

Equation 2.14 can be simplified to be:

$$\begin{aligned} R(\theta_o,\theta_v,\phi) = R_{BD}(\theta_o,\theta_v,\phi) &+ T^{\downarrow}_{DB}(\theta_o)R_{SBD}(\theta_o,\theta_v,\phi)T^{\uparrow}_{DB}(\theta_v) \\ &- T^{\downarrow}_{DB}(\theta_o)R_{SLB}(\theta_o)T^{\uparrow}_{DB}(\theta_v) \\ &+ (T^{\downarrow}_{DB}(\theta_o)R_{SLB}(\theta_o) + T^{\downarrow}_{BD}(\theta_o)R_{SLW})T^{\uparrow}_{D}(\theta_v) \\ &\times (1 + R_{SLW}R_{FD} + R^2_{SLW}R^2_{FD} + \ldots). \end{aligned} \tag{2.15}$$

As $R_{SLW}R_{FD}$ is less than 1, Equation 2.16 can be expressed as:

$$\begin{aligned} R(\theta_o,\theta_v,\phi) &= R_{BD}(\theta_o,\theta_v,\phi) + T^{\downarrow}_{DB}(\theta_o)\left(R_{SBD}(\theta_o,\theta_v,\phi) - R_{SLB}(\theta_o)\right)T^{\uparrow}_{DB}(\theta_v) \\ &+ \frac{\left(T^{\downarrow}_{DB}(\theta_o)R_{SLB}(\theta_o) + T^{\downarrow}_{BD}(\theta_o)R_{SLW}\right)T^{\uparrow}_{D}(\theta_v)}{1 - R_{SLW}R_{FD}}. \end{aligned} \tag{2.16}$$

2.3.2 Modelling aerosol transmission and reflectance

Aerosol related terms in Equation 2.16, R_{BD}, R_{FD}, T_{BD}, T_{DB} and T_D, are calculated for a set of wavelengths, geometries and aerosol classes by solving the radiative transfer equation with the assumption that there is no surface contribution:

$$\mu\frac{dL_\lambda(\tau_\lambda,\mu,\phi)}{d\tau} = L_\lambda(\tau_\lambda,\mu,\phi) - L^S_\lambda(\tau_\lambda,\mu,\phi), \tag{2.17}$$

where $L_\lambda(\tau_\lambda,\mu,\phi)$ is the radiative intensity along direction (μ,ϕ), μ is the cosine of the zenith angle and ϕ is the relative azimuth angle, τ_λ is the optical depth at wavelength λ, $L^S_\lambda(\tau_\lambda,\mu,\phi)$ is a function describing the source. Equation 2.17 is solved by the Discrete Ordinates Radiative Transfer (DISORT) software package. In order to save the computational time of solving Equation 2.17 at each run, ORAC uses a look up table (LUT) strategy. The LUTs describe the relationships between the radiative transfer parameters (transmission, reflectance) and aerosol properties, and are pre-calculated for a set of aerosol classes, optical depths, effective radii, and viewing geometries which are supposed to span the range of global aerosol conditions. As stated in Section 1.1.4 at any location in the atmosphere, aerosols are composed of particles from different sources, of various sizes and chemical compositions. To describe the wide range of possible compositions, aerosol particles are modelled as different classes which contain various components. Each component represents a collection of particles from the same source. It is assumed that in each class the components are mixed externally with different mixing ratios, particles from different components are independent of each other, and the size distribution of each component follows a lognormal distribution. For example, the marine clean class given by Hess and Schult (1998) has three components: water-soluble, fine mode sea salt, and coarse mode sea salt (Figure 2.4). Using Mie theory, extinction coefficient (β_j^{ext}), single scattering albedo (ω_j), and phase function (p_j) for each class can be calculated as:

$$\begin{aligned}
\beta_j^{ext} &= \frac{\sum \chi_i \beta_i^{ext}}{\sum \chi_i}, \\
\omega_j &= \frac{\sum \chi_i \beta_i^{ext} \omega_i}{\sum \chi_i \beta_i^{ext}}, \\
p_j &= \frac{\sum \chi_i \beta_i^{ext} \omega_i p_i}{\sum \chi_i \beta_i^{ext} \omega_i}, \qquad (2.18)
\end{aligned}$$

where χ_i, β_i^{ext}, ω_i and p_i are mixing ratio, extinction coefficient, single scattering albedo, and phase function of the i_{th} component in the j_{th} class.

Retrievals are performed for different aerosol classes, the retrieval fit quality and a priori constraints are used to select the most likely class for each pixel. The four classes used in this thesis are either dust or marine classes, maybe not appropriate for some specific locations, such as areas influenced by urban or biomass burning aerosols. In ORAC for each aerosol class LUTs are created for 20 aerosol loadings (logarithmically-spaced 550 nm AOD, between approximately 0.01 to 6), 20 effective radii (between 0.01 to 10 μm) and 10 Sun/satellite geometries (specified by 10 equally-spaced between 0° to 90°). Five LUTs for each aerosol class and instrument channel combination are produced for visible channels, R_{BD}, R_{FD}, T_{BD}, T_{DB} and T_D. In this version of ORAC, only the aerosol classes with coarse mode components which are supposed to have an impact on infrared spectra are used (Table 2.2). In the generation of LUTs which are a function of effective radius, a change in effective radius is achieved by perturbing the number mixing ratios among the components of each aerosol class. For example, as illustrated in Figure 2.5, when the effective radius increases, the number mixing ratios of the components with large size will be increased, while mixing ratios of the components with small size will be decreased. Therefore a change in effective radius not only implies a change in aerosol size, but also in the materials which make up the aerosol class.

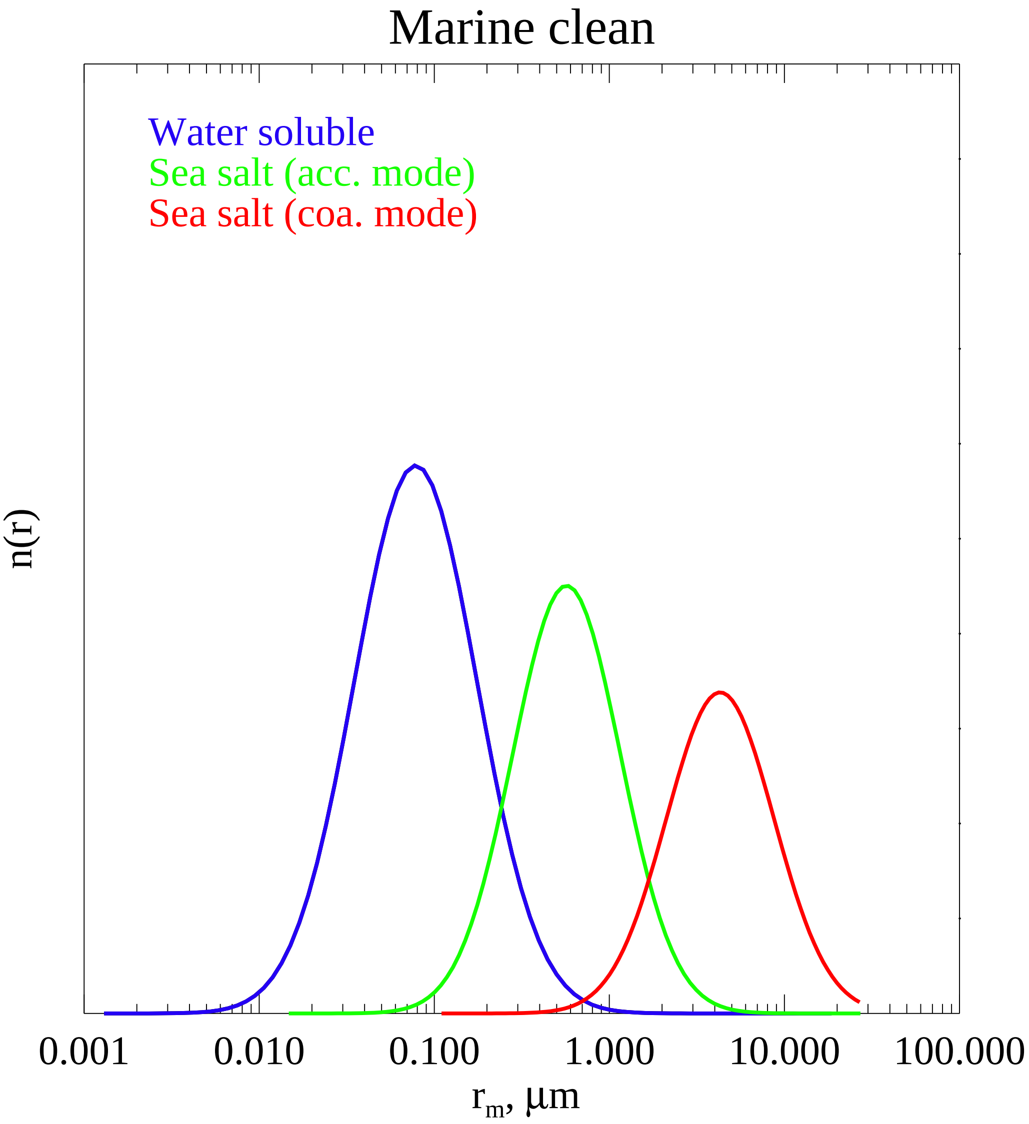

Figure 2.4: A schematic diagram of size distributions of three components of marine clean class (A05). Each component follows a lognormal distribution described by Equation 1.9. In reality, the number mixing ratios of sea salt are much lower than water-soluble.

ORAC label	class	RH	components	number mix ratio	σ	r$_m$, μm	ω, 0.55 μm
A05	marine clean	50%	water soluble	0.987	2.240	0.026	0.976
			sea salt (acc.)	0.013	2.030	0.336	1.000
			sea salt (coa.)	0.211E−5	2.030	2.820	1.000
A53	marine clean	80%	water soluble	0.987	2.240	0.031	0.987
			sea salt (acc.)	0.013	2.030	0.416	1.000
			sea salt (coa.)	0.211E−5	2.030	3.490	1.000
A03	spherical dust	50%	water soluble	0.870	2.240	0.026	0.976
			mineral (nuc.)	0.117	1.950	0.070	0.967
			mineral (acc.)	0.013	2.000	0.390	0.878
			mineral (coa.)	0.617E−4	2.150	1.900	0.666
A83	non-spherical dust	80%	water soluble	0.870	2.240	0.031	0.984
			mineral (nuc.)	0.117	0.696	0.082	0.994
			mineral (acc.)	0.013	0.692	0.475	0.977
			mineral (coa.)	0.617E−4	2.150	1.900	0.873

Table 2.2: Aerosol classes used in ORAC. RH represents relative humidity, σ is the spread of lognormal distribution, r$_m$ is the mode radius of distribution, ω is single scattering albedo. The microphysical characteristics of the first three aerosol classes (A05, A53, A03) are taken from Hess and Schult (1998), the characteristics of A83 are taken from Smith (2011). The mixing ratio, r$_m$ and ω are calculated with the values given by Hess and Schult (1998); Smith (2011), they will change in the retrieval.

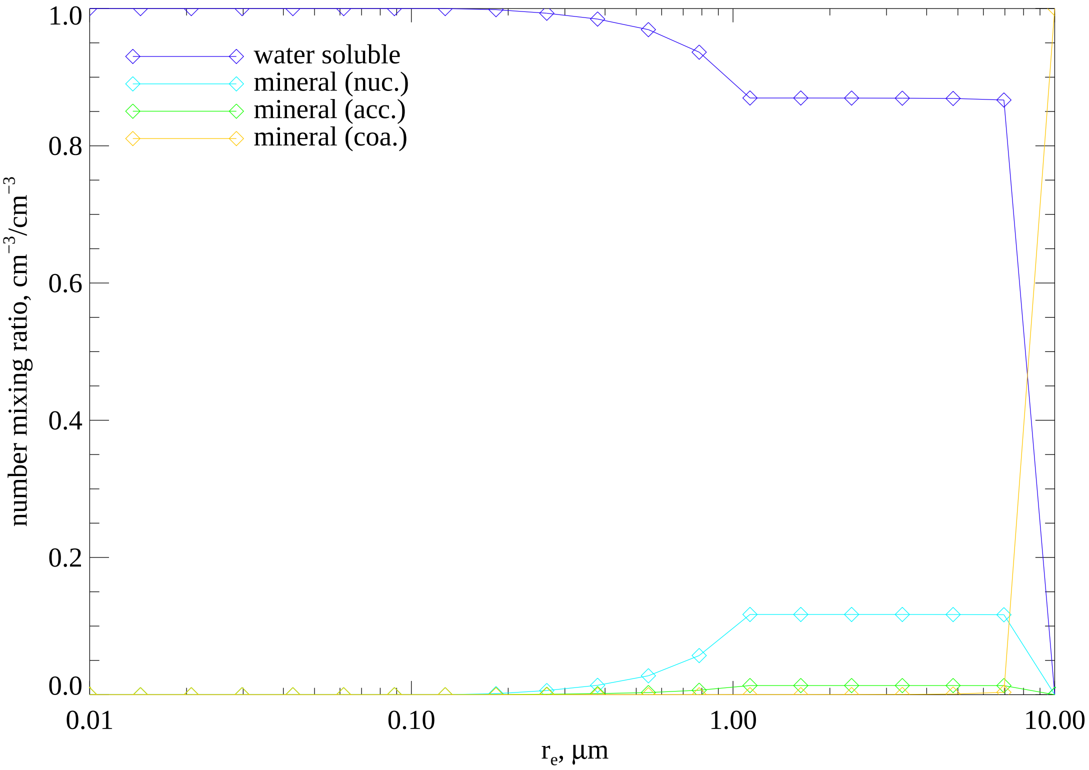

Figure 2.5: Variation in number mixing ratio of each component of A83 as effective radius increases.

In DISORT, the optical depth (τ_l), single scattering albedo (ω_l) and phase function (P_l) of the each layer are combined using the following equations:

$$\tau_l = \tau_a + \tau_R + \tau_g, \tag{2.19}$$

$$\omega_l = \frac{\tau_R + \omega_0 \tau_a}{\tau_a + \tau_R + \tau_g}, \tag{2.20}$$

$$P_l(\theta) = \frac{\tau_a \omega_a P_a(\theta) + \tau_R P_R(\theta)}{\tau_a \omega_a + \tau_R}, \tag{2.21}$$

where τ_a, τ_R, τ_g are the optical depths corresponding to aerosols, Rayleigh scattering and gas absorption within the layer respectively. The single scattering albedo of the layer (ω_l) is given as the average of the single scattering albedo of the aerosol, Rayleigh scattering and gas absorption (where $\omega_g = 0$), weighted by their optical depths. The phase function of each layer is also weighted mean, with weights being the fraction of the optical depth for each process due to scattering. For each layer bounded by lower and upper pressure levels p_l and p_u, τ_R is calculated as

$$\tau_R = \frac{\tau_{RT}[p_u - p_l]}{p_0}, \tag{2.22}$$

where p_0 is the ground level pressure and τ_{RT} is the Rayleigh scattering optical depth for a column of atmosphere extending from the surface to the TOA, it is obtained from Justus and Paris (1985) as

$$\tau_{RT}(\lambda) = \frac{p_0}{p_s} \times \frac{1}{117.03\lambda^4 - 1.316\lambda^2}, \tag{2.23}$$

where p_s is the standard pressure, the value of it is 1013.25 hpa.

For visible channels, compared to the light extinction due to aerosols, the contribution from gas absorption/emission to the TOA is weak. In addition, the visible wavelengths mainly locate in the atmospheric transparent regions without strong gas absorption. The temporal and statistical variation of gas concentration only give minor corrections to the measured radiance. Therefore, the gas absorption over the visible channels is computed by the MODTRAN code (Brown et al., 2004) using the mid-latitude summer atmospheric profile only. The modelled gas absorption is then convoluted with the instrument filter function to produce an optical depth (τ_g) due to the gas absorption (Thomas et al., 2009).

2.3.2.1 *A priori* information of aerosol and surface reflectance

ORAC makes use of *a priori* information on state vector to make the process less likely to retrieve an unphysical value of $\mathbf{x}$. The *a priori* values are also used as the first guess at the solution. The *a priori* information ($\mathbf{x_a}$) for aerosol, which listed in Table 2.2, is provided by Hess and Schult (1998) and Smith (2011). Each aerosol class has its own associated *a priori* optical depth and effective radius. as well as errors. They are listed in Table 2.3. The *a priori* of surface reflectance for the ocean surface is calculated by a BRAD model, uncertainty is of the order of 0.001, varying with wavelength and geometry. For land surface reflectance *a priori* is from MODIS product (Sayer, 2008) with uncertainty of 0.02.

2.3.2.2 An example of simulated TOA reflectance

An example of the TOA reflectance simulated by the visible forward model (Equation 2.16) as a function of AOD and effective radius (r_e) is shown in Figure 2.6. The ranges of AOD and r_e are chosen to include commonly encountered values for marine clean aerosol class. The changes in the TOA reflectance with state variable is larger than the uncertainties in the measurement noise (Table 2.1), showing that the forward model is sensitive to the state variables. Similar patterns are encountered for other geometries and aerosol classes.

ORAC label	aerosol class	optical depth $\log(\tau)$	error on $\log(\tau)$	log effective radius $\log(r_e)$, μm	error on $\log(r_e)$
A05	marine clean (RH=50 %)	-1.0	1.0	-0.08	0.5
A53	marine clean (RH=80 %)	-1.0	1.0	-0.08	0.5
A03	spherical dust (RH=50 %)	-0.54	1.5	0.14	0.5
A83	non-spherical dust (RH=80 %)	-0.54	1.5	0.14	0.5

Table 2.3: *A priori* information for the aerosol classes used in this version of ORAC. Quantities are logarithmic as this is the form in which the retrieval code deals with them.

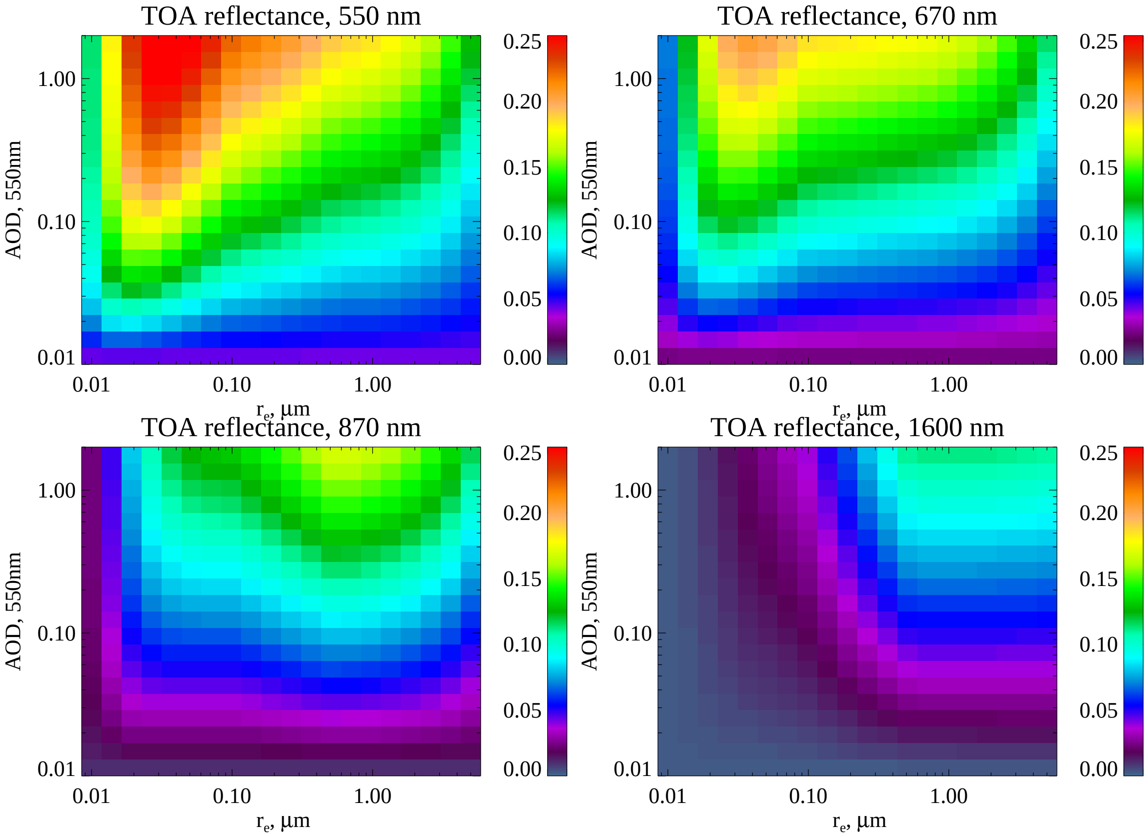

Figure 2.6: The TOA reflectance measured by AATSR visible channels as predicted by the visible forward model (Equation 2.16) for solar zenith angle $\theta_o = 0°$ and satellite viewing angle $\theta_v = 55°$ and marine clean aerosol class, clear sky 11 μm BT is 285.97 K and clear sky 12 μm BT is 284.54 K.

2.3.3 Forward model for infrared channels

2.3.3.1 Radiative transfer in the infrared spectra

A satellite-borne radiometer observing the Earth is sensitive to radiance which may emanate from both the Earth's surface and the atmosphere. In infrared spectra, the dominant components are, 1) radiance emitted by the Earth's surface, and modified by its passage through the atmosphere, L_s, 2) radiance emitted by the atmosphere, L_a, and, 3) radiance emitted by the atmosphere and reflected by the Earth's surface, L_a^R. The radiance from the Sun reflected by the Earth's surface is negligible compared to those three factors (Zavody et al., 1995). Therefore the monochromatic radiance at wavelength λ measured by a satellite radiometer L^{TOA} can be written as:

$$L^{TOA}(\lambda) \propto (L_s(\lambda), L_a(\lambda), L_a^R(\lambda)). \tag{2.24}$$

Surface component is calculated as:

$$L_s(\lambda) = \epsilon_s(\lambda) B(\lambda, T_s) t(\lambda, 0, H), \tag{2.25}$$

where $\epsilon_s(\lambda)$ is the surface emissivity at λ, $t(\lambda, 0, H)$ is transmission from surface to the TOA H, $B(\lambda, T_s)$ is black body radiance of surface at temperature T_s:

$$B(T_s, \lambda) d\lambda = \frac{2hc^2}{\lambda^5} \frac{1}{e^{\frac{hc}{\lambda \kappa T_s}} - 1}. \tag{2.26}$$

The $L_a(\lambda)$ in Equation 2.24 has a form of:

$$L_a(\lambda) = \int\limits_0^H L_A(\lambda, z, T_A) t(\lambda, z, H) dz, \tag{2.27}$$

where $t(\lambda, z, H)$ is transmission from height z to H, $L_A(z, \lambda, T_A)$ is atmospheric radiance at height z, T_A is atmospheric temperature at z. Assuming atmospheric emissivity at height z is $\epsilon_A(\lambda, z)$:

$$L_A(z, \lambda, T_A) = \epsilon_A(\lambda, z) B(\lambda, T_A). \tag{2.28}$$

If surface reflectance is $R_s(\lambda)$:

$$L_a^R(\lambda) = R_s(\lambda) t(\lambda, 0, H) \int\limits_0^H L_A(z, \lambda, T_A) t(\lambda, 0, z) dz, \tag{2.29}$$

where $t(\lambda, 0, z)$ is transmission from surface to height z. Equation 2.24 becomes:

$$\begin{aligned} L^{TOA}(\lambda) &= \epsilon_s(\lambda)B(\lambda, T_s)t(\lambda, 0, H) \\ &+ \int_0^H L_A(z, \lambda, T_A)t(\lambda, z, H)dz \\ &+ R_s(\lambda)t(\lambda, 0, H)\int_0^H L_A(z, \lambda, T_A)t(\lambda, 0, z)dz. \end{aligned} \tag{2.30}$$

From Equation 2.30, $L^{TOA}(\lambda)$ is a complex function of atmospheric state and surface state, including atmospheric optical depth (both gases and aerosols), surface emission and atmospheric emission:

$$L^{TOA}(\lambda) \propto f(T_s, T_A, \tau_g, \tau_a, \ldots), \tag{2.31}$$

where f is the forward function, simulated by the forward model F.

Due to the finite spectral response of the instrument, the monochromatic radiance at wavelength λ, $L(\lambda)$, needs to be integrated over the width of the channel using response function $\phi_i(\lambda)$ to derive in-band value, L_i:

$$L_i = \frac{\int_0^\infty L(\lambda)\phi_i(\lambda)d\lambda}{\int_0^\infty \phi_i(\lambda)d\lambda}. \tag{2.32}$$

Response functions ($\phi(\lambda)$) vary from instrument to instrument. Figure 2.7 gives the normalized response functions of the AATSR 11 μm and 12 μm channels. Usually, the integrated radiance (L_i) is converted to brightness temperature (BT_i): $L_i \longrightarrow BT_i$, Equation 2.31 becomes:

$$BT_i \propto f(T_s, T_A, \tau_g, \tau_a, \ldots). \tag{2.33}$$

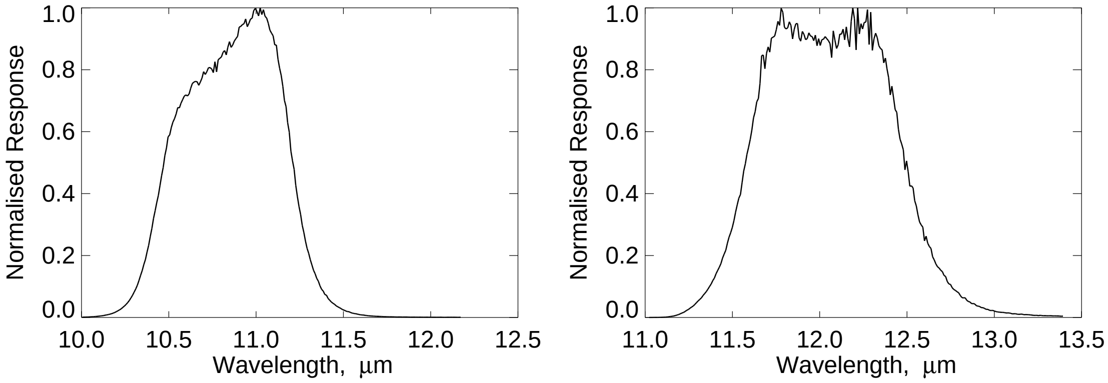

Figure 2.7: AATSR normalized filter response functions, left: 11 μm, and right: 12 μm.

2.3.3.2 Infrared forward model

An infrared forward model is developed to simulate the process described by Equation 2.30. It is a three-layer model and is based on the assumption that aerosols are concentrated within an infinitely thin layer at a variable height in the atmosphere (see Figure 2.8), infrared radiance at the TOA can be expressed as:

$$L^{TOA} = B_a^{\uparrow}\epsilon_a T_{al} + L_{al}^{\downarrow} R_a T_{al} + L_{al}^{\uparrow} + L_{bl}^{\uparrow} T_a T_{al} + L_{bl}^{\uparrow} T_{bl}^2 R_a R_s T_a T_{al} + L_{bl}^{\uparrow} T_{bl}^4 R_a^2 R_s^2 T_a T_{al} + \dots \tag{2.34}$$

The variables in Equation 2.34 are defined as

- T_{al}: transmission of the atmosphere above aerosol layer,
- $L_{al}^{\uparrow}$: upwelling radiance from the atmosphere above aerosol layer,
- $L_{al}^{\downarrow}$: downwelling radiance from the atmosphere above aerosol layer,
- T_a: transmission of the aerosol layer,
- R_a: reflectance of the aerosol layer,
- B_a: black body radiance of the aerosol layer,
- ϵ_a: emissivity of the aerosol layer,

- $L_{bl}^{\uparrow}$: total upwelling radiance below the aerosol layer,
- T_{bl}: transmission of the atmosphere below the aerosol layer,
- R_s: surface reflectance.

The $L_{bl}^{\uparrow}$ is contributed by the atmospheric radiance $L_{bl}^{\uparrow(atm)}$ and the surface emission $B_s\epsilon_s$:

$$L_{bl}^{\uparrow} = L_{bl}^{\uparrow(atm)} + B_s\epsilon_s T_{bl}, \tag{2.35}$$

where $L_{bl}^{\uparrow(atm)}$ is the upwelling atmospheric radiance at the bottom of the aerosol layer, B_s and ϵ_s are surface black body radiance and surface emissivity. Without taking into account the multiple reflections and scatterings between surface and aerosol layer, Equation 2.34 can be reduced to:

$$L^{TOA} = B_a^{\uparrow}\epsilon_a T_{al} + L_{al}^{\downarrow} R_a T_{al} + L_{al}^{\uparrow} + L_{bl}^{\uparrow} T_a T_{al}. \tag{2.36}$$

The four terms at the right side of the Equation 2.36 are:

- Thermal emission of the aerosol layer corrected by the above atmosphere, $B_a\epsilon_a T_{al}$, where ϵ_a is the aerosol emissivity and B_a is the aerosol black body radiance.
- Downwelling radiance from the atmosphere above the aerosol layer reflected by the aerosol layer, $L_{al}^{\downarrow} R_a T_{al}$, where R_a is the aerosol reflectivity and T_{al} is the transmission of the atmosphere above the aerosol layer.
- Upwelling radiance from the atmosphere above the aerosol layer $L_{al}^{\uparrow}$.
- Upwelling radiance below the aerosol layer, $L_{bl}^{\uparrow}$, corrected by the aerosol layer and the atmosphere above it, $L_{bl}^{\uparrow} T_a T_{al}$, where T_a is the aerosol layer transmission.

Aerosol related terms in Equation 2.36, R_a, T_a and ϵ_a are calculated using the LUTs strategy described in Section 2.3.2. The atmospheric transmission (T_{al}, T_{bl}),

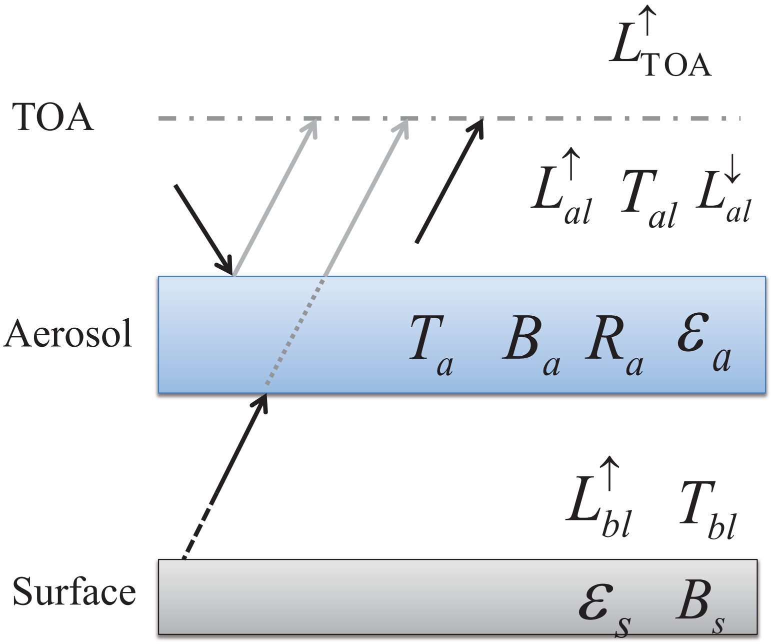

Figure 2.8: Atmospheric-surface interactions in the infrared forward model.

radiance (R_{al}, R_{bl}) and the Earth's surface emission ($B_s\epsilon_s$) are calculated with a radiative transfer model and a surface emissivity model which will be explained in Section 2.3.4. The auxiliary data, profiles of temperature, pressure, gases as well as 10-m wind, are from ECMWF reanalysis. It is important to understand the dependences of AATSR measurements on varying aerosols and atmospheric conditions.

2.3.3.3 Sensitivity of AATSR TOA BTs to atmospheric gases

To minimize the effects of the atmosphere, infrared band locations of AATSR (11 μm and 12μm) are selected to be within the atmospheric window between 8 μm and 14 μm. In this region the atmosphere is relatively transparent. The main absorbers are water vapour (H_2O) and carbon dioxide (CO_2); several other gases, like ozone (O_3), ammonia(NH_3), CFCs, also make small contributions to the total absorption (Moore et al., 2012; Moore and Remedios, 2008; Remedios et al., 2007a;

Buchwitz et al., 2005).

In order to simulate the gas effects on the TOA radiance, assuming no aerosol, the atmospheric transfer process in Equation 2.31 is calculated with the Reference Forward Model (RFM) for five reference atmospheres. RFM is a GENLN2-based line-by-line (LBL) radiative transfer model developed at AOPP, Oxford University, under an ESA contract to provide reference spectral calculations for the MIPAS launched on the ENVISAT satellite in 2002, more information can be found at http://www.atm.ox.ac.uk/RFM/. The five reference atmospheres are for mid-latitude daytime (day), polar winter (win), polar summer (sum), American standard atmosphere with one-sigma variation (var) and equator (equ) (Remedios et al., 2007b). These atmospheres describe the vertical distributions of thirty atmospheric gas species, including H_2O, CO_2, O_3, N_2O, NH_3, CH_4, CFCs, as well as the corresponding temperature and pressure profiles, between the surface and a height of 120 km with a vertical step size of 1 km. Unlike H_2O with dramatic variation in time and space, CO_2 is relative stable over years and well-mixed globally, as shown in Figure 2.9. These five atmospheres have similar distributions of CO_2, the equator atmosphere (equ) has the highest water vapour loading while the winter polar atmosphere has the lowest. As shown in Figure 2.10, for both nadir view and forward view the equator atmosphere has the lowest transmission while polar winter atmosphere has the highest transmission, this is due to the different water vapour loading. The transmission at 11 μm is higher than that at 12 μm. The transmission in forward view is lower than the nadir view due to its prolonged atmospheric path. For both views and both channels, transmission decreases with the increase of water vapour loading. It can be seen that although the AATSR channels are in the part of the electromagnetic spectra where the atmosphere is supposed to be relatively transparent, the influence of gases is not negligible.

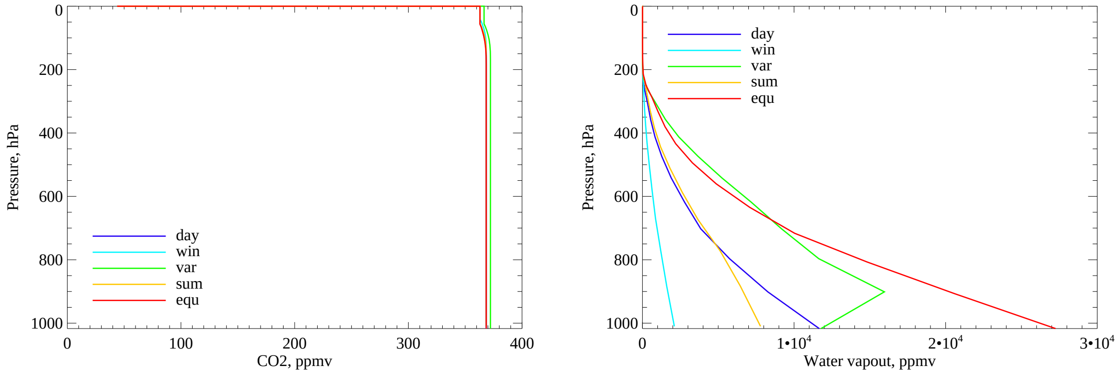

Figure 2.9: Vertical distributions of carbon dioxide (CO_2) and water vapour (H_2O) for five climatological atmospheres, mid-latitude daytime (day), polar winter (win), polar summer (sum), American standard atmosphere with one-sigma variation (var) and equator (equ).

2.3.3.3.1 Methodology

The aim of sensitivity study is to evaluate the effects of gases on AATSR TOA BT and to decide which gases should be taken into account in retrieval to achieve a high accuracy for SST. The main idea is to use a radiative transfer model to examine the dependences of measured AATSR TOA BT on a set of atmospheric and surface conditions.

To start, a criterion to judge the importance of a gas is needed. In order to get the required accuracy of SST (δT_s), the accuracy of BT_i for each channel i ($\delta\mathrm{BT}_i$) has to be achieved. The $\delta\mathrm{BT}_i$ is a complex function (g) of the Earth's surface and atmospheric conditions:

$$\delta BT_i \propto g(T_s, T_A, \tau_g, \tau_a, \delta T_s, \ldots), \tag{2.37}$$

the mathematical form of g depends on the particular radiative transfer model used in the calculation: here the RFM model is employed. The reference state of the atmosphere, including the reference TOA BT_i, BT_{i0}, is obtained with a standard atmospheric profile (with standard average concentrations of gases, temperature and pressure profiles). The corresponding change ($\delta\mathrm{BT}_i$) in BT_i is computed by disturbing

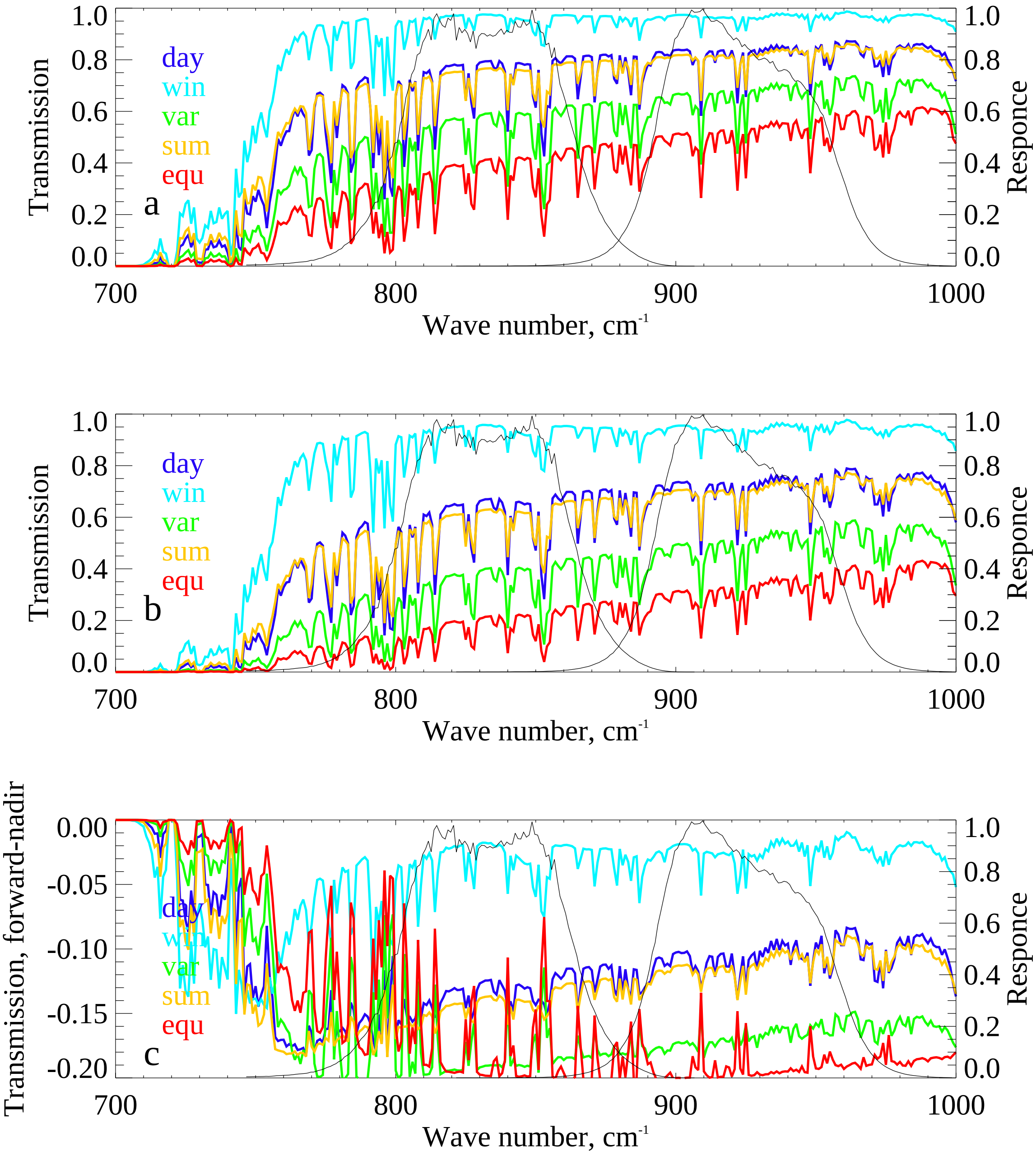

Figure 2.10: Theoretical spectral atmospheric transmission for five reference atmospheres, mid-latitude daytime (day), polar winter (win), polar summer (sum), American standard atmospherie with one-sigma variation (var) and equator (equ); the two black thin lines indicate response functions for two AATSR infrared channels centred at 11 μm and 12 μm; a) AATSR nadir view, b) AATSR forward view, and c) Difference in transmission between forward view and nadir view.

the surface temperature by a small number (such as $\delta T_s = 0.3$ K) while the other factors in the profile are unchanged. The δBT_i is thought to be the variation in BT_i introduced by the change of surface temperature. Inversely, an error δBT_i of BT_i at the TOA would introduce a bias of δT_s to the retrieved SST. In order to retrieve the SST within the required accuracy, the accuracy of BT_i has to be better than δBT_i.

The second step is to compute the variation of BT_i ($\Delta BT_i(gas_{pre})$) at the TOA caused by a chosen gas. This is calculated as the difference in BT_i obtained from the standard profile and obtained from the profile that assumes the absence of the gas with other parameters unchanged. If $\Delta BT_i(gas_{pre})$ is greater than or close to δBT_i, then this gas is defined to be an important gas and may play an important role in the TOA radiance, and could give a significant bias in the retrieval if being neglected, the retrieval algorithm should consider the effect of this gas. Otherwise, the gas can be safely neglected.

Finally, the concentration of some gases strongly varies with location, height and season (for example H_2O and HNO_3). It is also important to know the bias in BT_i caused by the dramatic change in the amount of such a gas. This effect is tested by increasing the concentration of the gas, keeping the other factors unchanged and obtaining the variation of BT ($\Delta BT_i(gas_{var})$) at the TOA. If $\Delta BT_i(gas_{var})$ is greater than or close to δBT_i, the variation in the contribution of the gas needs to be accounted for. The retrieval should use a temporal and spatial varying profile for the gas instead of a climatological average value.

2.3.3.3.2 Results

As shown in Figure 2.11, the possible important absorbing gases for the atmospheric window region are: C_2H_6, CO_2, F12, H_2O, HNO_3, NH_3, O_3, CCL_4, F11, F22. The mid-latitude standard atmosphere is used to produce the reference state of atmosphere, including the reference BT_i at the TOA. The reference surface temperature is defined as 290 K. It is assumed that all the gases are independent from each other. No aerosol is considered in this model. The mixing ratios of gases in the mid-latitude standard atmosphere and one-sigma variation are given in Table 2.4.

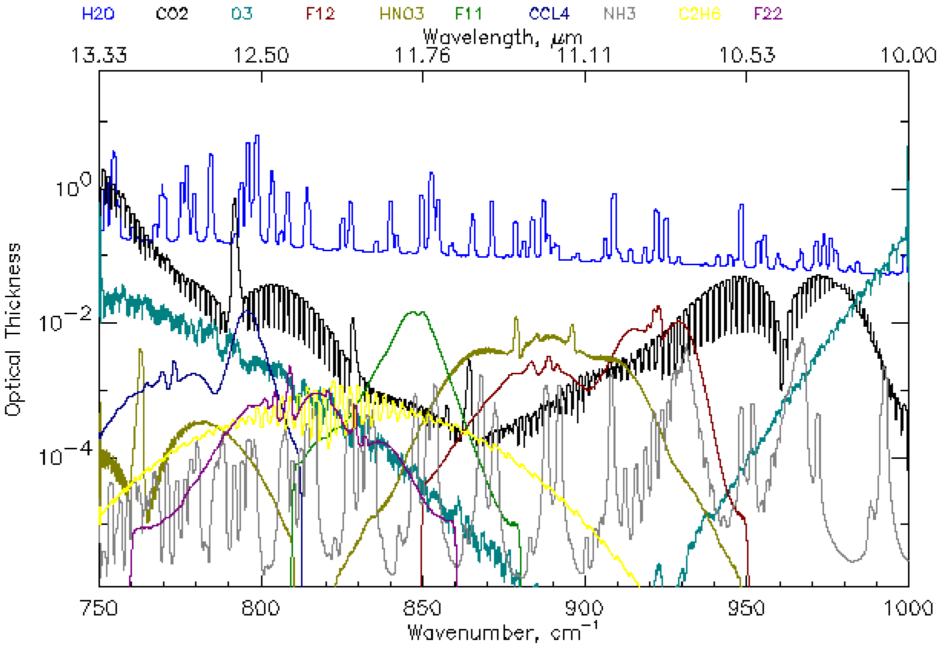

Figure 2.11: Gas optical depth (http://www.atm.ox.ac.uk/RFM/).

Table 2.4: The column mixing ratio of absorbing gases of mid-latitude standard atmosphere.

gas	mixing ratio (ppmv)	one sigma variation (ppmv)	percentage of variation (%)
C_2H_6	1.5E−4	8.0E−5	52.937
CO_2	3.0E+2	9.5E+1	3.159
F12	1.1E−4	2.0E−5	12.246
H_2O	3.1E+2	2.7E+2	86.400
HNO_3	8.7E−4	4.9E−4	56.383
NH_3	2.0E−5	5.0E−5	299.991
O_3	1.7E+1	5.0E+1	29.608
CCL_4	1.0E−5	1.0E−6	15.317
F11	5.0E−4	4.0E−5	7.923
F22	3.0E−4	3.0E−6	15.316

To get the required accuracy of BT$_i$ (δBT_i) at each channel, the surface temperature is increased by δT_s. Table 2.5 shows the variations in BTs corresponding to a change of 0.3 K in surface temperature. The required accuracies for the 12 μm channel in both views are higher than the 11 μm channel. For the two channels, the values of δBT$_i$ in forward view are smaller than nadir view. The reason is that the atmospheric path of forward view is nearly 1.75 times as long as the path in nadir view. Hence the atmospheric absorption is stronger than that for nadir view, for which higher accuracy is needed to estimate the effect of absorbing gases in the atmosphere. Very similar results (with a difference of $\sim$ 0.01 K) are obtained by using different surface temperatures (280 K, 285 K, 295 K).

Table 2.5: The required accuracy of δBT$_i$ for AATSR two infrared channels in two views.

channel (μm)	view	surface temperature (K)	δT_s (K)	δBT_i (K)
11	nadir	290	0.3	0.285
11	forward	290	0.3	0.278
12	nadir	290	0.3	0.276
12	forward	290	0.3	0.256

Based on the obtained criteria for different channels and views (the first right column of Table 2.5), the importance of each gas is determined. As mentioned above, to compute the effect of a gas, this gas is intentionally excluded from the reference profile to create a modified profile, i.e. in the modified profile the amount of this gas is zero and the other parameters, including surface temperature, are unchanged. This modified profile is used as the input for RFM to generate a new TOA BT$_i$ for each channel (BT$_{i1}$). The difference between BT$_{i1}$ and BT$_{i0}$, δBT$_i(gas_{pre})$, is thought to be the contribution from this particular gas. The results are shown in Table 2.6.

Table 2.6: The contribution of gases to BT$_i$ (ΔBT$_i(gas_{pre})$) at each channel and view.

channel (μm)	view	C_2H_6	CCL_4	CO_2	F11	F12	F22	H_2O	HNO_3	NH_3	O_3
11	nadir	0.0001	0.0000	0.2291	0.0004	0.2500	0.0000	0.5265	0.1213	0.0050	0.0057
11	forward	0.0004	0.0003	0.3824	0.0009	0.4305	0.0003	0.7694	0.2096	0.0088	0.0097
12	nadir	0.00074	0.0135	0.2533	0.1564	0.0056	0.0209	1.6358	0.0427	0.0017	0.0311
12	forward	0.0153	0.0250	0.4015	0.2703	0.0125	0.0385	2.2446	0.0764	0.0057	0.0547

Table 2.7: $\Delta BT_i(gas_{var})$ at 11 μm nadir (N) view.

11 μm, N	C_2H_6	CO_2	F12	H_2O	HNO_3	NH_3	O_3	CCL_4	F11	F22
$\frac{\partial BT}{\partial x}(K/\%)$	-0.000005	-0.00104	-0.00261	-0.00458	-0.00202	-0.00004	-0.000006	-0.00010	0.00140	0.00021
one-σ var (%)	52.937	3.1595	14.246	86.400	56.383	299.99	29.608	15.317	07.924	09.086
ΔBT (K)	0.00024	0.00329	0.03726	0.39644	0.11407	0.01351	0.00011	0.00153	0.00980	0.00190

Table 2.8: $\Delta BT_i(gas_{var})$ at 11 μm forward (F) view.

11 μm, F	C_2H_6	CO_2	F12	H_2O	HNO_3	NH_3	O_3	CCL_4	F11	F22
$\frac{\partial BT}{\partial x}$ (K/%)	0.00001	0.00192	0.00513	0.00680	0.00397	0.00009	0.00001	0.00017	0.00270	0.00040
one-σ var (%)	52.937	3.1595	14.246	86.400	56.383	299.99	29.608	15.317	07.924	09.086
ΔBT (K)	0.00050	0.00608	0.07303	0.58770	0.22424	0.02662	0.00023	0.00260	0.0189	0.00363

Table 2.9: $\Delta \mathrm{BT}_i(gas_{var})$ at 12 μm nadir(N) view.

12 μm, N	C_2H_6	CO_2	F12	H_2O	HNO_3	NH_3	O_3	CCL_4	F11	F22
$\frac{\partial BT}{\partial x}$ (K/%)	-0.00007	-0.00224	-0.00005	-0.00993	-0.00042	-0.00001	-0.00030	-0.00013	-0.00155	-0.00020
one-σ var (%)	52.937	3.1595	14.246	86.400	56.383	299.99	29.608	15.317	07.924	09.086
ΔBT (K)	0.00384	0.00709	0.00078	0.85827	0.0239	0.00481	0.00897	0.00206	0.01232	0.00189

Table 2.10: $\Delta \mathrm{BT}_i(gas_{var})$ at 12 μm forward (F) view.

12 μm, F	C_2H_6	CO_2	F12	H_2O	HNO_3	NH_3	O_3	CCL_4	F11	F22
$\frac{\partial BT}{\partial x}$ (K/%)	-0.00014	-0.00371	-0.00010	-0.01352	-0.00083	-0.00003	-0.00056	-0.00024	-0.00302	-0.00040
one-σ var (%)	52.937	3.1595	14.246	86.400	56.383	299.99	29.608	15.317	07.924	09.086
ΔBT (K)	0.00743	0.01174	0.001551	1.1682	0.04709	0.00934	0.01661	0.00378	0.02400	0.00368

In the 11 μm channel, the possible important gases for nadir view are CO_2, H_2O, F12, and HNO_3 while for forward view are CO_2, H_2O, F12 and HNO_3. The important gases in the 12 μm channel nadir view are CO_2, H_2O and F11, for forward view the important absorbers are CO_2, H_2O and F12. As a result, the gases mentioned above should be considered in the retrieval. The effects of O_3 in both views of the 12 μm channel are not as strong as the other gases.

Although the effects of some gases on BTs calculated using their standard average values are not always important, some gases, such as H_2O, HNO_3, have concentrations that are highly variable in time and space. Thus their effects would change in a wide range. It is important to obtain the variation of BT_i caused by the variation of gas concentration $\Delta\mathrm{BT}_i(gas_{var})$.

The $\Delta\mathrm{BT}_i(gas_{var})$ is calculated by using sensitivity of BT_i to variation of a gas $(\frac{\partial BT_i}{\partial x})$ times percentage of one-sigma variation of standard amount; x is the percentage of increase. The results are shown in Table 2.7, Table 2.8, Table 2.9 and Table 2.10. The only gas whose variation has a strong influence on BTs at both views of the 12 μm is H_2O, while for the 11 μm channel, H_2O has a strong influence and the effect of a variation in HNO_3 is not as strong as for H_2O, but is still greater than the other gases. As a result, the retrievals involved with infrared channels should use the realistic profiles for the two gases instead of climatological data.

2.3.3.4 Conclusions of the gas sensitivity study

A detailed sensitivity study based on LBL model RFM has been carried out investigating the effects of gases on AATSR infrared channels quantitatively. The results demonstrate that the two AATSR infrared channels show strong sensitivities to H_2O, CO_2, HNO_3 and CFCs. Therefore to simulate the AATSR measurements (Equation 2.36), the effects of these gases need to be taken into account. Although the RFM model is capable of simulating the radiative transfer process accurately, it is a LBL model and too time-consuming to be used for a real-time retrieval. Instead, ORAC uses the RTTOV model to simulate the effects of gases. RTTOV was designed for fast calculation of radiances measured by space-borne sensors (Saunders et al., 2012; Saunders, 2002), and covers the spectral range 3 μm to 20 μm in the infrared and frequency range 10 GHz to 200 GHz in the microwave. It supports a large number of platforms and sensors including AATSR, MODIS, SEVIRI. RTTOV uses regression coefficients derived from accurate LBL models to express optical depth as a linear combination of profile dependent predictors that are functions of temperature, absorber amount, pressure and viewing angle. In this study RTTOV version 10 is being used; the regression coefficients in version 10 were generated by LBL model LBLRTM.

RTTOV 10 for AATSR allows us to vary the amount of water vapour, and optionally ozone, while the other gases are treated as a well-mixed gas. The well-mixed gas includes CO_2, N_2O, CO, CH_4, O_2, NO, SO_2, NO_2, NH_3, HNO_3, OH, HF, HCl, HBr, HI, ClO, OCS, H_2CO, HOCl, N_2, and CFCs; the amounts are taken from a climatological mean profile. The sensitivity study indicates that using a climatological mean of HNO_3 may cause bias in the retrieval, however it is difficult to use a real-time profile for HNO_3 in RTTOV and this would be improved in future. Very similar results are reported by Embury et al. (2012b) and Noyes (2005). Embury et al. (2012b) also indicates the importance of N_2O.

Using a set of diverse atmospheric conditions, AATSR TOA BTs simulated by RTTOV have a bias of $\sim$ 0.1 K compared to those calculated by the RFM. This bias may be translated into the error in the retrieved SST and will be discussed in Chapter 3.

2.3.3.5 Effects of aerosols on the TOA BTs

Satellite infrared channels are generally chosen within the infrared atmospheric window ($8 - 14$ μm) to minimize gas absorptions. However, BTs in this spectra region show strong dependence on aerosols, varying with aerosol composition, AOD, size and altitude in the atmosphere. Figure 2.12 is an example of BTs predicted by the infrared forward model (Equation 2.36) as a function of AOD and r_e for marine clean class. Unity surface emissivity is used in this simulation. It can be seen that low AOD does not change BTs significantly; for a fixed r_e, TOA BTs decrease as AOD increases. For larger particles ($\mathrm{r}_e \geq 0.1$ μm) BTs decrease with both AOD and r_e. It is noticeable that for small particles ($\mathrm{r}_e < 0.1$ μm), variations in BTs decrease as r_e increases. For marine clean class, when r_e is at the low end (< 0.1 μm), according to Figure 2.4, the particles are composed of a large amount of water-soluble particles, and small amounts of sea salt particles. Using the refractive index given in OPAC package, the emissivity of water-soluble particles is 0.965 at 11 μm, lower than that of sea salt (0.988). As r_e increases, the proportion of sea salt particles with high emissivity begins to increase, therefore the emission of the aerosol layer increases. The increased emission from the aerosol layer will partially compensate for the reduction in the TOA radiance caused by aerosol extinction.

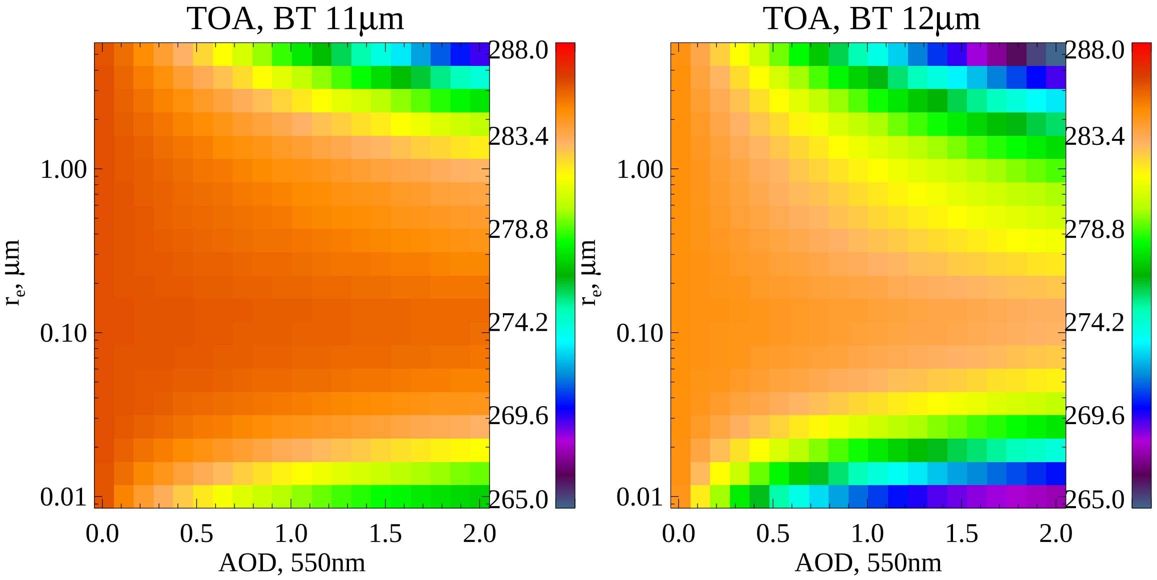

Figure 2.12: AATSR TOA BTs at the 11 μm and 12 μm channels as predicted by the infrared forward model (Equation 2.36) for $\theta_s = 0°$, $\theta_v = 55°$, $T_s = 288$ K, $P_a = 900$ hPa and marine clean aerosol class, clear sky BTs are 285.95 K for 11 μm and 284.53 K for 12 μm

.

Figure 2.13 and Figure 2.14 illustrate the changes in brightness temperature (ΔBT) in the nadir view of AATSR due to presence of aerosols with a range of AOD ($0 - 1$) and aerosol layer heights ($1000 - 400$ hPa) for four different aerosol classes; the main descriptions of aerosol classes are summarised in Table 2.2. At this step the effective radius of aerosol is fixed ($r_e = 0.97$ μm).

Aerosols from strong dust storms may reach a height of $3 - 8$ km (Yorks et al., 2009; Liu et al., 2008), corresponding to an approximate pressure range of 800 hPa $-$ 400 hPa. It can been seen that in general aerosols lead to a cooling effect on the TOA BTs, and the absolute value of ΔBT increases with both AOD and aerosol layer height. In the presence of aerosols the ΔBT can be a few Kelvins, much larger than

AATSR infrared channel noise (~ 0.1 K). Compared to marine aerosols, dust aerosols have a stronger effect on BTs. It is worth noting that the ΔBT caused by spherical dust is stronger than that caused by non-spherical dust. It has been showed that in aerosol retrieval the non-spherical assumption is more appropriate for dust compared to spherical assumption and the radiative forcing caused by non-spherical dust is smaller than spherical dust (Wang et al., 2013; Zhao et al., 2003; Mishchenk et al., 1995).

Figure 2.15 and Figure 2.16 show the variations of ΔBT with different effective radii and aerosol layer heights for a fixed AOD (AOD = 1). It can be seen that the sensitivity of infrared BT to the effective radius is a few Kelvins, of the same magnitude of sensitivity to optical depth. When the effective radius is less than 0.1 μm ΔBT decreases with the increase of effective radius, while for the regime of $r_e \geq$ 0.1 μm, ΔBT increases as the effective radius increases.

2.3.4 Ocean surface emissivity

For infrared spectra the sea surface emissivity is close to unity and can be altered by wind speed, salinity, viewing geometry, wavelength and surface temperature. The total sea surface emission is the sum of three types of emission. The first is the direct emission of the sea surface decided by surface temperature, wavelength, salinity and viewing geometry, it is the dominant factor in the total sea surface emission. The second is the Surface Emitted Surface Reflected radiation (SESR) which comes from direct emission intercepted by nearby facets and reflected into the sensor's direction. At high surface wind speed (≥ 10 ms^{-1}) and high emission angle conditions ($\geq 73.5°$) the SESR can enhance the emissivity by 0.02 to 0.03. The third term is the reflection of downwelling atmospheric radiance. The atmospheric radiance is dependent on viewing angle and the opacity of the atmosphere, normally the contribution of it to the emissivity is less than 0.003 even under strong wind conditions.

The infrared spectral emissivity properties have been studied both theoreti-

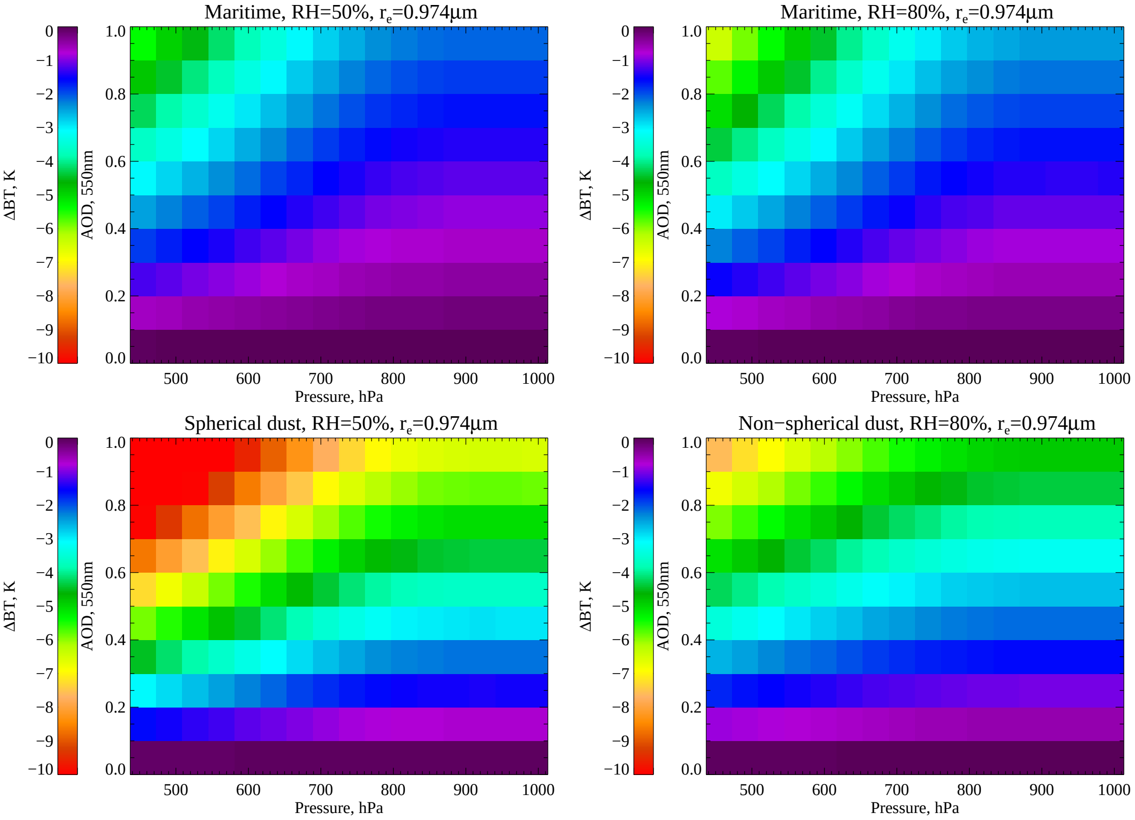

Maritime, RH=50%, r_e=0.974µm

Maritime, RH=80%, r_e=0.974µm

Spherical dust, RH=50%, r_e=0.974µm

Non−spherical dust, RH=80%, r_e=0.974µm

Figure 2.13: Sensitivity of brightness temperature (BT) (ΔBT = BT$_{AOD}$ − BT$_{clear}$) at the 12 μm channel to AOD and aerosol layer height for four aerosol classes, the aerosol classes are defined in Table 2.2, BT$_{clear}$ is the reference BT without aerosols, BT$_{AOD}$ is BT with the presence of aerosols.

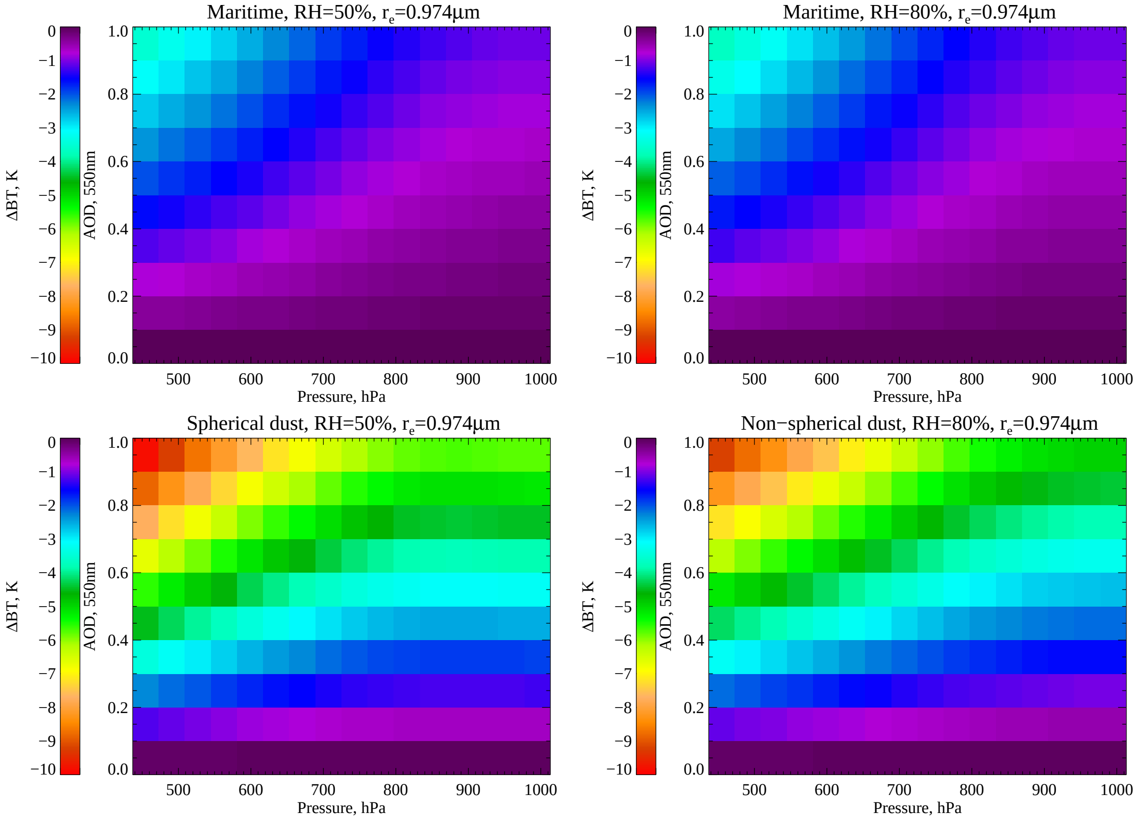

Figure 2.14: Same as Figure 2.13 but for the 11 μm channel.

cally and experimentally. The slope distribution of rough sea surface measured by Cox and Munk (1955) provides the basis for many emissivity models. For example, Masuda et al. (1988) model surface emissivity as a function of zenith angle and surface wind speed (12.5 m). This model does not consider the effect of multiple-reflection or the SESR radiation. It is adequate for small viewing angles if wind speed is less than 5 ms^{-1}. For large viewing angles, the difference between modelled emissivity and measured emissivity becomes significant. Watts et al. (1996) evaluate the emission and reflection properties of a rough sea surface for the wavelengths and viewing geometries of ATSR. This paper shows the effect of sea surface roughness does not play an important role for ATSR nadir view and it becomes significant when the viewing angle is greater than 30°. Masuda (2012) develops a model considering the influence of SESR and calculates emissivities for the wavelengths of 3.7 μm, 11 μm and 12 μm at four wind speeds. The calculated results show the effect of SESR is not significant for low viewing angle ($\leq 50°$) and low wind speed conditions ($\leq$ 10 ms^{-1}). Newman et al.

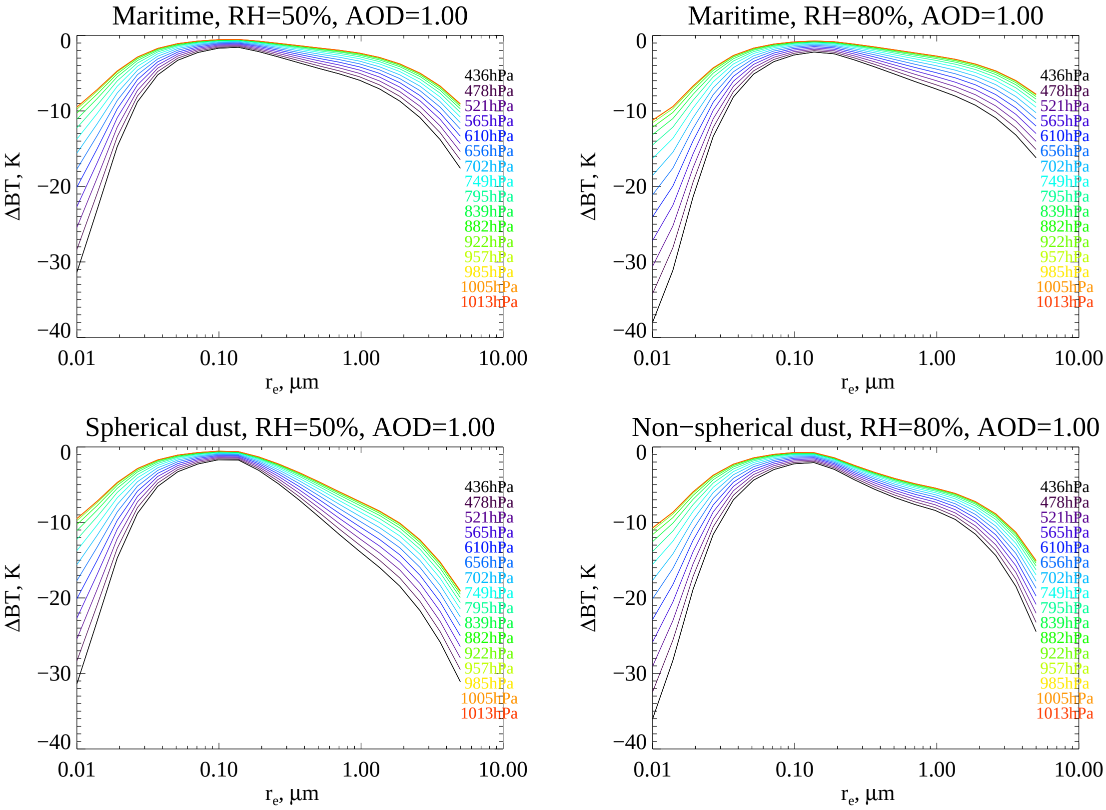

Figure 2.15: Sensitivity of brightness temperature (BT) (ΔBT = BT$_{AOD}$− BT$_{clear}$) at the 12 μm channel to effective radius (r$_e$) and aerosol layer height for four aerosol classes, the aerosol classes are defined in Table 2.2, BT$_{clear}$ is the reference BT without aerosols, BT$_{AOD}$ is the BT with the presence of aerosols.

(2005) investigate the dependences of the surface emissivity on water temperature and salinity using the measurements from aircraft and ground-based interferometers. The results indicate the effect of salinity is small, whereas the effect of temperature which is often neglected by emissivity model is great, and neglecting the temperature effect would lead a systematic error in SST retrieval. Wu and Smith (1997) update the emissivity model of Masuda et al. (1988) by incorporating reflected emission and using a new complex refractive index of the ocean water. The new model improves the remote sensing SST retrieval, and the emissivity of the new model is less sensitive to wind speed until the viewing angle is greater than 60°. Minnett and Hanafin (2005) access the dependences of sea surface emissivity on wavelength, emission angle, temperature and wind speed from ship-based measurements, and conclude that the wind dependence is not as strong as model predictions.

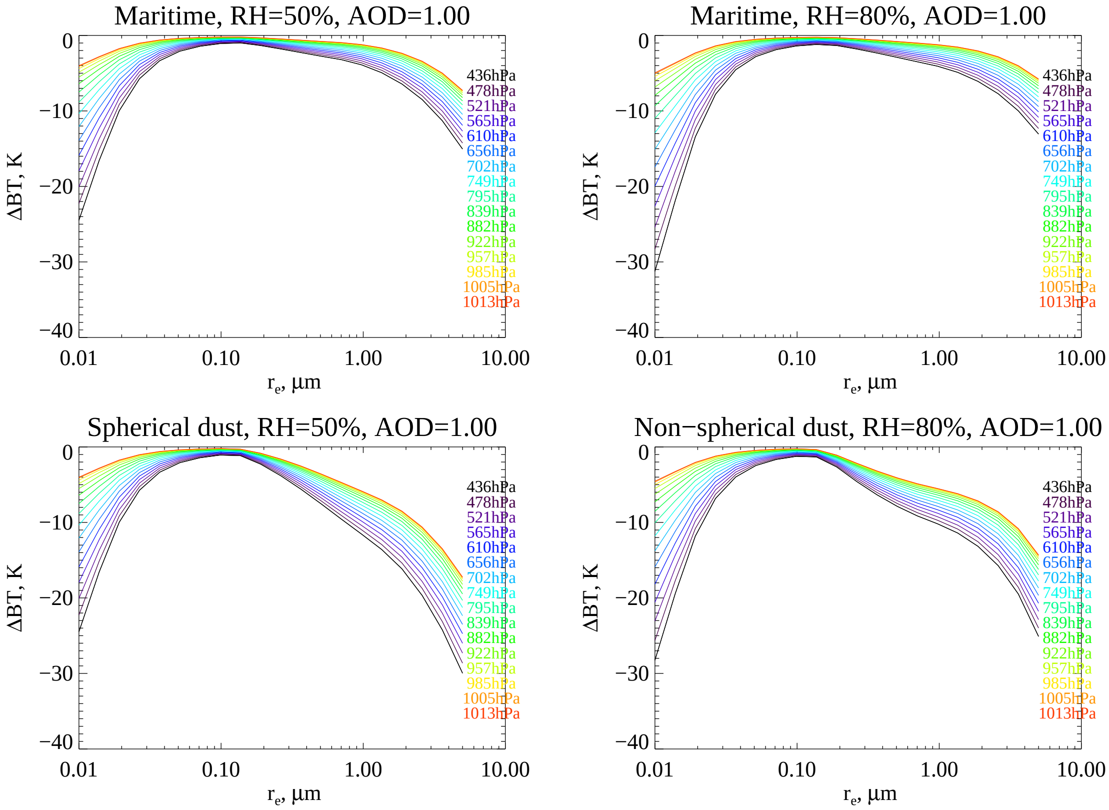

Figure 2.16: Same as Figure 2.15 but for the 11 μm channel.

ORAC uses a tabulated emissivity model (EMS) which was given by Embury (2012). This model considers the effects of wavelength, viewing angle, wind speed, surface temperature, as well as the channel response. Figure 2.17 shows the emissivity at different viewing angles, wind speeds and surface temperatures. It can be seen that viewing angle has a substantial effect on the calculated emissivity and wind speed begins to play a role when viewing angle is greater than 20°. Apart from the effects of viewing angle and wind speed, the emissivity also increases slightly as temperature increases.

2.4 Summary

ORAC is an OE scheme for aerosol and cloud retrievals from satellite measurements, a new version of ORAC for aerosol and surface properties has been developed. In this

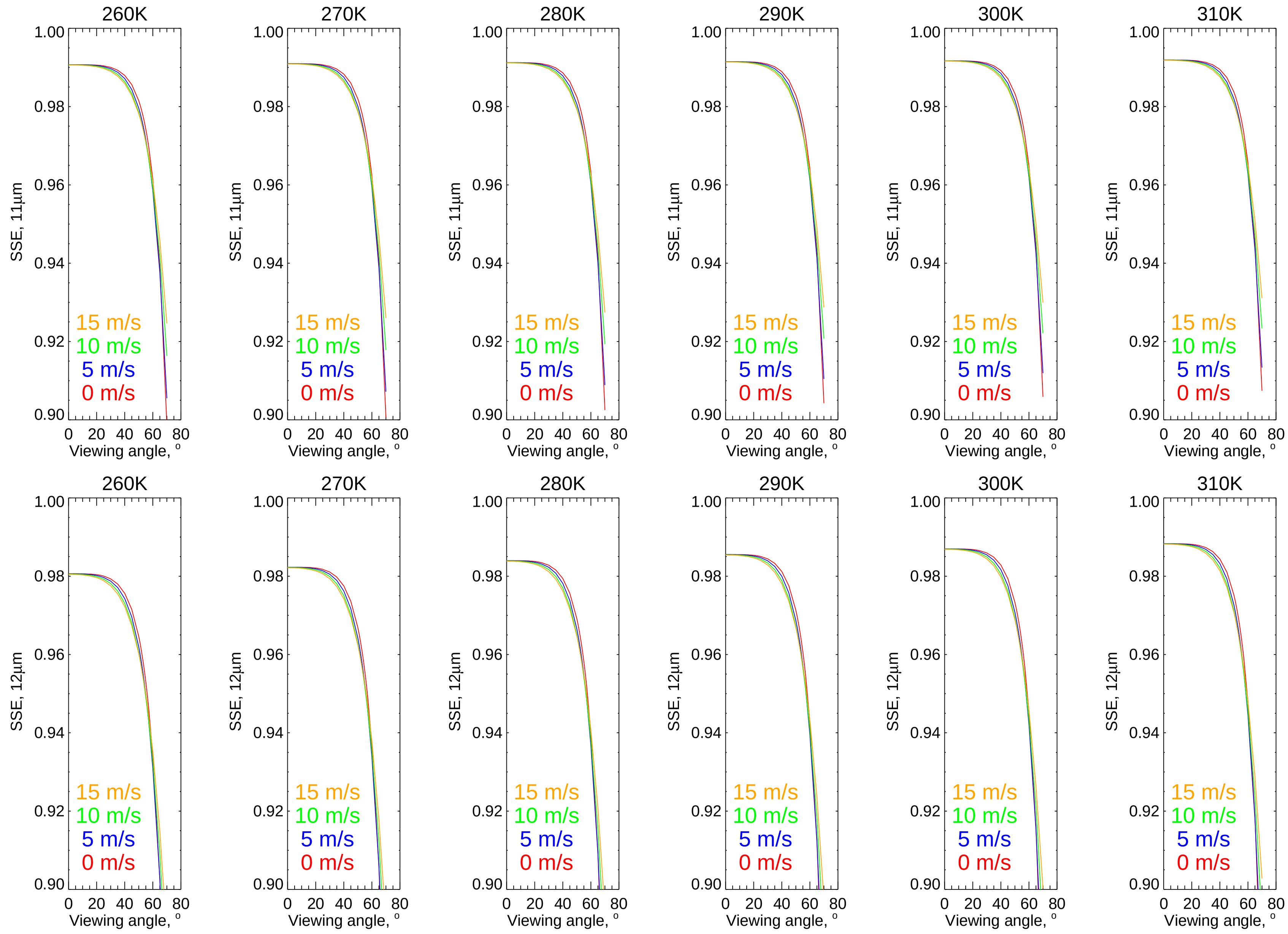

Figure 2.17: Sea surface emissivity (SSE) as a function of viewing angle, wind speed and temperature, top panel: AATSR 11 μm channel, bottom panel: AATSR 12 μm channel.

chapter, a comprehensive description of the new ORAC is provided, and in particular the infrared forward model is discussed in detail. The sensitivity study based on LBL model (RFM) demonstrates that under clear sky conditions, the presences of absorbing gases (i.e. H_2O, CO_2 and some CFCs) and aerosols can change the radiative transfer in infrared spectra significantly, and they may cause biases in the retrieved parameters if not simulated sufficiently.

Figure 2.18 is an example of the main retrieved parameters. ORAC generally retrieves low AOD over ocean, in contrast the AOD over land is high especially in dust (Saharan desert) and industrial regions (southern Asia, northern America). Another identifiable feature in AOD field is the high AOD over the continental outflow areas. Elevated effective radius can be observed over land particularly over northern Hemisphere continents. The retrieval of effective radius is constrained by the assumed aerosol classes, in this version of ORAC the aerosol classes are desert dust and marine clean, while the dominated aerosol class over northern Hemisphere is urban which is composed of small particles. The inappropriate aerosol class may explain the effective radius distribution over land. The retrieved surface temperature field looks much as expected, generally the surface temperature decreases from low latitudes to high latitudes, and the surface temperature over land is higher than that over ocean for the same latitude with the exception of Greenland where is covered by glaciers. The temperature over ocean has a low standard deviation, suggesting spatial and temporal homogeneities. The temperature over land shows a high variability, which is evidence of inhomogeneity. Aerosols are generally concentrated in the lowest levels of the atmosphere and aerosol layer height is closely related to the height of planetary boundary layer (PBL). The height of PBL over land is generally higher than over ocean, hence it is not surprising to see the retrieved aerosol layer height over ocean is lower compared to that over land. However, the retrieved aerosol layer height contains a strong constraint from the assumed aerosol class and the *a priori* information.

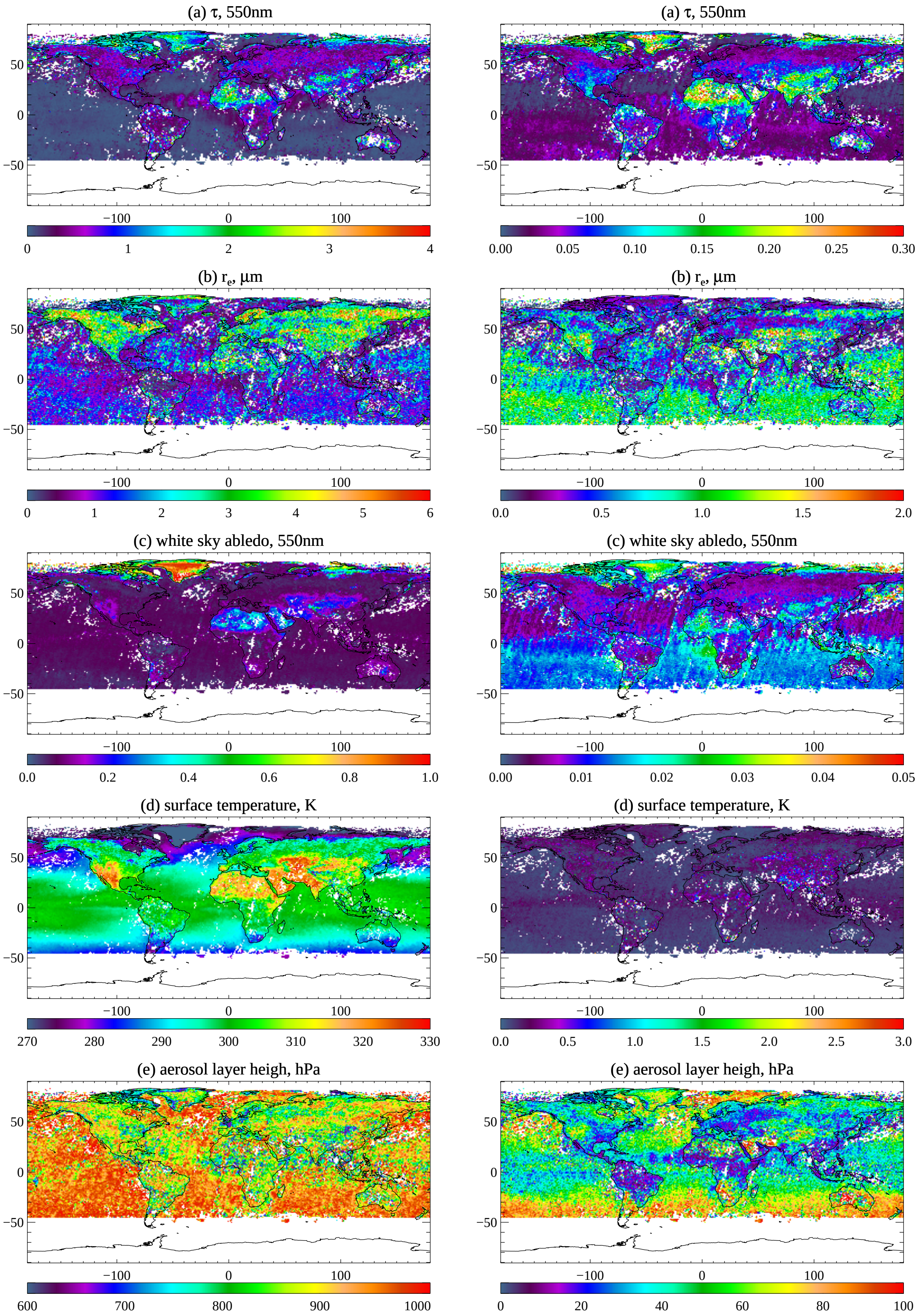

Figure 2.18: Global mean of a) AOD at 550 nm, b) effective radius, c) white sky albedo, 550 nm, d) surface temperature, and e) aerosol layer height, for the month of June 2006; left: monthly mean, right: standard deviation. The monthly mean is performed on a 1° × 1° latitude/longitude grid.

Chapter 3

Error budget

There are three components that influence infrared satellite SST retrieval: 1) instrument characteristics that introduce uncertainties into measurements; 2) processes in the atmosphere that modify the infrared radiation between the ocean surface and instrument; and 3) processes at the ocean surface that control the infrared emission. The three components rely on many factors, such as instrument designs, atmospheric conditions, surface states, and radiative transfer models. Errors or limitations in these factors potentially lead to the retrieved SST biased from the true values. The purpose of this chapter is to obtain a quantitative estimation of the impacts of errors in these factors on the ORAC retrieved SST.

3.1 Methodology

The principal of the experiment can be expressed as:

$$\delta SST_i = \frac{\partial SST}{\partial v_i} \delta v_i, \tag{3.1}$$

where $\delta\mathrm{SST}_i$ is the error in SST contributed by the i_{th} variable v_i, $\frac{\partial SST}{\partial v_i}$ is the sensitivity of SST to v_i, and δv_i is the error in v_i. It is assumed that all the variables are independent with each other. This experiment is composed of two steps:

- Firstly simulating the AATSR TOA measurements with the ORAC forward models based on a set of different surface and atmospheric conditions ($\mathbf{v}$). The simulated TOA measurements will be used as measurement vector $\mathbf{y}$ in the next step.
- Perturbing each variable (v_i) by a series of small and reasonable increments (Δv_i) and then getting a series of new retrieved SST ($\widehat{SST}$). Therefore $\frac{\partial SST}{\partial v_i}$ can be calculated as:

  $$\frac{\partial SST}{\partial v_i} = \frac{\widehat{SST} - SST_{true}}{\Delta v_i}, \tag{3.2}$$

  then choosing the error range (δv_i) for each variable (v_i) and using Equation 3.1 to get δSST_i.

3.2 AATSR TOA measurements simulation

In order to simulate the TOA measurements of a satellite radiometer, the instrument properties, the atmospheric and surface states are needed. Table 2.1 is used to provide the AATSR instrument properties. A diverse profile dataset is used to provide the atmospheric and surface states. This dataset was developed for the generation of RTTOV regression coefficients for Infrared Atmospheric Sounding Interferometer (IASI) and Atmospheric Infrared Sounder (AIRS) (Matricardi, 2009). It comprises 83 profiles describing 83 different atmospheric conditions. These profiles provide the concentrations of 15 atmospheric gases, including water vapour, ozone and carbon dioxide, between 1100 hPa and 0.005 hPa. The corresponding temperature and height profiles are also given. In this dataset many profiles are over very cold or warm surface, in general SST falls in a range of 265 K to 305 K, in this experiment, only the profiles with a surface temperature within this range are used. The surface temperature criterion leaves 53 profiles. Figure 3.1, Figure 3.2 and Figure 3.3 show the vertical distributions of temperature, water vapour and ozone for the 53 profiles.

In this simulation the aerosols are assumed to be spherical dust particles (A03) with an optical depth of 0.1 concentrated at the height of 800 hPa.

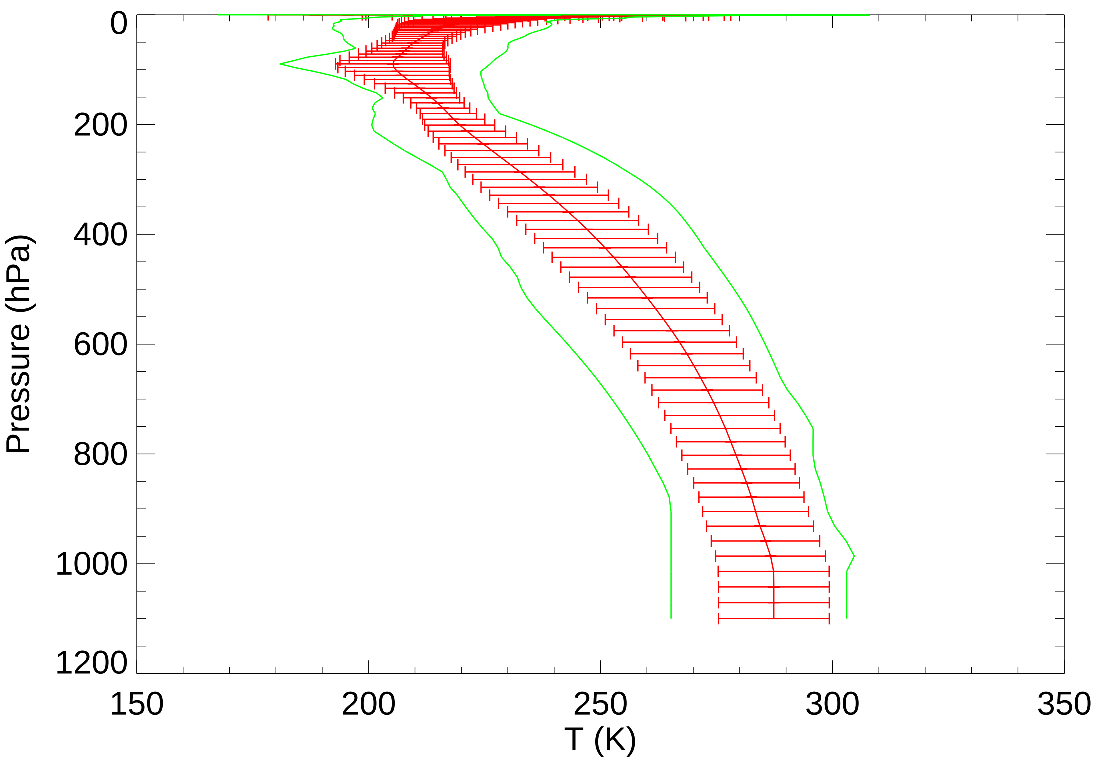

Figure 3.1: Statistics of temperature in the sampled dataset. The left thin green line indicates the minimum value and the right one indicates the maximum value. The red curve is the mean and the error bars are the standard deviation at each pressure layer.

3.3 Sensitivity calculation

The sensitivity of retrieved SST to a variable is examined by perturbing the variable by a small range for each scenario. For example, the sensitivity to surface emissivity is assessed by varying the surface emissivity within a reasonable range and retaining the other factors constant, the SST deficit (ΔSST) is obtained by evaluating how much the retrieved SST ($\widehat{SST}$) is changed from the reference SST (SST$_{true}$) which was used in the generation of the AATSR TOA measurements. The sensitivities of

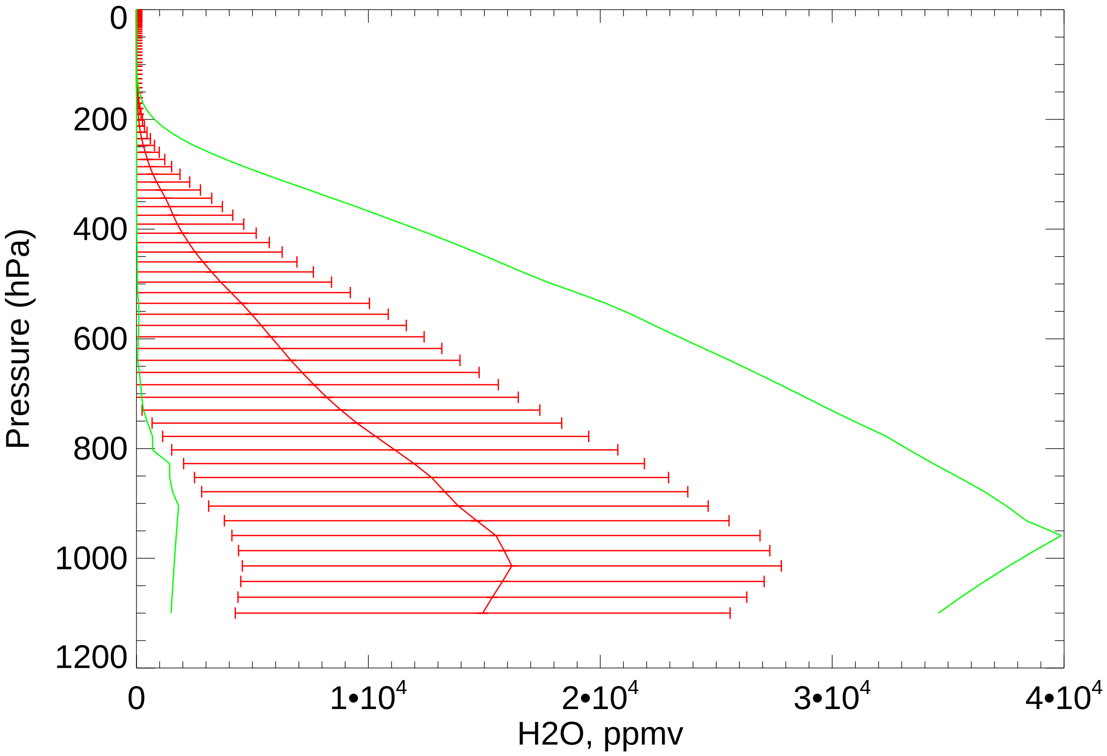

Figure 3.2: Same as Figure 3.1 but for water vapour.

SST to other variables are investigated using the same approach.

3.3.1 Instrument errors

To investigate the sensitivity of retrieved SST to infrared measurements, the infrared measurements are perturbed from the original values by a series of variations (ΔBT) from -0.3 K to 0.3 K at an increment of 0.1 K. Figure 3.4 presents variations in retrieved SST (ΔSST) with respect to the varying measurements (ΔBT) for the sampled 53 profiles (denoted by different colours). It can be seen that for each profile the relationship between ΔSST and ΔBT is approximately linear over the range of interest. The slope of each line is taken as the sensitivity of SST to the change in measurements (D_y).

For all the profiles the D_y are positive at nadir views and negative at forward

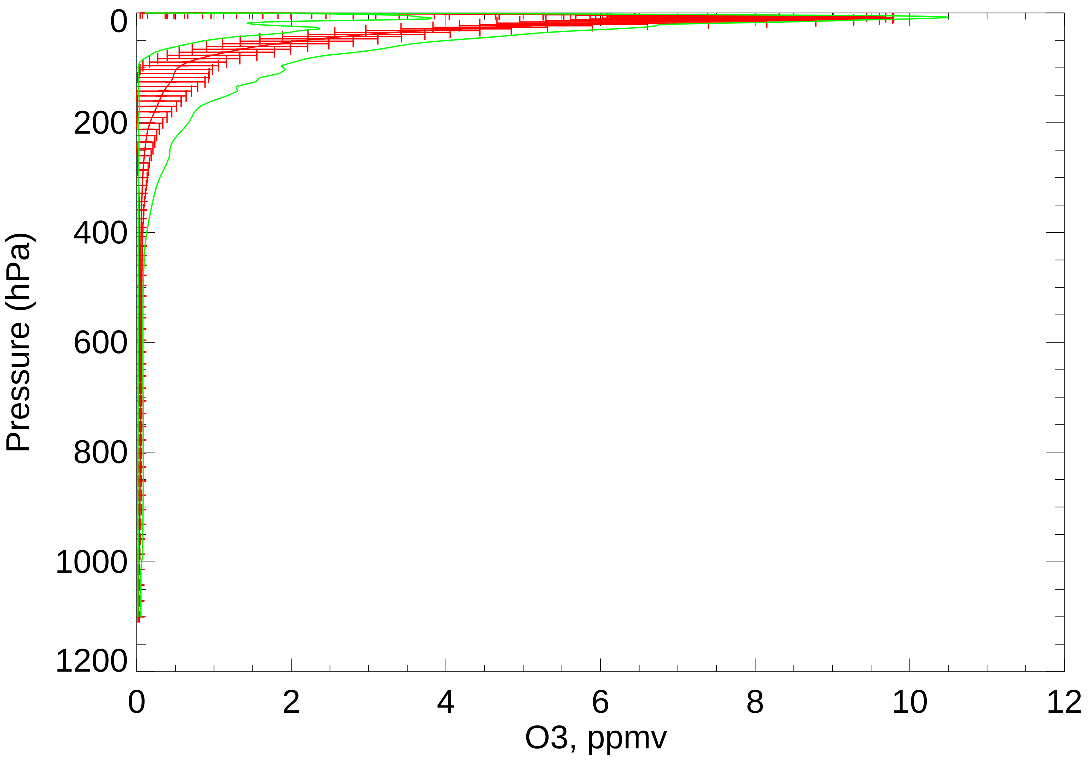

Figure 3.3: Same as Figure 3.1 but for ozone.

views, that is due to the fact that the nadir views get more information about the surface while the forward views get more information from the atmospheric path. The D_y for the 11 μm channel is stronger than that for the 12 μm channel. This is expected as the 12 μm channel is more sensitive to water vapour than the 11 μm channel, the signal from the surface is attenuated by water vapour.

According to Smith et al. (2012), the measurement errors of an infrared radiometer can be cataloged as radiometric bias and radiometric noise. The radiometric bias, also referred to as calibration error, is the difference in brightness temperature (BT) of a target measured by the radiometer and the actual BT of the target as determined from external accurate thermometers. Figure 3.5 presents the AATSR pre-launch calibration results for temperature ranging from 210 K to 315 K.

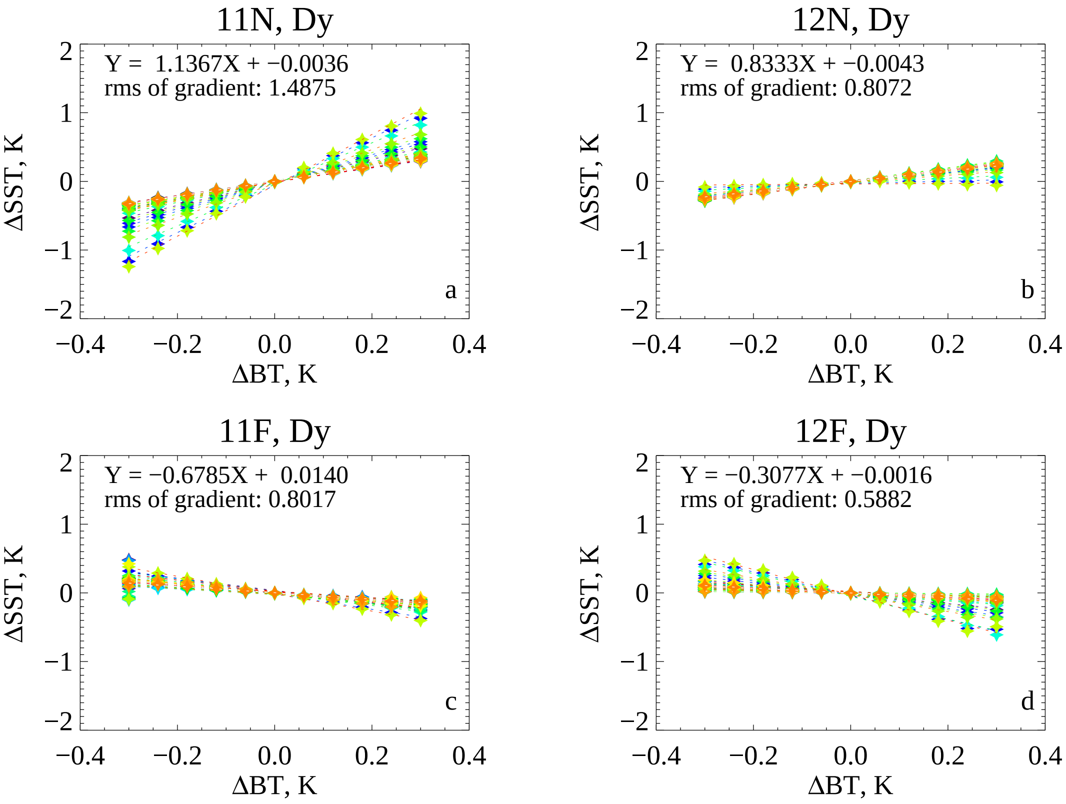

Figure 3.4: Response of SST (ΔSST) to change in AATSR infrared measurements (ΔBT) for 53 different profiles (denoted by different colours); a) 11 μm channel, nadir view; b) 12 μm channel, nadir view; c) 11 μm channel, forward view; and d) 12 μm channel, forward view. For each profile, the paired ΔSST and ΔBT are shown as diamonds and then regressed to the linear model, $Y = A + BX$ (dashed line). The equation on the left of each plot is given based on the median of A and B, the rms of gradients is the root mean square of A.

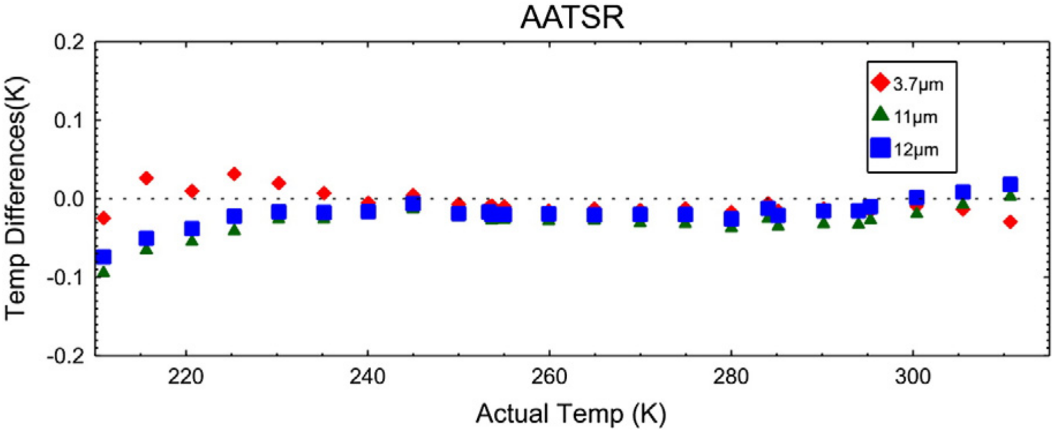

Figure 3.5: Results from the pre-launch radiometric calibration at the centre of nadir view under beginning of life (BOL) and thermal balance conditions for AATSR infrared channels, taken from Smith et al. (2012).

The radiometric noise is expressed as the noise equivalent brightness temperature difference, $NE\Delta T$:

$$NE\Delta T_\lambda = A_\lambda \Delta C_\lambda \left(\frac{\partial L_\lambda}{\partial T} |_T \right)^{-1}, \tag{3.3}$$

where ΔC_λ is the signal channel noise taken to be the standard deviation of the blackbody pixel counts, A_λ is the detector area, L_λ is the radiance at wavelength λ, and T is the scene temperature. The $NE\Delta T$ is measured as a function of T, the requirement for it is set for a scene temperature of 270 K. Figure 3.6 shows the $NE\Delta T$ for each infrared channel of AATSR as a function of T at the centre of nadir view.

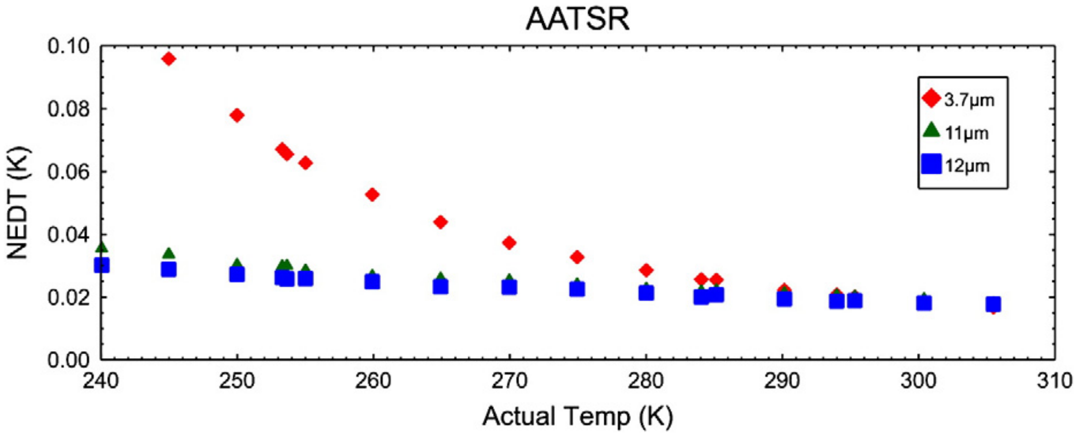

Figure 3.6: The NEΔT as a function of target temperature for AATSR at BOL thermal balance conditions, taken from Smith et al. (2012).

According to Figure 3.5, for the expected SST range (265 K − 305 K) the radiometric biases are no more than 0.05K for both the 11 μm and 12 μm channels. It is found that AATSR 12 μm channel has an offset of $\sim$ 0.2 K when compared to ATSR-2 (Embury, 2012; Nightingale and Birks, 2004). The offset is most likely on the AATSR side and caused by wavelength calibration errors or non-linearity between scene radiance and detector output. Closer inspection imply that the offset is dependent on the temperature or total column water vapour of the observed scene (Bali and Mittaz, 2012; Embury et al., 2012b).

Therefore in this study the radiometric bias for the 11 μm channel is assigned to be 0.05 K while for the 12 μm channel it is assigned to be 0.25 K to take the off-band response into account. As shown in Figure 3.6, for the temperature ranging from 240 K to 310 K, the $NE\Delta T$ of the 11 μm channel and the 12 μm channel are less than 0.040 K. At a temperature of 270 K, the $NE\Delta T$ for both the 11 μm and 12 μm channels given by Smith et al. (2012) are 0.025 K and 0.023 K respectively. As the mechanical characteristics of the forward views are the same as the nadir views, it is reasonable to assume the radiometric bias and radiometric noise of the forward views are the same as the nadir views. Taking the median of the sensitivities of SST to BT (D_y) of the 53 profiles, the contributions to SST from radiometric bias and radiometric noise can be calculated with Equation 3.1. The contributions to SST from radiometric biases of four channels (11 μm nadir view, 12 μm nadir view, 11 μm forward view, 12 μm forward view) are 0.057 ± 0.074 K, 0.208 ± 0.202 K, -0.034 ± 0.040 K and -0.077 ± 0.147 K respectively. As expected the radiometric bias of the 12 μm channel has a significant contribution to the error in the retrieved SST.

3.3.2 Atmospheric errors

ORAC employs a fast radiative transfer model (RTTOV) to simulate the effects of gases. The description of RTTOV has been given in Chapter 2. The only mandatory variable gas for RTTOV is water vapour, for AATSR the only optional gas is ozone. ORAC uses European Centre for Medium-Range Weather Forecasts (ECMWF) reanalysis data to provide temperature, pressure, water vapour and ozone profiles, and uses an extra model to yield surface emissivity. There are two types of errors related to the simulation of atmospheric attenuation: one is from the uncertainties in the atmospheric profiles and surface emissivity which are used as inputs to the radiative transfer model, referred to as input error; the other is originated from the uncertainties in the radiative transfer simulation referred to as simulation error.

3.3.2.1 Input errors

ECMWF uses an data assimilation scheme to provide global continuous analyses or forecast atmospheric data for the purposes of weather forecasting and environmental monitoring. The data assimilated into ECMWF come from a variety of sources, including satellite observations, in situ observations (ships, buoys, e.g.) and reanalysis dataset from other institutions. The accuracy of ECMWF varies with time and space because of the uneven distributions of observations. For example the data quality over southern oceans or polar regions especially during polar winter is constrained by the limited observations. Dee et al. (2011) and Morcrette (1991) give reviews about the forecast model, data assimilation method and input data used in generation of

ERA-Interim.

3.3.2.2 Temperature

The sensitivity of retrieved SST to atmospheric temperature profile is examined by perturbing the temperatures at all pressure levels between −0.5 K and 0.5 K with an increment of 0.1 K. The changes in the retrieved SST (ΔSST) with respect to the changes in temperature profile (ΔT) are shown in Figure 3.7. The change in atmospheric temperature has a significant effect on the derived SST and the variation of SST negatively correlates to the change in atmospheric temperature over the range of interest. The gradient of the relationship between ΔSST and ΔT spans a wide range corresponding to different profiles.

Limited information is available about the uncertainty of ECMWF temperature profile, the majority of the validation studies were carried out for some specific pressure layers or locations. For example, Uppala et al. (2005) access the quality of ECMWF ERA-40 temperature by comparing with the radiosonde observations at four layers, 50 hPa, 200 hPa, 500 hPa and 850 hPa, for a 11-year period (1991 to 2002). The result shows that the RMS between the two datasets falls in a range of 0.5 K to 2.5 K for northern Hemisphere, while for southern Hemisphere the RMS is slightly larger. The larger RMS in southern Hemisphere is probably due to the scarceness of measurements. Dee (2009) summarises that the RMS of ECMWF ERA-40 500 hPa temperature with respect to radiosonde observations for 1957–2001 is less than 1 K and the difference between monthly averaged 2-meter temperature from ECMWF ERA-Interim and Climatic Research Unit temperature database (CRUTEM3) is close to zero from 1989 to 2008. Christensen et al. (2007) compare the ECMWF ERA-40 temperature in the tropical lower stratosphere with measurements from balloon flights. The results show during the period of from 1988 to 2001, the anomaly is between 1 K to −0.46 K. By comparing ECMWF ERA-40 temperature with radiosondes at 100 hPa in the equatorial region from 1991 to 2002, Randel et al. (2004)

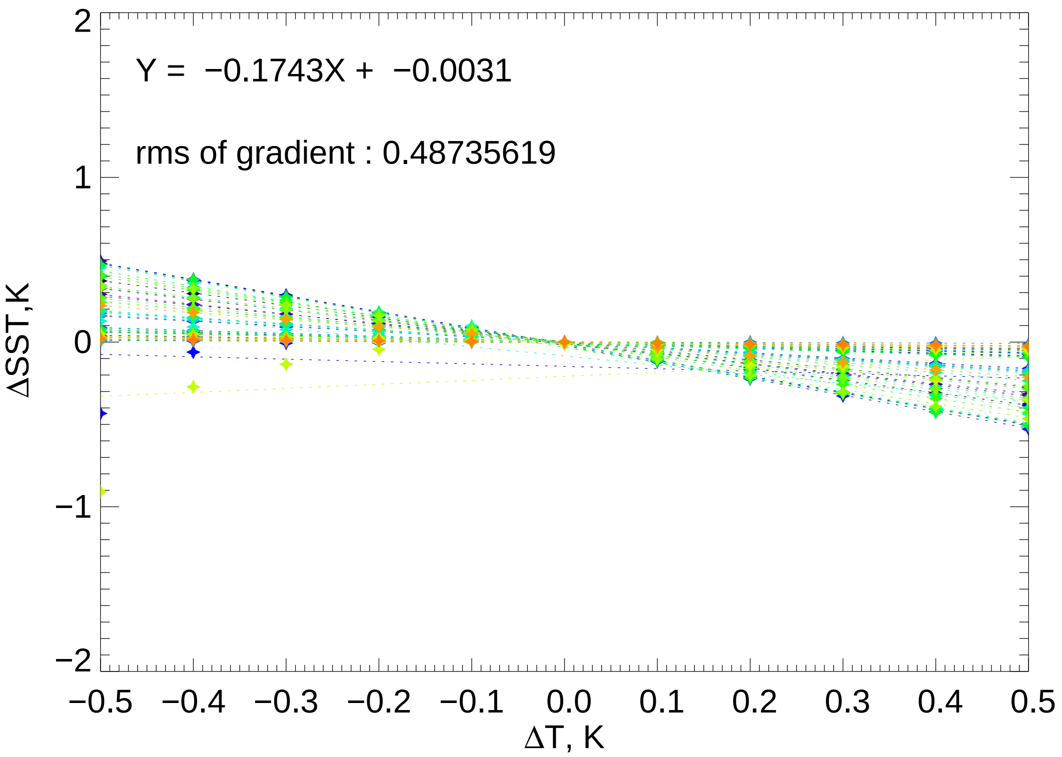

Figure 3.7: The change in SST (ΔSST) with respect to the change in temperature (ΔT) for different profiles (denoted by different colours). For each profile, the paired ΔSST and ΔT are shown as diamonds and then regressed to the linear model, $Y = A + BX$ (dashed line). The equation on the left of each plot is given based on the median of A and B, the rms of gradient is the root mean square (RMS) of A.

indicate the difference between the two datasets varies in a range of 1.0 K to −1.0 K. Gobiet et al. (2005) show an excellent agreement within 0.5 K between CHAllenging Minisatellite Payload (CHAMP) radio occultation (RO) satellite temperature measurements and ECMWF operational temperature in lower stratosphere for most of the global regions except for the polar areas. Knuteson et al. (2006) conclude that comparing with measurements from balloon floating at levels between 15 hPa and 80 hPa, the ECMWF operational temperature has a cold bias of −0.9 K over southern tropical and mid-latitude regions. Matricardi and Serio (2010) compare temperature profiles from ECMWF forecast model with those retrieved from IASI and find out that below 400 hPa the RMS errors in ECMWF are around 1 K, however in layers above 10 hPa the RMSs are remarkable (as much as 7 K). Betts and Ball (2003) compare surface temperature from ECMWF ERA-40 and Global Energy and Water Cycle Experiment Study over Mackenzie river basin, and conclude that the ERA-40 has a seasonal bias varying from 2 K to 3 K in winter and up to -1.5 K in July. The bias is supposed to be associated with the different surface albedo estimation models used by the two datasets. Additionally, according to the ECMWF data reception statistics, the difference in temperature between radiosonde observations and ECMWF is within 0.3 K (Figure 3.8).

Ohring et al. (2005) list out the accuracies of important meteorological variables required by the prediction of long term climate change. The required accuracy of temperature is 0.5 K for both the troposphere and the stratosphere. Using the required accuracy (0.5 K) as the error in temperature, and the sensitivity of SST to temperature of the 53 profiles (-0.1743 ± 0.4873 K/K), the contribution of temperature profile error to SST is around -0.0872 ± 0.2437 K.

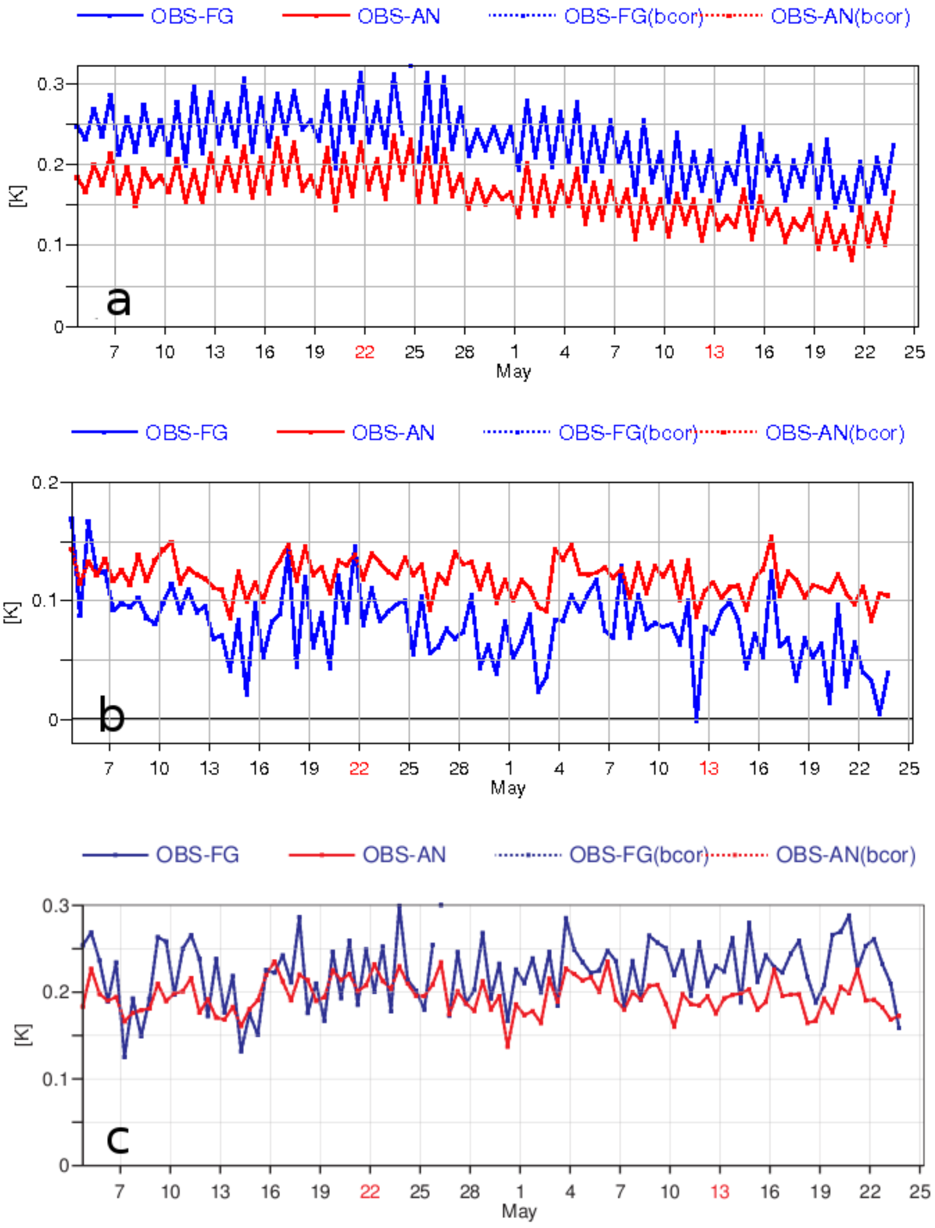

Figure 3.8: Time series of global averaged temperature difference between radiosonde observations and ECMWF analysis dataset for May of 2012, a) 0 − 400 hPa, b) 400 − 700 hPa and c) 700 − 1013.25 hPa , taken and modified from www.ecmwf.int..

3.3.2.3 Water vapour

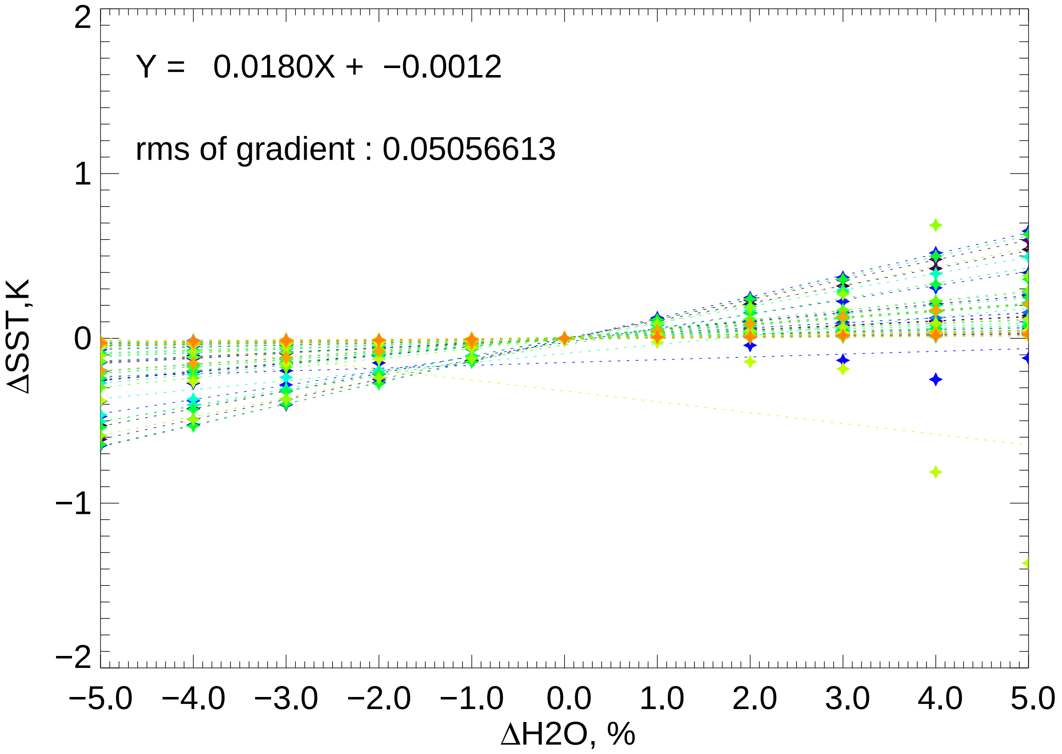

Figure 3.9: Same as Figure 3.7 but for water vapour (H_2O).

Water vapour plays a key role in climate as a dominant factor in moist dynamic and radiative transfer. It is an important source of precipitation, providing latent heating in the troposphere, and is the most important greenhouse gas with strong absorption in the infrared spectra. The SST sensitivity to water vapour is examined by perturbing the total column water vapour (TCWV) in the profiles between −5% and 5% at an interval of 1%. The results are plotted in Figure 3.9, the sensitivity of retrieved SST to TCWV varies in a significant wide range and it is almost linear over the range of interest, in general the ΔSST increases with increasing TCWV.

The concentration of water vapour is highly variable with time and location. According to Ohring et al. (2005), in order to capture the important signals of climate change, the required accuracy for water vapour should be better than 5%.

Flentje et al. (2007) compare tropospheric water vapour profiles from ECMWF forecast with measurements from airborne lidar across Brazil and Europe. The results show that the biases of ECMWF water vapour profiles with respect to the lidar measurements are 6%, 11% and 0% for three flight sections respectively. Ho et al. (2010) compare specific humidity profiles derived from Constellation Observing System for Meteorology, Ionosphere, and Climate (COSMIC) radio occultation with ECMWF over different regions. The comparisons show that the COSMIC specific humidity profiles agree well with ECMWF, the mean difference is very close to zero with a standard deviation of 0.5 g/kg. For global averaged comparison with satellite observations, a relative difference of around 10% exists for first three weeks of May 2012 (www.ecmwf.int). In this experiment, this relative difference of 10% is used as the error in the water vapour profiles. Using the sensitivity of retrieved SST to TCWV of 53 profiles, the contribution from water vapour error to the retrieved SST error falls in a range of 0.18 ± 0.50 K.

3.3.2.4 Ozone

Ozone is the other gas specified in ORAC besides water vapour. Although ozone is a minor component of the Earth's atmosphere, it has significant roles in atmospheric photochemistry as a powerful oxidizing agent and in atmospheric radiative process as a strong absorber. More than 90% of the ozone resides in the stratosphere and less than 10% is in the troposphere. The stratospheric ozone absorbs incoming shortwave radiation strongly and the tropospheric ozone tends to warm the Earth's surface through the greenhouse effect. The sensitivity of SST to ozone is calculated by perturbing the ozone total column from -5% to 5% at an interval of 1% (Figure 3.10). It can be seen that the sensitivity of SST to ozone is quite low and does not change much for different profiles.

Ohring et al. (2005) show the accuracy of ozone required by climate models are 5% for the stratosphere, 10% for the troposphere and 3% for the total column amount.

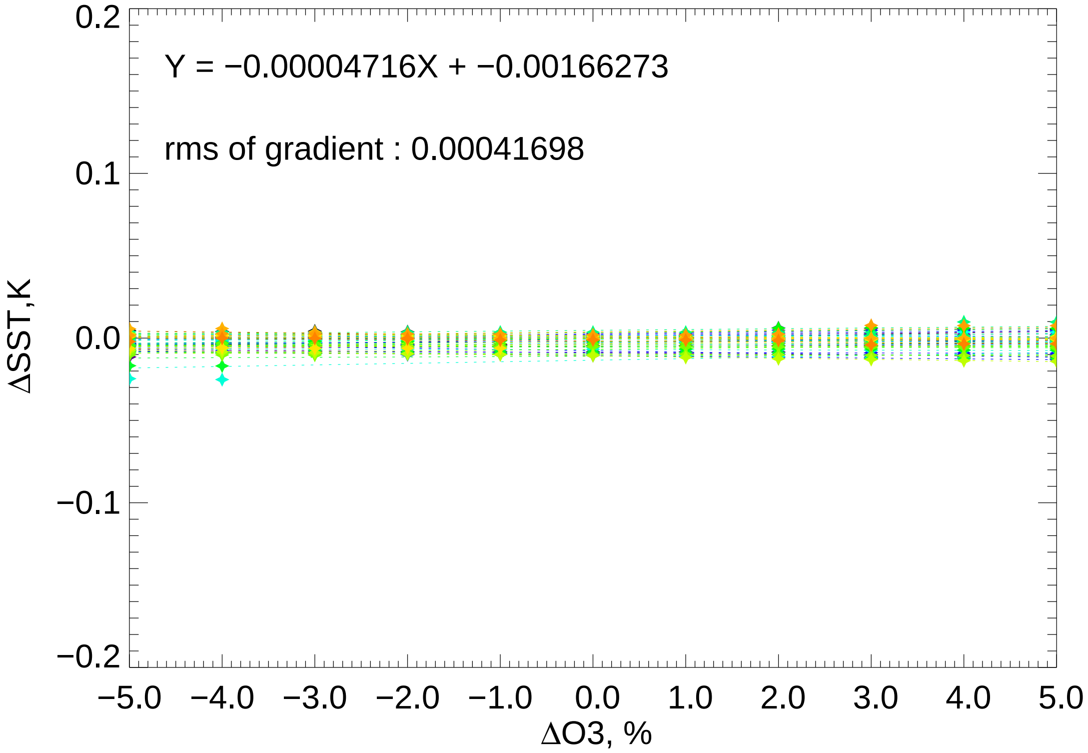

Figure 3.10: Same to Figure 3.7 but for ozone.

The distribution of ozone varies strongly with latitude as a result of large scale circulations between tropical and polar regions. The amount of ozone is from more than 400 Dobson unit (DU) for polar regions to less than 300 DU for tropical regions. The difference between satellite observations and ECMWF are within a range of −10 DU to 2 DU, comparing with the total amount values, the difference is less than 5%. Oikonomou and O'Neill (2006) present the comparisons of ECMWF ERA-40 stratospheric ozone data with independent observations from satellites and aircrafts, and show that the ERA-40 data tends to overestimate the ozone by 5% to 10%. Dragani (2011) accesses the quality of the ECMWF ERA-Interim ozone data by comparing with the observations merged from several satellites during the period from 1989 to 2008. For the mid-latitude regions the total column and the stratospheric ozone amount differences are less than 3% and 5% respectively, while for high latitudes the stratospheric ozone amount difference is up to −40% in polar winter due to the problems in model. Geer et al. (2006) compare the ozone data from seven different data assimilation systems with independent ozone observations from satellites. Most of the datasets perform poorly in the troposphere with large biases up to more than 50% compared to TOMS measurements, while for the stratosphere above 100 hPa, the biases are less than 10%. The difference between the ECMWF operational total column ozone data and TOMS is more than 50% over the high latitudes of southern Hemisphere during the period 18 August 2003 to 30 November 2003. The large bias probably results from the limited numbers of observations. As shown in Figure 3.10, the sensitivity to ozone is relatively low compared to water vapour or temperature, the contribution from ozone error to the retrieved SST is not significant.

3.3.2.5 Effects of Aerosols

As shown in Section 2.3.3.5, aerosols have influences on the TOA BTs, it can be expected that the influences may be present in the retrieved SST. Previous studies about the effects of aerosols on remote sensing of SST have been summarised in Section 1.2.3. One of the purposes of incorporating infrared channels to ORAC is to correct the effects of aerosols on the retrieved SST. OE scheme can be interpreted as adjusting the contributions to the TOA signals from surface and aerosols to get the best solution with minimum error. In the simulation of the TOA measurements, the aerosols are assumed to be spherical dust (A03) with an optical depth of 0.1 concentrated at the height of 800 hPa. And then applying the ORAC to the simulated measurements, the difference in the retrieved SST and the true SST for 53 profiles is 0.0018 ± 0.0015 K. The aerosol class used in retrieval is A03, same as in the measurement simulation. However, if using a different aerosol class in retrieval, for example, marine clean class (A05), the derived AOD has a bias of 0.063 from the true value, and the bias in SST increases to 0.0847 ± 0.0714 K. This result indicates the importance using appropriate assumptions in retrieval.

3.3.2.6 Surface emissivity

Sea surface emissivity is a critical component in SST retrieval because it determines the surface emission. A departure in emissivity from its reference value will result in a significant perturbation in the TOA BTs, this is particularly true if the atmosphere is relatively dry with a high transmittance (Figure 3.11).

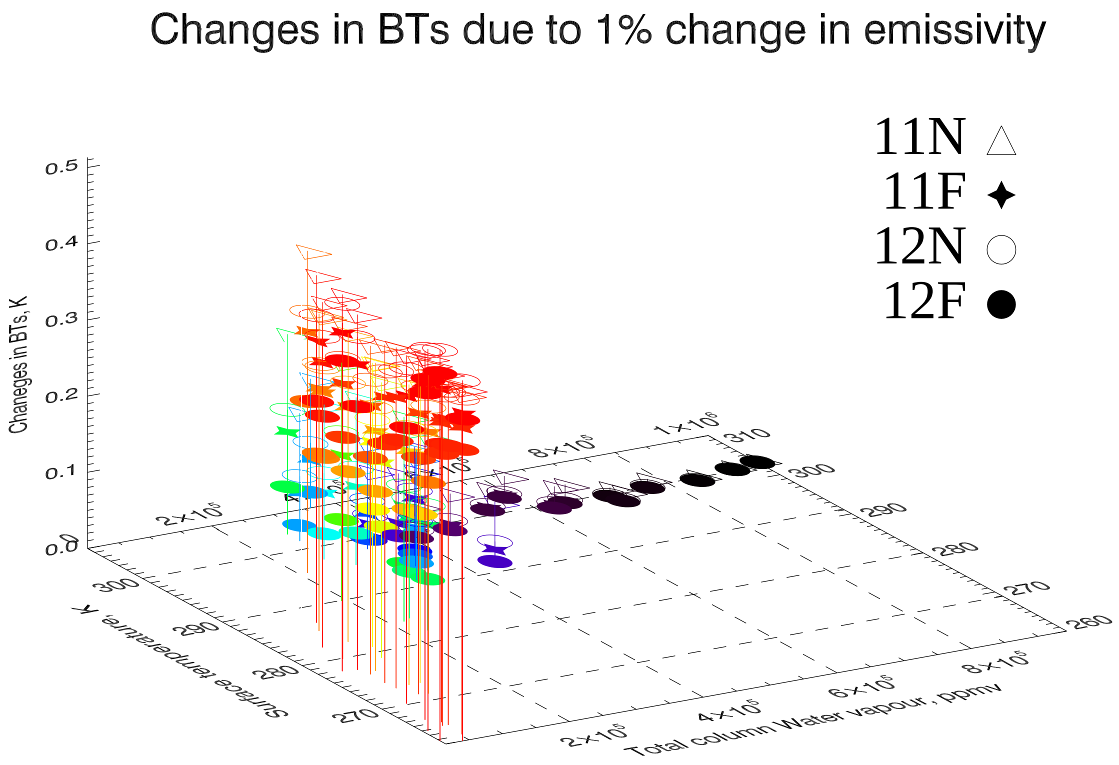

Figure 3.11: Change in the TOA BTs due to 1% change in surface emissivity. The x axis refers to total column water vapour, the y axis refers to surface temperature and the z axis refers to change in the TOA BTs. Different colours indicate different profiles, 11N: AATSR 11 μm nadir view; 11F: AATSR 11 μm forward view; 12N: AATSR 12 μm nadir view; 12F: AATSR 12 μm forward view.

A simplified model is adopted in RTTOV to calculate the sea surface emissivity as a function of wavelength and geometry. Figure 3.12 gives the comparison of the emissivity for 53 profiles obtained by EMS and RTTOV emissivity model. As RTTOV emissivity only varies with wavelength and geometry, for certain channel and view, the emissivity keeps constant for all profiles. Both the 11 μm and 12 μm channels for both views show the emissivity obtained by EMS is slightly lower than that from RTTOV. Except for the 11 μm nadir view, the difference of EMS from RTTOV is at a magnitude of 0.001. Figure 3.13 presents the change in SST with respect to the change in emissivity. In the nadir view, the change in the retrieved SST has a negative response to emissivity, while the opposite effect can be seen in the forward view. This is due to the fact that the nadir view gets more information from surface than the forward view. Assuming the emissivity error is of a magnitude of 0.5%, the errors in emissivity could contribute to the SST error by a magnitude of 0.1 K. This value is significant compared to the expected SST precision (0.3 K), hence it is necessary to get a good estimation of the surface emissivity.

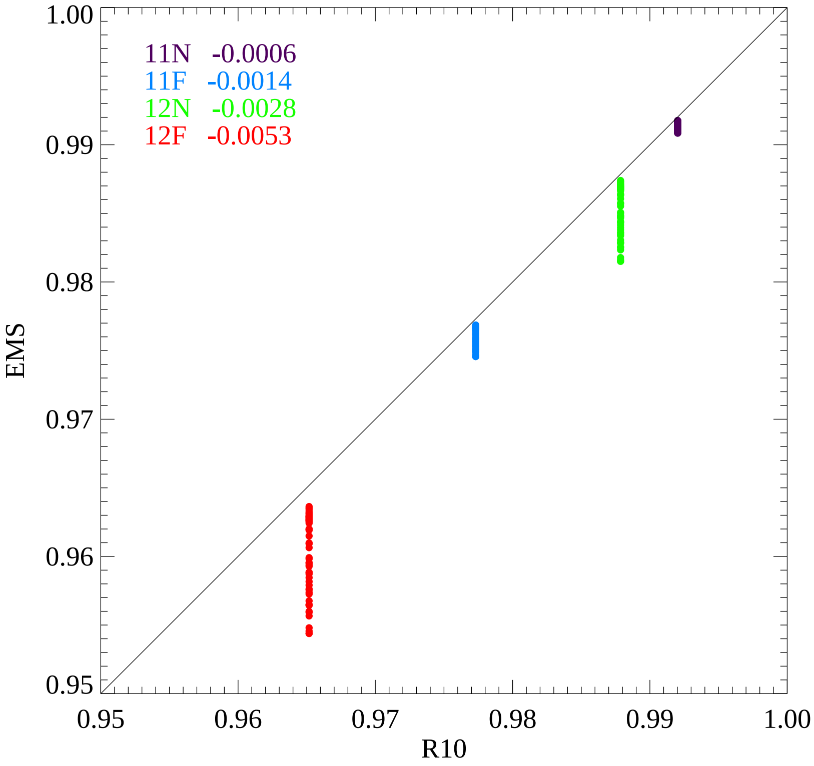

Figure 3.12: Comparison of emissivity calculated by the emissivity model (EMS) and RTTOV (RTTOV) for 53 profiles, the coloured fonts are the mean values of EMS minus RTTOV.

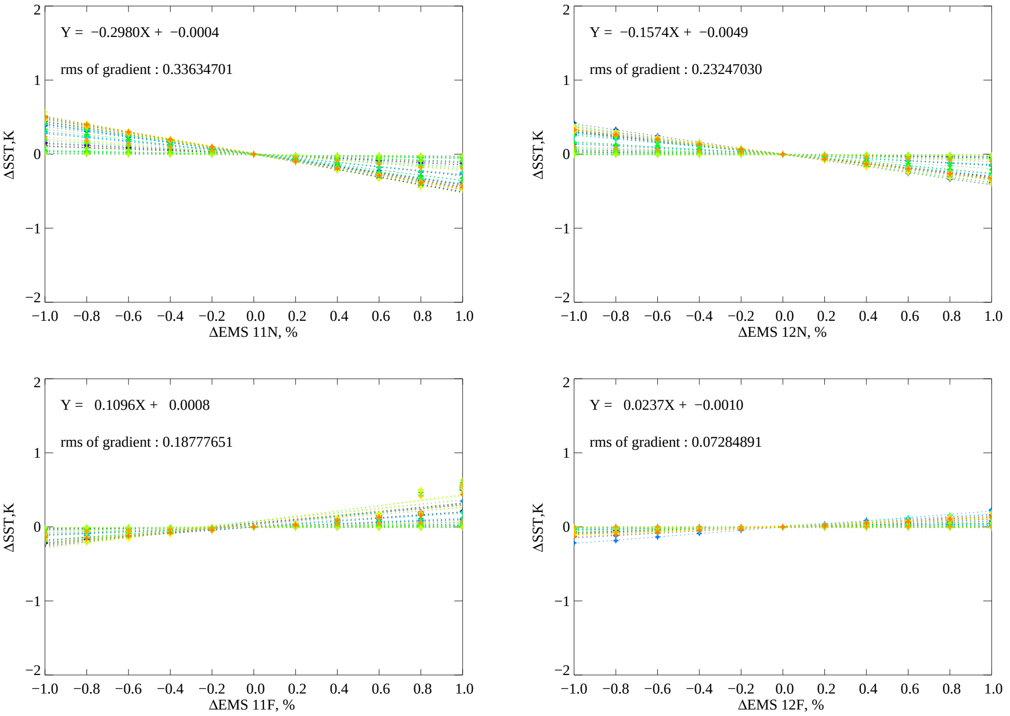

Figure 3.13: Same as Figure 3.4 but for emissivity.

3.3.3 Simulation errors

3.3.3.1 RTTOV accuracy

The accuracy of RTTOV is assessed by comparing the derived simulations with the corresponding values from a line-by-line (LBL) radiative transfer model (RFM). The RFM performs calculations of radiance at a high spectral resolution and achieves a high accuracy, however it is too computationally expensive to be used by a near real-time retrieval. The RFM calculates the monochromatic radiance at a resolution of 1 cm^{-1} then convolves with spectral response function to get the integrated radiance over the width of band. The BTs obtained with RFM and RTTOV are compared and plotted in Figure 3.14. The results clearly show that for both the 11 μm and 12 μm channels and two views the BTs calculated with RTTOV have systematic cold biases. The systematic cold biases of the forward views are approximately twice of these for the nadir views. There are two reasons that can be used to explain the biases in RTTOV. Firstly RTTOV performs simulations utilizing the regression coefficients generated by the LBLRTM model (Saunders et al., 2012) whereas the RFM is based on GENLN2 model. The different models may introduce discrepancies to the simulations. Secondly, RTTOV and RFM run with identical or equivalent temperature, pressure, water vapour and ozone profiles as well as the surface emissivity (set to be 1). However RTTOV treats the other gases, including CO_2, N_2O, CO, CH_4, NO, SO_2, NO_2, NH_3, HNO_3, OH, HF, HCl, HBr, HI, ClO, OCS, H_2CO, HOCl, N_2, and CFCs, as a well-mixed gas and the concentrations of the gases are taken from climatological profiles and are not allowed to vary, while in RFM the concentrations of the gases listed above are given by each profile instead of a climatological mean. The different treatments of gases may contribute to discrepancies in the simulated results. According to Figure 3.4, the retrieved SST strongly depends on the TOA BTs, therefore the discrepancies caused by using RTTOV may have a significant contribution to the retrieved SST.

3.3.3.2 Calculation of blackbody radiance

The radiance $L_\nu(T)$ emitted by a blackbody at temperature of T can be described by the Planck's Law:

$$\begin{aligned} L_\nu(T) &= \frac{B_1\nu^3}{\exp\left(\frac{B_2\nu}{T}-1\right)}, \\ B_1 &= 2hc, \\ B_2 &= \frac{hc}{K_B}, \end{aligned} \tag{3.4}$$

where ν is wavenumber, h is the Planck's constant, c is the speed of light and K_B is the Boltzman constant. The blackbody radiance measured by a radiometer with a finite band width can be calculated by convolving Equation 3.4 with channel response

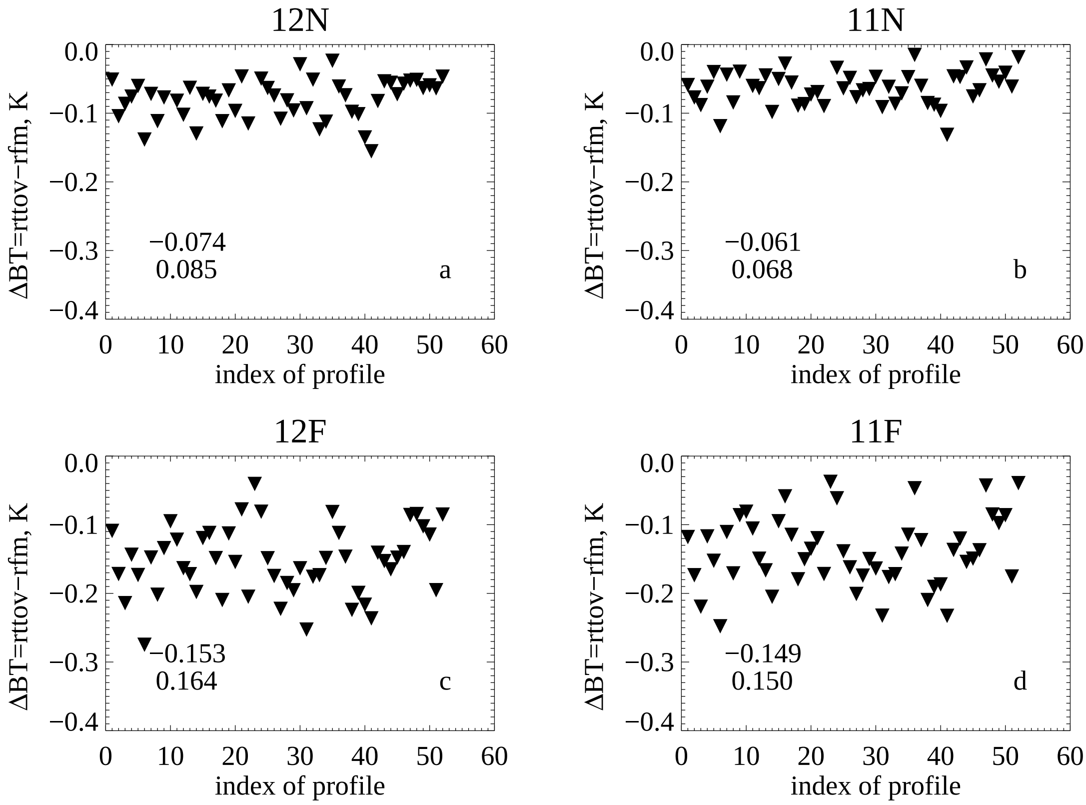

Figure 3.14: Difference in brightness temperature (ΔBT) between RTTOV and RFM, a) AATSR 12 μm nadir view, b) 11 μm nadir view, c) 12 μm forward view and d) 11 μm forward view. The mean difference and standard deviation are given in the left corner of each plots

function over the width of the channel:

$$L = \frac{\int_{\nu_1}^{\nu_2} L_\nu(T)\phi(\nu)d\nu}{\int_{\nu_1}^{\nu_2} \phi(\nu)d\nu}, \tag{3.5}$$

where L is the integrated blackbody radiance, ϕ is the response function over the band width, ν_1 and ν_2 are the lower and upper wavenumber limits of the band. However for radiometers with relative wide bands, such as AATSR (Figure 3.15), doing the convolution of Equation 3.5 with a fine spectral resolution is time-consuming. As a result, both ORAC and RTTOV utilize a modified Planck's law:

$$\begin{aligned} L'(T) &= \frac{B_1\nu'^3}{\exp\left(\frac{B_2\nu'}{T'} - 1\right)}, \\ T' &= a + bT, \end{aligned} \tag{3.6}$$

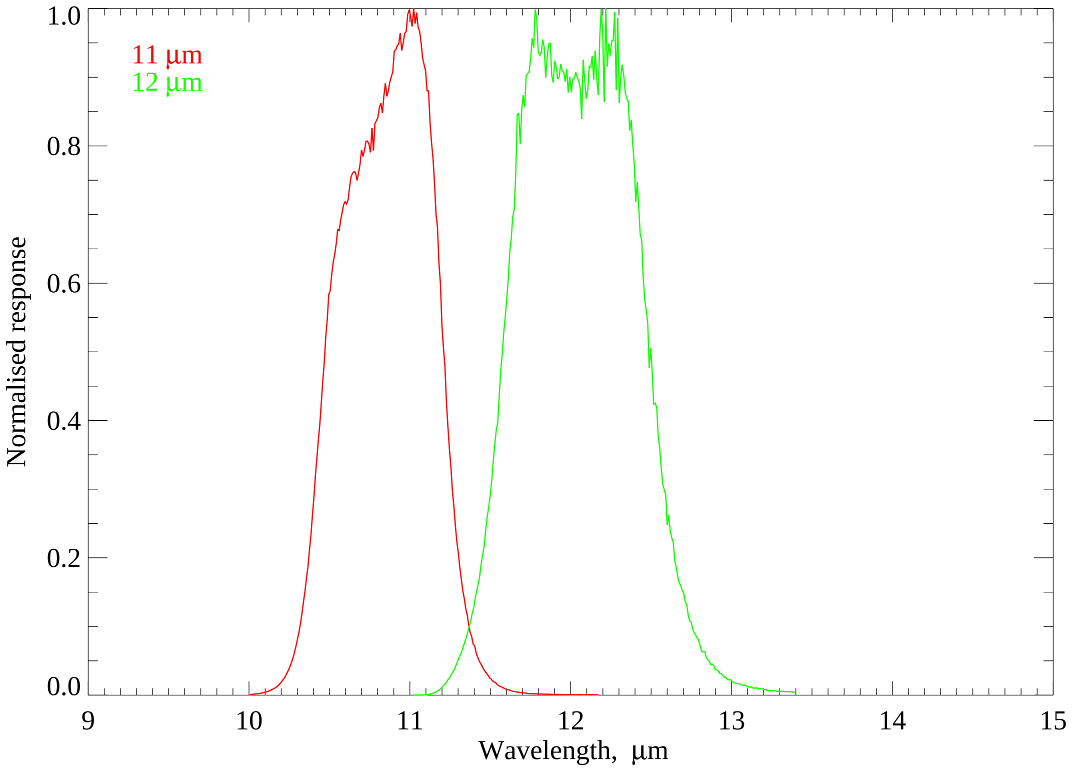

Figure 3.15: Response functions of AATSR channels.

where the L' is the radiance calculated by the modified Planck's Law, a and b are are the pre-calculated coefficients referred to as band correction coefficients and ν' is the central wavenumber or effective wavenumber:

$$\nu' = \frac{\int_{\nu_1}^{\nu_2} \nu\phi(\nu)d\nu}{\int_{\nu_1}^{\nu_2} \phi(\nu)d\nu}. \tag{3.7}$$

The values of a, b and ν' are specific for different instruments or response functions. The values given by previous version of ORAC and RTTOV are different. Figure 3.16 shows the radiance calculated based on the values of a, b and ν' given by previous version of ORAC and RTTOV. It is apparent that different a, b and ν' values can lead to significant differences in radiance. For the temperature range of 260 K to 310 K, the radiance calculated based on the a, b and ν' provided by RTTOV is closer to that obtained by Equation 3.5. Therefore the values of a, b and ν' in ORAC have been replaced with those from RTTOV.

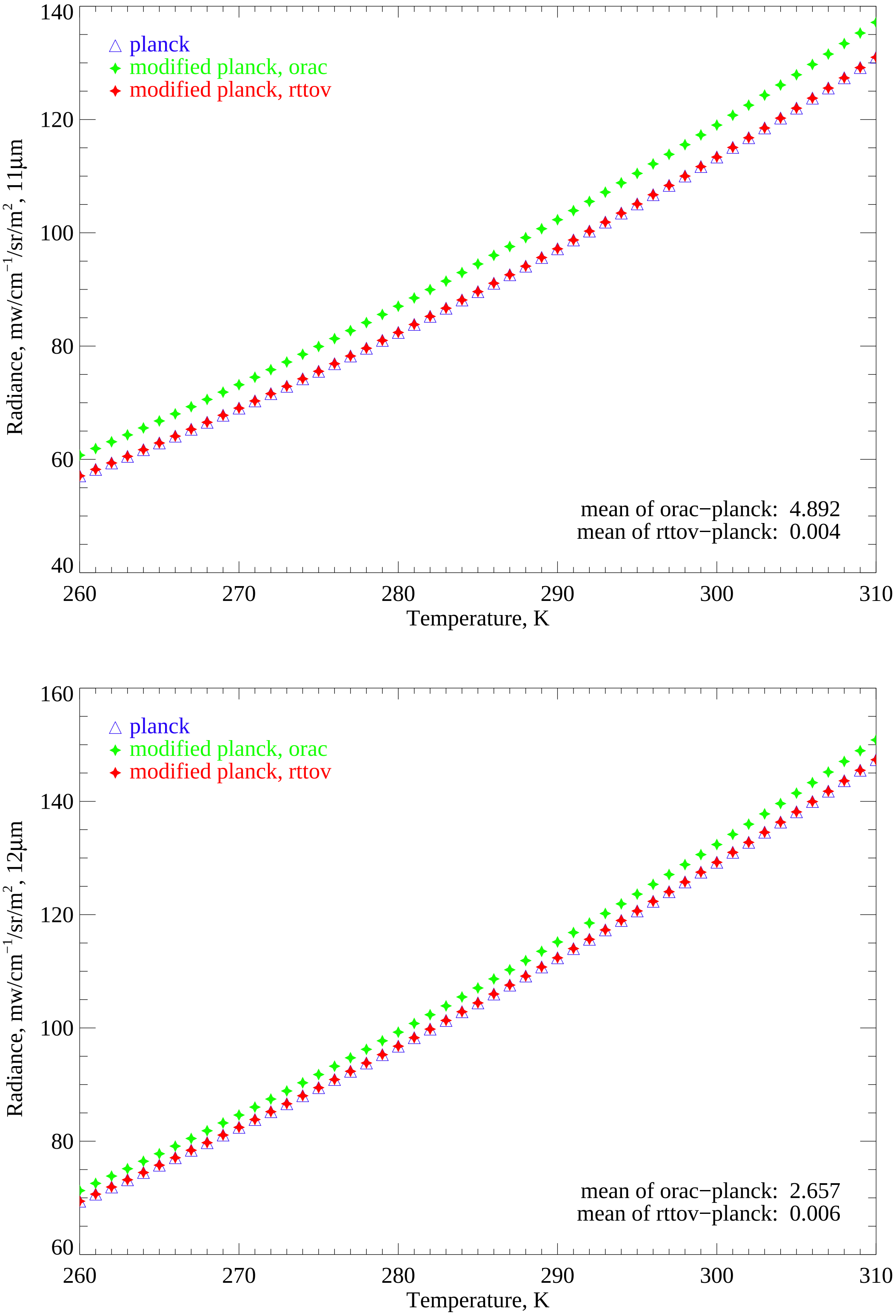

Figure 3.16: Radiance calculated for AATSR infrared channels by the Planck's law convolving with channel response function (Equation 3.5, indicated by blue triangles) and by the modified Planck's law using different a, b, ν' values given by RTTOV (red stars) and ORAC (green stars).

Figure 3.17 presents the difference in radiance calculated by Equation 3.6 and Equation 3.5. It can be seen that the modified Planck's law tends to overestimate the radiance for the SST range (265 K to 305 K). Considering the derivative of BT with respect to radiance (Figure 3.18), the change in BT can be calculated and the result is shown in Figure 3.19. It is exhibited that the difference in BT caused by using modified Planck's law is no more than 0.001 K for the interested temperature range. Related to the SST sensitivity to BT given by Figure 3.4, the maximum of the error in SST led by the modified Planck's law is no more than 0.002 K (using the maximum sensitivity and maximum BT difference).

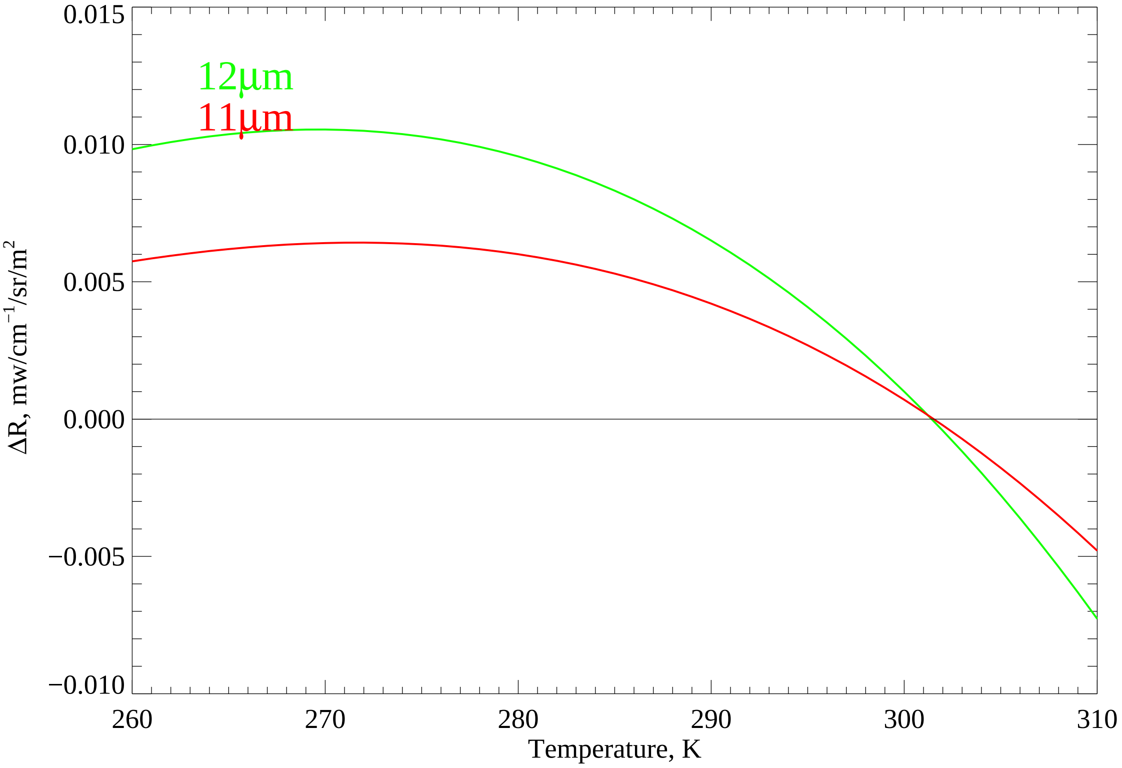

Figure 3.17: Difference in radiance calculated by modified Planck's law (Equation 3.6) and by Planck's law convolving with AATSR channel response (Equation 3.5) for two AATSR infrared channels.

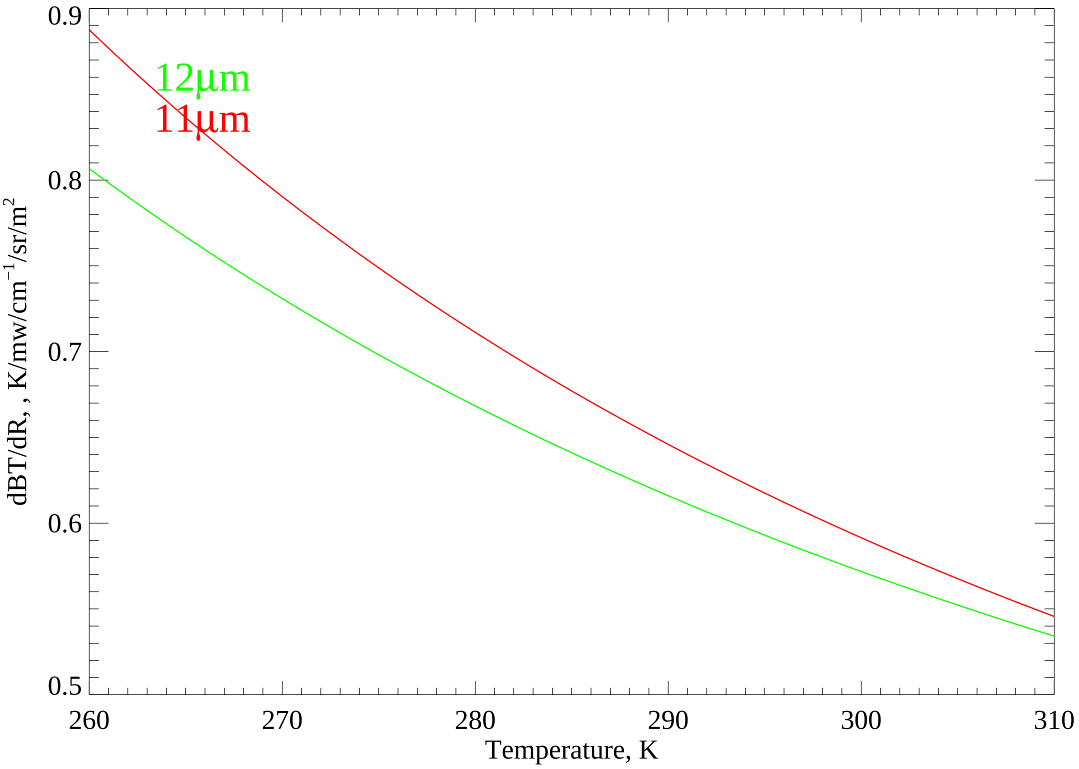

Figure 3.18: Derivative of BT with respect to radiance at AATSR infrared channels.

3.4 Conclusions

A sensitivity study has been carried out investigating the effects of a number of variables ($\mathbf{v}$) on the SST ($\frac{\partial SST}{\partial v}$, where v is an element of $\mathbf{v}$) retrieved by ORAC, the results are shown in Table 3.1. Many variables have been tested, including instrument calibration bias and calibration noise, atmospheric profiles, sea surface emissivity, RTTOV simulation and the simplified calculation of radiance.

The results demonstrate that the retrieved SST has very different sensitivities to different variables. This study is based on 53 atmospheric and surface states which cover a wide range of conditions, it is no surprise to see that for each variable the $\frac{\partial SST}{\partial v}$ spans a wide range and has a relatively large RMS. Given the sensitivity and error range, the contribution to the retrieved SST from the error in each variable can be estimated with Equation 3.1. The variable error ranges and types (random

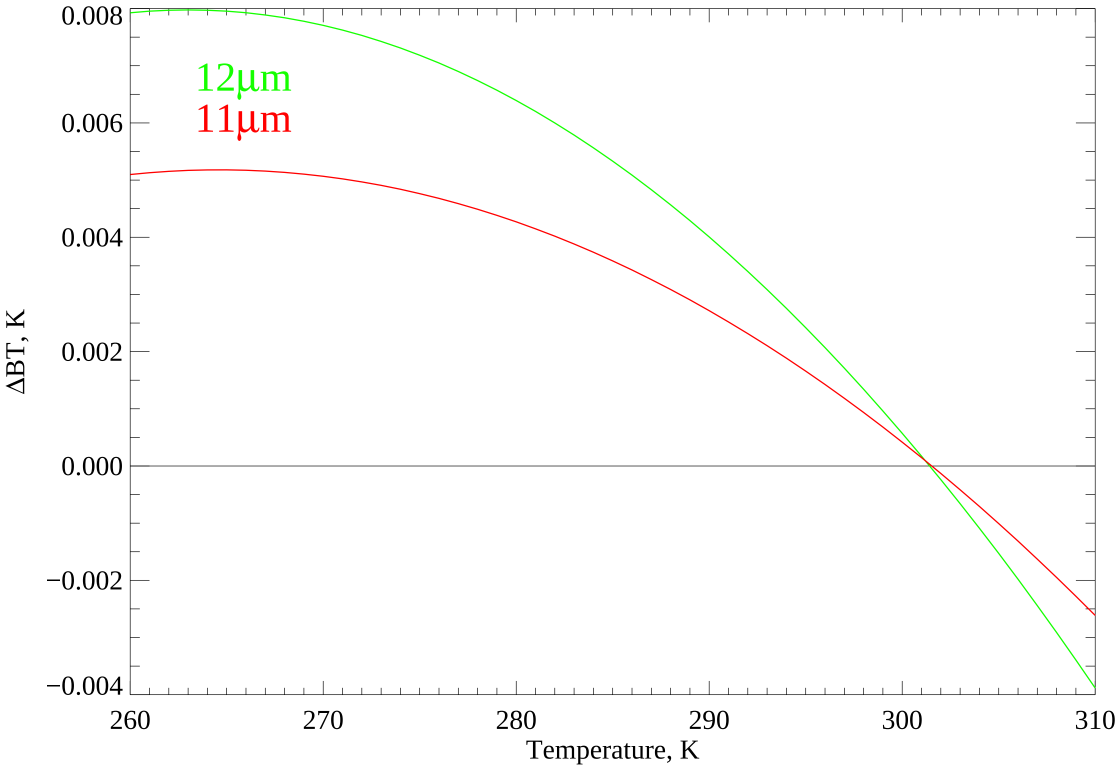

Figure 3.19: Difference in brightness temperature (ΔBT) due to the difference in radiance given by Figure 3.17 for two AATSR infrared channels.

or systematic) are taken from published literatures, may be subjective because some variables, for example, water vapour, emissivity, vary strongly with locations and seasons.

A box and whisker plot (Figure 3.20) is used to visual the statistics of the error analysis. In Figure 3.20 the systematic error terms and random error terms are denoted by the colours of gray and blue respectively. The total systematic error (ε_s) and total random error (ε_r) are calculated as:

$$\varepsilon_s = \sum_{i=1}^{n_s} \varepsilon_{s_i},$$
$$\varepsilon_r = \frac{\sqrt{\sum_{i=1}^{n_r} \varepsilon_{r_i}^2}}{n_r}, \tag{3.8}$$

where n_s and n_r are the numbers of systematic and random error terms, ε_{s_i} is the i_{th}

systematic error term and ε_{r_i} is the i_{th} random error term.

The sensitivities of the retrieved SST to AATSR nadir view BTs are relatively high. Decreased sensitivities are observed for the forward views, this is expected as the longer atmospheric path of the forward view can attenuate the change in surface emitted signals. The calibration noises of AATSR are tiny for both the 11 μm and 12 μm channels, thus the errors in SST caused by calibration noises are not significant (~ 0.01 K). However compared to ATSR-2, the AATSR 12 μm channel is subject to a systematic bias of ~ 0.2 K, as expected this systematic bias causes a significant error in SST.

The study also demonstrates that the retrieved SST is strongly dependent on atmospheric temperature profile and water vapour profile as the 11 μm and 12 μm channels are affected significantly by the atmosphere state. ORAC also shows high sensitivity to surface emissivity especially for the 11 μm channel in the nadir view. Any increase in error of the three variables will culminate in a much wide range in the error of the retrieved SST. In contrast the dependence of SST on ozone profile is negligible. It should be noted that the deficits of radiative transfer model (RTTOV) from accurate LBL model also contribute significantly to the retrieved SST at a magnitude of 0.1 K.

The results of this chapter have strong implications for the ORAC SST retrieval, the performance of the algorithm would benefit from improving the atmospheric profiles, emissivity model, and radiative transfer model. The results provide a basis for interpreting the comparisons between the retrieved SST and other SST datasets. Besides the parameters discussed in this chapter, undetected cloud contamination is also an important contributor to the bias of SST derived from satellite infrared sensors, the effects of cloud contamination will be investigated in the future work. Furthermore, the TOA BTs are sensitive to the vertical distributions of water vapour, aerosols and temperature. The height sensitivities are not included and will be carried out in the future work.

Error term (v)	Type	δv	Median $\frac{\partial SST}{\partial v}$	RMS $\frac{\partial SST}{\partial v}$	Median ΔSST, K	RMS $\Delta SST, K$
11N cali noise (N11N)	R	0.025, K	1.136, K/K	1.487, K/K	0.028	0.037
12N cali noise (N12N)	R	0.023, K	0.833, K/K	0.807, K/K	0.019	0.018
11F cali noise (N11F)	R	0.025, K	-0.678, K/K	0.801, K/K	-0.017	0.020
12F cali noise (N12F)	R	0.023, K	-0.307, K/K	0.588, K/K	-0.007	0.013
11N cali bias (B11N)	S	0.050, K	1.136, K/K	1.487, K/K	0.057	0.074
12N cali bias (B12N)	S	0.250, K	0.833, K/K	0.807, K/K	0.208	0.202
11F cali bias (B11F)	S	0.050, K	-0.678, K/K	0.801, K/K	-0.034	0.040
12F cali bias (B12F)	S	0.250, K	-0.307, K/K	0.588, K/K	-0.077	0.147
T profile (tem)	R	0.5, K	-0.174, K/K	0.487, K/K	-0.087	0.243
H_2O profile (h_2o)	R	10%	0.018, K/%	0.051, K/%	0.180	0.510
O_3 profile (o_3)	R	10%	4E-05, K/%	4E-05, K/%	4E-04	4E-04
11N emissivity (E11N)	S	0.5%	-0.298, K/%	0.336, K/%	-0.149	0.168
12N emissivity (E12N)	S	0.5%	-0.157, K/%	0.232, K/%	-0.079	0.161
11F emissivity (E11F)	S	0.5%	0.110, K/%	0.187, K/%	0.055	0.094
12F emissivity (E12F)	S	0.5%	0.024, K/%	0.072, K/%	0.012	0.036
11N RTTOV (R11N)	S	-0.074, K	1.136, K/K	1.487, K/K	-0.084	-0.110
12N RTTOV (R12N)	S	-0.061, K	0.833, K/K	0.807, K/K	-0.051	-0.049
11F RTTOV (R11F)	S	-0.153, K	-0.678, K/K	0.801, K/K	0.104	-0.126
12F RTTOV (R12F)	S	-0.149, K	-0.307, K/K	0.588, K/K	0.045	-0.087
11N modified Planck (P11N)	S	0.005, K	1.136, K/K	1.487, K/K	0.006	0.007
12N modified Planck (P12N)	S	0.008, K	0.833, K/K	0.807, K/K	0.007	0.006
11F modified Planck (P11F)	S	0.005, K	-0.678, K/K	0.801, K/K	-0.003	0.004
12F modified Planck (P12F)	S	0.008, K	-0.307, K/K	0.588, K/K	-0.002	0.005

Table 3.1: SST sensitivities to different variables ($\frac{\partial SST}{\partial v}$). In first column, 11 and 12 indicate the 11 μm and 12 μm channels, 'N' and 'F' indicate nadir and forward views respectively. In the second column, 'R' indicates random error and 'S' indicates systematic error, Median sensitivity is the median of the sensitivities of 53 profiles, RMS is the RMS of sensitivities of 53 profiles.

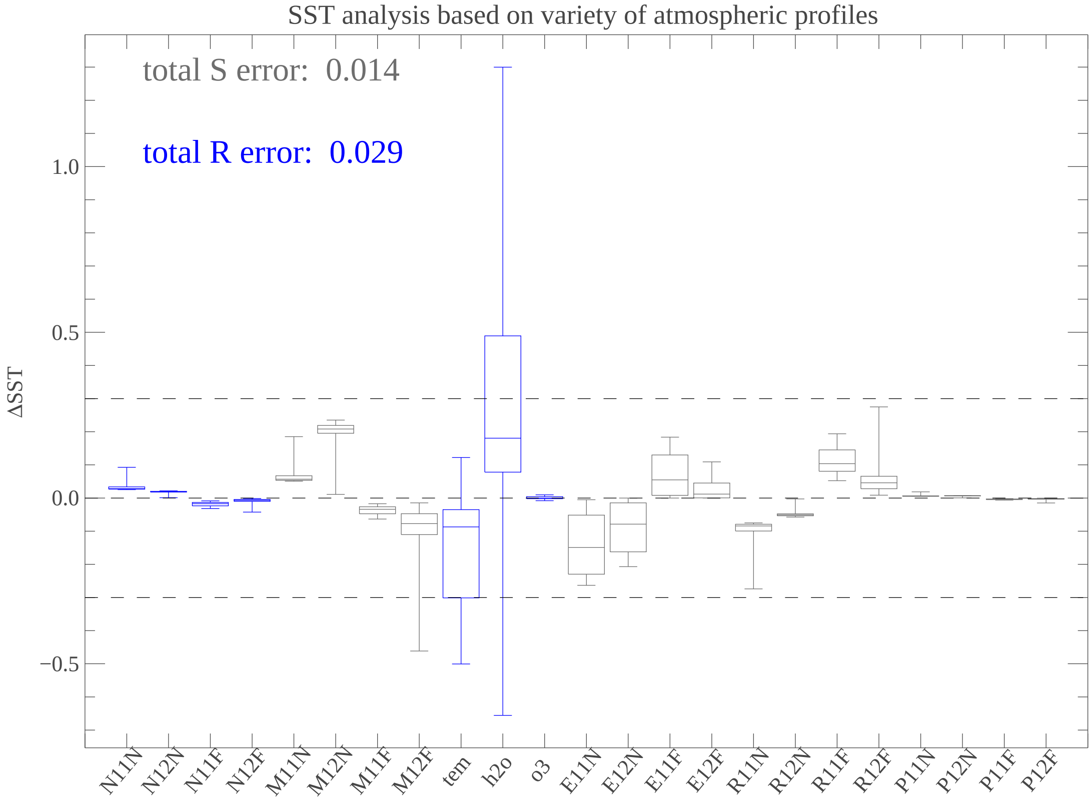

Figure 3.20: Box and whisker plot of contributions to SST from different parameters listed in Table 3.1, the box encloses the interquartile range (25% − 75%), the whiskers extend out to the minimum or maximum value of the data, and the horizontal line in each box indicates median value of the data.

Chapter 4

Aerosol validation

To evaluate the performance of the new ORAC algorithm, the retrieved aerosol properties are compared with the aerosol products from the previous version of ORAC algorithm: GlobAEROSOL; and with the measurements from ground-based instruments: AERONET.

AATSR instrumental resolution is 1 × 1 km, in this validation study ORAC retrieval is constructed on 10 × 10 km resolution for the purposes of saving computational time and suppressing instrumental noise. In the 10 × 10 km retrieval, AATSR instrumental pixels are organized into a group of super-pixels, each super-pixel contains 10 × 10 instrumental pixels. As aerosol retrieval is only possible in clear sky conditions, it is vital that the instrumental pixels containing cloud are not included in the retrieval. The cloud flag employed here is the AATSR operational cloud flag contained in the standard Level 1B data. Over ocean it uses a combination of thresholds on both infrared and visible channels, spatial coherence and ratios between different channels. Over land the flag uses two normalised difference vegetation index (NDVI) tests, which compare the TOA reflectance between 0.55 and 0.67 μm channels and the 0.67 and 0.87 μm channels (Birks, 2004). Each instrumental pixel is assigned with a binary flag (1 for cloudy, 0 for clear). ORAC only processes the super-pixels with at least 10 out of the 10 × 10 instrumental pixels are clear. The measurement of each super-pixel is calculated as the average of the clear instrumental pixels within this super pixel. The cloud fraction of each super-pixel is calculated as the fraction of cloudy pixels out of the 10 × 10 pixels.

4.1 Intercomparison with visible-channel retrieval algorithm

Satellite data have greatly improved the knowledge about atmospheric aerosols. There are many space-based remote sensing aerosol products; given the complication of retrieving aerosol information from satellite measurements, substantial differences in aerosol properties are present. Previous studies show that differences in aerosol properties can be as great as a factor of two between different datasets, in some cases it would be even higher. In general the best agreements of AOD are found in regions with high AOD, whereas the largest discrepancies are found over remote ocean regions (Myhre et al., 2005, 2004). Discrepancies in retrieved aerosol properties among different products may result from a wide range of factors, such as 1) the radiative transfer models, aerosol assumptions and surface treatments utilized by different algorithms; 2) instrumental designs, it is closely related to spectral locations of band, pixel sizes, swaths and calibration issues; 3) collocation processes and cloud flag schemes; and 4) different products report AOD at different wavelengths.

4.1.1 Overview of GlobAEROSOL

GlobAEROSOL is a European Space Agency (ESA) project aimed at producing a global aerosol dataset derived from a range of European satellite instruments, including ATSR-2, AATSR, MERIS and SEVIRI, spanning a twelve-year period from 1995 to 2007. In this chapter, of the four instruments, data from AATSR are used. GlobAEROSOL AATSR products were generated using the previous version of ORAC which only uses AATSR visible channels centred at 550, 670, 870 and 1600 nm, as opposed the new ORAC uses both visible and infrared channels. GlobAEROSOL AATSR products include AOD at 550 nm, aerosol effective radius and four surface white sky albedo at 550, 670, 870 and 1600 nm. GlobAEROSOL are performed using five different aerosol classes: continental clean, marine clean, desert dust, urban and biomass burning. The microphysical properties of the first four classes are from the Optical Properties of Aerosol and Cloud database (Hess and Schult, 1998) and biomass-burning derived from AERONET measurements of South American Cerraro fires (Dubovik et al., 2002).

Using GlobAEROSOL AATSR products as a reference for comparison can avoid the discrepancies introduced by the processes of collocation and AOD interpretation among different wavelengths. For convenience, the results retrieved by the new ORAC scheme are denoted by ORAC, and the GlobAEROSOL products are denoted by GlobAEROSOL.

4.1.2 Results

The month of September 2008 is processed by ORAC and then the results are compared to the GlobAEROSOL AATSR data. Comparison is made for the super-pixels converged successfully with a cost less than 20 and is restricted to ocean super-pixels. More than $1,000,000$ pairs of matches between ORAC and GlobAEROSOL are found for the one month period.

A summary of the mean and median statistics for ORAC and GlobAEROSOL are presented in Table 4.1. These results show that ORAC estimates, on global average, smaller values for AOD at 550 nm (τ_{550}) (and hence AOD at 870 nm (τ_{870})) than GlobAEROSOL, ORAC global averaged τ_{550} is 0.071, while for GlobAEROSOL it is 0.136. However, surface while sky albedo at 550 nm ($R_{SLW,550}$) retrieved by ORAC is significantly greater than GlobAEROSOL: this may explain the smaller retrieved AOD. The retrieved effective radius (r_e) is similar for both ORAC and

GlobAEROSOL. For both ORAC and GlobAEROSOL, the distributions of retrieved AOD and effective radius are skewed with the median values smaller than mean values. This maybe because stronger aerosol events with enhanced AOD or effective radius are relatively uncommon (the background AOD is low).

The monthly mean maps of τ_{550} for ORAC and GlobAEROSOL are presented in Figure 4.1. Due to the limitations introduced by the narrow swath of AATSR, and because both ORAC and GlobAEROSOL need visible channels, only the data from daylight are used. It can be seen that even with a one-month period, there remain areas with no coverage, and the retrieval fields still show evidence of orbital pattern. Figure 4.1 confirms results of many previous satellite studies that aerosol loading is generally higher near continents. Aerosol plumes off the west coast of Africa and the relatively high AOD in the Indian Ocean are clearly evident. The values of AOD in open ocean, where the aerosols are mainly sea salt and natural sulphate aerosols, are much lower. It is notable that compared to GlobAEROSOL, ORAC has a lower optical depth globally, and the discrepancy becomes more apparent in low latitude regions which are supposed to be influenced by desert dust or biomass burning aerosols. As shown by previous studies that infrared spectra are more sensitive to large particles (≥ 1 μm), the discrepancy in optical depth between the two products may be due to the usage of infrared channels.

Figure 4.2 presents the histograms of the retrieved τ_{550} over global ocean for the month of September, 2008. The histograms are constructed from all super-pixels with no spatial or temporal averaging. The frequency distributions of ORAC and GlobAEROSOL are similar with a high correlation coefficient ($R = 0.916$). Majorities of the two datasets fall within 0.2, the discrepancy between the two datasets is concentrated in a range of from -0.2 to 0.0, ORAC peaks at the lower regime with a median of 0.071 ± 0.173 (median ± RMS), while for GlobAEROSOL the median is 0.136 ± 0.250.

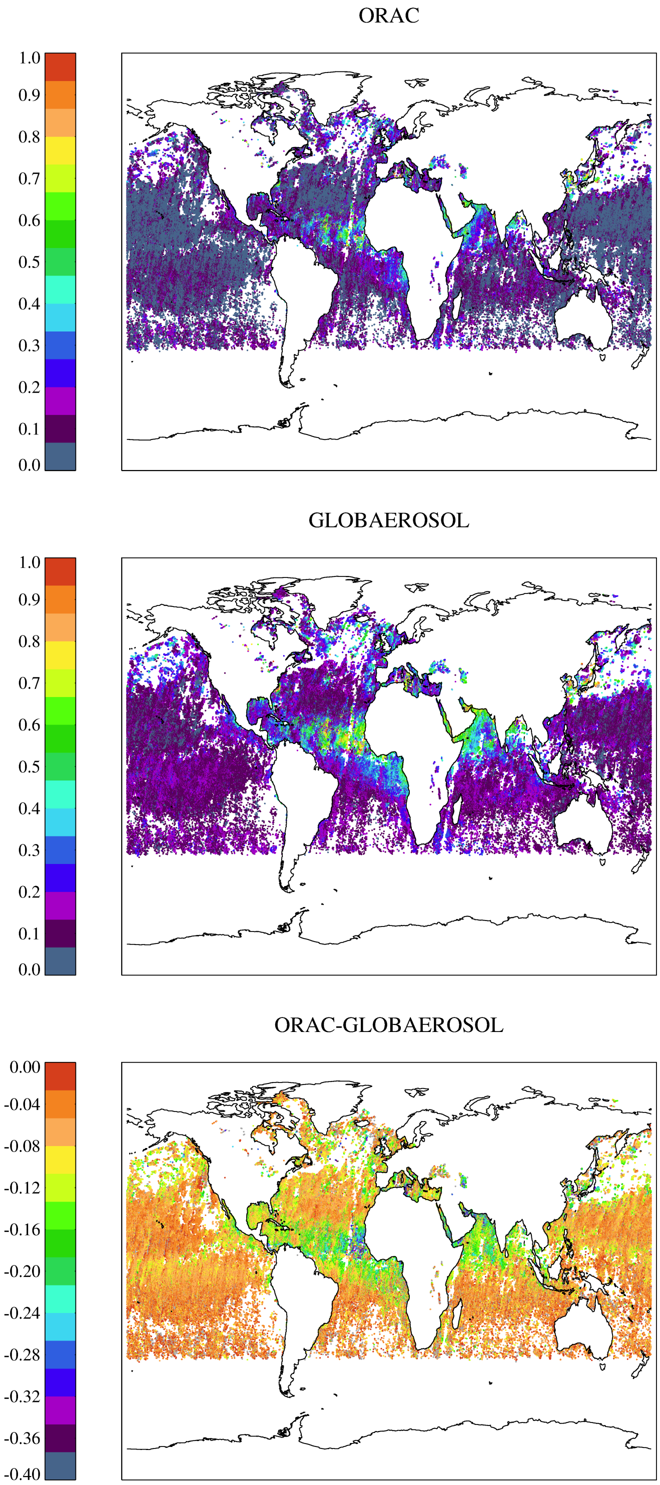

Figure 4.1: Global mean of AOD at 550 nm (τ_{550}), a) ORAC, b) GlobAEROSOL, and c) the difference between the two datasets (ORAC − GlobAEROSOL) for the month of September, 2008 over global water surface.

Retrieval quantity	median ORAC	mean ORAC	median GlobAEROSOL	mean GlobAEROSOL
τ_{550}	0.071±0.012	0.115±0.020	0.136±0.002	0.192±0.004
$R_{SLW,550}$	0.067±0.006	0.068±0.009	0.013±0.000	0.013±0.001
r_e	0.693±0.344	1.183±0.614	0.623±0.042	1.278±0.138
τ_{870}	0.057±0.013	0.091±0.020	0.116±0.002	0.155±0.004
T_s	295.171±0.083	298.223±0.084	-	-
P_a	904.503±100.055	1000.000±59.6129	-	-

Table 4.1: Comparative retrieval statistics for ORAC and GlobAEROSOL. Results presented for month of September, 2008 over global ocean. The uncertainties quoted are the mean or median retrieval uncertainty on each retrieval quantity over the month.

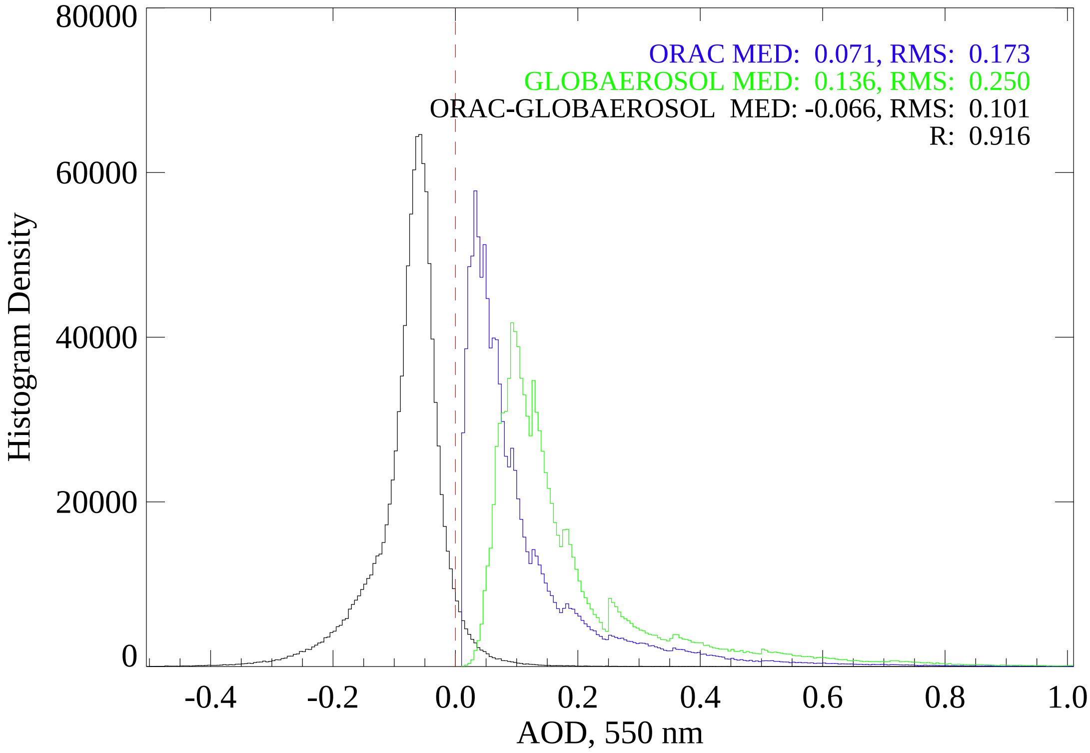

Figure 4.2: Histogram of AOD at 550 nm (τ_{550}) over global ocean for the month of September, 2008.

As well as comparisons at a global scale, it is important to examine the regional statistics to identify regional AOD differences and correlate them with expected predominant aerosol compositions. Figure 4.3 shows the zonally averaged AOD for the month of September, 2008. The zonal mean of AOD is calculated at intervals of

10°. As expected the AOD is higher in the northern Hemisphere than the southern Hemisphere where is dominated by ocean and is relatively pristine. The zonal means of AOD from ORAC and GlobAEROSOL agree well with correlation coefficients in the range of 0.717 to 0.947, the discrepancies between the two datasets are less than 0.1, for all latitude bands ORAC AOD is lower than GlobAEROSOL AOD. It is interesting to see that the correlations between ORAC and GlobAEROSOL over the southern Hemisphere are relatively low while the differences between the two datasets are small, while at the tropical regions and northern Hemisphere the correlations are high but differences are significant.

Further comparisons of AOD from ORAC and GlobAEROSOL are presented in Figure 4.4 and Figure 4.5 based on nine ocean regions defined by Quaas et al. (2008). These regions are believed to represent major aerosol types: for example, dust aerosols over the west coast of Africa and the Persian Gulf, marine aerosols over southern oceans and the central Pacific, natural and anthropogenic aerosols in eastern Asia, northern Atlantic and western Europe. Figure 4.4 shows that over most of the regions the two retrievals yield massive numbers of matches. In general, ORAC derives smaller AOD compared to GlobAEROSOL; the median differences are within -0.1. Good agreements are found in all nine regions with correlation coefficients falling in a range of 0.628 to 0.910. The largest differences with significant RMSs are found over the tropical Atlantic ocean (TAO) and the tropical Indian ocean (TIO), where the high AOD is most likely associated with dust emission from the Sahara. Despite the large differences, the correlation coefficients in the two regions are better than 0.9. Over southern oceans, southern Pacific ocean (SPO), southern Atlantic ocean (SAO) and southern Indian ocean (SIO), as well as the tropical Pacific ocean (TPO), the differences between ORAC and GlobAEROSOL are small but correlations are low. The ORAC median AOD over those four regions are 0.072, 0.107, 0.082 and 0.050 respectively, whereas the corresponding GlobAEROSOL median AOD are 0.117, 0.155, 0.132 and 0.108 respectively. The four regions are with low AOD and the dominant aerosol class is marine clean or a mixture of marine and biomass burning. Aerosol retrieval for low AOD conditions is challenging due to the signals from aerosol being weak compared to surface signals. Huang et al. (2010) and Poulsen et al. (2009) indicate that GlobAEROSOL tends to overestimate AOD over remote ocean. Thus the negative bias of ORAC compared to GlobAEROSOL is a promising performance. Both ORAC and GlobAEROSOL display high AOD at mid-latitudes of the northern hemisphere, particularly in the regions affected by the transportations of heavy aerosol loading from the continents. ORAC and GlobAEROSOL also display some anomalously high AOD at high latitudes of the northern hemisphere, which could be attributed to contamination by surface ice.

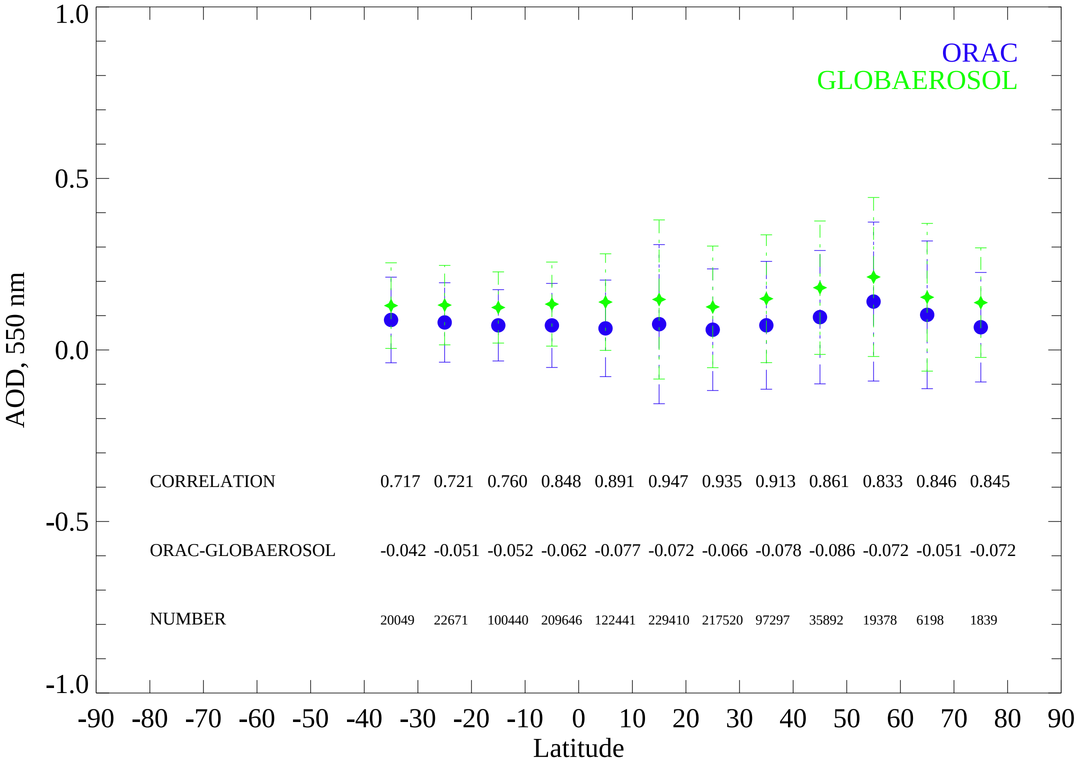

Figure 4.3: AOD at 550 nm (τ_{550}) from ORAC and from GlobAEROSOL plotted as a function of latitude (at an interval of 10°) for the month of September, 2008; the error bars are the root mean square (RMS) of τ_{550} in each latitude band of ten degrees, correlation between the two datasets, median difference (ORAC−GlobAEROSOL), and number of matches are also given.

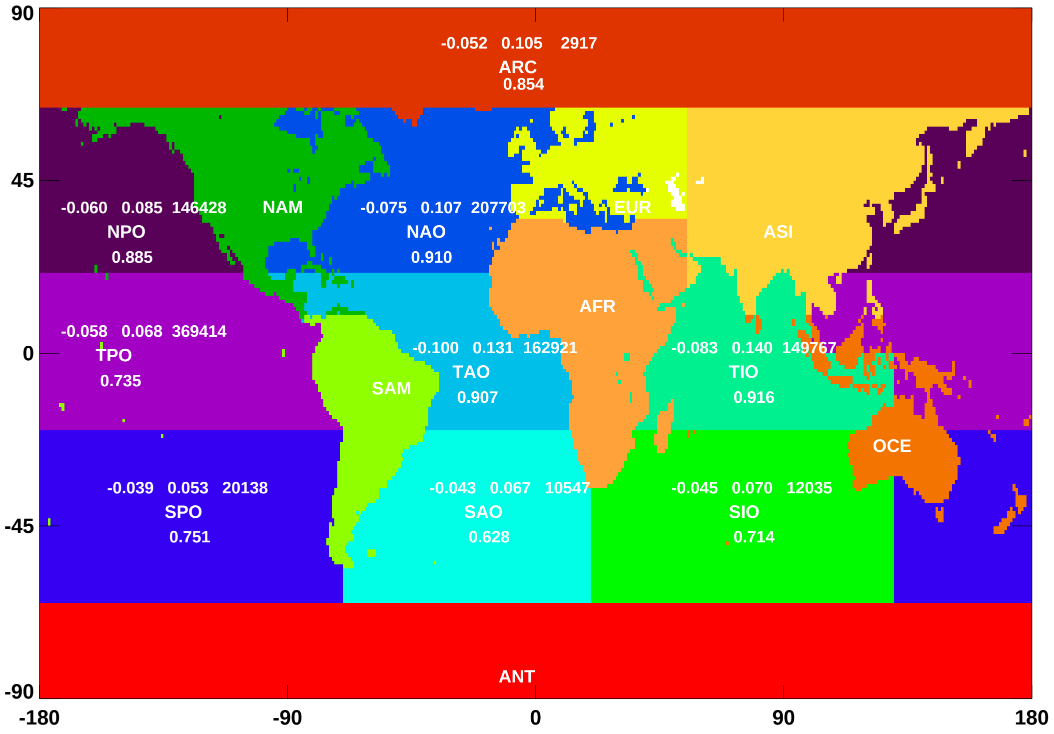

Figure 4.4: Regional statistics of AOD at 550 nm (τ_{550}) for the month of September, 2008; the three figures above the regional name in each region are the median of difference in AOD (ORAC−GlobAEROSOL), root mean square (RMS) and the number of acceptable matches, and the linear Pearson correlation coefficients are also given (figures below the regional names). The nine regions are Arctic (ARC), northern Pacific ocean (NPO), northern Atlantic ocean (NAO), tropical Pacific ocean (TPO), tropical Atlantic ocean (TAO), tropical Indian ocean (NIO), southern Pacific ocean (SPO), southern Atlantic ocean (SAO), and southern Indian ocean (SIO).

4.1.3 Discussions

This section shows that ORAC and GlobAEROSOL have similar patterns of the retrieved parameters with high correlations. There are, however, some noteworthy differences between the two datasets. Firstly, the ORAC shows somewhat lower optical depths and higher white sky albedo statistically and spatially which is a promising performance as studies show that AOD retrieved from GlobAEROSOL suffers a positive bias (Huang et al., 2010; Sayer, 2008). In satellite retrievals, the

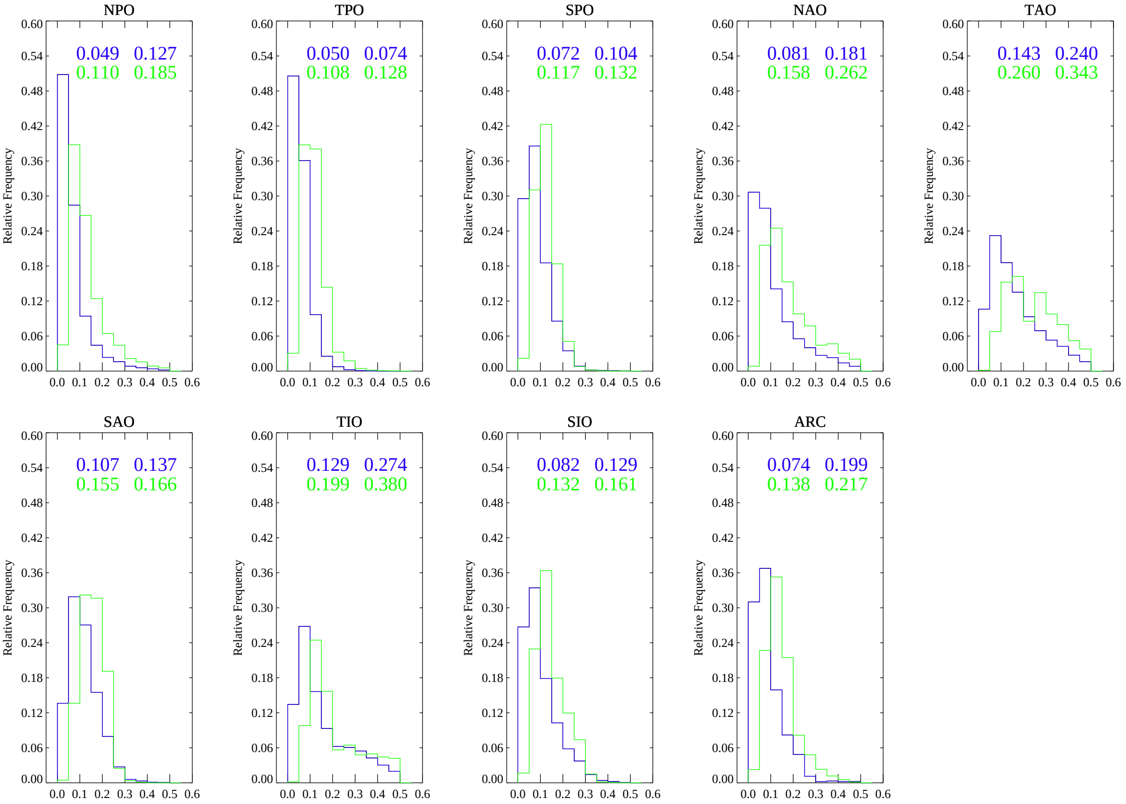

Figure 4.5: Histogram of the AOD at 550 nm (τ_{550}) based on the regions defined in Figure 4.4. Blue colour indicates ORAC and green colour indicates GlobAEROSOL, median and root mean square (RMS) are given above each histogram.

surface albedo and AOD compensate for each other. As shown in Figure 4.6, in contrast to the AOD distributions shown in Figure 4.2, the white sky albedo retrieved by GlobAEROSOL spreads in a narrow range and is significantly lower than ORAC (~ 0.055). With the reduced AOD, the increased surface albedo is expected.

The averaging kernel is a matrix that gives the sensitivity of the retrieved state to the true state, each entry of averaging kernel matrix is defined as:

$$A_{ij} = \frac{\partial \hat{x}_j}{\partial x_i}, \tag{4.1}$$

where $\hat{x}_j$ is the jth element of the state vector and the x_i is the ith element of the true state. The diagonal elements of the averaging kernel indicate the fraction of the retrieved state determined by the true value of that quantity, for a perfect retrieval

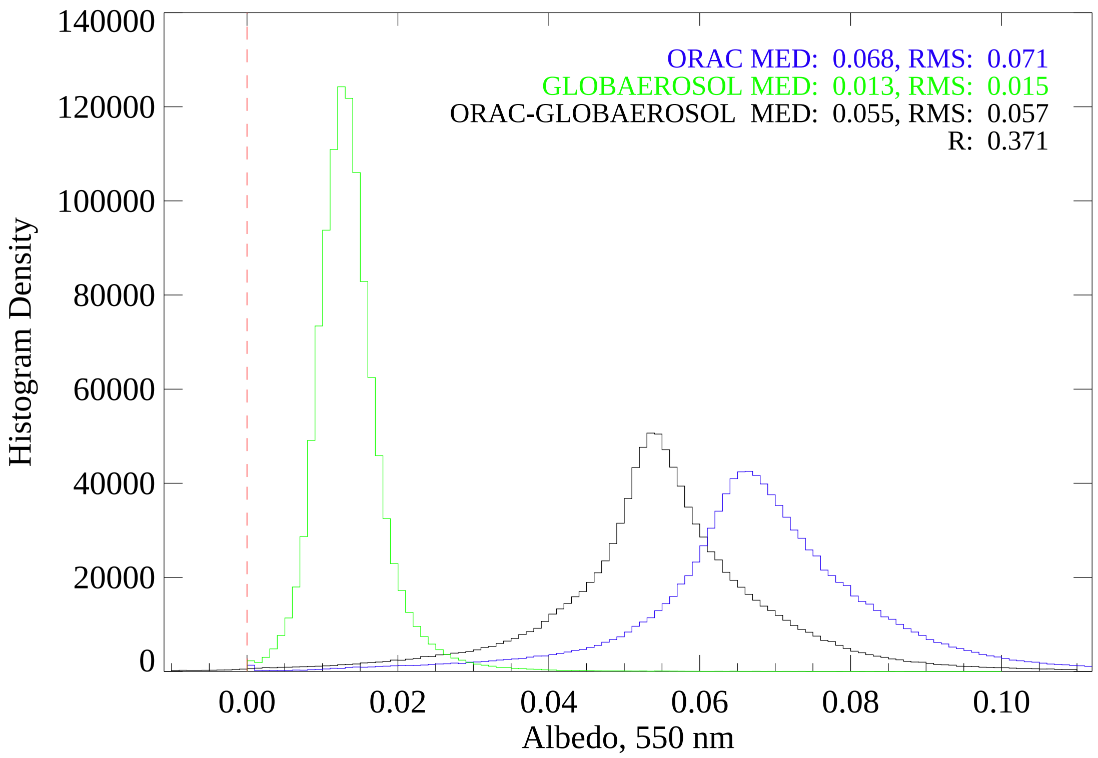

Figure 4.6: Histogram of surface white sky albedo at 550 nm ($R_{SLW,550}$) over global ocean for the month of September, 2008.

system would be an identify matrix, while a value of zero on the diagonal indicates that the corresponding state element is entirely determined by the *a priori* (Rodgers, 2000). Figure 4.7 shows the histograms of the diagonal elements of averaging kernel retrieved by ORAC. It can be seen that in general AOD and surface albedo are very sensitive to measurements, whereas aerosol layer height (P_a) and effective radius are the least well retrieved.

Secondly, as shown in Table 4.1 and Figure4.3 for most cases the uncertainties of ORAC are larger than GlobAEROSOL. The main factors having effects on the retrieved parameter uncertainties are cloud contamination, assumed surface albedo spectrum, measurement errors, assumed aerosol classes as well as radiative transfer models. One of the possible reasons for the larger ORAC uncertainties is that ORAC uses two more channels (11 μm and 12 μm), one of which has a greater systematic error

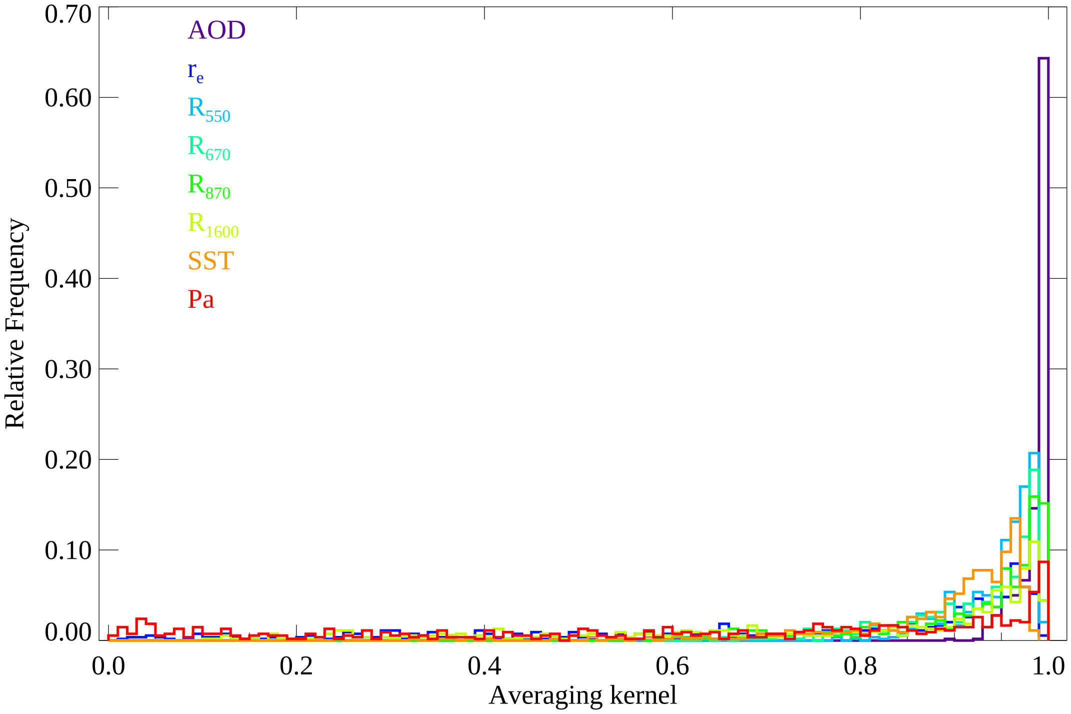

Figure 4.7: Histograms of the diagonal elements of averaging kernel for the state vector of ORAC.

of 0.2 K, as well as an extra radiative transfer model (infrared forward model). The errors associated with measurements and radiative transfer model can be propagated into retrieval uncertainties. Hopefully the uncertainties can be reduced by adjusting the measurement systematic error or improving the accuracy of radiative transfer model. The other likely source of the large uncertainties in ORAC is the assumed aerosol classes. The classes used in ORAC are only suitable for the ocean regions influenced by desert dust or for the remote ocean. For the regions, especially coastal waters, affected by industrial pollution or biomass burning the inappropriate classes may introduce errors.

4.2 Validation with AERONET

4.2.1 Overview of AERONET

One of the most useful tools supporting aerosol validation is the AErosol RObotic NETwork (AERONET) established by National Aeronautics and Space Administration (NASA), providing globally distributed observations of aerosols. The AERONET is composed of more than 300 Sun/sky scanning ground-based automated radiometers, providing a standardization for regional to global scale aerosol monitoring. The AERONET measurements are performed at a spectral region of 340 nm to 1020 nm through a large range of scattering angles, using a constant aerosol profile to retrieve size distribution, phase function and AOD (Dubovik et al., 2000). The estimated uncertainty in AERONET AOD is within ±0.02 under cloud free conditions (Knobelspiesse et al., 2004; Eck et al., 1999). In the following validation, the AERONET data used are from the AERONET Level 2.0 which are cloud screened and quality assured (Holben et al., 2006). There is no AERONET measurement at the AATSR wavelength of 550 nm, therefore the AERONET AOD at 550 nm, $\tau_{A,550}$, is interpolated from the AOD at 500 nm ($\tau_{A,500}$) and 870 nm ($\tau_{A,870}$) using Equation 4.2:

$$\tau_{A,550} = \tau_{A,870} \left(\frac{550}{870}\right)^{-\alpha_{A,500,870}}, \tag{4.2}$$

where $\alpha_{A,500,870}$ is the Ångström exponent between 500 nm and 870 nm given in the AERONET dataset. In ORAC the AOD at 550 nm (τ_{550}) is retrieved directly, the AOD at 870 nm (τ_{870}) is computed from τ_{550} and effective radius (r_e), the Ångström exponent (α) is calculated using τ_{550} and τ_{870}.

4.2.2 Results

The spatial and temporal sampling resolutions of AERONET and satellite data differ fundamentally in that AERONET samples one location at a high temporal frequency, while satellites measure data for a larger region but with a lower temporal resolution. Therefore, to optimize the representativeness of validation, the two datasets are averaged over a thirty-minute temporal window first and then the ORAC data are averaged over a circle of 0.3° radius centred on AERONET stations. In this chapter ORAC runs at a resolution of 10 km (super-pixel) which is approximately of 0.1°, and only those circular areas centred on AERONET stations with at least 9 available ORAC super-pixels are considered. The cloud fraction of each circular area is calculated as the averaged cloud fraction of the available ORAC super-pixels. Given the narrow swath of AATSR, the criteria yield 560 pairs of matched data from 127 AERONET stations during the period of June, 2008. Figure 4.8 shows the distribution of the 127 AERONET stations. Northern American and European stations dominate the matched data and most of the matched pairs are located in the continents or coastal areas. As shown in Figure 4.8, there is a good agreement between the ORAC and AERONET, with ORAC capturing the regional variability of AOD well. Compared with the AERONET observations, ORAC has a positive bias on the continents while for some coastal stations the ORAC has a negative bias.

Comparisons of spatio-temporally averaged ORAC and AERONET for the collocated data during June, 2008 are shown in Figure 4.9 to Figure 4.14, the linear regression equations and correlations are given at the top of each plot, error bars on the data are the standard deviation of the spatio-temporally averaged measurements. There are about 190 matches over ocean or coastal areas, the majority of the matches are with AOD less than 0.3 at both 550 nm and 870 nm (Figure 4.10 and Figure 4.12). Pearson's linear correlation coefficient R is 0.820 for 550 nm and 0.807 for 0.87 nm. There is a tendency for ORAC to overestimate AOD, differences between ORAC and AERONET are 0.067 ± 0.214 at 550 nm and 0.064 ± 0.167 at 870 nm. At higher AOD where the data become sparser, the error on each data becomes larger.

Ångström exponent can be used as an indicator of aerosol particle size: the greater Ångström exponent, the smaller dominant aerosol particle in size distribution. According to Figure 4.13, the ORAC Ångström exponent is poorly correlated to that of AERONET even for the ocean stations ($R \sim 0.1$). Ångström exponent is inversely proportional to particle size, one possible reason for this discrepancy is the different size of aerosols retrieved by ORAC and the algorithm used by AERONET. This may be also due to the different wavelength-dependence of AOD used by ORAC and AERONET.

The number of matches over the continents is 371; however, the comparisons of AOD clearly show that ORAC retrieval performs less satisfactorily over land. The Pearson's linear correlation coefficients are 0.312 for 550 nm and 0.275 for 870 nm. The positive bias in ORAC AOD suggests a potential underestimate of the land surface reflectance. The low agreements of AOD over the continental AERONET stations may be explained by three reasons: residual cloud contamination due to poor performance of the cloud flag scheme over land, inappropriate aerosol classes, and complexity of the land surface state.

ORAC retrieval uses the AATSR operational cloud screening scheme used for SST and land surface temperature (LST) retrievals (Birks, 2004; Zavody et al., 2000).

However this scheme is relatively loose over land, especially for very thin cirrus or small warm convective cloud (Poulsen et al., 2009). Figure 4.15 shows the correlation coefficient (R) between the AERONET and ORAC as a function of cloud fraction. According to Figure 4.15, for the ocean AERONET stations, the correlation coefficient slightly decreases with the increase of cloud fraction. For the continental stations, the correlation coefficient decreases dramatically with the increase of cloud fraction. The strong dependence of correlation coefficient on cloud fraction indicates a possible cloud contamination in ORAC retrieval over land.

As the majority of AERONET stations in this study are continental or coastal stations, located in the northern hemisphere where is strongly influenced by urban aerosols. The most appropriate aerosol class to use is urban class. However, the size of urban aerosols is relatively small, in order to emphasise the effect of infrared channels, this version of ORAC only uses marine class or dust class which are of coarse mode components and are supposed to have an impact on infrared signals. Inappropriate aerosol class assumptions may contribute to the significant discrepancy of AOD over land.

Due to the high inhomogeneity of land surface, ORAC does not calculate the land surface emissivity; instead, the ocean surface emissivity is applied. This may have an impact on the retrieval over land.

Additionally, the sampling and super-pixel methods can also give rise to discrepancies in validation (Kahn et al., 2011; Hyer et al., 2011).

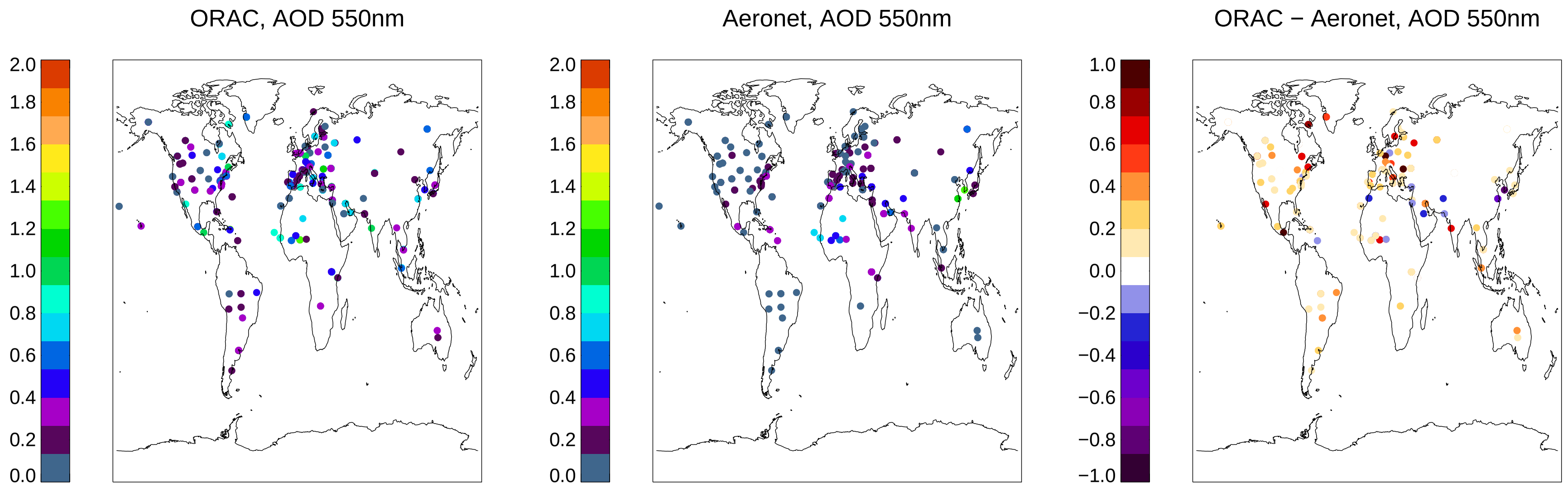

Figure 4.8: Map of AOD at 550 nm, (left) ORAC, (middle) AERONET, (right) the difference between the two datasets, with criteria of 30 minutes in time and 0.3 degree in space for June, 2008.

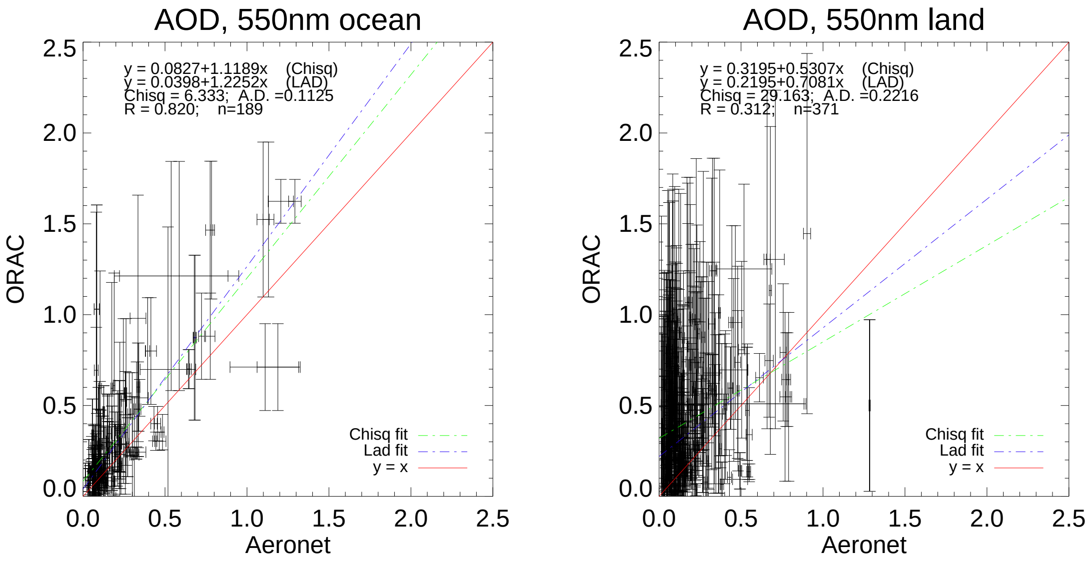

Figure 4.9: Comparison of spatio-temporally averaged ORAC and AERONET AOD at 550 nm for the month of June, 2008, (left) ocean AERONET stations and (right) continental AERONET stations. In each plot the red line is the 1:1 line, the green and the blue dashed lines denote the Chi-square linear regression and the robust least absolute deviation linear regression. Chisq: Chi-square error, A.D.: mean absolute deviation. R: correlation coefficient, n: number of matches. Error bars on the data are the standard deviations of the spatio-temporally averaged measurements.

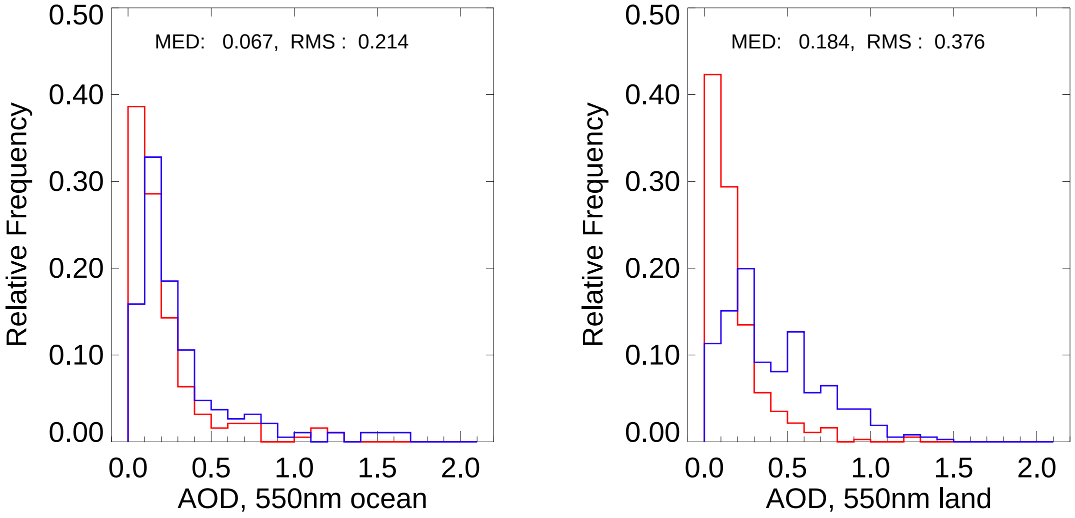

Figure 4.10: Frequency of AOD at 550 nm for June, 2008; (left) ocean stations and (right) continental stations, ORAC AOD is shown by the blue line and AERONET AOD is shown by the red line, MED: median difference between ORAC and AERONET, RMS: root mean square.

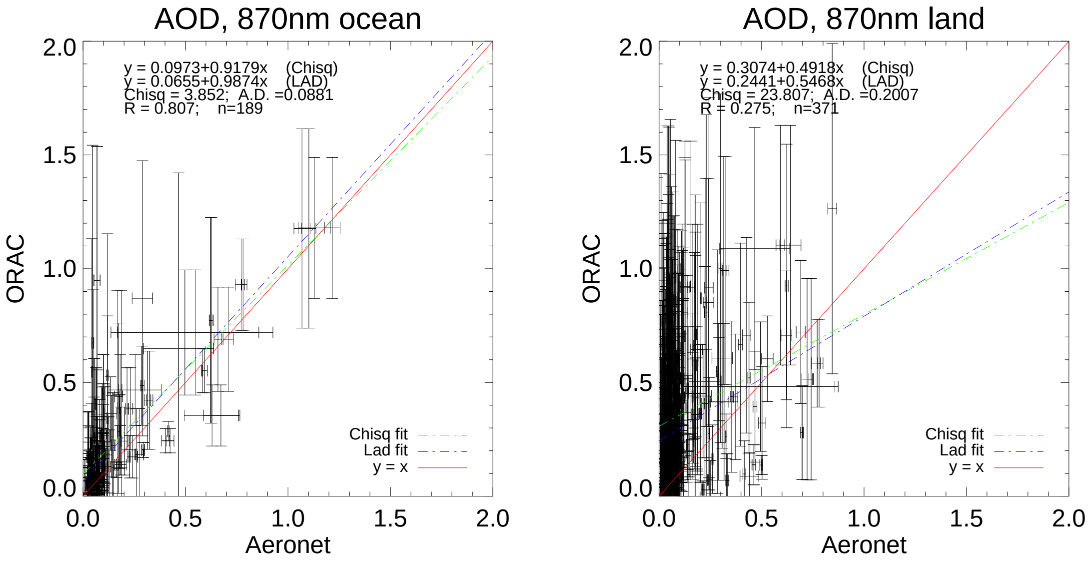

Figure 4.11: Same as Figure 4.9 but for AOD at 870 nm.

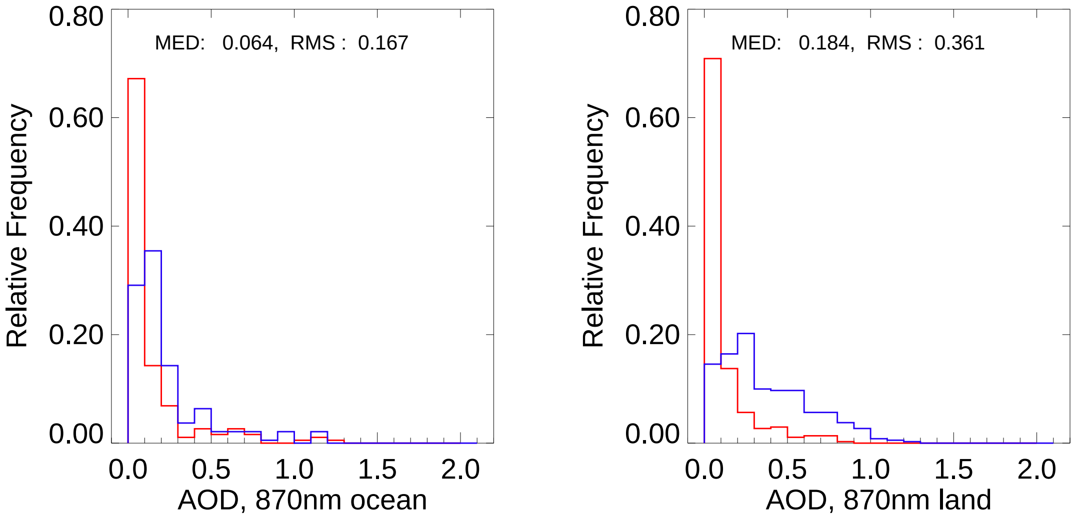

Figure 4.12: Same as Figure 4.10 but for 870 nm AOD.

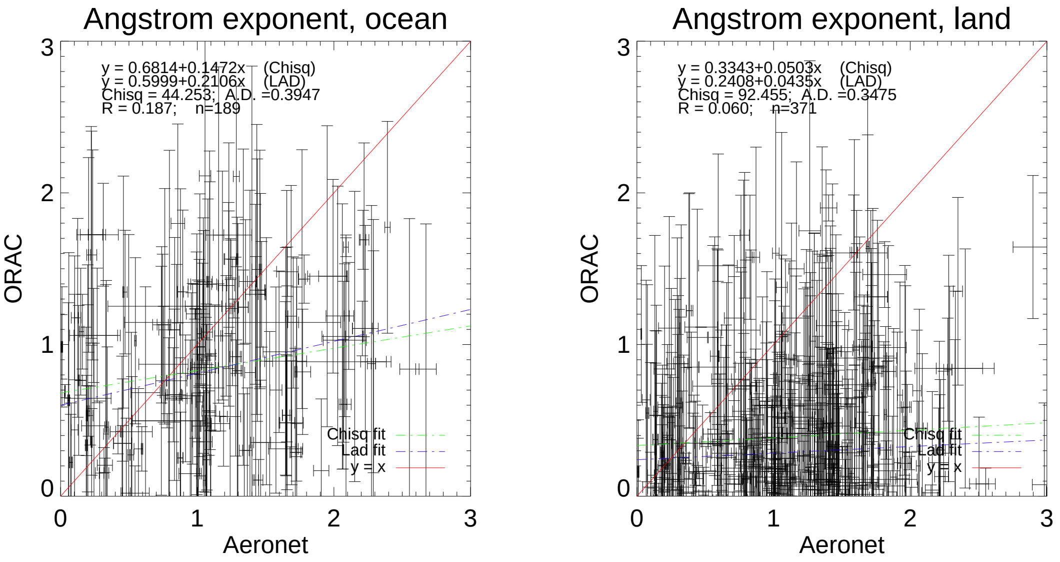

Figure 4.13: Same as Figure 4.9 but for Ångström exponent.

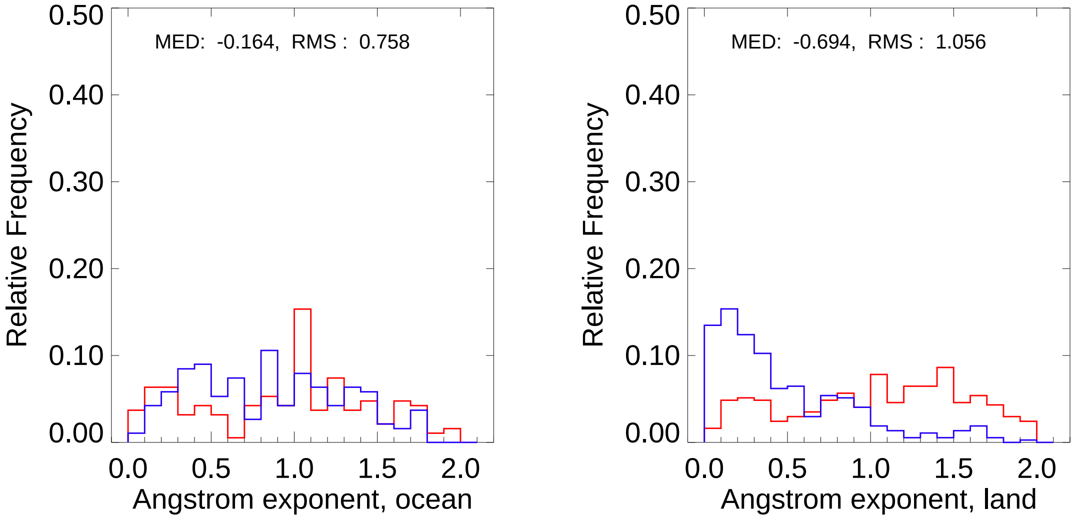

Figure 4.14: Same as Figure 4.10 but for Ångström exponent.

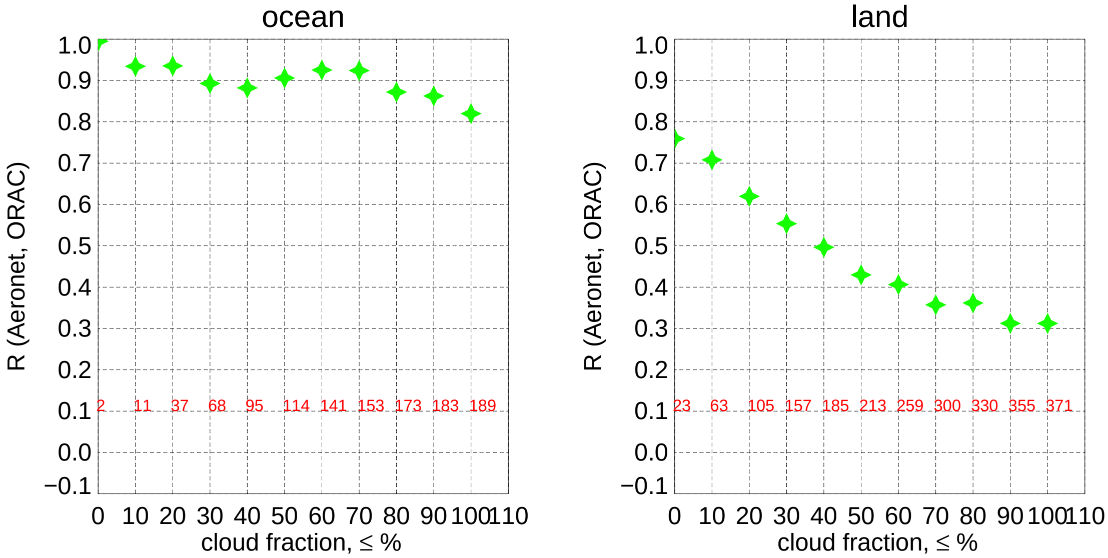

Figure 4.15: Linear Pearson correlation coefficient between ORAC AOD and AERONET AOD at 550 nm as a function of cloud fraction, (left) ocean AERONET stations, (right) continental AERONET stations.

4.2.3 Comparisons of GlobAEROSOL, ORAC and AERONET

Figure 4.16 presents the validations of ORAC and GlobAEROSOL against AERONET for the month of September 2008. The two scatter plots reveal both ORAC and GlobAEROSOL have good agreements with AERONET and tend to overestimate the AOD at 550 nm. The median difference between ORAC and AERONET data is relatively low (0.001 ± 0.1238) and the difference between GlobAEROSOL and AERONET is 0.0706 ± 0.1481. The linear Pearson correlation coefficient between ORAC and AERONET is 0.8181, while the correlation between GlobAEROSOL and AERONET is relatively higher with a coefficient of 0.9361.

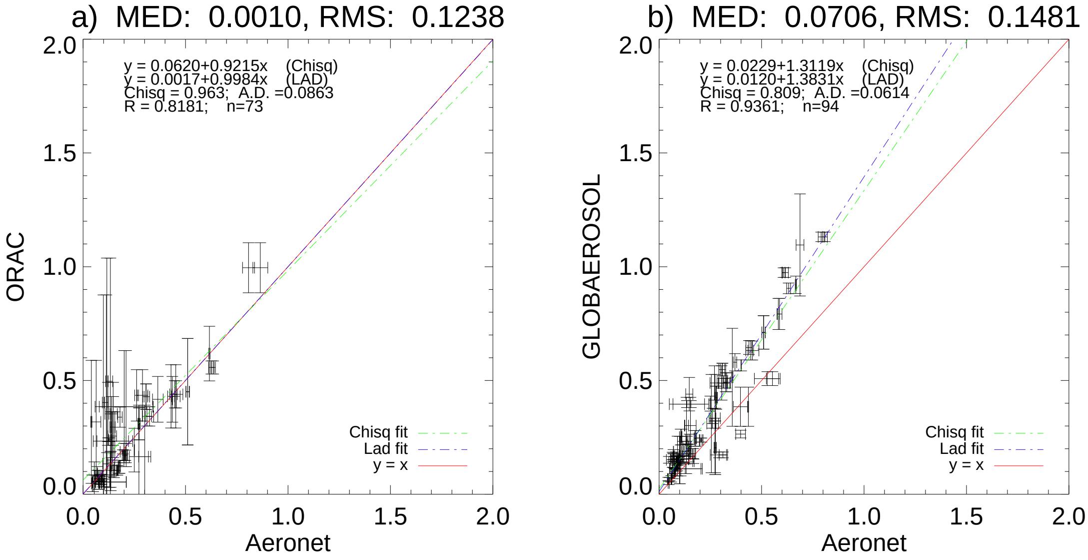

Figure 4.16: Comparison of spatio-temporally averaged AERONET AOD at 550 nm versus a) ORAC and b) GlobAEROSOL during September 2008. In each plot the red line is the 1:1 line, the green and blue dashed lines denote the Chi-square linear regression and the robust least absolute deviation linear regression. Chisq: Chi-square error, A.D.: mean absolute deviation, R: correlation coefficient, n: number of matches. Error bars on the data are the standard deviations of the spatio-temporally averaged measurements. Median difference (MED) and root mean square difference (RMS) are indicated above each plot.

4.3 Conclusions

In this chapter, aerosol properties retrieved with ORAC are compared with GlobAEROSOL AATSR products and AERONET measurements. The comparison with GlobAEROSOL reveals that over ocean ORAC tends to underestimate AOD globally and regionally. For the month of September, 2008 the global correlation between the two datasets is 0.916 and the global median difference is -0.066 ± 0.101. The large differences and high correlations occur in the tropical Atlantic ocean (TAO) and the tropical Indian ocean (TIO) where aerosol loadings are high and are influenced by dust plumes from the Saharan area. The analysis concerning surface white sky albedo R_{SLW} shows that ORAC retrieves significantly higher R_{SLW}. This would explain the reduced level of ORAC AOD.

It follows from the validation of coincident ORAC and AERONET data that the collocated ORAC and AERONET data substantially agree well over ocean. Over ocean, the correlations between ORAC AOD and AERONET AOD are 0.820 for 550 nm and 0.807 for 870 nm, the differences in AOD between the two datasets are 0.067 ± 0.214 for 550 nm and 0.064 ± 0.167 for 870 nm. It comes as no surprise that the validation between ORAC and AERONET over land are not as good as over ocean. Many factors could contribute to the significant discrepancies over land, for example cloud contamination, inappropriate aerosol class assumptions used in ORAC, inadequate land surface simulation. Most of the AERONET data used in this chapter are limited to coastal or continental stations and they do not provide enough samples over open ocean where most of the ocean retrievals take place. The Maritime Aerosol Network (MAN) is a new aerosol observation network that provides ship-based measurements over open ocean: it offers an opportunity of validating ORAC over open ocean, and this will be attempted in future work.

Chapter 5

SST validation

Satellite derived SST data have been widely applied in atmospheric and ocean studies. Among a variety of applications, numerical ocean prediction and numerical weather prediction require stringent precisions of better than 0.3 K (Llewellyn-Jones and Remedios, 2012; Jacobowitz, 1997; Cornillon, 1989; Yates et al., 1985).

The accuracy of SST derived from a well-calibrated space radiometer is strongly dependent on the effectiveness of atmospheric correction. The conventional approach of validation is to compare the satellite derived SST with in situ measurements which are free of influence from the atmosphere. There are two types of in situ measurements that can be used to validate the satellite derived SST: direct measurements and indirect measurements. The direct measurements are skin temperature measurements obtained from radiometers of similar spectral characteristics to satellite instruments; the indirect measurements are bulk temperatures at specified depths collected by buoys or buckets. The validation with in situ measurements is difficult and costly: an in situ dataset must include observations with wide geographic and temporal distributions to encompass a broad range of ocean and atmospheric conditions (Donlon et al., 2002).

Great efforts have been made to validate the satellite derived SST in global or regional scales. Since the launch of the first sensor of ATSRs, several studies have been carried out to access the accuracy of derived SST. A summary of previous validations of ATSRs SST is given in Table 5.1.

5.1 Validation with ship-based radiometer

5.1.1 Overview of ISAR

The infrared SST autonomous radiometer (ISAR) is a self-calibrating scanning radiometer developed specifically for SST validation. It can be deployed on voluntary observing ships (VOS), five ISAR instruments are built and used in the United States, China and Europe (Donlon et al., 2008).

The ISAR instrument used in this analysis is installed on the P & O Ferry Pride of Bilbao, runs a regular routine from Portsmouth, UK to Bilbao, Spain through the English channel and Bay of Biscay. This routine is repeated twice per week and crosses coastal, shelf seas and open ocean environments. The ISAR is mounted at a height of 25 meters above sea surface, views the sky at an angle of 25° from vertical and views sea surface at an angle of 25° to the nadir (Donlon et al., 2008). Under no precipitation conditions, ISAR is capable of making a measurement every two to three minutes. ISAR measures skin SST with a single wide spectral band (9.6 μm to 11.5 μm). For a calm sea surface, the emissivity at a spectral region $9 - 12$ μm is approximately unity when the viewing angle is less then 40° (Niclo's et al., 2005; Wu and Smith, 1997; Bertie and Lan, 1996). The SST retrieval algorithm used by ISAR assumes the sea surface emissivity is 0.9916. The accuracy of ISAR SST is ±0.1 K (Donlon et al., 2008).

Figure 5.1 shows a composite of ship tracks given by the ISAR's on-board GPS for the period from February, 2006 to December, 2008, revealing the slight variations

reference	period	scale	instrument	bias, K	precision, K	(A)ATSR resolution
Mutlow et al. (1994)	04-05.1992	global	ATSR vs drifting buoys	-0.36	0.42	0.5°
Harris and Saunders (1996)	02-03.1992	global	ATSR vs drifting buoys	-0.19	0.62	1 km
Carroll and Watts (2006)	08.2002-08.2003	global	AATSR vs Moored and drifting buoys	0.02	0.39	10 arc min
Noyes et al. (2006)	01.2003-12.2003	Caribbean Sea	AATSR vs ship-based radiometer	-0.05	0.26	1 km
Corlett et al. (2006)	06.2002-06.2003	regions	AATSR vs ship-based radiometer	0.11	0.33	1 km
Stark et al. (2008)	08.2002-07.2006	global	AATSR vs buoys	0.17	-	1 km
Wimmer et al. (2012)	03.2004-04.2009	Bay of Biscay - English channel	AATSR vs ship-based radiometer	-0.04	0.39	1 km

Table 5.1: Previous validation research about the ATSRs daytime SST retrieval (dual-view, two-channel).

in the actual ship routines.

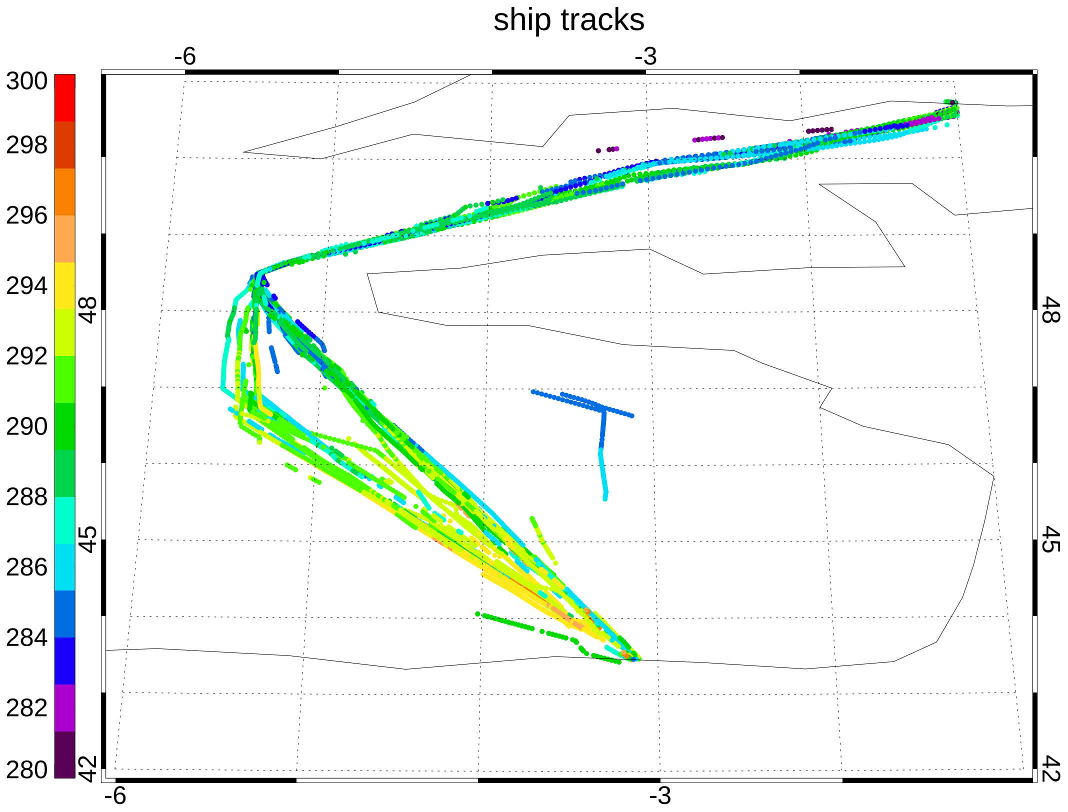

Figure 5.1: Ship tracks of Pride of Bibao during the period from February, 2006 to December, 2008. Each skin SST measurement obtained by the ISAR is plotted as a dot. Breaks in the ship tracks indicate that no measurements were obtained due to bad weather conditions.

ORAC SST used in this section is generated at a resolution of 1 km. Before validation, a database containing paired near-simultaneous ISAR and ORAC observations was created. For each ISAR observation all ORAC observations taken within the temporal window and spatial window were found and then the ORAC measurement with the closest distance to the ISAR observation was selected. Three sets of criteria for the temporal and spatial windows were chosen:

- **Grade 1** Temporal match within ±1 hour and spatial match within ±1 km.
- **Grade 2** Temporal match within ±2 hours and spatial match within ±1 km. These are the matching criteria used by the AATSR validation protocol

(Robinson and Wimmer, 2008).

- **Grade 3** Temporal match within ±3 hours and spatial match within ±10 km.

5.1.2 Results

Table 5.2 is a summary of the statistics of comparison between ORAC and ISAR SST for the period from February, 2006 to December, 2008, the comparison between ISAR and corresponding AATSR operational SST product (OP) is also given. AATSR operational SST product is generated using the split-window technique (Equation 1.21). There are four types of operational SST product, labeled as N2 (single-view 2-channel), N3 (single-view 3-channel), D2 (dual-view 2-channel) and D3 (dual-view 3-channel). The N3 and D3 algorithms are performed in the nighttime because in the daytime the 3.7 μm channel is significantly contaminated by solar radiation, D3 has a better accuracy than the other three (Embury et al., 2012a; Wimmer et al., 2012). The D2 product is used in this comparison because ORAC runs in the daytime with dual-view. The median difference (MED) is used to describe the central value of the distribution of the difference between the ORAC retrieved SST and in situ SST, the root mean square (RMS) is used to describe the spread of the difference distribution. According to Table 5.2 for the period the number of matches increases from 117 for Grade 1 to 427 for Grade 3. For the three different match grades, OP SST agrees ISAR well with median values close to zero, while ORAC has a warm bias. In ISAR SST algorithm, sea surface emissivity is assumed to be constant (0.9916) over the width of band. ORAC calculates sea surface emissivity as a function of viewing geometry, wind speed, temperature and wavelength, the calculated emissivity is lower than 0.9916, the reduced emissivity may lead to an overestimate of SST. Scatter diagrams of ISAR and ORAC, as well as histograms of the difference between ISAR and ORAC for the three grades are presented in Figure 5.2. The most encouraging result is the linear correlation coefficients between ORAC and ISAR are significant, 0.991, 0.986, and 0.988 for the three grades respectively. However, the correlation coefficients, as well as the median differences and RMS are still worse than that obtained from comparison between OP and ISAR, indicating ORAC needs further improvements.

grade	orac−isar med	op−isar med	orac−isar rms	op−isar rms	num of matches	min isar	max isar
Grade 1	0.117	-0.010	0.430	0.349	117	279.64	290.940
Grade 2	0.117	-0.020	0.492	0.338	221	279.64	291.420
Grade 3	0.150	0.000	0.481	0.324	427	279.64	291.420

Table 5.2: Statistics of the comparisons between ISAR SST and ORAC SST for three match criteria, the comparisons between ISAR and AATSR operational SST product (OP) are also given.

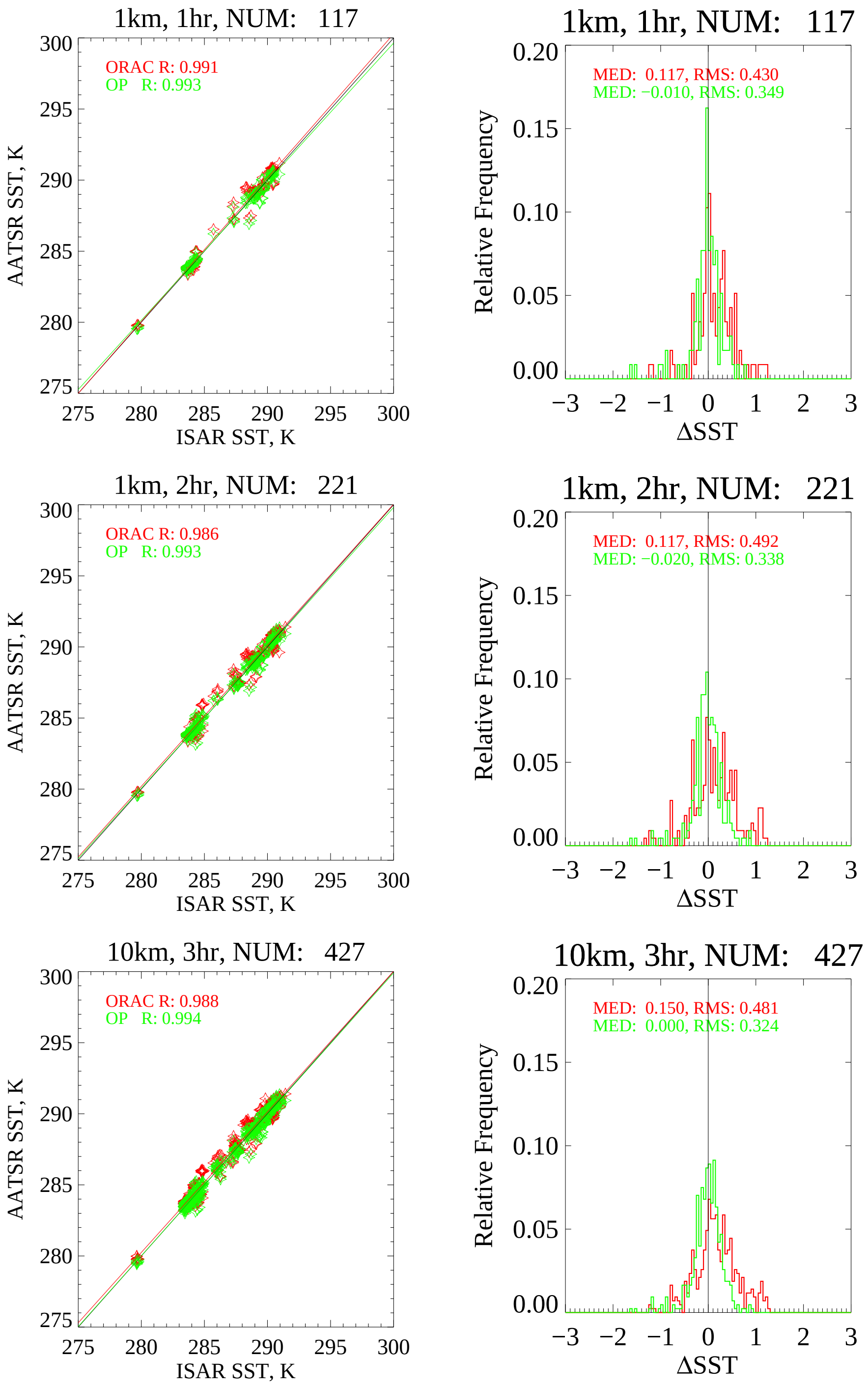

Figure 5.2: Scatter diagram of ORAC SST versus ISAR SST (left column) and the frequency distribution of the difference between ORAC and ISAR (right column) for three match grades for the period from February, 2006 to December, 2008. The comparisons of AATSR operational SST product (OP) and ISAR SST are also given. The correlation coefficients between ISAR SST and ORAC SST or OP SST are given on the left corner of each scatter plot, the median and RMS are given on the left corner of each histogram plot.

5.2 Validation with drifting buoys

Drifting and moored buoys play essential roles in the development of SST retrieval from satellite sensors. The measurements from buoys are used to derive the retrieval coefficients for split window methodology (Equation 1.21) (Walton et al., 1998; Strong and McClain, 1989; Walton, 1988; McClain, 1981), and to evaluate the accuracy of satellite SST products and diagnose possible sources of bias (Castro et al., 2008; Carroll et al., 2008; Corlett et al., 2006; May et al., 1992). The main objective of this section is to access the accuracy of ORAC SST by comparing with the SST measurements obtained by drifting buoys. The satellite measurements used for retrieval and buoys measurements for validation are from the Sea Surface Temperature Climate Change Initiative (SST CCI) project.

5.2.1 Overview of SST CCI

The SST CCI project is a part of ESA Climate Change Initiative project, aims to evaluate the performances of different satellite SST retrieval algorithms and then to select the best algorithm or the combination of algorithms (http://www.esa-sst-cci.org/). In order to do the inter comparison of algorithms, the SST CCI project has created a multiple-sensors matchup data (MMD) package which provides all the necessary data for a SST retrieval and validation process. The SST CCI project MMD package is composed of satellite measurements, in situ measurements, auxiliary data and forward modelled parameters. The SST CCI project has three steps and MMD data package has three subsets (Corlett and Merchant, 2011):

- **Training data** This subset is used for determining the regression coefficients for split-window methodology based algorithms. Because ORAC is an optimal estimation scheme, and does not need regression coefficients, the training data are not used.

- **Test data** This subset is used to access the performances of retrieval algorithms. It includes satellite measurements and ancillary atmospheric profiles data which are required by the SST retrieval, and drifting buoys measurements which are used to validate the retrieved SST. This subset is used in this section.

- **Selection data** This subset will be used to carry out the algorithm selection, it only includes limited data fields sufficient to derive SST but without drifting buoys measurements. At the time of writing this section, this subset has not been released.

5.2.2 Results

Before validation, the drifting buoys SST measurements, denoted by BUOYS, are collocated with the ORAC SST data, denoted by ORAC. For each ORAC point the BUOYS points within 3 hours in time and 10 km in distance are selected. If more than one BUOYS points are found then the median of these BUOYS points is used. The other option is to use the closest BUOYS point to the ORAC point in distance instead of the median value. This option only makes differences to the validation results of the order of 0.001 K. In this section, the median values are used if nothing else is stated.

Outliers in validation results can be caused by the failure of cloud detection, error of in situ measurements, satellite pixel ending up with large retrieval cost and mismatch between satellite retrieved products and in situ measurements. In some studies a data point is identified as an outlier if it is greater than ±3 or ±4 standard deviations of the data (IASI, 2011; Alwis et al., 2007; Carroll and Watts, 2006; Ostle and Malone, 1988). Aumann (2003) uses 3 K in difference between satellite derived SST and in situ data as a threshold to filter out the outliers in SST validation. In this section a data point is identified as an outlier if its value is beyond four times of the RMS difference between ORAC and BUOYS. Therefore the ratio between the number of outliers and total number of matches is around 2 : 1000 satisfying the commonly accepted ratio of 1 : 100. Some of the outliers correspond to very warm surface temperature, low water vapour content and low TOA BTs, indicating a good possibility of contamination from undetected cloud.

The retrieval of SST involved with satellite infrared measurements is only possible for cloud free conditions. Considering the reliability of ORAC retrieval, the validations are limited only to the matches with ORAC pixels flagged as cloud free. AATSR contains a detailed cloud flag scheme which labels each AATSR pixel as being cloudy or clear sky. AATSR operational cloud flag scheme comprises a sequence of threshold tests based on the spectral and spatial properties of the TOA measurements (Birks, 2004; Zavody et al., 2000). This approach has many limitations, in particular these related to the difficulty of setting thresholds. Alternatively, the SST CCI project uses a probabilistic scheme based on a Bayesian inversion to detect cloud. Given the observed radiance and *a priori* knowledge of the atmospheric state, the scheme estimates the probability of each ORAC pixel being flagged as clear sky (Old and Merchant, 2007; Merchant et al., 2005). The presence of dust aerosols has an effect on the SST retrieval, the SST CCI project also provides a dust flag scheme (Good et al., 2012).

The validation result statistics are given in Table 5.3 for different clear sky probability thresholds. It shows that the total number of matches decreases when the clear sky probability threshold becomes more stringent. After removing outliers, the RMS decreases significantly while the median value barely changes ($\sim$ 0.0001 K).

cloud flag	num of matches	bias^1, K	RMS^1,K	num of outliers	bias^2, K	RMS^2, K
no flag	56393	-0.0498	0.7453	197	-0.0495	0.4363
50% flag	26780	-0.0595	0.6490	83	-0.0592	0.3751
90% flag	19339	-0.0671	0.5959	67	-0.0666	0.3663
90% and dust flag	17905	-0.0743	0.6497	51	-0.0738	0.3724

Table 5.3: Statistical results of SST validation between ORAC and drifting buoys from January, 2006 to December, 2010 using different clear sky probability thresholds. No flag: no cloud flag and no dust flag is used, i.e. all matches; 50% flag: matches with clear sky probabilities greater than 50%; 90% flag: matches with clear sky probabilities greater than 90%; 90% and dust flag: matches with clear sky probabilities greater than 90% and dust free. The superscript 1 indicates all the data points, the superscript 2 indicates the data points after removing outliers.

According to Section 1.2.1, because of high emissivity of water, infrared radiometers operating at spectral range of 3.7 μm to 12 μm measure the skin temperature within the top layer of the ocean ($\sim$ 10 μm), while drifting buoys measure the bulk temperature at a depth of 0.5 – 1.0 m below the surface. Skin temperature and bulk temperature cannot be compared directly because the vertical gradient of temperature at the upper ocean is complex due to net radiative flux from the ocean to the atmosphere and absorption of incoming solar radiation. The upper ocean ($\sim$ 10 m) can be significantly influenced by solar radiation; in the daytime a stratified layer will be formed if wind speed is low, this thermal stratified layer will break as wind speed increases and a well-mixed layer will be formed in the upper ocean as a result of wind-induced shear. The difference between skin temperature and bulk temperature is small under high wind speed and weak (or no) solar radiation conditions. Donlon et al. (2002) conclude that during the nighttime at wind speeds greater than 6 ms^{-1} the difference between skin temperature and bulk temperature is relatively constant and well characterised by a cool bias of -0.17 ± 0.07 K. ORAC results are only for daytime when buoy measurements are potentially influenced by the thermally stratified layer. As the conversion between skin temperature and bulk temperature is not the focus of this study, the effect of thermal stratification is reduced by only using matches in the high wind regime (wind speed $\geq$ 6 ms^{-1}), in these cases the difference between skin SST and bulk SST is small. For each match, wind speed is calculated from ECMWF 10 m zonal and meridional velocities provided by the SST CCI MMD package. The validation is carried out for two groups according to wind speed: wind speed greater or equal to 0 ms^{-1}, i.e. all matches; and wind speed greater or equal to 6 ms^{-1}, i.e. matches with high wind speeds.

Figure 5.3 shows a zonal distribution of the numbers of matches using different clear sky probability thresholds. It indicates a reasonable latitudinal coverage of the matches with more points at the mid-latitude regions. The number of matches decreases as the cloud flag becomes more stringent. Only one-third of the matches can be flagged as having a clear sky probability better than 90%. In the following study 90% is used as the clear sky probability threshold, which is also used by some other SST CCI participants (Cox, 2012).

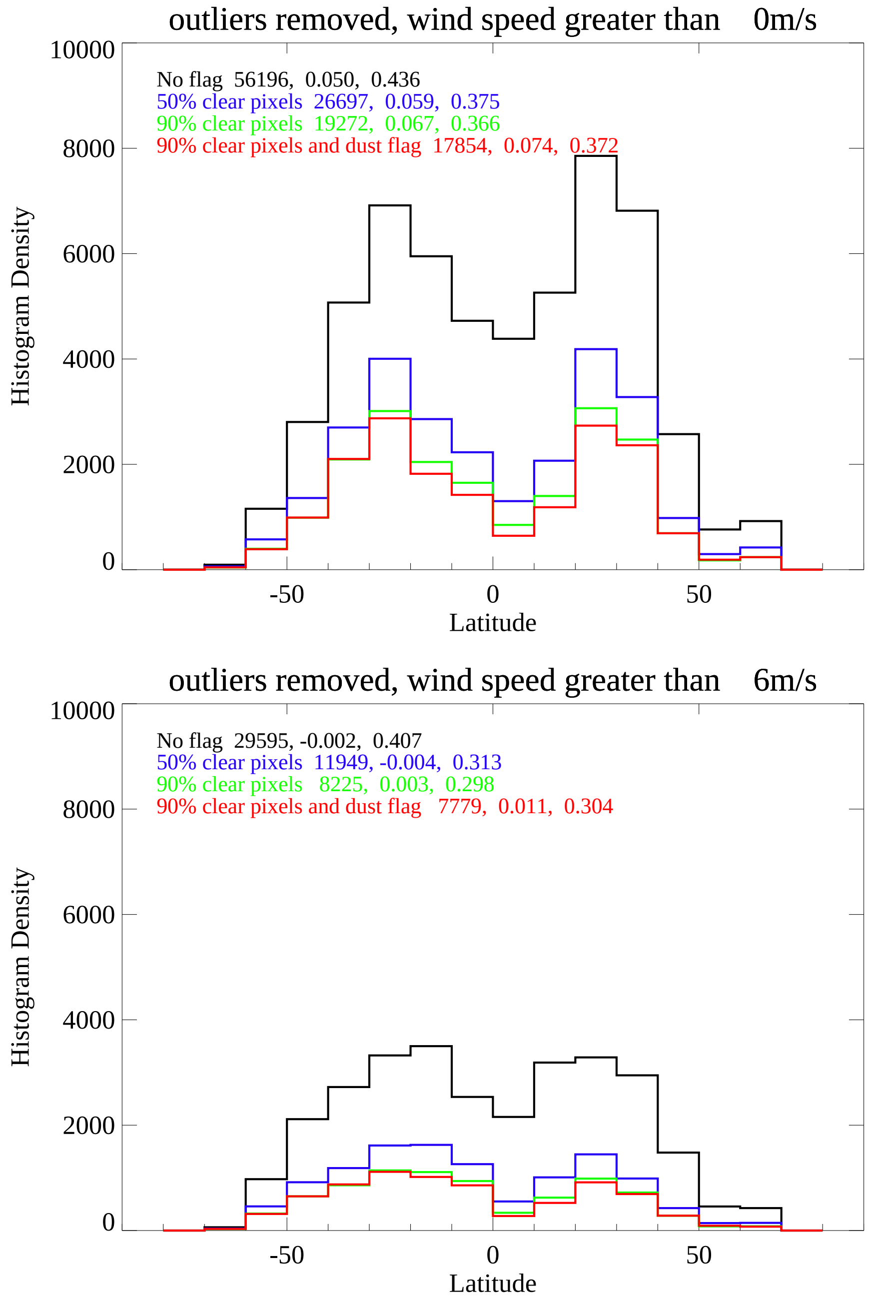

Figure 5.3: Latitudinal distribution of numbers of matches using different clear sky probabilities and two wind speed thresholds, 0 ms^{-1} (top) and 6 ms^{-1} (bottom).

Figure 5.4 shows the latitudinal average of the difference between ORAC SST and BUOYS SST (ΔSST=ORAC$-$BUOYS). For all latitude bands, ΔSST roughly falls within the range from 0.3 K to -0.3 K. ORAC SST has negative biases for many of the latitudinal bands and he biases decrease slightly when only the matches with high wind speeds are taken into consideration. At high latitudes, especially in the northern Hemisphere, the biases get stronger. This is probably due to the small sample numbers in high latitude regions.

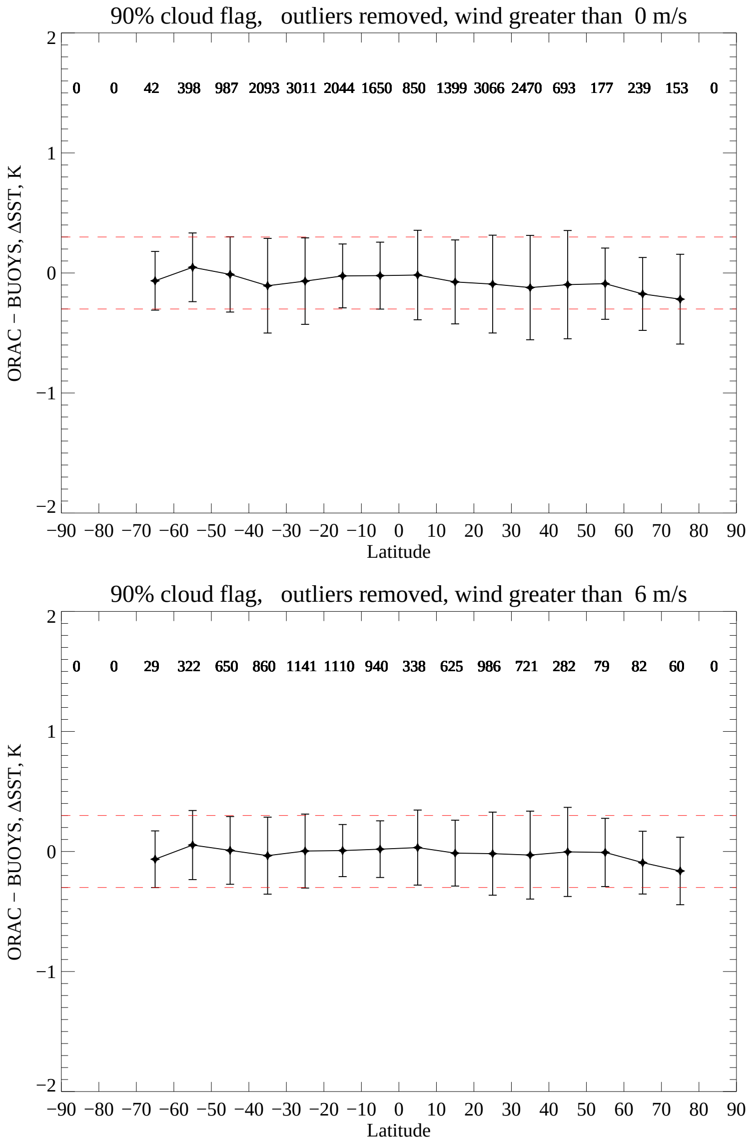

Figure 5.4: Variation of the difference in SST between ORAC and BUOYS (ΔSST=ORAC$-$BUOYS) with latitude for five years from January, 2006 to December, 2010. Top: all the pixels, bottom: only the pixels with wind speed ≥ 6 ms^{-1}. Each error bar indicates the standard deviation of the difference between ORAC SST and buoys SST within each 10° latitude band.

Figure 5.5 shows global distribution of the difference between ORAC SST and BUOYS SST for five years from January, 2006 to December 2010, blue and red dots depict cold bias and warm bias respectively. Using the 6 ms^{-1} threshold reduces the number of matches dramatically, the percentage of matches suffering a cold bias reduces by nearly 10%. This is probably due to the fact that strong wind can disrupt the thermal stratified layer formed by diurnal cycle heating, and decrease bulk temperature, therefore weaken the skin effect. Figure 5.6 shows the histograms of the difference between ORAC SST and BUOYS SST. ORAC generally has a cold bias, and this cold bias decreases from -0.067 K for all matches to -0.003 K for matches with high wind speeds. The RMS of the difference at the strong wind conditions is 0.298 K, within the expected SST precision (0.3 K) for which the ATSRs series were designed.

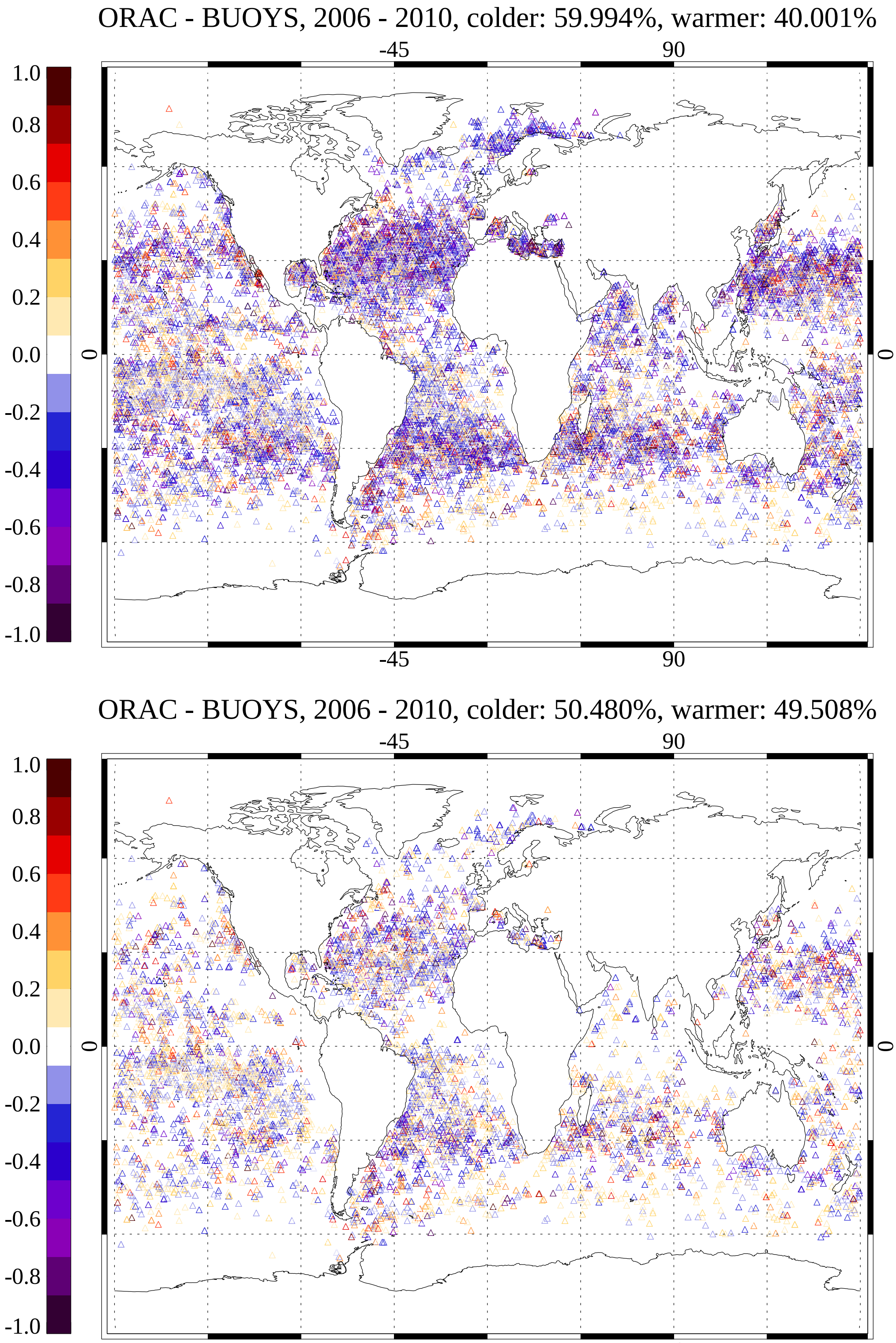

ORAC - BUOYS, 2006 - 2010, colder: 59.994%, warmer: 40.001%

ORAC - BUOYS, 2006 - 2010, colder: 50.480%, warmer: 49.508%

Figure 5.5: Global distribution of the differences between ORAC SST and BUOYS SST (ΔSST=ORAC$-$BUOYS) for January, 2006 to December, 2010. Top: matches with wind speeds ≥ 0 ms^{-1}; bottom: matches with wind speeds ≥ 6 ms^{-1}.

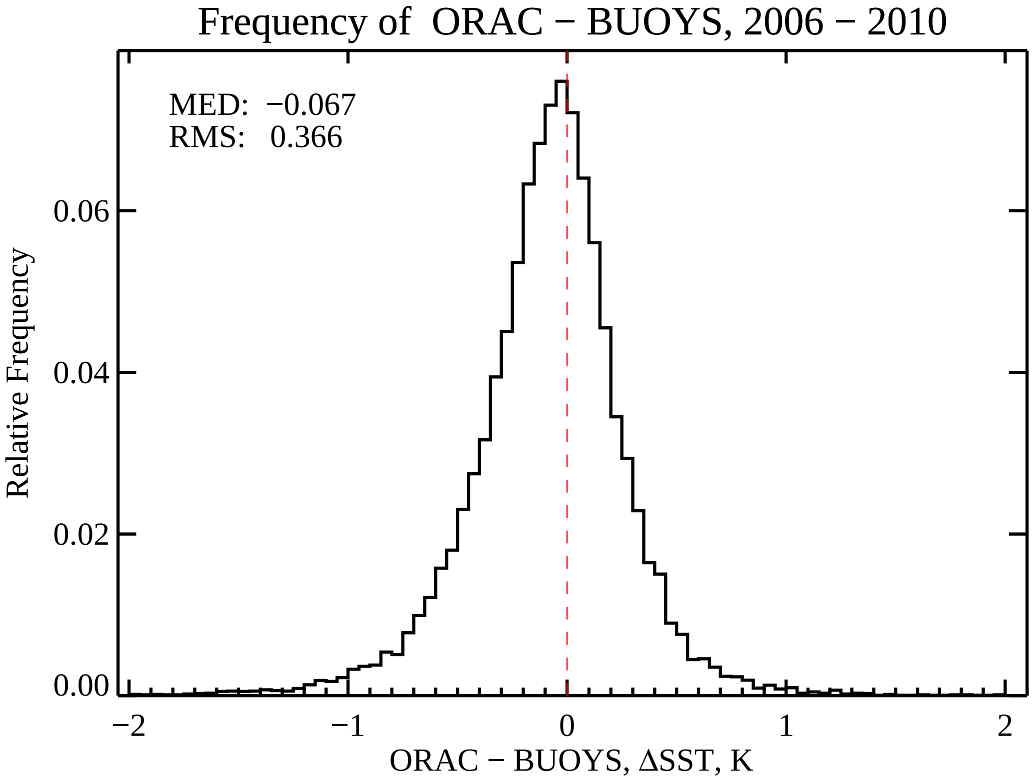

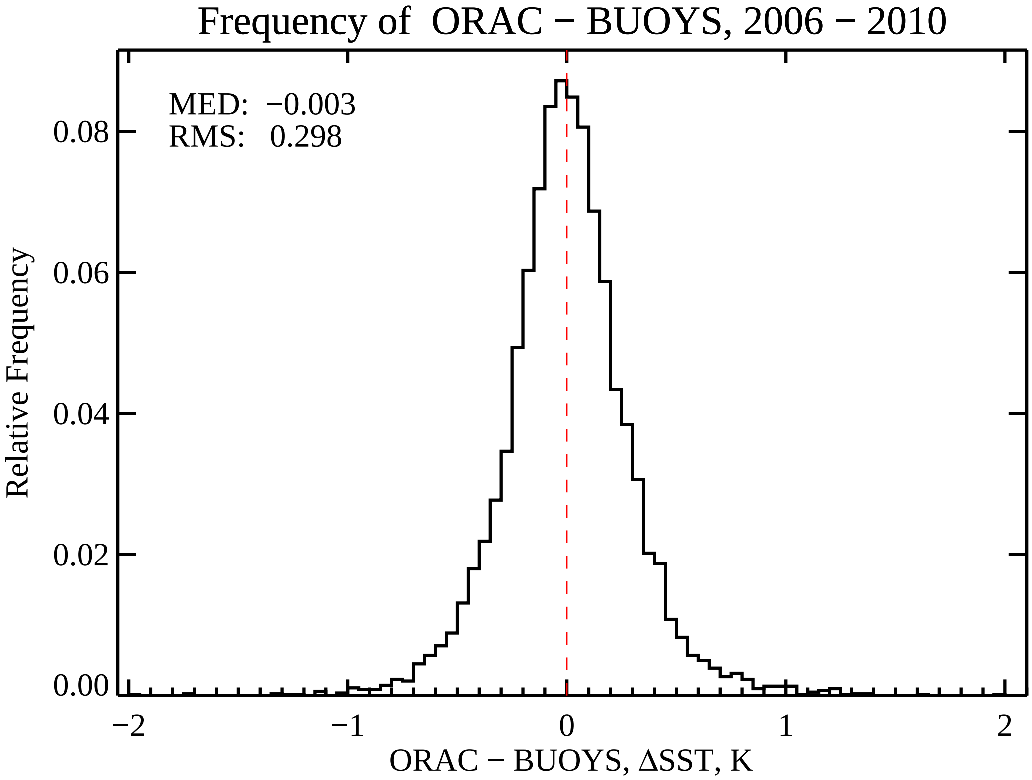

Figure 5.6: Frequency of the differences between ORAC SST and BUOYS SST (ΔSST=ORAC−BUOYS) from January, 2006 to December, 2010. Top: matches with wind speed ≥ 0 ms^{-1}, bottom: matches with wind speed ≥ 6 ms^{-1}.

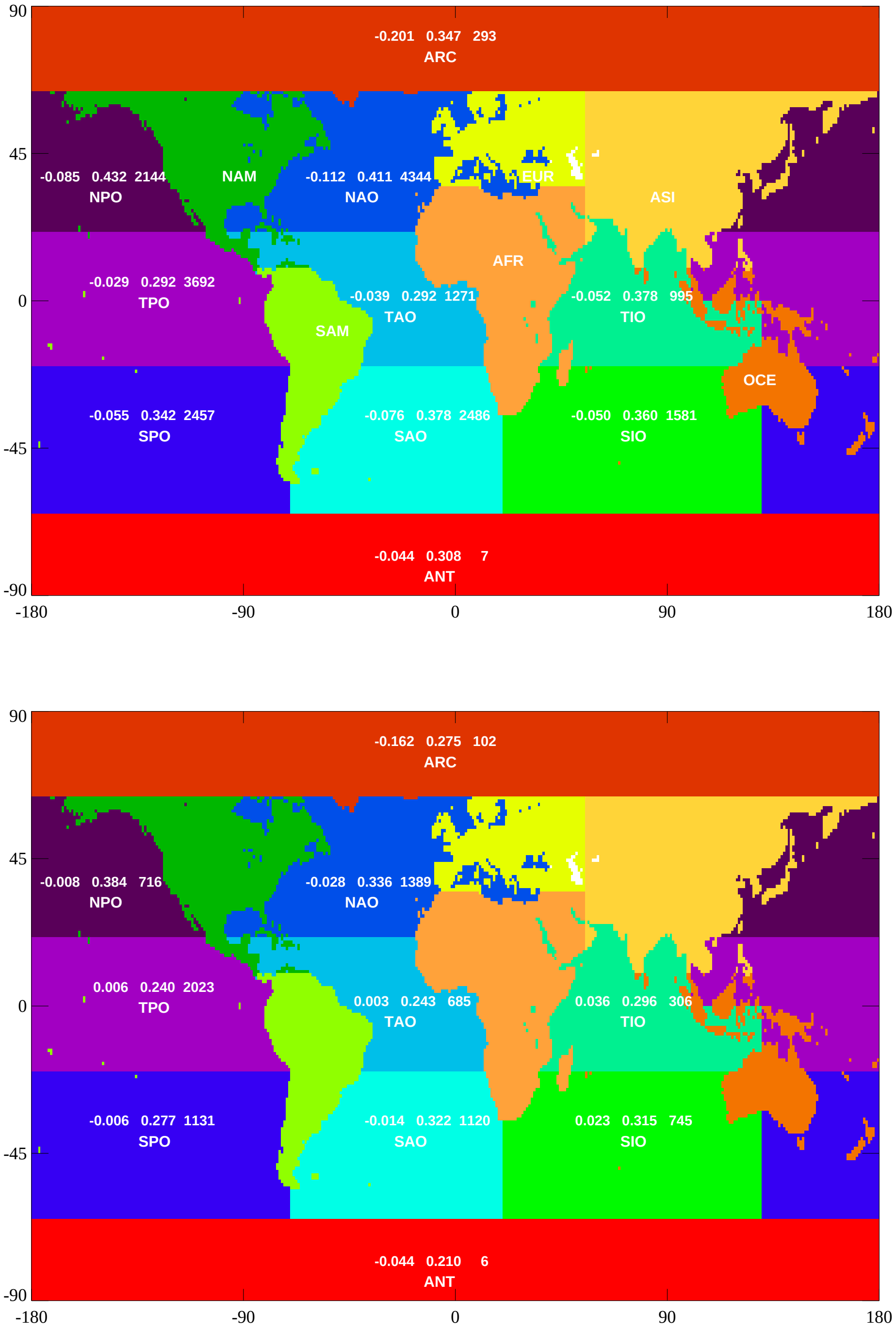

Figure 5.7: Regional statistics of the differences of SST (ΔSST=ORAC−BUOYS), the three numbers for each region correspond to median difference, RMS difference and number of matches. Top: matches with wind speeds ≥ 0 ms^{-1}, bottom: matches with wind speeds ≥ 6 ms^{-1}. The ocean regions are Arctic (ARC), northern Pacific ocean (NPO), northern Atlantic ocean (NAO), tropical Pacific ocean (TPO),tropical Atlantic ocean (TAO), tropical Indian ocean (NIO), southern Pacific ocean (SPO), southern Atlantic ocean (SAO), southern Indian ocean (SIO), and Antarctic (ANT).

Regional statistics for the differences between ORAC SST and BUOYS SST are shown in Figure 5.7, Figure 5.8 and Figure 5.9 for the five-year period. ORAC SST shows a small cold deviation from drifting buoys measurements (around ~ -0.1 K) with a relatively larger RMS (around ~ 0.4 K) for most of regions except for the Arctic area (-0.201 ± 0.347 K). The numbers of matches over the polar regions are small comparing with the other regions. After the matches with low wind speeds ($<$ 6 ms^{-1}) are filtered out, the ORAC SST bias of each region decreases significantly, indicating the influence of skin effect in the SST validation. The biases in northern Pacific ocean (NPO), tropical Pacific ocean (TPO), southern Pacific ocean (SPO) and tropical Atlantic ocean (TAO) are of the order of 0.001 K. Northern Atlantic ocean (NAO), NPO and tropical Indian ocean (TIO), which are influenced by outflow from continents, the RMS differences are larger compared to the other regions, while TPO and TAO have a small RMS of less than 0.3 K.

5.2.3 Discussions

5.2.3.1 Difference between bulk SST and skin SST: wind effect

The difference between bulk SST and skin SST is primarily decided by two factors: stratification formed by absorbing solar radiation and net heat flux from the sea to the atmosphere. The formation and strength of stratification are dependent on surface turbulence, which is closely related to the near surface wind stress. Donlon et al. (2002) give an empirical parameterization of the difference between bulk SST and skin SST as a function of wind speed (u) for the nighttime:

$$SST_{bulk} - SST_{skin} = 0.14 + 0.30 \exp(-u/3.7). \tag{5.1}$$

Equation 5.1 shows that the difference decreases as wind speed increases. Figure 5.10 gives the difference between ORAC SST and BUOYS SST (ΔSST=ORAC−BUOYS) versus wind speed. The wind speeds are concentrated in the range of 3 ms^{-1} to 10

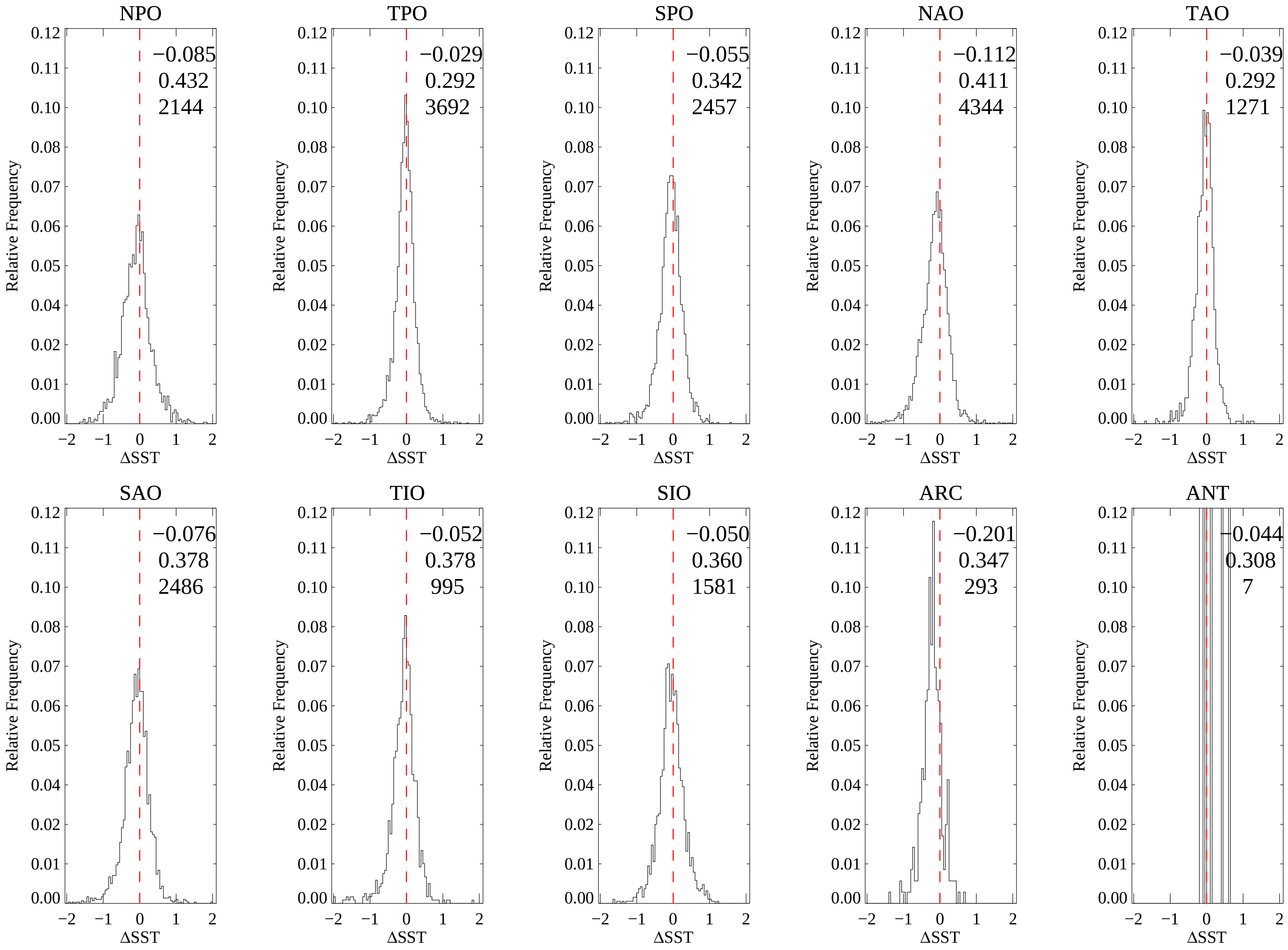

Figure 5.8: Regional histogram of biases in SST (ΔSST=ORAC−BUOYS) for pixels with wind speed ≥ 0 ms^{-1}, the three numbers for each region correspond to the median difference, RMS difference and number of matches, see the caption of Figure 5.7 for definition of acronyms for ocean regions

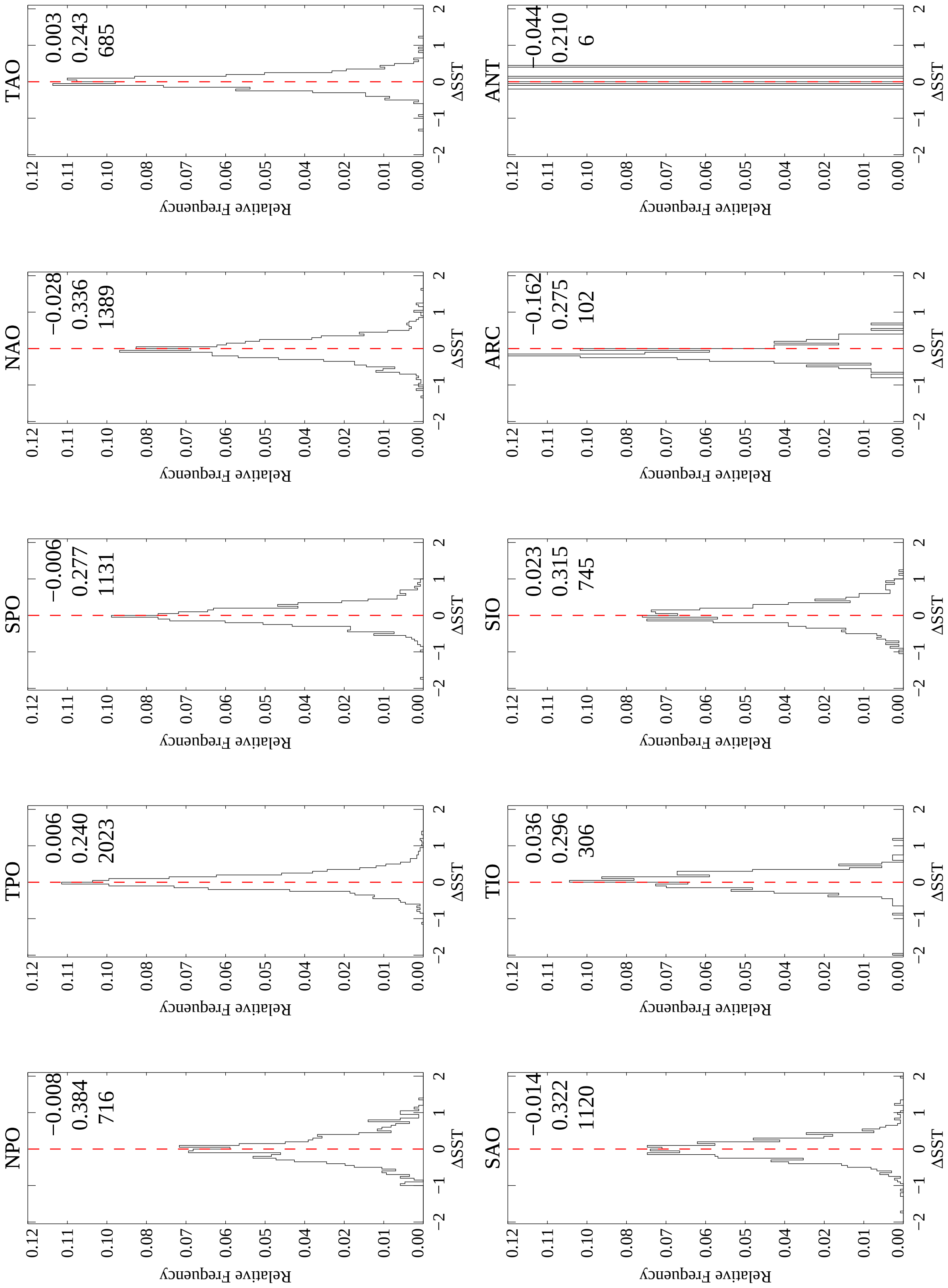

Figure 5.9: Same as Figure 5.8 but for matches with wind speed ≥ 6 ms^{-1}

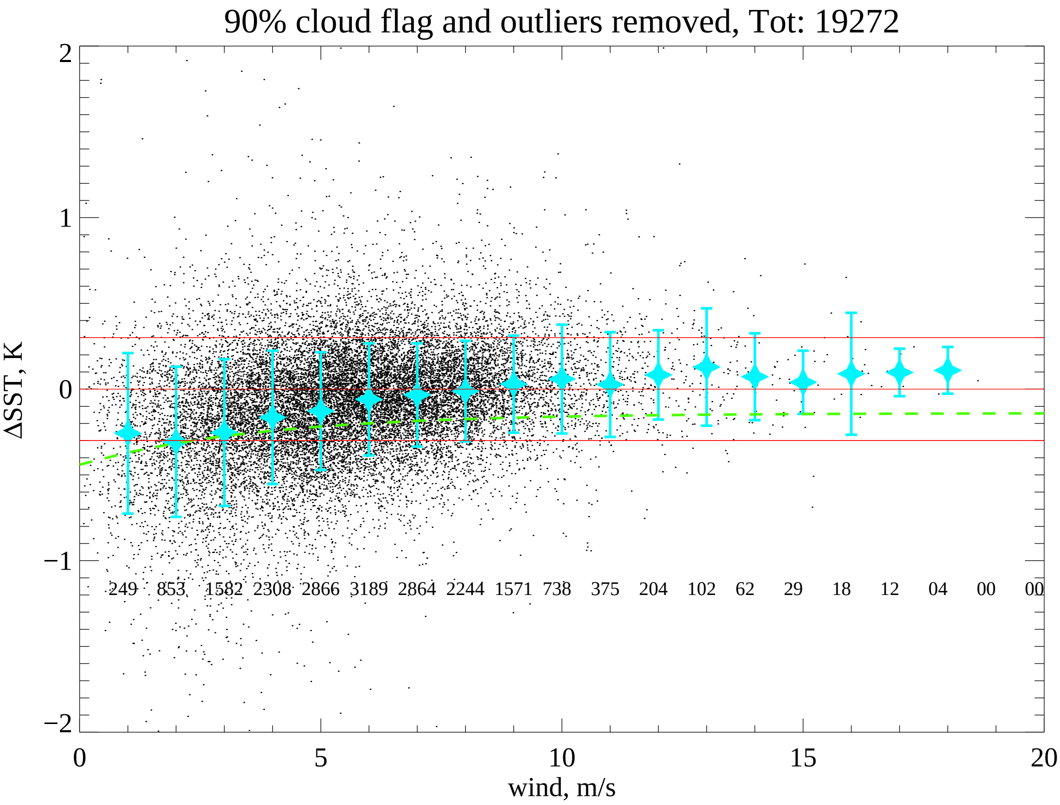

Figure 5.10: Difference between ORAC SST and BUOYS SST (ΔSST= ORAC−BUOYS) as a function of ECMWF 10 m wind speed (black dots). Data are also binned in order of ascending wind speeds with a bin size of 1 ms^{-1}, the blue stars indicate the medians of binned ΔSST, the error bars indicate the RMS on the bin-averaged ΔSST; the green dashed curve indicates the relationship between ΔSST and wind speed predicted in Equation 5.1. The aimed precision of satellite derived SST of 0.3 K is indicated by two red thin lines.

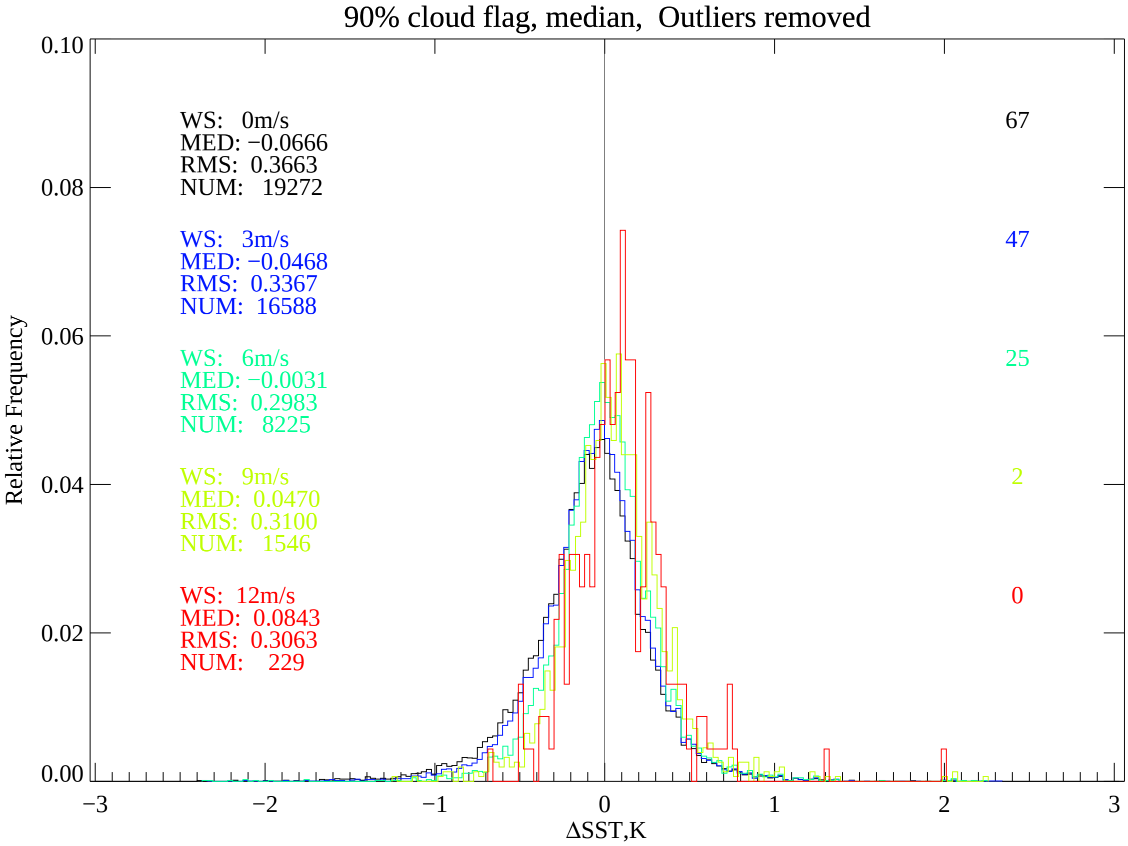

Figure 5.11: Histogram of difference between ORAC SST and BUOYS SST (ΔSST=ORAC−BUOYS) according to different wind speed thresholds. The coloured fonts at left are the statistical results of the difference using different wind speed thresholds. The coloured fonts at the right of the plot indicate the numbers of outliers that have been removed.

ms^{-1}. The cold bias existing at low wind regime (< 6 ms^{-1}) gets weaker as wind speed increases. This bias is close to zero (-0.0031 K) when wind speed reaches 6 ms^{-1} and the spread of the difference is 0.2983 K, close to the required SST precision. At the high wind speed regime, the bias becomes slightly positive, this positive bias is also indicated in Figure 5.7. This may be due to the limited number of data points, and the turbulence of the sea surface under strong wind conditions is quite complicated and difficult to model. The median bias is slightly warmer than that predicted by Equation 5.1 which was obtained from nighttime data, indicating a possible compensation to the skin effect from solar heating during the daytime. Figure 5.11 shows the histograms of ΔSST using different wind speed thresholds. It can be seen that the magnitude of the negative bias decreases with the wind speed threshold increases, and when wind speed is greater than 9 ms^{-1} the bias becomes positive; the RMS difference decreases from 0.3663 K to 0.2983 K as the wind speed threshold increases from 0 ms^{-1} to 6 ms^{-1}.

5.2.3.2 Match criteria

Match criteria used by a validation study should reduce the variability introduced by space-time separations between in situ and satellite observations, as well as provide sufficient matches for validation. The temporal and spatial match criteria used in this study are 3 hours and 10 km. Figure 5.12 shows the histograms and statistics of validations using 3 hours as the temporal criterion and four different spatial criteria, 10 km, 5 km, 2 km and 1 km. As the spatial criteria get more stringent, the cold bias in ORAC SST is more obvious and the RMS of the discrepancy is bigger. Keeping the spatial criterion as 10 km and reducing the temporal criteria from 3 hours to 2 hours, the number of matches is decreased by about 700. The bias is -0.065 ± 0.366 K (median ± RMS) for the 3-hour criterion, and is -0.057 ± 0.369K for the 2-hour criterion, it can be seen that changing time window from 3-hour to 2-hour makes little difference to the validation results. In this study, in each pair of the matches, the in situ data is taken as the median of buoys SST within the circular area with a radius of 10 km centred at the ORAC pixel. In stead of using a median, the other option is to use the buoys measurement which is the closest in distance to the ORAC pixel. This approach gives a median of -0.0675 K and a RMS of 0.3771 K.

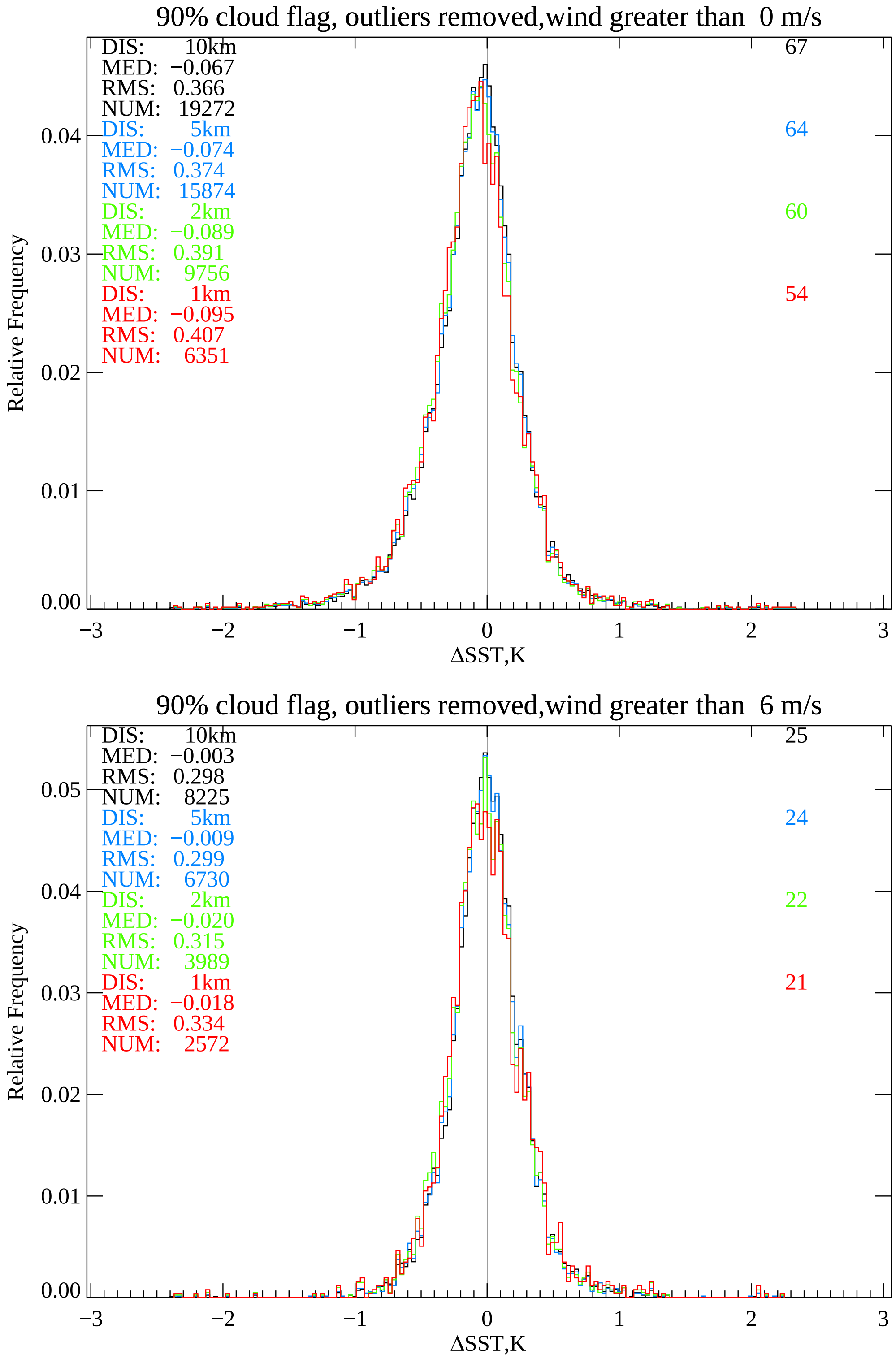

Figure 5.12: Histogram of difference between ORAC SST and BUOYS bulk SST. The coloured fonts at left of each plot indicate the statistics of the difference by using different spatial criteria. The coloured fonts at the right of the plot indicate the numbers of outliers that have been removed. Top: matches with wind speeds ≥ 0 ms^{-1}, bottom: matches with wind speeds ≥ 6 ms^{-1}.

5.2.3.3 Atmospheric aerosols and total column water vapour

As described in Section 1.2.3, aerosols can affect the SST retrieved from satellite measurements. Besides aerosols, water vapour absorption is also an important source of error in SST retrieval.

The difference between ORAC SST and BUOYS SST (ΔSST) is presented as a function of ORAC retrieved AOD in Figure 5.13. There is little systematic variation of the SST median difference with AOD, except for the high AOD conditions (AOD $\geq$ 0.5) where the number of data points becomes sparser. Figure 5.14 shows that ΔSST barely changes with total column water vapour. ORAC is an OE scheme that finds the best match between measurements and simulations by adjusting the contributions from different state parameters. The results are plausible in that the retrieved SST is not influenced significantly by the presence of aerosols or total column water vapour. However one can see from Figure 5.13 that most of the values of AOD used in this study are relatively low, further research is needed to investigate the accuracy of ORAC SST under high aerosol loading conditions.

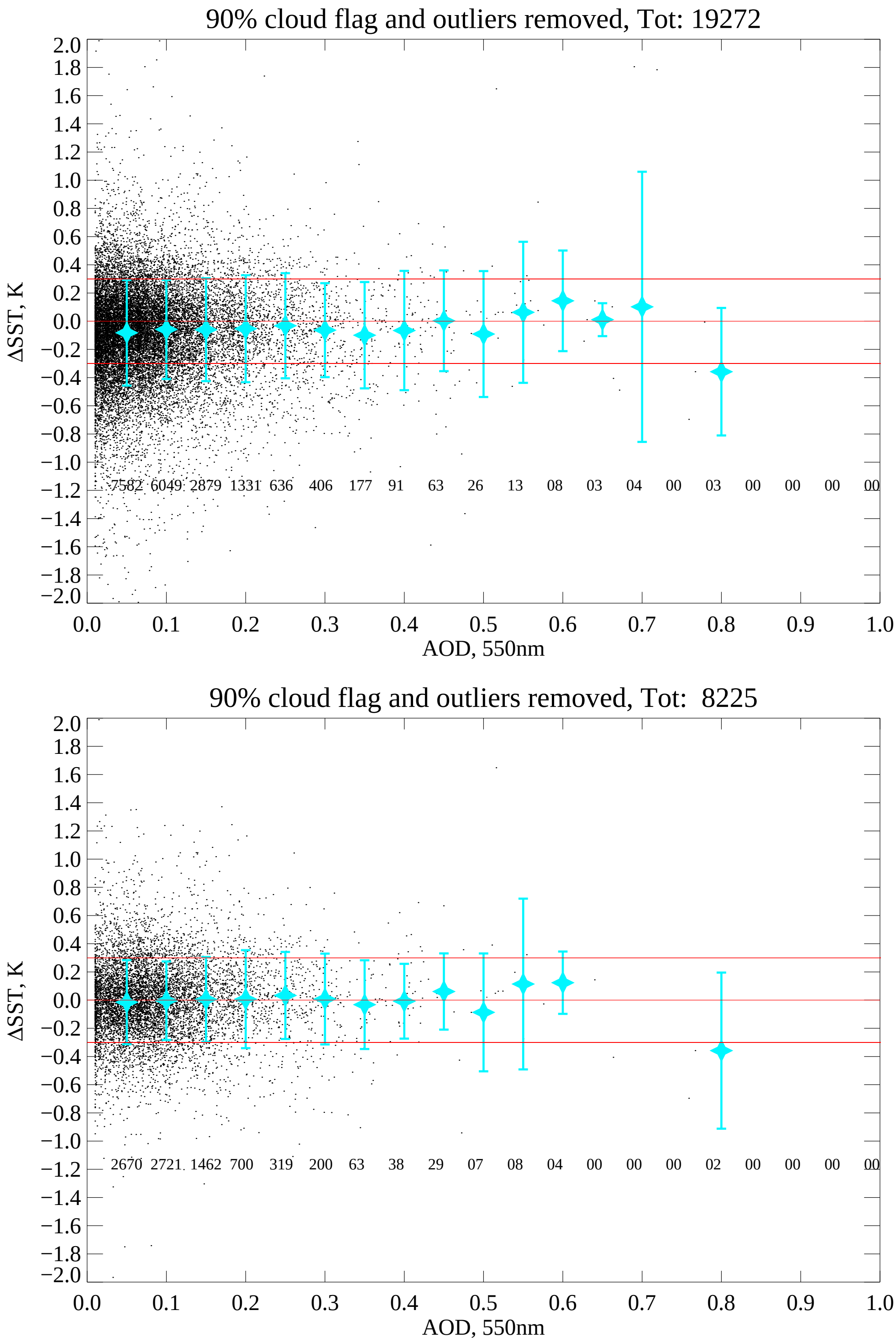

Figure 5.13: Difference between ORAC SST and BUOYS SST (ΔSST=ORAC−BUOYS) as a function of AOD at 550 nm (black dots). Data are also binned in order of ascending AOD with a bin size of 0.05, the blue stars indicate the medians of binned ΔSST, the error bars indicate the RMS on the bin-averaged ΔSST. The aimed precision of satellite derived SST of 0.3 K is indicated by two red thin lines. Top: matches with wind speed ≥ 0 ms^{-1}; bottom: matches with wind speed ≥ 6 ms^{-1}.

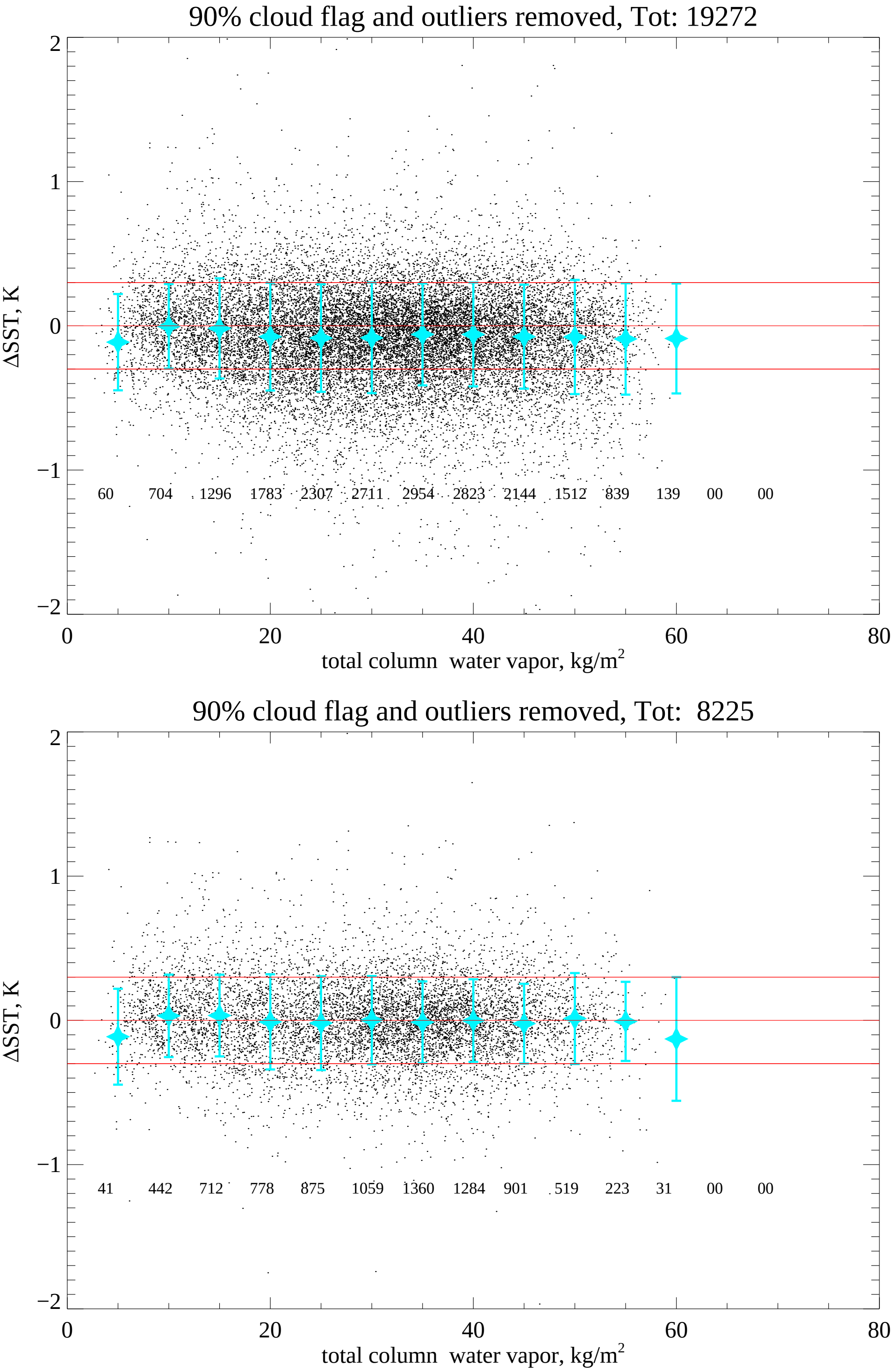

Figure 5.14: Same as Figure 5.13 but for total column water vapour.

5.3 Conclusions and discussions

In this chapter the SST derived by ORAC from AATSR has been validated with ship-based radiometer measurements and drifting buoys measurements.

The ship-based measurements have been obtained from the ISAR deployed on the Pride of Bilbao cruise ship which routinely travels between Portsmouth and Bilbao through the English channel and the Bay of Biscay. The validation pairs for ISAR and ORAC are constructed by choosing the closest ISAR data in distance to each ORAC data point within the temporal window and spatial window. During the period from February, 2006 to December, 2008, 427 validation pairs of ORAC and ISAR data are acquired within 10 km and 3 hours. The comparison shows a positive bias in ORAC SST of 0.150 K with a RMS of 0.481 K. Using more stringent criteria for the spatial window and the temporal window, 1 km and 2 hours, 221 pairs of matches are found and the bias in ORAC SST is 0.117 ± 0.492 K. Then, using 1 km and 1 hour as the spatial window and temporal window, the number of matches decreases to 117 and the bias in ORAC SST becomes 0.117 ± 0.430 K. The validation results between AATSR operational D2 product and ISAR are also given. Comparing with the performance of the D2 product (0.000 ± 0.324 K for 1 km and 1 hour), the ORAC SST needs further improvements. ISAR SST algorithm assumes sea surface emissivity is a constant (0.9916). ORAC calculates sea surface emissivity as a function of many variables and is generally lower than 0.9916. As suggested in Chapter 3 emissivity is one of the important impactors of the retrieved SST and 1 % difference can cause a difference in SST of the order of 0.1 K , one would expect that the systematic reduced emissivity leads to an overestimate of SST. The next step of validation would be set the ORAC emissivity to be the same as ISAR to test the influence of emissivity on retrieved SST under real atmospheric/surface conditions.

Validation of ORAC SST against the drifting buoys measurements provided by the SST CCI project indicates an excellent performance of ORAC in the retrieval of SST. The difference between ORAC SST and drifting buoys SST is -0.067 ± 0.366

K for all the matches. In order to minimize the skin effect, the matches are classified using wind speed threshold (≥ 6 ms^{-1}). Under high wind speed conditions the bias of ORAC SST can be improved to be -0.003 ± 0.298 K. The statistics of regional validations also show a good performance of ORAC SST, especially over the tropical oceans where RMSs are less than 0.3 K for high wind speeds. From the study carried out in Chapter 3, the calibration error in the 12 μm channel is an important source of bias in the SST. In this validation 12 μm measurements have been adjusted by adding 0.2 K, the adjustment is a likely explanation for the retrieved SST accuracy is not biased significantly by the calibration error in the measurements. Water vapour and temperature profile are also important sources of SST uncertainties, one can expect the coarse spatial resolution of the ECMWF atmospheric data would be a potential source of SST bias. However, as shown in Figure 3.20 and confirmed in the validation results, the uncertainties in the auxiliary data or *a priori* used by the retrieval can be translated into errors in SST and may offset each other to some extent, resulting a relatively low overall error.

It should be noticed that the wind speed threshold (≥ 6 ms^{-1}) used here is regressed from nighttime data by Donlon et al. (2002), during the daytime solar heating may also cause thermal stratification of the upper ocean which can be broken as the wind speed increases. According to Embury et al. (2012a) the difference between skin SST and bulk SST is almost independent on wind speed when wind speeds are greater than 3 ms^{-1}, it is reasonable to assume that at higher a wind speed regime the effect introduced by solar heating is at a minimum. In the future it would be useful to correct the daytime skin effect using a model provided by Met office. The model is based on Fairall et al. (1996) method in which the effects of solar heating and wind are considered. Another noteworthy feature of the regional validation is the relatively larger RMSs over the northern oceans. The effects of wind speed, match criteria, aerosols and total column water content on the validation results are discussed. The understanding of such effects can aid the interpretation of the algorithm performance.

The validation results reveal that the new ORAC can retrieve SST to a good degree of accuracy under low AOD conditions. It is necessary to examine the performance of the algorithm under heavy aerosol loading conditions, for example dust plumes from continents. However, since the cloud flag may mistake pixels with heavy aerosols as cloudy and miss important aerosol events, it is necessary to improve the cloud flag (or other flags, like dust flag) by adding more measurements to provide better spectral characterisation of the atmosphere. The validation of SST with heavy aerosol loadings will still be constrained by the narrow swath (512 km) and long repeat cycle (3 days) of AATSR. Because some events with heavy aerosols have a relatively short lifetime, AATSR may not able to sample sufficiently, implying the performance of retrieval can be benefited through widening sensor swath.

Chapter 6

Application of GlobAEROSOL data

The surface-leaving radiance can be attenuated by aerosols through scattering and absorption, one of the objectives of the new ORAC is to eliminate aerosol contamination on the satellite derived SST. As shown in Chapter 5, the accuracy of derived SST is not severely sensitive to aerosols when AOD is low, it is worthwhile to examine the retrieval performance under high aerosol loading conditions. High aerosol loading over ocean can be caused by transportation from continents or generation of marine aerosols. It has been shown that wind speed is a major driver behind the aerosol production over ocean, therefore it is useful to understand how marine aerosol loading reacts to wind speed.

6.1 Introduction

Marine aerosol constitutes one of the largest natural aerosol systems and plays an important role in the Earth's radiative budget. It comprises two distinct aerosol types: I) primary sea salt aerosol, and II) secondary sulphate aerosol. Many studies show that sea salt particles make a significant contribution to both submicron and supermicron maritime aerosol modes (Gras and Ayers, 1983; Hoppel et al., 1990; Fitzgerald, 1991; O'Dowd et al., 2001; Heintzenberg et al., 2003; Clarke et al., 2003). The major sources of sea salt aerosol are the bursting of bubbles formed primarily by breaking waves and mechanical disruption of wave crests by the wind (Exton et al., 1985; Andreas, 1998; O'Dowd and Leeuw, 2007). Marine aerosol influences the radiative budget both directly and indirectly. These particles are the main contributors to light scattering in the cloud-free atmosphere in those regions with marine atmosphere. They also participate in cloud processes, serving as the dominant cloud condensation nuclei (CCN) source over the remote oceanic regions (Latham and Smith, 1990; Hegg, 1992; Ghan et al., 1998; Lohmann and Feichter, 2005; Satheesha and Moorthy, 2005). Therefore elucidating the background sea salt aerosol is important to understand the atmospheric radiative budget.

The effects of wind on aerosol properties over the oceans have been studied, but mostly focused on the aerosol concentration and size distribution. Definite correlation has been found between surface wind speed and sea salt aerosol concentration (McDonald et al., 1982; O'Dowd and Smith, 1993; Nilsson et al., 2001). The influence of wind speed on marine AOD (τ) is a much more difficult problem (Platt and Patterson, 1986; Villevalde et al., 1994; Smirnov et al., 1995; Moorthy et al., 1997). The link between marine AOD and wind speed is difficult to quantify because it can be masked by long-range transport from land based sources. Thus, selecting oceanic regions with no influence of long-range transportation is important for studying such a relationship. Moorthy and Satheesh (2000) found an exponential increase in daily averaged AOD with wind speed at Minicoy in Arabian Sea. However, the region in that study is close to the land, it cannot be considered as a pristine marine environment. Making use of AOD derived from MODIS and wind from NECP, Satheesh and Srinivasan (2006) examined the contribution of sea salt to composite AOD over different regions of the Arabian Sea and found the contribution of sea salt varies with season and latitude. Based on long term (1988-2005) aerosol data from AVHRR, Mishchenko and Geogdzhayev (2007) found a downward trend of global aerosol loading which was consistent with ground based observation, though an increasing trend of AOD was also observed in the region of 40° S - 60° S. They indicated a positive correlation between the AOD and the wind speed, and also hinted that the correlation might not be very reliable due to the constant wind speed used in their aerosol retrieval algorithm. Mulcahy et al. (2008) obtained a power-law relationship at four different wavelengths at Mace Head, located on the west coast of Ireland. This site is also cannot be considered as representative of the remote ocean.

Based on one month of AOD data from the Sea-viewing Wide Field-of-view Sensor (SeaWiFS) and 10 meter wind data from ECMWF, Glantz et al. (2009) found a power-law relationship between wind speed and AOD over the north Pacific. However in their study, a constant surface reflectance was used in the retrieval of AOD from SeaWiFS. The increased reflectance of the ocean due to increased surface roughness and white caps generated by enhanced wind could not be ruled out effectively.

Though many studies have been performed, there is still no consensus on the relationship between wind speed and observed AOD. Additionally, all of the previous studies were from different locations using different instruments and also in different time-periods. Hence a direct comparison between those results is difficult to make and it is hard to extrapolate the results to other areas. Also, some locations where the experiments were carried out are close to continents. In this chapter, we first determine which oceanic areas can be taken as remote ocean based on the wind direction and AOD, and then investigate the relationship between AOD and wind speed over these regions, where the influence of continental aerosol can be considered minimal. The chapter is organized as follows: In Section 6.2, we briefly explain the data and the instruments used. A quantitative method to distinguish remote oceanic regions from areas influenced by continental outflow is introduced in Section 6.3. Preliminary results and simple discussion are presented in Section 6.4. Concluding remarks are given in Section 6.5.

6.2 Data

The AOD used in the chapter is at the wavelength of 0.55 μm, daily for the whole year of 2004 from GlobAEROSOL AATSR product. GlobAEROSOL provides AOD at 0.55 μm and 0.87 μm on a 10×10 km sinusoidal grid. The data has been regridded onto the $1 \times 1^\circ$ dataset which is used in the chapter. Chapter 4 shows GlobAEROSOL has a positive positive bias of 0.076 while Portela et al. (2009) obtains a bias of 0.056. Although these results are only for land based or coastal AERONET stations, and thus may not be directly applicable to the remote ocean, it does suggest that the GlobAEROSOL AATSR product has a positive bias in its AOD values. However, since the bias appears to be relatively independent of AOD (Portela et al., 2009), it should have a limited impact on the observed AOD and wind speed relationship. A possible reason for the possible bias in the AATSR AOD is contamination by residual cloud. Although the AATSR cloud mask is considered quite stringent, it is possible that thin cirrus, which is now believed to be very common (Baran, 2009) , might not be removed. This could cause a small, consistent offset in the observed AOD.

The wind data used in this chapter is 10 meter wind from European Centre for Medium-Range Weather Forecasts (ECMWF), at the same temporal and spatial resolutions as the AOD data. The ECMWF wind is generated four times per day with a time interval of six hours. Wind fields have been interpolated to Envisat nominal overpass time by using the two time slots which are the nearest to the ENVISAT overpass time. The life time of marine aerosol in the marine boundary layer (MBL) is within a range of hours to days, so the error introduced by this coarse temporal resolution should be minimal.

Based on zonal (u) and meridional (v) wind components given by ECMWF, the wind speed (s) is calculated: $s = \sqrt{u^2 + v^2}$ and wind direction is defined as shown in Figure 6.1a.

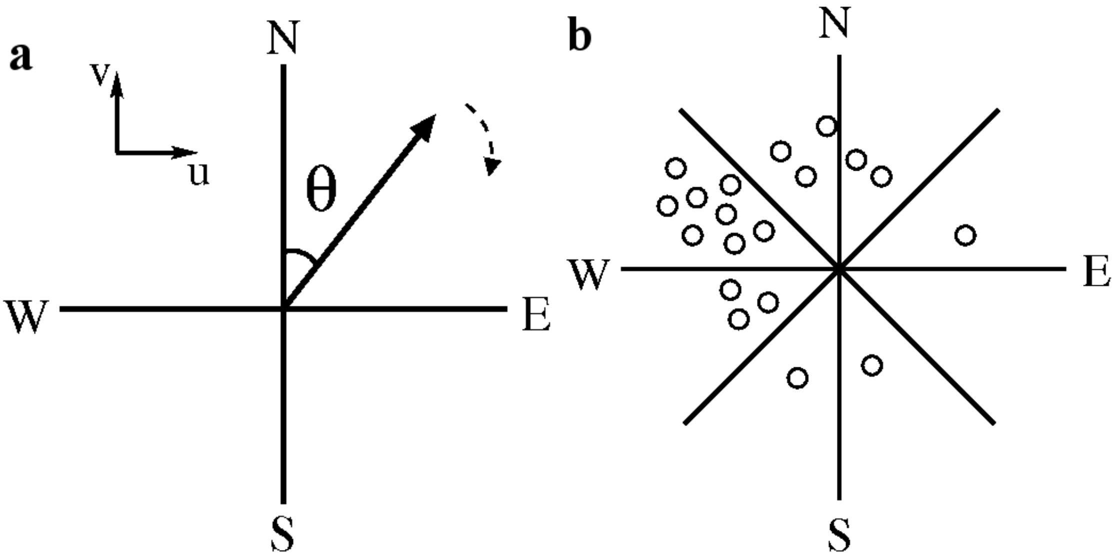

Figure 6.1: a). Definition of wind direction. b). AOD (indicated by the circles) are categorized by wind directions.

6.3 Method

To get a clear understanding of the relationship between wind speed and AOD, the first step is to define the remote oceanic regions. A heuristic argument can be made that, for truly remote oceanic regions, the only aerosol source is the ocean and thus the AOD (τ) should not strongly depend on wind direction but only on wind speed and other parameters such as temperature and relative humidity. For each $1 \times 1°$ grid cell in the global ocean, the wind direction ranges from 0° to 359° as shown in Figure 6.1a. The wind directions are divided into 36 bins with an interval of 10°. The daily τ data are sorted into different bins according to the corresponding daily wind directions. Figure 6.1b illustrates a simple example with only 8 bins chosen. We then calculate the average value (τ_{av}) of τ in each bin and the standard deviation of τ_{av} over all wind direction bins, $\sigma_{\tau_{av}}$. The value of $\sigma_{\tau_{av}}$ indicates the dependence of τ on wind direction. If $\sigma_{\tau_{av}}$ is large, the τ at the this point changes markedly as wind direction changes, indicating that a possible external source of aerosol exists. On the other hand, if the $\sigma_{\tau_{av}}$ is small, the τ shows no or weak dependence on wind direction, indicating that the corresponding area is a possible pristine oceanic candidate. This is shown stylistically in Figure 6.2.

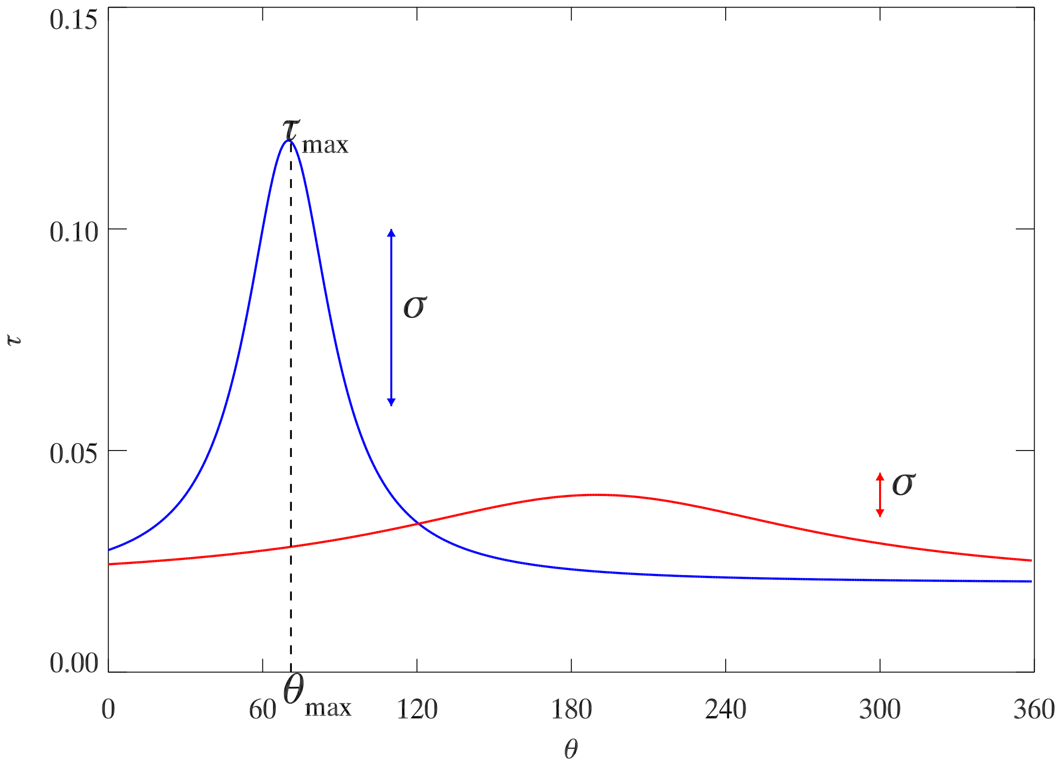

Figure 6.2: For each 1° × 1° point, the τ is expressed as a function of wind direction. The blue curve represents the case where τ depends strongly on wind direction and so has a large σ_τ. The red curve represents the case where τ does not depend on wind direction and so has a small σ_τ. The τ_{max} shows the wind direction in which the τ has the largest value.

The histogram of $\sigma_{\tau_{av}}$ for all global oceanic points is plotted in Figure 6.3. The main peak in Figure 6.3 is interpreted as the typical variability of τ as a function of direction. The large tail of high variability denotes aerosol being transported from preferred directions. To differentiate locations with typical τ, from those demonstrating a preferred direction we have used a threshold, $\sigma_{\tau_{av}^{\mathrm{th}}}$, of about 2/3 of the peak values (i.e. a value of 0.035). For any point, if $\sigma_{\tau_{av}} \geq \sigma_{\tau_{av}^{\mathrm{th}}}$, it implies there are possible external aerosol sources other than the ocean itself: we take this type of points to be candidates of non-remote ocean. For these points, the corresponding preferred wind direction θ_{max} is found where the τ_{av} is maximum.

A global map of $\theta_{\max}$ is shown in Figure 6.4. If the direction in indicated by $\theta_{\max}$ includes an obvious source of non-maritime aerosol, then that location is taken to be non-remote ocean. It should be noted that some regions are dominated by winds from a single direction, or where the wind speed is strongly correlated with its direction. In such regions there is a strong relationship between τ and wind direction, even if there is no non-maritime aerosol source. Thus, if a region has a $\theta_{\max}$ value which doesn't indicate a non-maritime aerosol source, it can still be considered to meet the remote-ocean criteria.

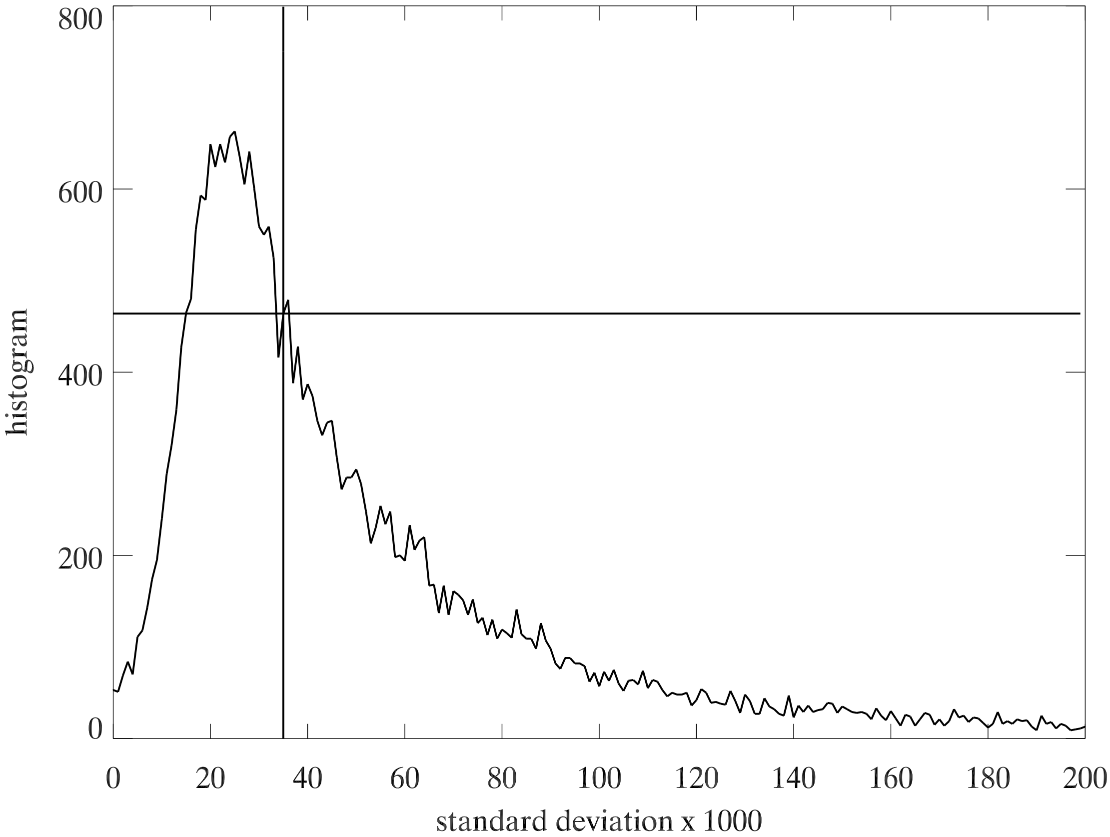

Figure 6.3: Histogram of $\sigma_{\tau_{av}}$ for global ocean, the cross point of black vertical and horizontal lines represents the chosen threshold:0.035

6.4 Results and discussions

6.4.1 Results

The Figure 6.4 indicates the source direction of transported aerosol for these points. This map roughly matches the large-scale flow field and storm tracks. For the mid-latitude ocean (30° N - 60° N) of the northern hemisphere, enhanced aerosol loading occurs with the wind direction is westerly, taking heavy-industry pollutants from East Asia and North America.

For the tropical and sub-tropical Atlantic regions, it is obvious that North Africa is the main source of aerosol for its surrounding areas. Over the sub-tropical and tropical Atlantic ocean, the $\theta_{\max}$ matches the direction of trade winds that transport dust from the Sahara. Over the year, the AATSR observes the highest aerosol loading over the Persian Gulf, where wind comes from the southwest. For the points locating in the east central Pacific, the τ is maximum with an east wind, indicating that the large values of τ of these points probably relate to long-range transport aerosol from biomass burning in South America or dust from Sahara. Over the west central Pacific, as well as the southern China sea, the τ is largest when wind comes from a roughly northerly direction. This could be related to sand storms in northern China and Mongolia.

Over the southern oceans (between 30° S -60° S), the largest τ occurs when wind directions in a range of 70° to 140° (see Figure 6.1a), i.e. westerlies. Strong westerly winds are almost ubiquitous in the southern oceans which causes the dependence of τ on s, rather than a particular source of transported aerosol. Indeed, as there are no large continents in this region, it can be thought of as a remote oceanic region with little influence from continents.

From Figure 6.4, many regions, especially in the northern hemisphere, cannot be regarded as pure remote oceans. This interpretation is supported by the carbon

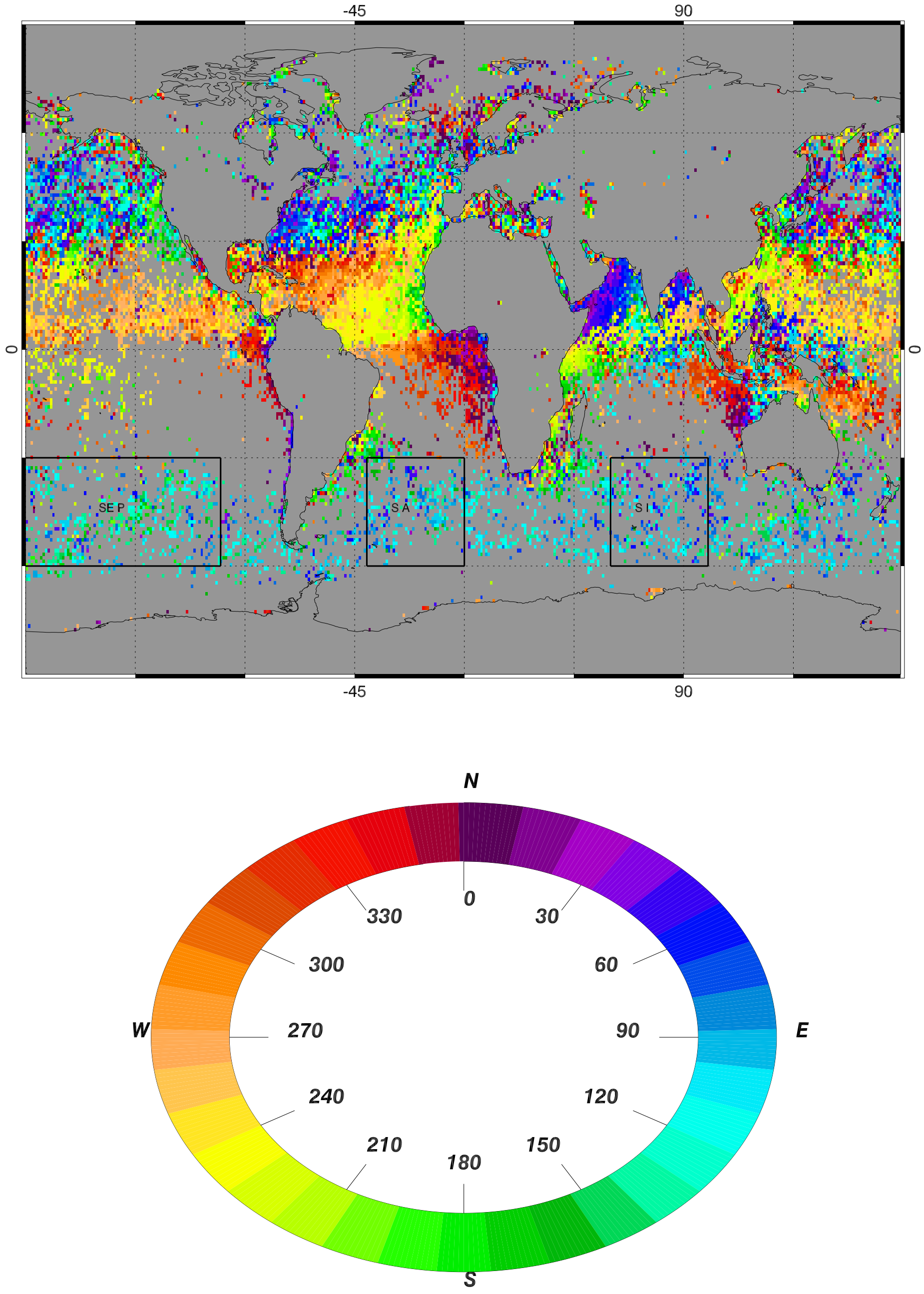

Figure 6.4: The preferred wind direction $\theta_{\max}$ for the locations where σ_τ is greater than 0.035.

monoxide (CO) distribution map from Measurements Of Pollution In The Troposphere (MOPITT), shown in Figure 6.5. The two main sources for CO are industrial pollution and biomass burning (Sanderson, 2002; Singer, 1975). Although CO has a longer life time than aerosol, and thus cannot be taken as a proxy for aerosol, its distribution can provide a "worst case" indication of the regions which could be subject to long range aerosol transport. The high CO in the northern hemisphere indicates that those regions may be influenced by long distance transportation from land, while the regions between 30° S - 60° S have relatively low CO concentrations. Experiments in regions showing evidence of influence of transport from continental sources aimed at measuring aerosol properties over remote ocean could lead to unreliable results.

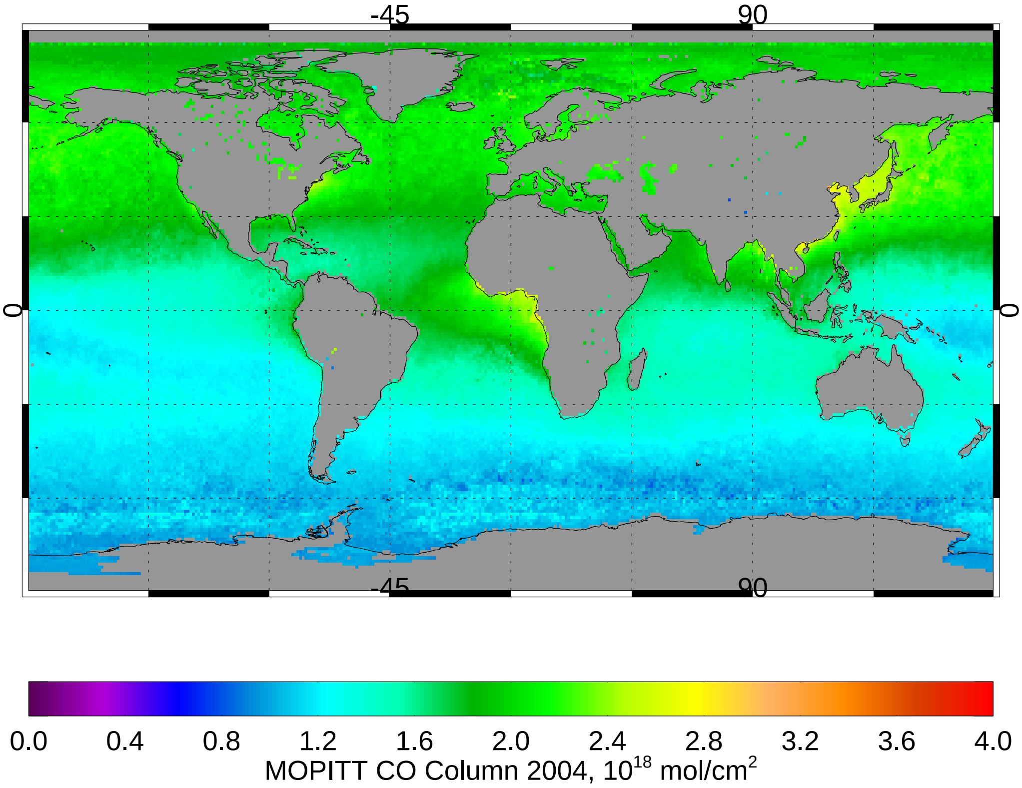

Figure 6.5: Column CO distribution, MOPITT, 2004

Based on this analysis, we choose remote ocean points over three regions, shown as black frames in Figure 6.4. Since they suffer less influence from continents, the loading aerosol for these regions are free from contamination by long-range transported aerosol and it is possible to establish a link between marine τ and wind speed. The relationships between wind speed and τ for these three regions are plotted in Figure 6.6, Figure 6.7 and Figure 6.8. The error bar in the plots is the standard deviation of AOD in each wind interval (0.5 ms^{-1}). All plots show a similar relationship between wind speed and AOD, which is largely linear up to $s = 20$ ms^{-1}. The AOD is observed to increase by around 0.1 over a wind speed range of 4 to 20 ms^{-1}. We interpret this significant increase to the enhanced contribution of sea salt particles. Importantly, there is no indication that an exponential function is a better fit to the measurements than a straight line. A linear curve (green line) and an exponential curve (red line) are fitted to the data. Figure 6.9 shows the averaged relationship among the three regions. The linear fit to these data (green line) yields the equation:

$$\tau = (0.0850 \pm 0.0002) + (0.0040 \pm 0.0002) \times s$$

This result is different from (Mulcahy et al., 2008) and (Glantz et al., 2009), which are taken from the northern Pacific and northern Atlantic respectively, but is very similar to the results of (Smirnov et al., 2003) and (Jennings et al., 2003), which were taken from Midway Island and Tahiti, which are largely thought to be remote ocean due to their long distances from the mainland. The same analysis has also been performed on the data of 2003 and was in agreement with the 2004 results presented here.

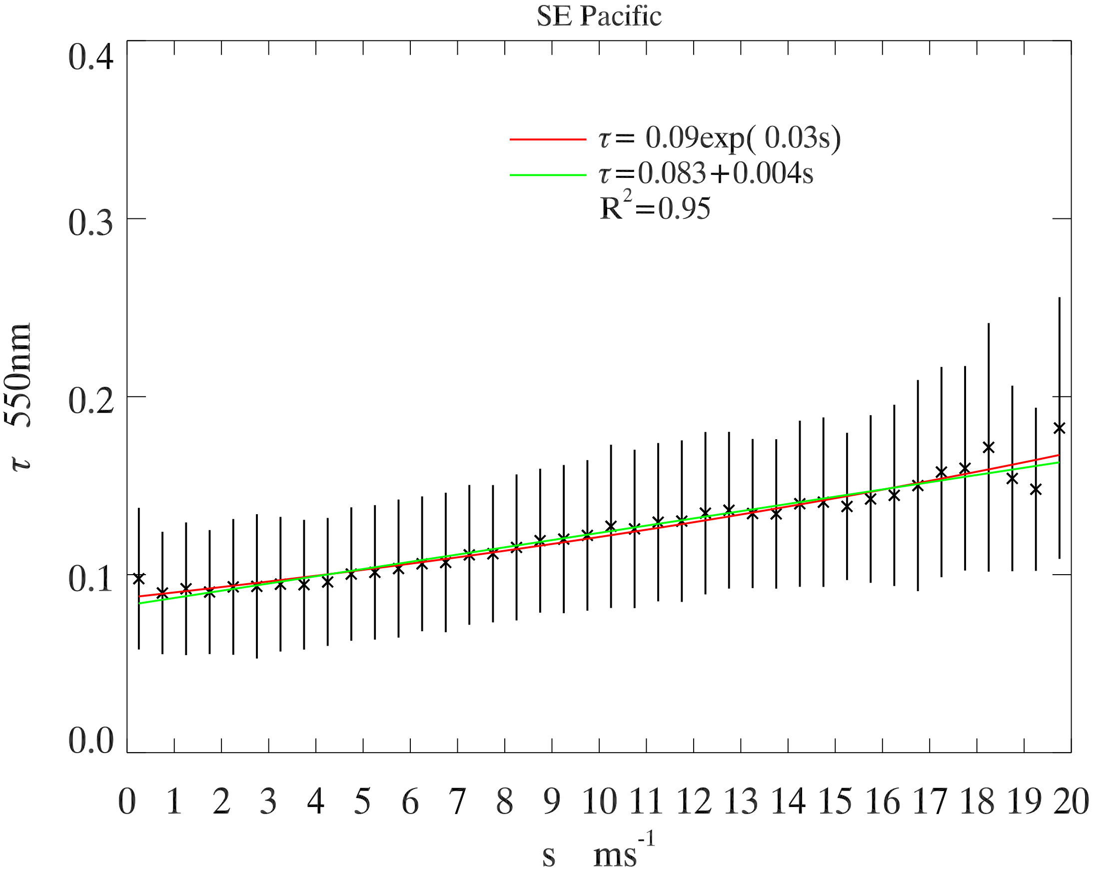

Figure 6.6: Relationship between wind speed s and AOD τ over the South East Pacific. The R^2 in the plot is the linear correlation coefficient between wind speed s and AOD τ

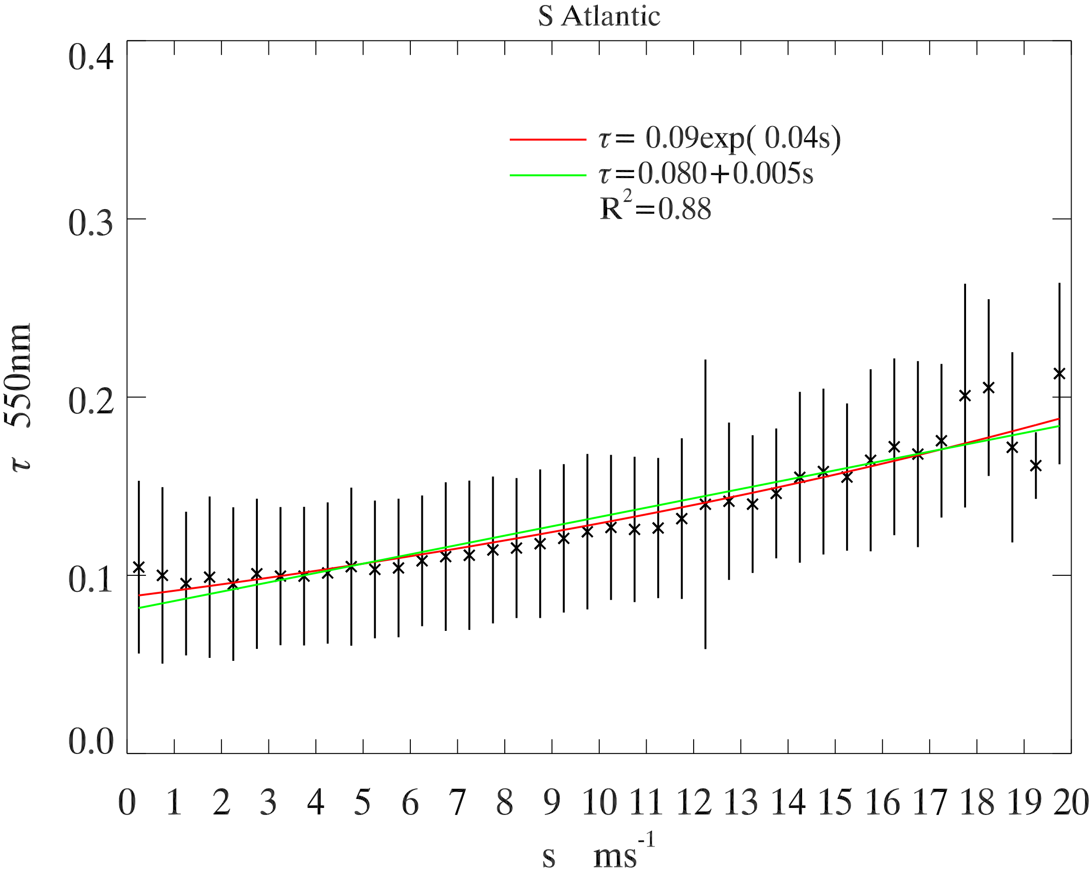

Figure 6.7: Relationship between wind speed s and AOD τ over the South Atlantic.

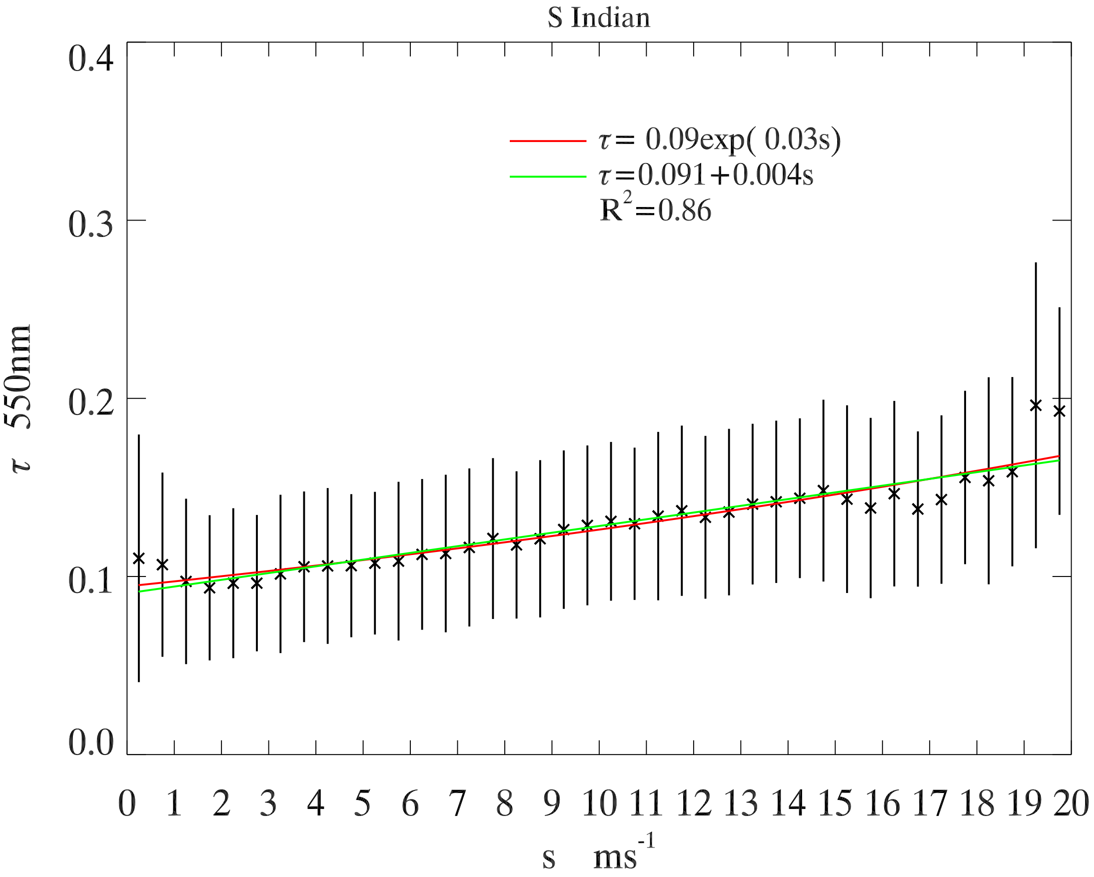

Figure 6.8: Relationship between wind speed s and AOD τ over the South Indian.

6.4.2 Discussions

We interpret the enhanced AOD at higher wind speed as a consequence of heavy marine aerosol production introduced by wind. The size distribution of sea salt moves towards the coarse mode as the wind speed increases. Such increase in the number of large particles would result in an increased extinction efficiency at longer wavelengths. Thus, theoretically, one might expect the relationship between wind speed and AOD to be stronger at longer wavelengths.

We have examined the relationship between wind speed and the AOD at 0.87μm. The results obtained are similar to the results of 0.55μm channel presented in the chapter. It is difficult to explain why the GlobAEROSOL results do not show a

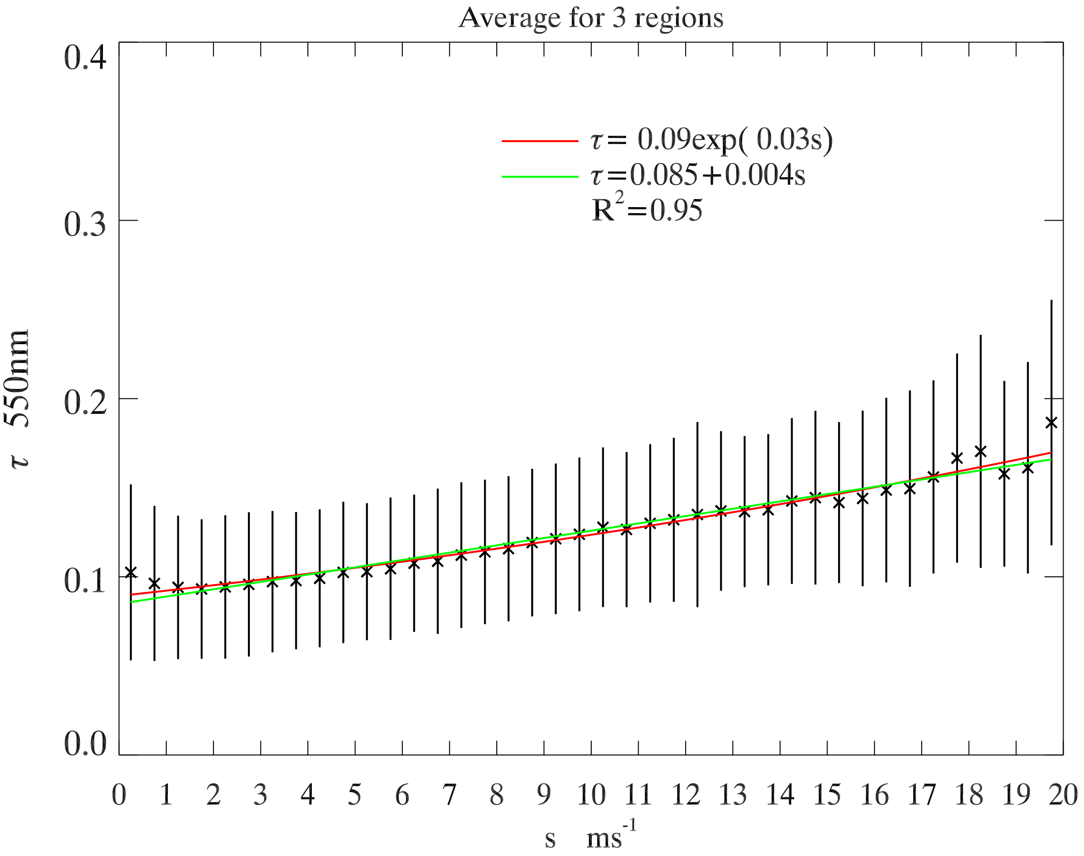

Figure 6.9: Relationship between wind speed s and AOD τ over the three regions. over the three regions

stronger AOD dependence on wind speed at longer wavelengths. Possible explanations include deficiencies in the assumed properties (refractive index and size distribution) of the OPAC aerosol class used in the retrieval or the increase in average particle size with increasing wind speed is not significant enough to be apparent in these results.

It should be noted that the values of AOD low wind speeds shown in this chapter are somewhat larger than have been found for marine by other authors (Mulcahy et al., 2008; Glantz et al., 2009).

In order to test the AOD at low wind speeds, we calculate the clean marine AOD at different wind speeds theoretically. The model used is OPAC (Optical Properties of Aerosols and Clouds) software package. In the marine boundary layer, the aerosol optical properties is dependent on the number concentration (NC), size distribution of

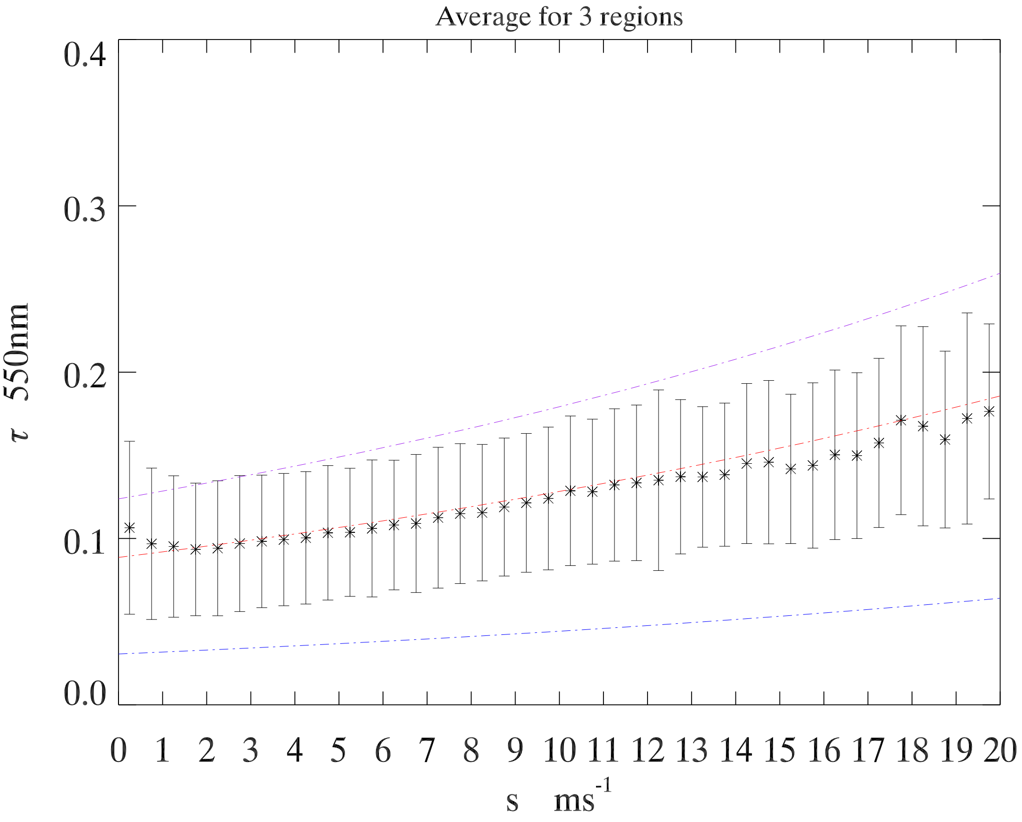

Figure 6.10: The relationship between wind speed s and AOD τ at RH 80%, the black crosses are the averaged result for three regions as shown in Figure 6.9, the three dash lines are the OPAC modelled result using different values of N_0 of sea salt, purple: 30 cm^{-3}, close to the upper limit of sea salt number concentration; red: 20 cm^{-3}, the default value of sea salt number concentration given OPAC; blue: 3.5 cm^{-3}, closed to the lower limit of sea salt number concentration.

the particles and ambient relative humidity (RH). According to Lewis and Schwartz (2004), the typical RH of the ocean is around 80%, and ECMWF RH data are consistent with this. In OPAC, marine clean aerosol is composed of three compositions: water soluble sulfate, fine mode sea salt, and rare coarse mode sea salt with a default number concentration of 1500, 20, 0.023 cm^{-3} respectively. The size distribution of each composition is assumed to follow the log normal distribution. The aerosol optical properties (including AOD) are calculated by Mie theory. The source function of production used here is the well-accepted exponential function : $N = N_0 exp(a_0 U_{10})$, where the N is the number concentration of particles and N_0 is the number concentration of particles at 0 ms^{-1} wind speed, the value of it decides the offset of the source function, while a_0 is the slope parameter with a range of $0.02 - 0.39$, the value found in southern oceans is from 0.031 to 0.049 with an average of 0.037 (Bigga et al., 1995), the U_{10} is the 10 meter wind speed.

Using the default clean marine aerosol parameters given by OPAC and three values of N_0, the relationship of AOD and wind speed under the RH of 80% is modelled (Figure 6.10). The modelled and observation results have the similar slopes but different offsets, which are sensitive to the value of N_0. Though the aerosol properties from OPAC are generalized and contain many assumptions, it confirms that the slope of our result is not effected by the systematic error discussed in the Sect. 6.2. On the offset, more works are required to understand the systematic error in the retrieval algorithm.

6.5 Conclusions

In this study, we examine the oceanic AOD at 0.55 μm obtained from AATSR as a function of the 10 meter wind fields from the ECMWF. The remote oceanic regions are defined by the wind direction and AOD. Using this criteria, the majority of the oceanic regions cannot be considered as pristine remote ocean because of long-range aerosol transportation from continents.

A linear relationship with a high correlation coefficient is found between wind speed and AOD at 0.55 μm in clear marine environment. The slope of the relationship is unequivocally determined but the offset is probably influenced by the systematic error. Thus more understanding about the systematic error in the retrieval is required.

Chapter 7

Conclusions and future work

7.1 Conclusions

AATSR is one of the most accurate space-borne radiometers. It measures the TOA radiance corresponding to seven spectral channels (from 550 nm to 12 μm) and has the ability of measuring the same area of the Earth's surface at two viewing angles (0° and 55°) with different atmospheric paths, which can provide additional information for atmospheric correction.

Aiming to improve the current knowledge of aerosol and surface properties, in particular over ocean, this thesis proposes a new algorithm based on the optimal estimation approach. This new algorithm is a further development of the ORAC, comparing with the previous version described in Thomas et al. (2011) and Sayer (2008), it has two new features:

- The algorithm now makes use of both AATSR visible and infrared channels, getting more measurement information about the atmosphere and surface.
- The implement of the infrared channels enables the retrieval of surface temperature and aerosol layer height.

The new ORAC algorithm is set up to retrieve the AOD at 550 nm, effective radius, surface white sky albedo at four wavelengths (550, 670, 870, and 1600 nm), surface temperature, and aerosol layer height. In order to access the performance of the new algorithm quantitatively, the principal retrieval parameters, AOD at 550 nm and SST, have been validated with measurements from other algorithms or instruments.

Comparing with the GlobAEROSOL products, the new algorithm (denoted by ORAC) retrieves lower AOD (0.071 ± 0.012) and higher sea surface albedo globally (0.067 ± 0.006). The lower AOD, which also occurs in regional scales, is a promising result as previous studies showed GlobAEROSOL overestimated AOD especially over open ocean. The retrieved AOD also has been validated with ground-based measurements (AERONET). The results show a good agreement between ORAC and AERONET over ocean, the correlation is 0.820 at 550 nm and 0.807 for 870 nm. In contrast the validation with continental AERONET stations indicates a poor performance of ORAC over land. The possible reasons include cloud contamination, inappropriate assumed aerosol classes and insufficient treatments of land surface properties.

The retrieved SST has been compared with measurements from ship-based radiometers (ISAR) and drifting buoys. The comparison with ISAR indicates the ORAC SST has a very high correlation with ISAR SST (better than 0.980). For three collocation criteria the ORAC SST has positive biases (0.150 to 0.117 K) with relatively large RMSs (0.481 to 0.430 K). The comparison between ISAR and AATSR operational D2 product exhibits the D2 product has smaller biases ($\sim$ 0.01 K) and RMSs ($\sim$ 0.3 K), indicating the ORAC SST needs further improvements.

The validation with five-year drifting buoy measurements shows the ORAC SST has a median bias of -0.067 ± 0.366 K for approximately $20,000$ matches. In order to avoid the skin effect, only consider the matches with high wind speeds (≥ 6 ms^{-1}), the median bias decreases to -0.003 K and the RMS decreases to 0.298 K.

In addition, a theoretical error budget of SST has been carried out based on a wide range of the atmospheric and surface conditions. The results demonstrate the uncertainties in water vapour, temperature profiles are the dominant contributors to the error in SST, followed by the uncertainties in sea surface emissivity and radiative transfer model.

7.2 Directions for future work

During the development and validation of the algorithm, several points where further efforts may result in improved results have been uncovered.

7.2.1 Improve cloud/dust flags

Both aerosol and SST retrievals are only possible under cloud free conditions. Although ORAC uses sophisticated cloud flag scheme contained in the AATSR Level 1B data, in some scenes the scheme would fail in picking up residual cloud, especially over the northern Hemisphere (Thomas, 2012) and over land. Undetected cloud may cause problems in retrieval. Additionally, in some situations of heave loading aerosols, such as strong dust storms, may be flagged as cloud, leading to such events being missed.

7.2.2 Improve aerosol classes

Current ORAC retrieval contains four aerosol classes which have obvious impacts on infrared spectra, the validation results indicate that only using these four classes is not sufficient especially over land. In order to extend the capability of ORAC to detect aerosols, more aerosol classes are needed. Starting from literature and microphysical properties developed for the visible ORAC retrieval, new aerosol classes, like urban, volcanic, biomass burning, will be implemented.

7.2.3 Further retrieval validation

Due to the scarceness of AERONET, most of the AERONET stations used in this study are limited to coastal or continental stations and they do not provide enough sampling over open ocean where most of ocean retrievals take place. The Maritime Aerosol Network (MAN) data is a new aerosol observation network that provides ship-based measurements over open ocean, it offers an opportunity of validating ORAC over open ocean, this will be an attempt in the further work.

After implementing new aerosol classes which is suggested above, it is possible to retrieve aerosol over terrain or urban areas. In the thesis the retrieved aerosol parameters are validated at a spatial resolution of 10 × 10 km, this resolution is sufficient under favorable conditions. However, it is not enough on local or urban scales due to inherent aerosol variability and complicated surface properties. Therefore to carry out aerosol validation at a finer resolution is necessary. Furthermore, the validation in this study is for one month period, it is statistically robust to depict the retrieval quality. However to do the validation for a longer period can make the results more convincing if time permits.

On the other hand, most SST validation results presented in this thesis are under conditions of low AOD, it can been seen that the retrieved SST is not severely biased. Further validation is required to estimate the performance of ORAC at different levels of aerosol loading.

7.2.4 Improve precision of infrared forward model

Comparing with the LBL model RFM, the brightness temperature simulated by RTTOV suffers a relative significant cold bias. This work has quantified the precision of RTTOV is one of the important contributors to the error in SST. Increasing the precision of the forward model will allow for a better discrimination of aerosol and surface effects on the TOA measurements.

7.2.5 Improve retrieval over land

Beside enabling the retrieval of surface temperature and aerosol layer height, the other advantage of incorporation of infrared channels is to improve the aerosol retrieval over land, especially over bright surface. However this potential has not been fully explored due to the fact that land surface properties, including surface type and surface emissivity, are highly variable and hard to model. The RTTOV version 10 provides a land surface emissivity model, this model would be suitable to use for future work. Land surface temperature plays a central role in climate research and weather forecasting, it is necessary and possible for ORAC to get a good land surface temperature product.

7.2.6 Incorporate the 3.7 μm channel

The 3.7 μm channel is not used in the daytime retrieval because it is severely affected by solar radiation. Extending the algorithm to use the 3.7 μm channel may improve the characterisation of aerosol products and cloud flagging, as an increased number of measurements would make aerosol and surface signatures more distinct.

7.2.7 Implications for future sensors

As described in literature, AATSR performed exceptionally well over the mission time (2002-2012), generated the high quality data needed for accurate SST retrieval and other scientific purposes (LST, aerosol, cloud). The design and concept of AATSR, like the dual-view capability and high radiometric accuracy, shall be carried on by new sensors.

Due to the relatively narrow swaths (512 km) AATSR achieves global coverage around every three days. This may limit the capability of catching daily variation or tracking some events with short lifetime (such as dust storm, cyclone). The narrow swath of AATSR may also lead to small match-up databases with in-situ measurement. It is therefore necessary to for the future sensors to utilize a wider swath.

LST from satellite is increasingly useful for many different applications. The land surface exhibits highly heterogeneity in the visible spectrum, and also is strong related to the proportion of vegetation in the measurement FOV. The retrieval of LST may benefit from an improved resolution in visible channels.

The retrievals of SST and LST using infrared spectrum are only possible under cloud free conditions. The derived SST and LST are often contaminated by undetected cloud. Inclusion of more spectral channels can enhance cloud detection. The Sea and Land Surface Temperature Radiometer (SLSTR) on the ESA/EU GMES Sentinel-3 mission is the next instrument to maintain continuity with the ATSRs series. SLSTR builds directly on a proven heritage pioneered by AATSR, with advanced features. These include increased swath width, high resolution at solar channels and two additional spectral channels (1.375 μm and 2.25 μm) in support of cloud detection and fire minoring. It is hoped that the two additional channels will lead to an improvement in cloud detection which will eventually benefit the retrieval of SST/LST.

Bibliography

Ackerman, S. A.: Remote sensing aerosols using satellite infrared observations, Journal of Geophysical Research, 102, 17 069 – 17 079, 1997.

Alam, K., Trautmann, T., and Blaschke, T.: Aerosol optical properties and radiative forcing over mega-city Karachi, Atmospheric Research, 101, 773 – 782, 2011.

Alwis, D., Ignatov, A., Dash, P., Sapper, J., Pichel, W., Li, X., and Kihai, Y.: Validation of the NESDIS operational sea surface temperature products from AVHRR onboard NOAA 16-18, 2007.

Andreae, M. O. and Crutzen, P. J.: Atmospheric aerosols: Biogeochemical sources and role in atmospheric chemistry, Science, 276, 1052 – 1058, 1997.

Andreae, M. O. and Merlet, P.: Emission of trace gases and aerosols from biomass burning, Global Biogeochemical Cycles, 15, 955 – 966, 2001.

Andreae, M. O., Rosenfeld, D., Artaxo, P., Costa, A. A., Frank, G. P., Longo, K. M., and Silva-Dias, M. A. F.: Smoking rain clouds over the Amazon, Science, pp. 1337 – 1342, 2004.

Andreas, E. L.: A new sea spray generation function for wind speeds up to 32 m/s, Journal of Physical Oceanography, 28, 2175 – 2184, 1998.

Andrews, E., Sheridan, P. J., Fiebig, M., McComiskey, A., Ogren, J. A., Arnott, P., Covert, D., Elleman, R., Gasparini, R., Collins, D., Jonsson, H., Schmid, B., and Wang, J.: Comparison of methods for deriving aerosol asymmetry parameter, Journal of Geophysical Research, 111, D05S04, 2006.

Aumann, H. H.: Cloud-filtering and residual cloud screening, URL `http://airs.jpl.nasa.gov/documents/science_team_meeting_archive/2003_10/slides/Aumann_21oct03.science.survey.ppt`, 2003.

Bali, M. and Mittaz, J.: Inter-Comparison of IASI and AATSR IR channels, in: EUMETSAT Meteorological Satellite Conference, 2012.

Baran, A. J.: A review of the light scattering properties of cirrus, Journal of Quantitative Spectroscopy and Radiative Transfer, 110, 1239 – 1260, 2009.

Barton, J. J.: Interpretation of satellite-derivedseasurfacetemperatures, Advances in Space Research, 28, 165 – 170, 2001.

Bellouin, N., Boucher, O., Haywood, J., and Reddy, M. S.: Global estimate of aerosol direct radiative forcing from satellite measurements, Nature, 438, 1138 – 1141, 2005.

Benas, N., Hatzianastassiou, N., Matsoukas, C., Fotiadi, A., Mihalopoulos, N., and Vardavas, I.: Aerosol shortwave direct radiative effect and forcing based on MODIS Level 2 data in the Eastern Mediterranean (Crete), Atmospheric Chemistry and Physics, 11, 12 647 – 12 662, 2011.

Bergstrom, R. W., Pilewskie, P., Russell, P. B., Redemann, J., Bond, T. C., Quinn, P. K., and Sierau, B.: Spectral absorption properties of atmospheric aerosols, Atmospheric Chemistry and Physics, 7, 5937 – 5943, 2007.

Bertie, J. E. and Lan, Z. D.: Infrared intensities of liquids XX: The intensity of the OH stretching band of liquid water revisited, and the best current values of the optical constants of H2O(l) at 25C between 15,000 and 1 cm, Applied Spectroscopy, 50, 1047 – 1057, 1996.

Betts, A. K. and Ball, J. H.: Evaluation of the ERA-40 surface water budget and surface temperature for the Mackenzie River basin, Journal of Hydrometeorology, 4, 1194 – 1211, 2003.

Bigga, E. K., Gras, J. L., and Mossop, D. J. C.: Wind-produced submicron particles in the marine atmosphere, Atmospheric Research, 36, 55 – 68, 1995.

Birks, A.: Improvements to the AATSR IPF relating to land surface temperature, Tech. rep., Rutherford Appleton Laboratory, 2004.

Blanchard, D. C.: The production, distribution and bacterial enrichment of the sea-salt aerosol, pp. 407 – 454, Reidel, Boston, USA, 1983.

Bogdanoff, A. S.: Impact of airborne dust on sea surface temperature retrievals, Master's thesis, Florida State University, 2010.

Bollasina, M., Nigam, S., and Lau, K.-M.: Absorbing aerosols and summer monsoon evolution over South Asia: an observational portrayal, Journal of Climate, 21, 1138 – 1141, 2008.

Brown, J. H., Doherty, M., Anderson, G., and Berk, A.: `http://www.kirtland.af.mil/library/factsheets/factsheet.asp?id=7915`, 2004.

Brown, S. J., Harris, A. R., and Mason, I. M.: New aerosol robust sea surface temperature algorithms for the along-track scanning radiometer, Journal of Geophysical Research, 102, 27 973 – 27 989, 1997.

Buchwitz, M., de Beek, R., Burrows, J. P., Bovensmann, H., Warneke, T., Notholt, J., Meirink, J. F., Goede, A. P. H., Bergamaschi, P., Korner, S., Heimann, M., and Schulz, A.: Atmospheric methane and carbon dioxide from SCIAMACHY satellite data: initial comparison with chemistry and transport models, Atmospheric Chemistry and Physics, 5, 941 – 962, 2005.

Cappa, C. D., Onasch, T. B., Massoli, P., Worsnop, D. R., Bates, T. S., Cross, E. S., and Davidovits, P.: Radiative absorption enhancements due to the mixing state of atmospheric black carbon, Science, 337, 1078 – 1081, 2012.

Carroll, A. G. O. and Watts, J. G.: Validation of the AATSR Meteo product sea surface temperature, Journal of Atmospheric and Oceanic Technology, 23, 711 – 726, 2006.

Carroll, A. G. O., Eyre, J. R., and Saunders, R. W.: Three-way error analysis between AATSR, AMSR-E, and in situ sea surface temperature observations, Journal of Atmospheric and Oceanic Technology, 25, 1197 – 1207, 2008.

Castro, S. L., Wick, G. A., Jackson, D. L., and Emery, W. J.: Error characterization of infrared and microwave satellite sea surface temperature products for merging and analysis, Journal of Geophysical Research, 113, 2008.

Charlson, R. J. and Heintzenberg, J.: Aerosol forcing of climate, Chichester, UK; New York, NY: Wiley, 1995.

Chin, M., Kahn, R. A., Remer, L. A., and Yu, H.: Atmospheric aerosol properties and climate impacts, Tech. rep., NASA Goddard Space Flight Center, 2009.

Christensen, T., Knudsen, B. M., Pommereau, J.-P., Letrenne, G., Hertzog, A., Vial, F., Ovarlez, J., and Piot, M.: Evaluation of ECMWF ERA-40 temperature and wind in the lower tropical stratosphere since 1988 from past long-duration balloon measurements, Atmospheric Chemistry and Physics Discuss., 7, 3423 3450, 2007.

Chung, C. E., Ramanathan, V., and Kiehl, J. T.: Effects of the south Asian absorbing haze on the northeast monsoon and surface-air heat exchange, Journal of Climate, 15, 2462 – 2476, 2002.

Clarke, A., Kapustin, V., Howell, S., and Moore, K.: Sea-salt size distributions from breaking waves: Implications for marine aerosol production and optical extinction measurements during SEAS, Journal of Atmospheric and Oceanic Technology, 20, 1362 – 1374, 2003.

Coll, C. and Caselles, V.: Analysis of the atmospheric and emissivity influence on the split window equation for sea surface temperature, International Journal of Remote Sensing, 15, 1915 – 1932, 1994.

Cooke, W. F., Liousse, C., and Cachier, H.: Construction of a 1 x 1 fossil fuel emission data set for carbonaceous aerosol and implementation and radiative impact in the ECHAM4 model, Journal of Geophysical Research, 104, 22 137 – 22 162, 1999.

Corlett, G. and Merchant, C.: Round robin protocol, Tech. rep., University of Leicester, University of Edinburgh, 2011.

Corlett, G. K., Barton, I. J., Donlon, C. J., Edwards, M. C., Good, S., Horrocks, L., Llewellyn-Jones, D. T., Merchant, C., Minnett, P., Nightingal, T. J., Noyes, E. J., Carroll, A. G. O., Remedios, J. J., Robinson, I. S., Saunders, R. W., and Watts, J. G.: The accuracy of SST retrievals from AATSR: An initial assessment through geophysical validation against in situ radiometers, buoys and other SST data sets, Advances in Space Research, 37, 764 – 769, 2006.

Cornillon, P.: Sea surface temperature products for the oceanographic scientific research community, Joint Oceanographic Institutions, Inc., URL `http://books.google.co.uk/books?id=RaUPAQAAIAAJ`, 1989.

Cox, C.: Personal communication, 2012.

Cox, C. and Munk, W.: Some problems in optical oceanography, Journal of Marine Research, 14, 63 – 78, 1955.

Dee, D.: ECMWF reanalyses: Diagnosis and application, in: Seminar on Diagnosis of Forecasting and Data Assimilation Systems, 2009.

Dee, D. P., Uppala, S. M., Simmons, A. J., Berrisford, P., Poli, P., Kobayashi, S., Andrae, U., Balmaseda, M. A., and Vitarta, F.: The ERA-Interim reanalysis: configuration and performance of the data assimilation system, Quarterly Journal of the Royal Meteorological Society, 137, 553 – 597, 2011.

DeSouza-Machado, S. G., Strow, L. L., Hannon, S. E., and Motteler, H. E.: Infrared dust spectral signature from AIRS, Geophysical Research Letters, 33, 2006.

Diaz, J. P., Arbelo, M., and Exposito, F. J.: Relationship between errors in AVHRR derived sea surface temperature and the TOMS Aerosol Index, Geophysical Research Letters, 28, 1989 – 1992, 2001.

Dobbie, S., Li, J., Harvey, R., and Chylek, P.: Sea salt optical properties and GCM forcing at solar wavelengths, Atmospheric Research, 65, 211 – 233, 2003.

Donlon, C., Robinson, I. S., Reynolds, M., Wimmer, W., Fisher, G., Edwards, R., and T, J. N.: An infrared sea surface temperature autonomous radiometer (ISAR) for deployment aboard Volunteer Observing Ships (VOS), Journal of Atmospheric and Oceanic Technology, 25, 93 – 113, 2008.

Donlon, C. J. and Robinson, I. S.: Radiometric Validation of ERS-1 Along-Track Scanning Radiometer Average Sea Surface Temperature in the Atlantic Ocean, Journal of Atmospheric and Oceanic Technology, 15, 647 – 660, 1998a.

Donlon, C. J. and Robinson, I. S.: Radiometric validation of ERS-1 Along-Track Scanning Radiometer average sea surface temperature in the Atlantic ocean, Journal of Atmospheric and Oceanic Technology, 15, 635 – 646, 1998b.

Donlon, C. J., Minnett, P. J., Gentemann, C., Nightingale, T. J., Barton, I. J., Ward, B., and Murray, M. J.: Toward improved validation of satellite sea surface skin temperature measurements for climate, Journal of Climate, 15, 353 – 369, 2002.

Dragani, R.: On the quality of the ERA-Interim ozone reanalyses: comparisons with satellite data, Quarterly Journal of the Royal Meteorological Society, 137, 1312 – 1326, 2011.

Dubovik, O., Smirnov, A., Holben, B. N., King, M. D., Kaufman, Y. J., Eck, T. F., and Slutsker, I.: Accuracy assessments of aerosol optical properties retrieved from Aerosol Robotic Network (AERONET) Sun and sky radiance measurements, Journal of Geophysical Research, 105, 9791 – 9806, 2000.

Dubovik, O., Holben, B., Eck, T. F., Smirnov, A., and Kaufman, Y. J.: Variability of absorption and optical properties of key aerosol types observed in worldwide locations, Journal of the Atmospheric Sciences, 59, 590 – 608, 2002.

Eck, T. F., Hokben, B. N., and Reid, J. S.: Wavelength dependence of the optical depth of biomass burning, urban, and desert dust aerosols, Journal of Geophysical Research, 104, 31 333 – 31 349, 1999.

El-Metwally, M., Alfaro, S., Wahab, M. M. A., Favez, O., Mohamed, Z., and Chatenet, B.: Aerosol properties and associated radiative effects over Cairo (Egypt), Atmospheric Research, 99, 263 – 276, 2011.

Ellrod, G. O. and Connell, B. H.: Improved detection of airborne volcanic ash using multispectral infrared satellite data, Journal of Geophysical Research, 108, 2003.

Embury, O.: Personal communication, 2012.

Embury, O., Merchant, C. J., and Corlett, G. K.: A reprocessing for climate of sea surface temperature from the along-track scanning radiometers: Initial validation, accounting for skin and diurnal variability effects, Remote Sensing of Environment, 116, 62 – 78, 2012a.

Embury, O., Merchant, C. J., and Filipiak, M. J.: A reprocessing for climate of sea surface temperature from the along-track scanning radiometers: Basis in radiative transfer, Remote Sensing of Environment, 116, 32 – 46, 2012b.

Emeryand, W. J., Baldwin, D. J., Schlssel, P., and Reynolds, R.: Accuracy of in situ sea surface temperatures used to calibrate infrared satellite measurements., Journal of Geophysical Research, 106, 2387 – 2405, 2001.

Erickson, D. J. I. and Duce, R. A.: On the global flux of atmospheric sea salt, Journal of Geophysical Research, 93, 14 079 – 14 088, 1988.

ESA: ATSR Product Handbook. Version 2.2, `http://envisat.esa.int/handbooks/aatsr//`, 2007.

Exton, H. J., Latham, J., Park, P. M., Perry, S. J., Smith, M. H., and Allan, R. R.: The production and dispersion of marine aerosol, Quarterly Journal of the Royal Meteorological Society, 111, 817 – 837, 1985.

Fairall, C. W., Bradley, E. F., Godfrey, J. S., Wick, G. A., Edson, J. B., and Young, G. S.: Cool-skin and warm-layer effects on sea surface temperature, Journal of Geophysical Research, 101, 1295 – 1308, 1996.

Feingold, G., Jiang, H., and Harrington, J. Y.: On smoke suppression of clouds in Amazonia, Geophysical Research Letters, 32, L02 804, 2007.

Fitzgerald, J. W.: Marine aerosols: a review, Atmospheric Environment, 25A, 533 – 546, 1991.

Flentje, H., Dornbrack, A., Ehret, A. F. G., and Holm, E.: Evaluation of ECMWF water vapour fields by airborne differential absorption lidar measurements: a case study between Brazil and Europe, Atmospheric Chemistry and Physics, 7, 5033 5042, 2007.

Franois, C.: Sea surface temperature retrieval (NOAA14 and GOES-8) for the ocean and sea ice SAF, Tech. rep., CETP, 1999.

Gangale, G., Prata, A. J., and Clarisse, L.: The infrared spectral signature of volcanic ash determined from high-spectral resolution satellite measurements, Remote Sensing of Environment, 15, 414 – 425, 2010.

Garca, O. E., Daz, J. P., Expsito, F. J., Daz, A. M., Dubovik, O., Derimian, Y., Dubuisson, P., , and Roger, J.-C.: Shortwave radiative forcing and efficiency of key aerosol types using AERONET data, Atmospheric Chemistry and Physics, 12, 5129 – 5145, 2012.

Geer, A. J., Lahoz, W. A., Bekki, S., Bormann, N., Errera, Q., Eskes, H. J., Fonteyn, D., Jackson, D. R., Juckes, M. N., Massart, S., Peuch, V.-H., Rharmili, S., and Segers, A.: The ASSET intercomparison of ozone analyses: method and first results, Atmospheric Chemistry and Physics, 6, 5445 – 5474, 2006.

Gentemann, C. L., Donlon, C. J., Stuart-Menteth, A., and Wentz, F. J.: Diurnal signals in satellite sea surface temperature measurements, Geophysical Research Letters, 30, 1 – 4, 2003.

Gentemann, C. L., Wentz, F. J., and Mears, C. A.: In situ validation of tropical rainfall measuring mission microwave sea surface temperatures, Journal of Geophysical Research - Oceans, 109, 1 – 9, 2004.

Ghan, S. J., Guzman, G., and Abdul-Razzak, H.: Competition between sea salt and sulfate particles as cloud condensation, Journal of the Atmospheric Sciences, 55, 3340 – 3347, 1998.

Ginoux, P., Chin, M., Tegen, I., and Prospero, J. M.: Sources and distributions of dust aerosols simulated with the GOCART model, Journal of Geophysical Research, 160, 20 255 – 20 273, 2001.

Giorgi, F. and Bi, X.: Direct radiative forcing and regional climatic effects of anthropogenic aerosols over East Asia: A regional coupled climate-chemistry/aerosol model study, Journal of Geophysical Research, 107, 4439, 2002.

Glantz, P., Nilsson, E. N., and Hoyningen-Huene, W.: Estimating a relationship between aerosol optical thickness and surface wind speed over the ocean, Atmospheric Research, 92, 58 – 68, 2009.

Gobiet, A., Foelsche, U., Steiner, A. K., Borsche, M., Kirchengast, G., and Wickert, J.: Climatological validation of stratospheric temperatures in ECMWF operational analyses with CHAMP radio occultation data, Geophysical Research Letters, 32, L12 806, 2005.

Gong, S. L., Barrie, L. A., Blanchet, J. P., and Spacek, L.: Modeling size-distributed sea salt aerosols in the atmosphere: An application using Canadian climate models, pp. 337 – 344, Plenum Press New York, 1998.

Good, E. J., Kong, X., Embury, O., and Merchant, C. J.: An infrared desert dust index for the Along-Track Scanning Radiometers, Remote Sensing of Environment, 116, 159 – 176, 2012.

Gras, J. L. and Ayers, G. P.: Marine aerosol at southern mid-latitudes, Journal of Geophysical Research, 88, 10 661 – 10 666, 1983.

Griggs, M.: A method to correct satellite measurements of sea surface temperature for the effects of atmospheric aerosols, Journal of Geophysical Research, 90, 12 951 – 12 959, 1985.

Grini, A., Myhre, G., Sundet, J. K., and Isaksen, I. S. A.: Modeling the annual cycle of sea salt in the global 3D model Oslo CTM2: Concentrations, fluxes, and radiative impact, Journal of Climate, 15, 1717 – 1730, 2002.

Gu, L., Baldocchi, D., Verma, S. B., Black, T. A., Vesala, T., Falge, E. M., and Dowty, P. P.: Advantages of diffuse radiation for terrestrial ecosystem productivity, Journal of Geophysical Research, 107, 1 – 23, 2002.

Hansen, J., Johnson, D., Lacis, A., Lebedeff, S., Lee, P., Rind, D., and Russell, G.: Climate impact of increasing atmospheric carbon dioxide, Science, 213, 957 – 966, 1981.

Hansen, J., Sato, M., and Rueby, R.: Radiative forcing and climate response, Journal of Geophysical Research, 102, 6831 – 6864, 1997.

Hansen, J. E. and Pollack, J. B.: Near-infrared light scattering by terrestrial clouds, Journal of Atmospheric Science, 27, 799 – 808, 1970.

Harris, A. R. and Saunders, M. A.: Global validation of the along-track scanning radiometer against drifting buoys, Journal of Geophysical Research, 101, 12 127 – 12 140, 1996.

Haywood, J. and Boucher, O.: Estimates of the direct and indirect radiative forcing due to tropospheric aerosols: A review, Reviews of Geophysics, 38, 513 – 543, 2000.

Haywood, J. M. and Shine, K. P.: The effect of anthropogenic sulfate and soot aerosol on the clear-sky planetary radiation budget, Geophysical Research Letters, 22, 513 – 543, 1995.

Hegg, D. A.: Modelling the effects of heterogeneous cloud chemistry on the marine particle size distribution, Journal of Geophysical Research, 97, 12 927 – 12 933, 1992.

Heintzenberg, J., Charlson, R. J., Clarke, A. D., Liousse, C., Ramanathan, V., Shine, K. P., Wendisch, M., and Helas, G.: Measurements and modelling of aerosol single-scattering albedo:Progress, problems and prospects., Beitraege zur Physik der Atmosphaere, 70, 249 – 263, 1997.

Heintzenberg, J., Covent, D. C., and Dongenen, R. V.: Size distribution and chemical composition of marine aerosols: a compilation and review, Tellus Series B: Chemical and Physical Meteorology, 52, 1104 – 1122, 2003.

Hess, M. and Schult, I.: Optical properties of aerosols and clouds: The software package OPAC, Bulletin of the American Meteorological Society, 79, 831 – 844, 1998.

Hildemann, L. M., Markowski, G. R., and Cass, G. R.: Chemical composition of emissions from urban sources of fine organic aerosol, Environmental Science and Technology, 25, 744 – 759, 1991.

Ho, S. P., Zhou, X., Kuo, Y. H., Hunt, D., and hong Wang, J.: Global evaluation of radiosonde water vapor systematic Biases using GPS Radio Occultation from COSMIC and ECMWF analysis, Remote Sensing, 2, 1320 – 1330, 2010.

Holben, B. N., Eck, T. F., Slutsker, I., Smirnov, A., Sinyuk, A., Schafer, J., Giles, D., and Dubovik, O.: Aeronet's Version 2.0 quality assurance criteria, in: Conference on Remote Sensing of the Atmosphere and Clouds, Goa,India, 2006.

Hoppel, W. A., Fitzgerald, J. W., and Mack, E. J.: Aerosol size distributions and optical properties found in the marine boundary layer over the Atlantic Ocean, Journal of Geophysical Research., 95, 3659 – 3686, 1990.

Huang, H., Fang, W., and Zheng, G. G.: Aircraft observation of aerosol distribution in Beijing urban boundary layer during falltime, Acta Scientiarum Naturalium Universitatis Pekinensis, 45, 273 – 278, 2009.

Huang, H., Thomas, G. E., and Grainger, R. G.: Relationship between wind speed and aerosol optical depth over remote ocean, Atmospheric Chemistry and Physics, 10, 5943 – 5950, 2010.

Hyer, E. H., Reid, J. S., and Zhang, J.: An over-land aerosol optical depth data set for data assimilation by filtering, correction, and aggregation of MODIS Collection 5 optical depth retrieval, Atmospheric measurement Technology, 4, 379 – 408, 2011.

I. N, S. and Toon, O. B.: Direct radiative forcing by anthropogenic airborne mineral aerosols, Nature, 381, 681 – 683., 1996.

Iacobellis, S. F., Frouin, R., and Somerville, R. C. J.: Direct climate forcing by biomass burning aerosols: Impact of corrections between controlling variables, Journal of Geophysical Research, 104, 12 031 – 12 045, 1999.

Iacovazzi, R. A.: Along Track Scanning Radiometers (ATSR) and their potential use for inter-calibration, GSICS Quarterly, 3, 1 –6, 2009.

IASI: Validation of IASI L2Pcore sea surface temperature, Tech. rep., EUMETSAT, 2011.

IPCC, ed.: Intergovernmental panel on climate change (IPCC) (2007), climate change 2007. The fourth assessment report of the IPCC, Cambridge University Press, Cambridge,U.K., 2007.

Jacobowitz, H.: Climate measurement requirements for the National Polar-orbiting Operational Environmental Satellite System (NPOESS), University of Maryland, College Park, MD, 27-29 February 1996: workshop report, University Corporation for Atmospheric Research, URL `http://books.google.co.uk/books?id=w1gRAQAAIAAJ`, 1997.

Jacobson, M. Z.: Global direct radiative forcing due to multicomponent anthropogenic and natural aerosols, Journal of Geophysical Research, 106, 1551 – 1568, 2001a.

Jacobson, M. Z.: Strong radiative heating due to the mixing state of black carbon in atmospheric aerosols, Nature, 409, 695 – 697, 2001b.

Jacobson, M. Z.: Control of fossil-fuel particulate black carbon and organic matter, possibly the most effective method of slowing global warming, Journal of Geophysical Research, 107, 4410, 2002.

Jacobson, M. Z.: Climate response of fossil fuel and biofuel soot, accounting for soots feedback to snow and sea ice albedo and emissivity, Journal of Geophysical Research, 109, D21 201, 2004.

Janhll, S., Andreae, M. O., and Pschl, U.: Biomass burning aerosol emissions from vegetation fires: particle number and mass emission factors and size distributions, Atmospheric Chemistry and Physics, 10, 1427 – 1439, 2010.

Jennings, S. G., Kleefeld, C., O'Dowd, C. D., Junker, C., Spain, T. G., O'Brien, P., Roddy, A. F., and O'Connor, T. C.: Mace Head atmospheric research station - Characterization of aerosol radiative parameters, Boreal Environment Research, 8, 303 – 314, 2003.

Justus, C. G. and Paris, M. V.: A model for Solar spectral irradiance and radiance at the bottom and top of a cloudless atmosphere, Journal of Climate and Applied Meteorology, 24, 193 – 205, 1985.

Kahn, R. A., Garay, M. J., Nelson, D. L., Levy, R. C., Bull, M. A., Martonchik, D. J. D. J. V., Hansen, E. G., Remer, L. A., and Tanr, D.: Response to toward unified satellite climatology of aerosol properties: 3. MODIS versus MISR versus AERONET, Journal of Quantitative Spectroscopy and Radiative Transfer, 112, 901 – 908, 2011.

Kanakidou, M., Seinfeld, J. H., Pandis, S. N., Barnes, I., Dentener, F. J., Facchini, M. C., and Dingenen, R. V.: Organic aerosol and global climate modelling: a review, Atmospheric Chemistry and Physics, 5, 1053 – 1123, 2005.

Kanamitsu, M. and Hwang, S.: The role of sea surface temperature in reanalysis, Monthly Weather Review, 134, 532 – 552, 2006.

Kanniah, K. D., Beringer, J., North, P., and Hutley, L.: Control of atmospheric particles on diffuse radiation and terrestrial plant productivity: A review, Progress in Physical Geography, 36, 209 – 237, 2012.

Kaplan, A., Cane, M. A., Kushnir, Y., Clement, A. C., Blumenthal, M. B., and Rajagopala, B.: Analyses of global sea surface temperature 1856-1991, Journal of Geophysical Research, 103, 18 567 – 18 589, 1998.

Kaufman, Y. J., Tanr, D., and Boucher, O.: A satellite view of aerosols in the climate system, Nature, 419, 215 – 223, 2002.

Kaufman, Y. J., Boucher, O., Tamré, D., Chin, M., Remer, L. A., and Takemura, T.: Aerosol anthropogenic component estimated from satellite data, Geophysical Research Letters, 32, L17 804, 2005.

Kim, N. K., Kim, Y. P., and Kang, C. H.: Long-term trend of aerosol composition and direct radiative forcing due to aerosols over Gosan: TSP, PM10, and PM2.5 data between 1992 and 2008, Atmospheric Environment, 45, 6107 – 6155, 2011.

King, M. D., Kaufman, Y. J., Tanr, D., and Nakajima, T.: Remote sensing of tropospheric aerosols from space: past, present, and future, Bulletin of the American Meteorological Society, 80, 2229 – 2259, 1999.

Klein, S. A., Soden, B. J., and Lau, N. C.: Remote sea surface temperature variations during ENSO: Evidence for a tropical atmospheric bridge, Journal of Climate, 12, 917 – 932, 1999.

Knobelspiesse, K. D., Pietras, C., Fargion, G. S., Wang, M. H., Frouin, R., Miller, M. A., Subramaniam, S., and Balch, W. M.: Maritime aerosol optical thickness measured by handheld sun- photometers, Remote Sensing Environment, 93, 87 – 106, 2004.

Knuteson, B. M., Christensen, T., Hertzog, A., Deme, A., Vial, F., and Pommereau, J.: Accuracy of analysed temperatures, winds and trajectories in the Southern Hemisphere tropical and midlatitude stratosphere as compared to long-duration balloon flights, Atmospheric Chemistry and Physics, 6, 5391–5397, 2006.

Koch, D.: The transport and direct radiative forcing of carbonaceous and sulfate aerosols in the GISS GCM, Journal of Geophysical Research, 106, 20 311 – 20 332, 2001.

Kohler, C. H., Trautmann, T., Lindermeir, E., Vreeling, W., Lieke, K., Kandler, K., and Wenzierl, B.: Thermal IR radiative properties of mixed mineral dust and biomass aerosol during SAMUM-2, Tellus, 63, 751 – 769, 2011.

Kulmala, M., Pirjola, U., and Makela, J. M.: Stable sulphate clusters as a source of new atmospheric particles, Nature, 404, 66 – 69, 2000.

Kvalevag, M. M.: Human impact on direct and diffuse solar radiation during the industrial era, Journal of Climate, 20, 4874 – 4883, 2007.

Latham, J. and Smith, M. H.: Effect on global warming of wind-dependent aerosol generation at the ocean surface, Nature, 347, 372 – 373, 1990.

Lehahn, Y., Koren, I., Altaratz, O., and Kostinski, A. B.: Effect of coarse marine aerosols on stratocumulus cloud, Geophysical Research Letters, 38, L20 804, 2011.

Lewis, E. R. and Schwartz, S. E.: Sea salt aerosol production: mechanisms, methods, measurements, and models, American Geophysical Union, 2004.

Liu, D., Wang, Z., Liu, Z., Winker, D., and Trepte, C.: A height resolved global view of dust aerosols from the first year CALIPSO lidar measurements, Journal of Geophysical Research, 113, D16 214, 2008.

Liu, P., Zhao, C., Zhang, Q., Deng, Z., Huang, M., Ma, X., and Tie, X.: Aircraft study of aerosol vertical distributions over Beijing and their optical properties, Tellus, 61, 756 – 767, 2009.

Llewellyn-Jones, D. and Remedios, J.: The Advanced Along Track Scanning Radiometer (AATSR) and its predecessors ATSR-1 and ATSR-2: An introduction to the special issue Preface, Remote Sensing of Environment, 116, 1 – 3, 2012.

Llewellyn-Jones, D., Edwards, M. C., Mutlow, C. T., Birks, A. R., Barton, I. J., and Tait, H.: AATSR: global-change and surface-temperature measurements from Envisat, ESA Bulletin, 105, 11 – 21, 2001.

Lohmann, U. and Feichter, J.: Global indirect aerosol effects: a review, Atmospheric Chemistry and Physics, 5, 715 – 737, 2005.

Mann, M. E., Bradlet, R. S., and Hughes, M. K.: Global-scale temperature patterns and climate forcing over the past six centuries, Nature, 392, 779 – 787, 1998.

Mantua, N. J. and Hare, S. R.: The Pacific decadal oscillation, Journal of Oceanography, 58, 35 – 44, 2002.

Masuda, K.: Influence of wind direction on the infrared sea surface emissivity model including multiple reflection effect, Meteorology and Geophysics, 63, 1 – 13, 2012.

Masuda, K., Takashima, T., and Takayama, Y.: Emissivity of pure and sea waters for the model sea surface in the infrared window regions, Remote Sensing of Environment, 24, 313 – 329, 1988.

Matricardi, G. M. M. and Serio, C.: The use of IASI data to identify systematic errors in the ECMWF tempeaature analysis in the upper stratosphere, Atmospheric Chemistry and Physics Discuss, 10, 22 725 – 22 764, 2010.

Matricardi, M.: An assessment of the accuracy of the RTTOV fast radiative transfer model using IASI data, Atmospheric Chemistry and Physics Discussion, 9, 9491 – 9535, 2009.

May, D. A., Stowe, L. L., Hawkins, J. D., and McClain, E. P.: A correction for Saharan dust effects on satellite sea surface temperature Measurements, Journal of Geophysical Research, 97, 3611 – 3619, 1992.

McClain, E. P.: Multiple atmospheric window techniques for satellite derived sea surface temperature, Oceanography From Space, 13, 73 – 85, 1981.

McClain, E. P., Pichel, W. G., and Walton, C. C.: Comparative performance of AVHRR-based multichannel sea surface temperatur, Journal Geophysical Research, 90, 11 587 – 11 601, 1985.

McDonald, R. L., Unni, C. K., and Duce, R. A.: Estimation of atmospheric sea salt dry deposition: Wind speed and particle size dependence, Journal of Geophysical Research, 87(C2), 1246 – 1250, 1982.

Menon, S., Hansen, K., Nazarenko, L., and Luo, Y.: Climate effects of black carbon aerosols in China and India, Science, 297, 2250 – 2253, 2002.

Merchant, C. J. and Saunders, M. A.: Infrared Satellite Retrievals in the Presence of Stratospheric Aerosol, Journal of Atmospheric and Oceanic Technology, 15, 835 – 840, 1998.

Merchant, C. J., Harris, A. R., Murray, M. J., and Zavody, A. M.: Toward the elimination of bias in satellite retrievals of sea surface temperature 1. Theory, modeling and interalgorithm comparison, Journal of Geophysical Research, 104, 23 565 – 23 578, 1999.

Merchant, C. J., Harris, A. R., Maturi, E., and Maccallum, S.: Probabilistic physically based cloud screening of satellite infrared imagery for operational sea surface temperature retrieval, Quarterly Journal of the Royal Meteorological Society, 131, 2735 – 2755, 2005.

Merchant, C. J., Embury, O., Borgne, P. L., and Bellec, B.: Saharan dust in nighttime thermal imagery: Detection and reduction of related biases in retrieved sea surface temperature, Remote Sensing of Environment, 104, 15 – 30, 2006.

Merchant, C. J., Borgne, P. L., Marsouin, A., and Roquet, H.: Optimal estimation of sea surface temperature from split-window observations, Remote Sensing of Environment, 112, 2469 – 2484, 2008.

Merchant, C. J., Borgneb, P. L., Roquetb, H., and Marsouinb, A.: Sea surface temperature from a geostationary satellite by optimal estimation, Remote Sensing of Environment, 113, 445 – 457, 2009.

Merchant, C. J., Borgne, P. L., Roquet, H., and Legendre, G.: Extended optimal estimation techniques for sea surface temperature from the Spinning Enhanced Visible and Infra-Red Imager (SEVIRI), Remote Sensing of Environment, 131, 287 – 297, 2013.

Meywerk, J. and Ramanathan, V.: Observations of the spectral clear-sky aerosol forcing over the tropical Indian Ocean, Journal of Geophysical Research, 104, 24 359 – 24 370, 1999.

Minnett, P. J. and Hanafin, J. A.: At-sea measurements of surface emissivity in the thermal infrared, presented by poster in the Match 2005 MODIS Science Team Meetings, Baltimore, U.S., 2005.

Mishchenk, M. I., Lacis, A. A., Carlson, B. E., and Travis, L. D.: Non sphericity of dust-like tropospheric aerosols: Implications for aerosol remote sensing and climate modeling, Geophysical Research Letters, 22, 1077 – 1080, 1995.

Mishchenko, M. I. and Geogdzhayev, I. V.: Satellite remote sensing reveals regional tropospheric aerosol trends, Optics Express, 15, 7423 – 7438, 2007.

Monahan, E. C., Spiel, D. E., and Davidson, K. L.: A model of marine aerosol generation via whitecaps and wave disruption in oceanic whitecaps, pp. 167 – 174, D. Deidel Publishing, Dordrecht, Holland, 1986.

Moore, D. P. and Remedios, J. J.: Growth rates of stratospheric HCFC-22, Atmospheric Chemistry and Physics, 8, 73 – 82, 2008.

Moore, D. P., Remedios, J. J., and Waterfall, A. M.: Global distributions of acetone in the upper troposphere from MIPAS spectra, Atmospheric Chemistry and Physics, 12, 757 – 768, 2012.

Moorthy, K. K. and Satheesh, S. K.: Characteristics of aerosols over a remote island, Minicoy in the Arabian Sea: Optical properties and retrieved size characteristics, Quarterly Journal of the Royal Meteorological Society, 126, 81 – 109, 2000.

Moorthy, K. K., Satheesh, S. K., and Murthy, B. V. K.: Investigations of marine aerosols over the tropical Indian Ocean, Journal of Geophysical Research, 102, 827 – 842, 1997.

Morcrette, J.: Radiation and cloud radiative rroperties in the European Centre for Medium Range Weather Forecasts forecasting system, Journal of Geophysical Research, 96, 9121 – 9132,, 1991.

Mulcahy, J. P., O'Dowd, C. D., and Ceburnis, S. G. J. D.: Significant enhancement of aerosol optical depth in marine air under high wind conditions, Geophysical Research Letters, 35, L16 810 – L16 813, 2008.

Murray, M. J., Allen, M. R., Merchant, C. J., Harris, A. R., and Donlon, C. J.: Direct observations of skin-bulk SST variability, Geophysical Research Letters, 27, 1171 – 1174, 2000.

Mutlow, C. T., Zavody, A. M., Barton, I. J., , and Llewellyn-Jones, D. T.: Sea surface temperature measurements by the along-track scanning radiometer on the ERS-1 satellite: Early results, Journal Geophysical Research, 99, 22 575 – 22 588, 1994.

Myhre, G., Berntsen, T. K., Haywood, J. M., Sundet, J. K., Holben, B. N., Johnsrud, M., and Stordal, F.: Modeling the solar radiative impact of aerosols from biomass burning during the Southern African Regional Science Initiative (SAFARI-2000) experiment, Journal of Geophysical Research, 108, 8501, 2003.

Myhre, G., Stordal, F., Johnsrud, M., Ignatov, A., and Mishchenko, M. I.: Intercomparison of satellite retrieved aerosol optical depth over ocean, Journal of Atmospheric Science, 61, 499 – 513, 2004.

Myhre, G., Stordal, F., Johnsrud, M., Diner, D. J., Geogdzhayev, I. V., Haywood, J. M., Holben, B. N., Holzer-Popp, T., Ignatov, A., Kahn, R. A., Kaufman, Y. J., Loeb, N., Martonchik, J. V., Mishchenko, M. I., Nalli, N. R., Remer, L. A., Schroedter-Homscheidt, M., Tanr, D., Torres, O., and Wang, M.: Intercomparison of satellite retrieved aerosol optical depth over ocean during the period September 1997 to December 2000, Atmospheric Chemistry and Physics, 5, 1697 – 1719, 2005.

Myhre, G., Samset, B. H., Schulz, M., and Balkanski, Y.: Radiative forcing of the direct aerosol effect from AeroCom Phase II simulations, Atmospheric Chemistry and Physics Discussion, 12, 22 355 – 22 413, 2012.

Nalli, N. R. and Reynolds, R. W.: Sea surface temperature daytime climate analyses derived from aerosol bias-corrected satellite data, Journal of Climate, 19, 410 – 428, 2006.

Nalli, N. R. and Stowe, L. L.: Aerosol correction for remotely sensed sea surface temperatures from the National Oceanic and Atmospheric Administration advanced very high resolution radiometer, Journal Geophysical Research, 107, 3172, 2002.

Newman, S. M., Smith, J. A., Glew, M. D., Rogers, S. M., and Taylor, J. P.: Temperature and salinity dependence of sea surface emissivity in the thermal infrared, Quarterly Journal of the Royal Meteorological Society, 131, 2539 – 2557, 2005.

Niclo's, R., Valor, E., V.Caselles, Coll, C., and Sanchez, J. M.: In situ angular measurements of thermal infrared sea surface emissivityValidation of models, Remote Sensing of Environment, 94, 83 – 93, 2005.

Nightingale, T. J. and Birks, A. R.: AATSR Algorithm Verification: Comparison of AATSR and ATSR-2 Data, AATSR Technical Note, Tech. rep., Rutherford Appleton Laboratory, 2004.

Nilsson, E. D., Rannik, U., and Norman, M.: Turbulent aerosol fluxes over the Arctic Ocean 2: Wind-driven sources from the sea, Journal of Geophysical Research, 106, 32 139 – 32 154, 2001.

Noyes, E. J.: An investigation into the accuracy of surface temperatures retrieval from the AATSR, Ph.D. thesis, University of Leicester, 2005.

Noyes, E. J., Minnett, P. J., J. J. Remedios a, G. K. C., Good, S. A., and Llewellyn-Jones, D. T.: The accuracy of the AATSR sea surface temperatures in the Caribbean, Remote Sensing of Environment, 101, 38 – 51, 2006.

O'Donnell, D., Tsigaridis, K., and Feichter, J.: Estimating the direct and indirect effects of secondary organic aerosols using ECHAM5-HAM, Atmospheric Chemistry and Physics, 11, 8635 – 8659, 2011.

O'Dowd, C. and Leeuw, G.: Marine aerosol production: a review of the current knowledge, Philosophical Transactions of the Royal Society A: Physical, Mathematical and Engineering Sciences, 365, 1753 – 1774, 2007.

O'Dowd, C. D. and Smith, M. H.: Physicochemical properties of aerosols over the northeast Atlantic: Evidence for wind-speed-related submicron sea-salt production, Journal of Geophysical Research, 98, 1137 – 1149, 1993.

O'Dowd, C. D., Smith, M. H., Consterdine, I. E., and Lowe, J. A.: Marine aerosol, sea-salt, and the marine sulphur cycle: a short review, Atmospheric Environment, 10, 1352 – 2310, 2001.

Ohring, G., Wielicki, B., Spencer, R., Eemry, B., and Datla, R.: Satellite instrument calibration for measuring global climate change, in: Workshop on satellite instrument calibration for measuring global climate change, 2005.

Oikonomou, E. K. and O'Neill, A.: Evaluation of ozone and water vapor fields from the ECMWF reanalysis ERA-40 during 1991 1999 in comparison with UARS satellite and MOZAIC aircraft observations, Journal of Geophysical Research, 111, 2006.

Old, C. and Merchant, C.: (A)ATSR re-analysis for climate - cloud clearing methodology, in: Envisat Symposium 2007, 2007.

Ostle, B. and Malone, L. C.: Statistics in research: Basic concepts and techniques for research workers, Iowa State University Press, 4th edition edn., 1988.

Palacios-Orueta, A., Chuvieco, E., Parra, A., and Carmona-Moreno, C.: Biomass burning emissions: A review of models using remote-sensing data, Environmental Monitoring and Assessment, 104, 189 – 209, 2004.

Pandithurai, G., Dipu, S., Dani, K. K., Bisht, S. T. D. S., Devara, P. C. S., , and Pinker, R. T.: Aerosol radiative forcing during dust events over New Delhi, India, Journal of Geophysical Research, 113, 3209, 2008.

Penner, J. E., Dickinson, R. E., and ONeill, C. A.: Effects of aerosol from biomass burning on the global radiation budget, Science, 256, 1432 – 1434, 1992.

Penner, J. E., Chuang, C. C., and Grant, K.: Climate forcing by carbonaceous and sulfate aerosols, Climate Dynamics, 14, 839 – 851, 1998.

Picchiazzi, P. J. and Gautier, C.: Sensitivity of clear-sky diffuse radiation to in situ aerosol scattering parameters, in: Thirteenth ARM Science Team Meeting Proceedings, Broomfield, 2003.

Platt, C. M. R. and Patterson, G. R.: The interpretation of baseline atmospheric turbidity measurements at Cape Grim, Journal of Atmospheric Chemistry, 4, 187 – 197, 1986.

Portela, O., Thomas, G., Poulsen, C., and Grainger, D.: Globaerosol final report, Tech. rep., European space agency and Oxford University and Rutherford Appleton Laboratory, 2009.

Poulsen, C. A., Siddans, R., Thomas, G. E., Sayer, A., Grainger, R. G., Perez-Navarro, O., Portela-Arjona, O., and Deschamps, P. Y.: ESA GlobAerosol: Final validation and intercomparison report Version 3.2, Tech. rep., Rutherford Appleton Laboratory, U.K., University of Oxford, U.K. and GMV Aerospace, Spain and University of Lille, France, 2009.

Prospero, J. M.: Long-range transport of mineral dust in the global atmosphere: Impact of African dust on the environment of the southeastern United States, in: National Academy of Sciences colloquium Geology, Mineralogy, and Human Welfare, vol. 96, pp. 3396 – 3403, Arnold and Mabel Beckman Center in Irvine, CA, 1998.

Qian, Y., Wang, W., Leung, L. R., and Kaiser, D. P.: Variability of solar radiation under cloud-free skies in China: The role of aerosols, Geophysical Research Letters, 34, L12 804, 2007.

Quaas, J., Boucher, O., Bellouin, N., and Kinne, S.: Satellite-based estimate of the direct and indirect aerosol climate forcing, Journal of Geophysical Research, 113, D05 204, 2008.

Ramanathan, V. and Carmichael, G.: Global and regional climate changes due to black carbon, Nature Geoscience, 1, 221 – 227, 2008.

Randel, W. J., Wu, F., Oltmans, S. J., Rosenlof, K., and Nedoluha, G. E.: Interannual changes of stratospheric water vapor and correlations with tropical tropopause, Journal of the Atmospheric Sciences, 61, 2133 – 2148, 2004.

Rao, C. R. N.: Aerosol radiative corrections to the retrieval of sea surface temperatures from infrared radiances measured by the Advanced Very High Resolution Radiometer (AVHRR), International Journal of Remote Sensing, 13, 1757–1769, 1992.

Reid, J. S., Koppmann, R., Eck, T. F., and Eleuterio, D. P.: A review of biomass burning emissions part II: intensive physical properties of biomass burning particles, Atmospheric Chemistry and Physics, 5, 799 – 825, 2005.

Remedios, J. J., Allen, G., Waterfall, A. M., Oelhaf, H., Kleinert, A., and Moore, D. P.: Detection of organic compound signatures in infra-red, limb emission spectra observed by the MIPAS-B2 balloon instrument, Atmospheric Chemistry and Physics, 7, 1599 – 1613, 2007a.

Remedios, J. J., Leigh, R. J., Waterfall, A. M., Moore, D. P., Sembhi, H., Parkes, I., Greenhough, J., Chipperfield, M. P., and Hauglustaine, D.: MIPAS Reference Atmospheres and comparisons to v4.61/v4.62 MIPAS level 2 geophysical data sets, Atmospheric Chemistry and Physics Discussion, 7, 9973 – 10 017, 2007b.

Reynolds, R. W.: Impact of Mount Pinatubo aerosols on satellite-derived sea surface temperatures., Journal of Climate, 6, 768 – 774, 1993.

Robinson, I. and Wimmer, W.: Validation of AATSR Sea Surface Temperature Products using the ship borne ISAR Radiometer - Phase 2 Final Report, Tech. rep., National Oceanography Centre, Southampton,U.K., 2008.

Rodgers, C. D.: Inverse methods for atmospheric sounding: Theory and practice, World Science, 2000.

Rodwell, M. J., Rowell, D. P., and Folland, C. K.: Oceanic forcing of the wintertime North Atlantic Oscillation and European climate, Nature, 398, 320 – 323, 1999.

Rosenfeld, D., Lohmann, U., Raga, G. B., O'Dowd, C. D., Kulmala, M., Fuzzi, S., Reissell, A., and Andreae, M. O.: Flood or drought: How do aerosols affect precipitation?, Science, 321, 1309 – 1313, 2008.

Rosenfeld, D., Clavner, M., and Nirel, R.: Pollution and dust aerosols modulating tropical cyclones intensities, Atmospheric Research, 102, 66 – 76, 2011.

Ruescas, A. B., Arbelo, M., Sobrino, R. A., and Mattar, C.: Examining the effects of dust aerosols on satellite sea surface temperatures in the Mediterranean sea using the Medspiration matchup database, Journal of Atmospheric and Oceanic Technology, 28, 684 – 697, 2011.

Sanderson, M. G.: Emission of carbon monoxide by vegetation and soils, Tech. rep., Hadley Centre, Metoffice, 2002.

Sandu, I., Brenguier, J.-L., Geoffroy, O., Thouron, O., and Masson, V.: Aerosol impacts on the diurnal cycle of marine stratocumulus, Journal of the Atmospheric Sciences, 65, 2705 – 2718, 2008.

Satheesh, S. K. and Srinivasan, J.: Contribution of sea-salt to aerosol optical depth over the Arabian Sea derived from MODIS observations, Geophysical Research Letters, 33, L03 809 – L03 813, 2006.

Satheesha, S. K. and Moorthy, K. K.: Radiative effects of natural aerosols: A review, Atmospheric Environment, 39, 2089 – 2110, 2005.

Saunders, R.: RTTOV-7 users guide, Tech. rep., Met Office UK, 2002.

Saunders, R., Hocking, J., Rayer, R., Matricardi, M., Geer, A., Bormann, N., Brunel, P., Karbou, F., and Aires, F.: RTTOV-10 sciences and validation report, Tech. rep., EUMETSAT Satellite Application Facility, 2012.

Sayer, A.: Aerosol remote sensing using AATSR, Ph.D. thesis, University of Oxford, 2008.

Schnaiter, M., Gimmler, M., Llamas, I., Linke, C., Jäger, C., and Mutschke, H.: Strong spectral dependence of light absorption by organic carbon particles formed by propane combustion, Atmospheric Chemistry and Physics, 6, 2981 – 2990, doi:10.5194/acp-6-2981-2006, URL `http://www.atmos-chem-phys.net/6/2981/2006/`, 2006.

Schulz, M., Textor, C., Kinne, S., Balkanski, Y., Bauer, S., Berntsen, T., Berglen, T., Boucher, O., Dentener, F., and Guibert, S.: Radiative forcing by aerosols as derived from the AeroCom present-day and pre-industrial simulations, Atmospheric Chemistry and Physics, 6, 5225 – 5246, 2006.

Seinfeld, J. H. and Pandis, S. N.: Atmospheric chemistry and physics: From air pollution to climate change, J. Wiley, New York, 1st edition edn., 1998.

Simoneit, B. R. T.: Biomass burning a review of organic tracers for smoke from incomplete combustion, Applied Geochemistry, 17, 129 – 162, 2002.

Singer, S. F.: The changing global environment, D. Reidel Publ. Co., Dordrecht-Holland Boston-USA, 1975.

Smirnov, A., Villevalde, Y., O'Neill, N. T., Royer, A., and Tarussov, A.: Aerosol optical depth over the oceans: Analysis in terms of synoptic air mass types, Journal of Geophysical Research, 16, 639 – 650, 1995.

Smirnov, A., Holben, B. N., Dubovik, O., Frouin, R., Eck, T. F., and Slutsker, I.: Maritime component in aerosol optical models derived from Aerosol Robotic Network data, Journal of Geophysical Research, 108(D1), 4033 – 4044, 2003.

Smith, A.: Microphysical modelling of aerosols in the ORAC retrieval, Ph.D. thesis, University of Oxford, 2011.

Smith, D.: ATSR-2 and AATSR instrument performance, in: AATSR and MERIS workshop, Rutherford Appleton Laboratory, 2008.

Smith, D., Mutlow, C., Delderfield, J., Warkins, B., and Mason, G.: ATSR infrared radiometric calibration and in-orbit performance, Remote Sensing of Environment, 116, 4 – 16, 2012.

Spitters, C. J. T., Toussaint, H. A. J. M., and Goudriaan, J.: Separating the diffuse and direct component of global radiation and its implications for modeling canopy photosynthesis Part I. Components of incoming radiation, Agricultural and Forest Meteorology, 38, 217 – 229, 1986.

Stark, J. D., Donlon, C., and Carroll, A. O.: Determination of AATSR biases using the OSTIA SST analysis system and a matchup database, Journal of Atmospheric and Oceanic Technology, 25, 1208 – 1217, 2008.

Strong, A. E. and McClain, E. P.: Improved ocean surface temperatures from space–Comparisons with drifting buoys, Bulletin of the American Meteorological Society, 65, 138 – 142, 1989.

Sykes, P., While, J., Sellar, A., and Martin, M.: Diurnal variability in sea surface temperature: Observation and model assessment, Tech. rep., Met Office, 2011.

Takemura, T., Nakajima, T., Dubovik, O., Holben, B. N., and Kinne, S.: Single-scattering albedo and radiative forcing of various aerosol species with a global three-dimensional model, Journal of Climate, 15, 333 – 352, 2002.

Tegen, I., Lacis, A., and Fung, I.: The influence of mineral aerosols from disturbed soils on climate forcing, Nature, 380, 419 – 422, 1996.

Tegen, I. P., Chin, M., Fung, I., Jacob, D., and Penner, J. E.: Contribution of different aerosol species to the global aerosol extinction optical thickness: Estimates from model results, Journal of Geophysical Research, 102, 23 895 – 23 915, 1997.

Thomas, G.: Personal communication, 2012.

Thomas, G. E., Carboni, E., Sayer, A. M., Poulsen, C. A., Siddans, R., and Grainger, R. G.: Satellite aerosol remote sensing over land, chap. 7, pp. 193 – 225, Edited by: A. A. Kokhanovsky and G. de Leeuw , Springer, Berlin, Germany, 2009.

Thomas, G. E., Poulsen, C. A., Siddans, R., Carboni, E., Sayer, A. M., and Grainger, R. G.: ORAC v3 dual-view aerosol retrieval from (A)ATSR, Tech. rep., AOPP,Oxford and RAL, 2011.

Thomas, G. E., Chalmers, N., Harris, B., Grainger, R. G., and Highwood, E. J.: Regional and monthly and clear-sky aerosol direct radiative effect (and forcing) derived from the GlobAEROSOL-AATSR satellite aerosol product, Atmospheric Chemistry and Physics, 13, 393 – 410, 2013.

Twomey, S.: Atmosperic aerosols, Elsevier, 1977.

Uppala, S. M., Allberg, P. W. K., Simmons, A. J., Andrae, U., Fiorino, M., Gibson, J. K., Haseler, J., Hernandez, A., Kelly, G. A., Li, X., Onogi, K., Saarinen, S., Sokka, N., Allan, R. P., Andersson, E., Arpe, K., Balmaseda, M. A., Beljaars, A. C. M., de Berg, V. L., Bidlot, J., Bormann, N., Caires, S., Chevallier, F., Dethof, A., Dragosavac, M., Fisher, M., Fuentes, M., Hagemann, S., Hólm, E., Hoskins, B. J., Isaksen, L., Janssen, P. A. E. M., Jenne, R., Mcnally, A. P., Mahfouf, J. F., Morcrette, J. J., Rayner, N. A., Saunders, R. W., Simon, P., Sterl, A., K. E. Trenberth, A. U., Vasiljevic, D., Viterbo, P., and Woollen, J.: The ERA-40 re-analysis, Quarterly Journal of the Royal Meteorological Society, 131, 2961 – 3012, 2005.

Valenzuela, A., Olmo, F. J., Lyamani, H., Anton, M., Quirantes, A., and Alados-Arboledas, L.: Aerosol radiative forcing during African desert dust events (2005-2010) over Southeastern Spain, Atmospheric Chemistry and Physics, 12, 10 331 – 10 351, 2012.

Vazquez-Cuervo, J. and Armstrong, E. M.: The effect of aerosols and clouds on the retrieval of infrared sea surface temperatures, Journal of Climate, 17, 3921 – 3933, 2004.

Villevalde, Y. V., Smirnov, A. V., O'Neill, N. T., Smyshlyaev, S. P., and Yakovlev, V. V.: Measurement of aerosol optical depth in the Pacific Ocean and the North Atlantic, Journal of Geophysical Research, 99, 983 – 988, 1994.

Vinoj, V. and Satheesh, S.: Direct and indirect radiative effects of sea salt aerosols over Arabian Sea, Current Science, 86, 1381 – 1390, 2004.

Walton, C.: Measurement of sea surface temperature in the presence of volcanic aerosols, Journal of Climate and Applied Meteorology, 24, 501 – 506, 1985.

Walton, C.: Nonlinear multichannel algorithms for estimating sea surface temperature with AVHRR satellite data, Journal of Applied Meteorology, 27, 115 – 124, 1988.

Walton, C. C., Pichel, W. G., Sapper, J. F., and May, D. A.: The development and operational application of nonlinear algorithms for the measurement of sea surface temperatures with the NOAA polar-orbiting environmental satellites, Journal of Geophysical Research, 103, 27 999 – 28 012, 1998.

Wang, C.: A modeling study on the climate impacts of black carbon aerosols, Journal of Geophysical Research, 109, D03 106, 2004.

Wang, C.: Impact of anthropogenic absorbing aerosols on clouds and precipitation: A review of recent progresses, Atmospheric Research, 122, 237 – 249, 2013.

Wang, Z., Zhang, H., Jing, X., and Wei, X.: Effect of non-spherical dust aerosol on its direct radiative forcing, Atmospheric Research, 120, 112 –126, 2013.

Watts, P., Allen, M., and Nightingale, T.: Sea surface emission and reflection for radiometric measurements made with the along-track scanning radiometer, Journal of Atmospheric and Oceanic Technology, 12, 126 – 141, 1996.

Watts, P. D., Mutlow, C. T., Baran, A. J., and Zavody, A. M.: Study on cloud properties derived from Meteosat second generation observations, Tech. rep., Rutherford Appleton Laboratory, 1998.

Wentz, F. J., Gentemann, C., and Smith, D.: Satellite measurements of sea surface temperature through clouds, Science, 288, 847 – 850, 2000.

Whitby, K. T. and Cantrell, B. K.: Atmospheric aerosols: characteristics and measurement, in: International Conference on Environmental Sensing and Assessment (ICESA), Institute of Electrical and Electronic Engineers (IEEE), 1976.

Wilcox, E. M.: Stratocumulus cloud thickening beneath layers of absorbing smoke aerosol, Atmospheric Chemistry and Physics, 10, 11 769 – 11 777, 2010.

Wild, M., Gilgen, H., Roesch, A., Ohmura, A., Long, C. N., Dutton, E. G., Forgan, B., Kallis, A., Russak, V., and Tsvetkov, A.: From dimming to brightening: Decadal changes in solar radiation at Earth's surface, Science, 308, 847 – 850, 2005.

Wimmer, W., Robinson, I. S., and Donlon, C. J.: Long-term validation of AATSR SST data products using shipborne radiometry in the Bay of Biscay and English Channel, Remote Sensing of Environment, 116, 17 – 31, 2012.

Wood, R.: Cancellation of aerosol indirect effects in marine stratocumulus through cloud thinning, Journal of the Atmospheric Sciences, 64, 2657 – 2669, 2007.

Wu, X. and Smith, W. L.: Emissivity of rough sea surface for 8 - 13 mum: Modelling and verification, Applied Optics, 36, 2609 – 2619, 1997.

Xue, H., Feingold, G., and Stevens, B.: Aerosol effects on clouds, precipitation, and the organization of shallow cumulus convection, Journal of the Atmospheric Sciences, 65, 392 – 406, 2008.

Yates, H., Cotter, D., and Ohring, G.: Operational satellite support to scientific programs, ENVIROSAT-2000 report, National Oceanic and Atmospheric Administration, National Environmental Satellite, Data, and Information Service, URL `http://books.google.co.uk/books?id=ipZZXwAACAAJ`, 1985.

Yoon, Y. J. and Brimblecombe, P.: Modelling the contribution of sea salt and dimethyl sulfide derived aerosol to marine CCN, Atmospheric Chemistry and Physics, 2, 17 – 30, 2002.

Yorks, J. E., McGill, M., Rodier, S., Vaughan, M., and HU, Y.: Radiative effects of African dust and smoke observed from Clouds and the Earths Radiant Energy System (CERES) and Cloud-Aerosol Lidar with Orthogonal Polarization (CALIOP) data, Journal of Geophysical Research, 114, D00H04, 2009.

Yu, H., Kaufman, Y. J., Chin, M., Feingold, G., Remer, L. A., Anderson, T. L., Balkanski, Y., Bellouin, N., Boucher, O., Christopher, S., DeCola, P., Kahn, R., Koch, D., Loeb, N., Reddy, M. S., Schulz, M., Takemura, T., and Zhou, M.: A review of measurement-based assessments of the aerosol direct radiative effect and forcing, Atmospheric Chemistry and Physics, 6, 613 – 666, 2006.

Yu, T., Rose, W. I., and Prata, A. J.: Atmospheric correction for satellite-based volcanic ash mapping and retrievals using split window IR data from GOES and AVHRR, Journal of Geophysical Research, 107, 2002.

Zavody, A. M., Mutlow, C. T., and Llewellyn-Jones, D. T.: A radiative transfer model for sea surface temperature retrieval for the along-track scanning radiometer, Journal of Geophysical Research, 100, 937 – 952, 1995.

Zavody, A. M., Mutlow, C. T., and Liewellyn-Jones, D. T.: Cloud clearing over the ccean in the processing of data from the Along-Track Scanning Radiometer (ATSR), Journal of Atmosperic and Oceanic Technology, 17, 595 – 615, 2000.

Zhang, H., Ma, J., and Zheng, Y.: Modeling study of the global distribution of radiative forcing by dust aerosol, Acta Meteorologica Sinica, 24, 558 – 570, 2010.

Zhao, T. X. P., Laszlo, I., Dubovik, O., Holben, B. N., Sapper, J., Tanre, D., and Pietra, C.: A study of the effect of non-spherical dust particles on the AVHRR aerosol optical thickness retrievals, Geophysical Research Letters, 30, 1317, 2003.